Analysis Note for $\gamma p \to p\phi\eta$

Bradford E. Cannon

June 18, 2019

Table of Contents

List of Tables

List of Figures

Chapter 1

Data, Codes, and Procedures

Contained within this document is a thorough description of how an analysis of the reaction $\gamma p \rightarrow p\phi\eta; \phi \rightarrow K^+K^-; \eta \rightarrow \gamma\gamma$ was performed. It should be immediately noted that this document is intended for any and all collaborating members of GlueX; including but not limited to: undergraduates, graduates, postdocs, staff scientists, and professors. Most of the information contained within this analysis note has been directly transfered from the thesis titled: "Search for New and Unusual Strangeonia States Using $\gamma p \rightarrow p\phi\eta$ With GlueX at Thomas Jefferson National Accelerator Facility". This work was completed by Bradford E. Cannon at Florida State University in order to obtain a PhD in Physics. The final version of the thesis can be found in the Publication→Theses→2019 section of the GlueX Wiki [1].

This first chapter will be dedicated towards answering three primary questions.

1. (Data Location) Where can the data and MC be found within the FSU/JLAB computing system, for a given section in this analysis note?

2. (Code Location) Where can the C++ codes be found within the FSU/JLAB computing system, for a given section in this analysis note?

3. (Relevant Procedures) What were the procedures to either run the C++ code, or to create the MC data, for a given section in this analysis note?

To do this, the subsections of this chapter will match the names of all chapters and subsections after it. If a subsequent chapter or subsection contains special data, an elaborate C++ code, or a technical computing procedure, instructions or examples will be provided here. It should be noted that not all future chapters and subsections will be highlighted here; only those which require additional information or explanation. Lastly, the information included here is specifically for individuals who have a good/decent understanding of: the GlueX analysis, C++, shell scripting, and distributed computing. If you feel that you may not be at this level, be sure to try the GlueX Analysis Workshops provided on the GlueX Wiki before attempting the material in this document.

1. (FSU) `HOME_DIR==/d/grid12/bcannon/PhiEta`

2. (JLAB) `HOME_DIR==/work/halld/home/bcannon/Analysis_Note`

1.1 Monte Carlo

Data Location:

This file is the sum total of all six Monte Carlo run numbers. This tree is after generation, hdgeant, mcsmear, and hdroot.
`HOME_DIR/Monte_Carlo_Data/genr8/Coherent/t_15/tree_kpkmgg.root`

Code Location:

The file which generates $\phi\eta$ phase space is given here. This is the file that is read by the command genr8.
`HOME_DIR/Monte_Carlo_Data/genr8/Coherent/t_15/PhiEta.input`
The file which describes the conditions for the generated Monte Carlo entering the detector is found here. This is the file that is read by the command hdgeant.
`HOME_DIR/Monte_Carlo_Data/genr8/Coherent/t_15/control.in`

Relevant Procedures:

Since this Monte Carlo generates roughly 1.7 million events for each run number, a 'poor mans' job submission was used on the FSU computing system. In order to recreate what is currently in this directory, one would need to run the following shell script with a run number passed as an argument. The shell script then takes care of everything by copying the appropriate files into a new directory and running all of the Monte Carlo codes in there. For each run number that is generated, there should be a separate hadron session associated with it; either by means of a new terminal or by opening a new vnc session.
`HOME_DIR/Monte_Carlo_Data/genr8/Coherent/t_15/generate.sh`

1.2 Data Selection

Data Location:

The trees that are run over by my DSelector can be found here.
`/d/grid13/bcannon/PhiEta/RunPeriod-2017-01/tree_ggkpkm/tree_ggkpkm__B4_*.root`
The resulting root file with an ntuple (that is used for the Quality Factor Analysis) can be found here. This output root file also contains ALL of the cuts utilized to select the $\gamma p \to pK^+K^-\gamma\gamma$ final state, which are administered by the DSelector.
`HOME_DIR/DSelector/kpkmgg/FinalCuts_NoCuts.root`

Code Location:

The DSelector that is used to select the $\gamma p \to pK^+K^-\gamma\gamma$ final state can be found here.
`HOME_DIR/DSelector/kpkmgg/DSelector_FinalCuts.C`
`HOME_DIR/DSelector/kpkmgg/DSelector_FinalCuts.h`

Relevant Procedures:

To run the DSelector over all of the aforementioned trees, the following codes were used. The shell script can take no argument, or an integer argument (numbers 1 through 6). Passing no argument will cause the shell script to run over the entire data set; while passing an integer argument will cause the shell script to run over one sixth of the data set. The purpose of this approach is to allow a 'poor mans' job submission. To run over the data more quickly, open six different terminal or vnc sessions, and then pass a different integer for each session.
`HOME_DIR/DSelector/kpkmgg/test_DSelector_RunNumber.sh`
The C++ code provided below is called by the shell script. This code will access the ROOT ProofLite package utilized by the DSelector library in order to incorporate a multi-threaded approach.
`HOME_DIR/DSelector/kpkmgg/test_DSelector_RunNumber.cxx`

1.3 Analysis

1.3.1 Probabilistic Weightings for $\phi\eta$ Events

Data Location:

The below root file is the sum total of all Spring 2017 data after selection cuts. This file includes the ntuple which is used to run the Probabilistic Event Weightings.
`HOME_DIR/DSelector/kpkmgg/FinalCuts_NoCuts.root`
When this file is run by the codes below, a new ntuple will be written to it which has multiple weight entries for each event in the old ntuple. An example output root file can be found here:
`HOME_DIR/QValue/PhiEta/MMSQ/Poly3/FinalCuts_NoCuts.root`

Code Location:

The C++ code which includes all of the intricacies of the Probabilistic Event Weighting can be found here. This code is called by the next C++ code, `Execute_QValue_Relativistic_PhiEta.C`.
`HOME_DIR/QValue/PhiEta/MMSQ/Poly3/Calculate_QValue_Relativistic_PhiEta.C`
The next C++ file is the primary code which defines all of the important fit functions and will grab the ntuple to be used for calculation.
`HOME_DIR/QValue/PhiEta/MMSQ/Poly3/Execute_QValue_Relativistic_PhiEta.C`

Relevant Procedures:

To run this code, I strongly suggest running root in batch mode and in a vnc session, as this will save a lot of time. As of right now, running this code over the 2017 data takes a little less than one day. Therefore it is imperative to utilize a vnc session. To run, type the command:

root -l -q -b `Execute_QValue_Relativistic_PhiEta.C()`

Be sure that `Calculate_QValue_Relativistic_PhiEta.C` and the appropriate root file are in the same directory.

1.3.2 Removal of N* Background

Data Location:

There are two relevant locations for this MC study. One of them contains the information about the N*, which can be found here:
`HOME_DIR/Monte_Carlo_Data/genr8/Coherent/NStar/NStar.gamp`
The other contains information about the generated states which came from the $\phi(1680)$ and $\phi(1850)$ mesonic topologies.
`HOME_DIR/Monte_Carlo_Data/genr8/Coherent/Flat/PhiEta.gamp`

Code Location:

The N* phase space is produced by calling genr8 which takes this as an input file:
`HOME_DIR/Monte_Carlo_Data/genr8/Coherent/NStar/NStar.input`
The $\phi(1680)$ and $\phi(1850)$ phase space is produced by calling genr8 which takes this as an input file:
`HOME_DIR/Monte_Carlo_Data/genr8/Coherent/Flat/PhiEta.input`

Relevant Procedures:

The important thing to remember with this study is that only generated events were used. It was not necessary to include acceptance or smearing. Also, the input file for the mesonic states were altered by simply changing the mass and width of the resonance which decayed to $\phi\eta$.

1.3.3 Acceptance Corrections for $\phi\eta$ Invariant Mass and $cos(\theta)_{GJ}$ Distributions

Data Location/Code Location/Relevant Procedures:

There are a number of different data sets, codes, and procedures that are used to make the acceptance plots. Since many of them are entangled and somewhat complicated, I have decided to put everything into one section.

The first step is to make files with the mass and GJ distributions. To do this, the file
`HOME_DIR/DSelector/kpkmgg/FinalCuts/TNtuple_Plot.C`
is used to make histograms for the dissertation. Contained within this file are many functions. However, the relevant information for the MC can be found at the bottom, in the primary macro `TNtuple_Plot()`. The macro has many procedures that are commented out. Be sure

that the procedures which call the MC are uncommented, and all others are commented out. The input file that this code expects is a file named `FinalCuts.root`, which will eventually be written to. To be very clear, because `TNtuple_Plot()` can make plots for many different data sets, `FinalCuts.root` can also represent many different data sets. Be careful with this fact. Once you have run `TNtuple_Plot()`, `FinalCuts.root` has changed and will contain new histograms, so it should be immediately renamed to save the results. Also, if you want to change the analysis that is being looked at, the initial `FinalCuts.root` must have the correct ntuple inside of it so that the correct results come out.

To get a version of `FinalCuts.root` that represents the generated MonteCarlo, use:
`HOME_DIR/Monte_Carlo_Data/genr8/Coherent/Acceptance/run.C`
which takes the output of a generated MC file and turns it into a root file with the same ntuple structure as the data. To get a version of `FinalCuts.root` that represents the accepted MonteCarlo, simply generate, simulate, smear, then reconstruct MC data then run the DSelector code:
`HOME_DIR/Monte_Carlo_Data/genr8/Coherent/DSelector/DSelector_FinalCuts.C/h`
After doing this for generated and accepted MC, the names of the output root files were changed and copied to a directory. The two relevant Monte Carlo files used are:
`HOME_DIR/DSelector/kpkmgg/FinalCuts/FinalCuts_MCAccepted.root`
`HOME_DIR/DSelector/kpkmgg/FinalCuts/FinalCuts_MCGenerated.root`
These files are used as input for the program:
`HOME_DIR/DSelector/kpkmgg/FinalCuts/MakeAcceptance.C`
The output of this program is a file called:
`HOME_DIR/DSelector/kpkmgg/FinalCuts/Correction.root`
All of the relevant histograms are inside this file. It should be noted that `MakeAcceptance.C` also expects a data file as well. This will not effect the results of the generated and accepted MC. It is there so that other histograms, namely the acceptance corrected data histograms, can be easily created.

1.3.4 Analysis of $\phi\eta$ Invariant Mass Plot and $cos(\theta)_{GJ}$ Distributions

If you have not done so already, read the second chapter of the previous section. It is relevant here as well.

Data Location:

The input data for this section comes from the output of Probabilistic Weightings for $\phi\eta$ Events; where the root file will now have a new ntuple with several weights assigned to each event. This input file must have the name:
`HOME_DIR/DSelector/kpkmgg/FinalCuts/FinalCuts.root`
As stated in paragraph two of the previous section, the output will be the same file, only with some histograms added to it. Be sure to change the name of the file if you want to save the results.

Code Location:

There is one very important code which creates all of the output histograms that are not acceptance corrected. This file is:
`HOME_DIR/DSelector/kpkmgg/FinalCuts/TNtuple_Plot.C`
Contained within this file are many functions. However, the relevant information for making the histograms can be found at the bottom, in the primary macro `TNtuple_Plot()`. The macro has many procedures that are commented out. Depending on which Quality Factor analysis you want to look at, you should uncomment the Plots anf Cuts files associated with that particular analysis. Each different analysis should be grouped together and it should be self explanatory as to which files correspond to which analysis. For example, if you want to look at the results for the quality factor analysis which only considers the weight of the ϕ, then uncomment the `*_QValuePhi.C` codes, and be sure that all other groupings are commented out.

The codes that declare and make the histograms for the ϕ only example are below. Contained withing the "Plots" code are the lines which fill the histogram. The important thing to notice here is that the weight which is used to fill the histograms is specific to the ϕ only analysis.
`HOME_DIR/DSelector/kpkmgg/FinalCuts/kpkmggCuts_QValuePhi.C`
`HOME_DIR/DSelector/kpkmgg/FinalCuts/kpkmggPlots_QValuePhi.C`
There is one more important detail that needs to be mentioned. Contained within the "Plots" code are functions named AddHists or DrawHists (depending on the analysis that is being considered). These functions will take in either two, or three inputs, depending on what you want to do. Since this analysis was highlighted by fitting the $\phi\eta$ invariant mass, there is an option to tell the code to include the fit or not. Since this section does not want to include a fit to this histogram, be sure that when these functions are called, there are only two inputs passed; not three. The two inputs that need to be passed are the canvas and histogram, but NOT the boolean "True".

Relevant Procedures:

root -l `TNtuple_Plot.C()`

1.3.5 Fitting $\phi\eta$ Invariant Mass Plots for Signal Distributions

Data Location:

The data explanation for this section is the same as above. This section will only highlight how to correctly fit.

Code Location:

The codes for this section are the same as the section above. However, in order to fit the $\phi\eta$ invariant mass, one needs to make edits to the "Plots" code, for a given analysis. As mentioned in the last paragraph of the previous section, each "Plots" code contains functions named AddHists or DrawHists (depending on the analysis that is being considered). These

functions will take in either two, or three inputs, depending on what you want to do. Since this analysis was highlighted by fitting the $\phi\eta$ invariant mass, there is an option to tell the code to include the fit or not. Since this section includes a fit to this histogram, be sure that when these functions are called, there are three inputs passed. The three inputs that need to be passed are the canvas, histogram, and the boolean "True". This boolean variable will access a portion of code inside an IF statement which is protected by this switch.
Since this analysis tested many different fit hypotheses, the code contained inside this IF statement has many lines which need to be correctly written, depending on which hypothesis is being considered. Each hypothesis has a block of code associated with it which is initiated by a comment line that describes the type of fit. Following the comment line are a series of commands which set the proper fit parameters or values, depending on the hypothesis. After this, the histogram is fit, then additional signal and background functions collect the fit parameters so that they can be drawn as well. Only one fit hypothesis may be done at a time and if chosen, the other three blocks of code must be commented out.

Relevant Procedures:

Make all proper adjustments to the "Plots" code, including the boolean "True", and the fit hypothesis adjustment. Then run:
root -l `TNtuple_Plot.C()`

Chapter 2

Monte Carlo

2.1 Monte Carlo Features of $\gamma p \to p\phi\eta$

In order to better understand the acceptance of the $\gamma p \to p\phi\eta$ topology in the GlueX spectrometer, a generated Monte Carlo sample was analyzed. More specifically, the exact sample that was produced was $\gamma p \to pX; X \to \phi\eta; \phi \to K^+K^-; \eta \to \gamma\gamma$. This Monte Carlo sample consisted of 1,666,667 generated events for each of the run numbers 030408, 030620, 030699, 030802, 030900, and 031029. The run numbers were chosen because two have beam polarizations in the PARA/PERP directions at low intensity (030408 and 030620), two have PARA/PERP orientations at high intensity (030802 and 031029), and two of the run numbers are from amorphous radiators (030699 and 030900). The total number of generated $\phi\eta$ events is therefore 10 million. The events were generated using a combination of a coherent and an incoherent bremsstrahlung beam energy spectrum ranging from 3 GeV to 12 GeV. These events were also generated with a t-slope of 2.5 $(GeV/c^2)^2$. To be more clear, the thrown beam particles were not polarized in this sample; only the beam energy spectrum matched that of a polarized beam spectrum plus an incoherent beam spectrum (Figure [2.1]). All final state particle kinematics were generated using the GlueX Monte Carlo generator (genr8). The generated final state phase space did not include any spin information from parent or daughter states. The $\gamma, K^+, K^-, \phi, \eta$, and p particles were generated using the invariant mass values and widths provided in the PDG. The photo-produced X mass was distributed between the lower kinematic limit $m_\phi + m_\eta$ and the upper kinematic limit which is a function of the momentum transfer t, and the thrown beam energy.

An example of what the generated beam energy distribution looks like for this Monte Carlo sample is given in Figure [2.1]. It should be noted that this particular Monte Carlo sample includes both coherent and incoherent beam structures, where the peaks in the image come from coherent Monte Carlo. The lower energy region of the beam energy spectrum comes primarily from the incoherent data. It should also be noted that the slow rise of the beam energy in this region is due to Lorentz factor weighting, or phase space.

Momentum versus θ distributions are also provided in Figures [2.2], [2.3], [2.4], and [2.5]. These figures are generated Monte Carlo and represent the distributions of final state particles in the lab frame before running hdgeant, mcsmear, and `hd_root`. Still, the figures provide some insight into the expected kinematic distributions of the final state particles.

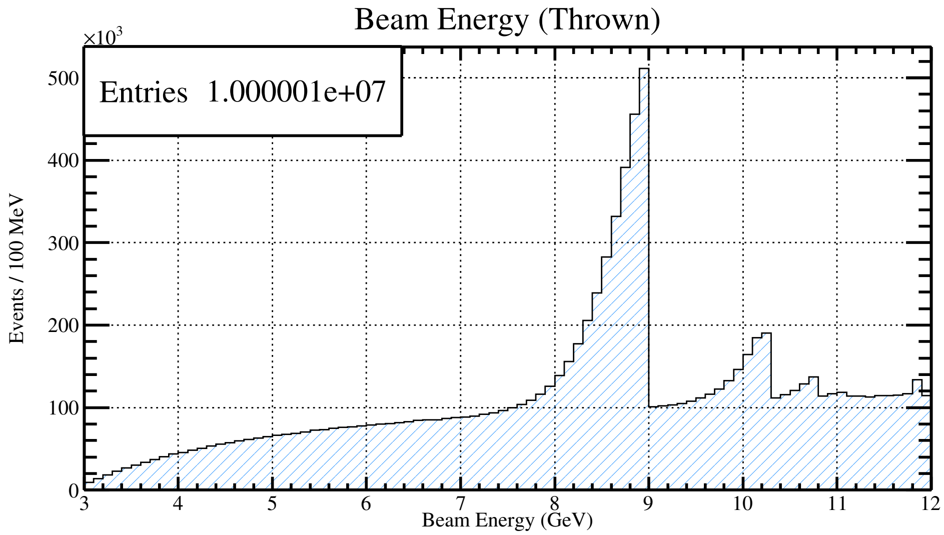

Figure 2.1: A histogram which includes the thrown beam statistics from the generated Monte Carlo example. In the figure one can easily see the coherent peak which maximizes at 9 GeV. Additionally, one can also see other secondary peaks at higher energy.

For example, Figure [2.2] displays the momentum versus theta distribution for the recoil proton. This figure shows that we should expect the proton to have a very low momentum and high recoil angle relative to the beam direction for this final state.

Additionally, Figures [2.3][2.4] seem merely identical in shape and contour. This is expected and the reason for this is that both kaons are decaying from the ϕ meson, and the K^+ and K^- are anti- particles. In these figures, it is clear that Kaons will preferentially travel towards the TOF/FCAL and with a momentum that should include a lot of pion contamination (see Figures [3.18][3.26] for more information on pion contamination at high momentum).

Lastly, Figure [2.5] shows that the final state photons will be mostly forward going and therefore we should expect to see the majority of them interacting with the FCAL rather than the BCAL. It is not surprising that the Monte Carlo has generated photons and kaons that favor the forward direction, while the recoil proton has low momentum and a highly transverse direction. This is simply a consequence of the fact that a low t interaction was programmed into the Monte Carlo, resulting in Figure [2.6].

The last few figures to be discussed in this section involve the study of invariant mass spectra. The first of which is the invariant mass of $\phi\eta$ (Figure [2.7]) which shows a phase space distribution between the values of 1.5 to 3.2 GeV/c^2; then the slope of the distribution changes drastically from 3.3 to 4 GeV/c^2. These features may seem incorrect at first glance since the generated Monte Carlo mass is supposed to just show phase space. However, upon further inspection, it is clear that these features manifest themselves within the Monte Carlo data because of the shape of the beam spectra. The best way to see this behavior is by considering Figure [2.8]. This figure shows the generated beam energy on the vertical axis, and the generated $\phi\eta$ mass on the horizontal axis. Since the primary peak from the coherent bremsstrahlung will dominate most of the statistics in this generated sample, the $\phi\eta$ invariant

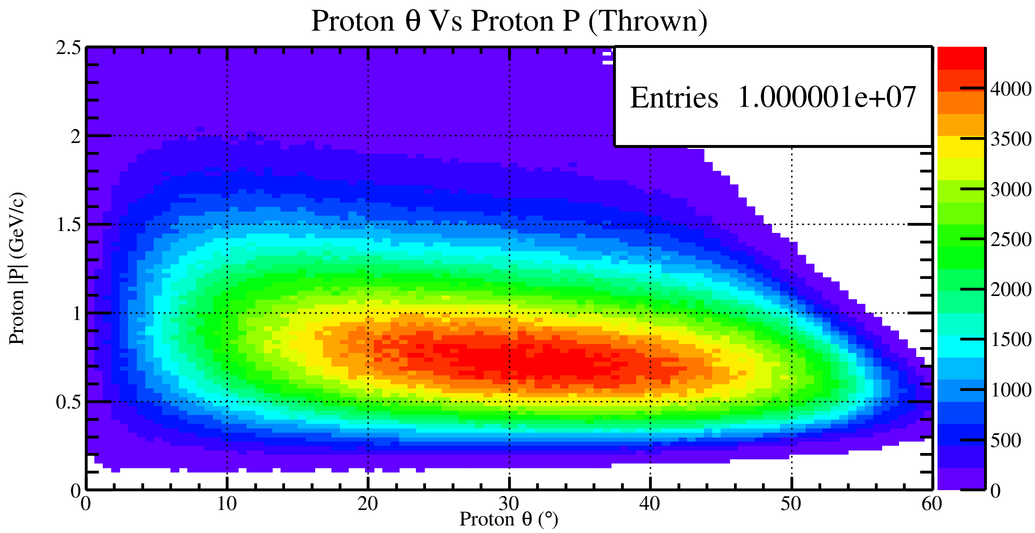

Figure 2.2: A two dimensional histogram which includes the thrown kinematic information of the recoil proton. In the histogram, the horizontal axis represents the generated θ angle in the lab frame, and the vertical axis represents the generated momentum magnitude in the lab frame. One interesting feature of this Monte Carlo data is that the kinematics of the recoil proton appear to be constrained between $[0.2-2.0] GeV/c$ in momentum, and $[0.0-60.0]^{\circ}$ in angle.

mass range which it couples too will be most dominant as well. Inspecting Figure [2.8], one can clearly see the coherent peak at 9 GeV, and the corresponding $\phi\eta$ invariant mass ranging from 1.5 to 3.2 GeV/c^2.

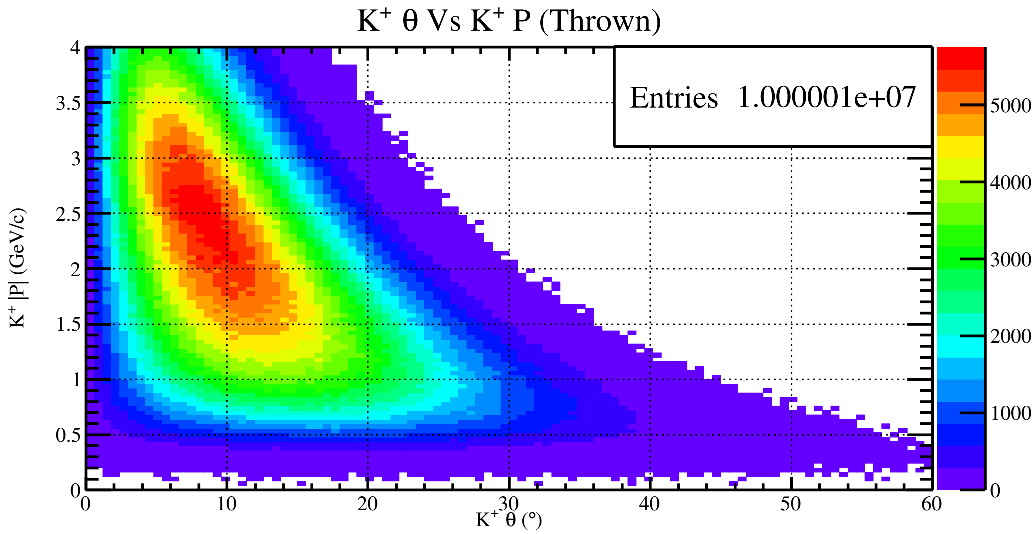

Figure 2.3: A two dimensional histogram which includes the thrown kinematic information of the generated K^+. In the histogram, the horizontal axis represents the generated θ angle in the lab frame, and the vertical axis represents the generated momentum magnitude in the lab frame.

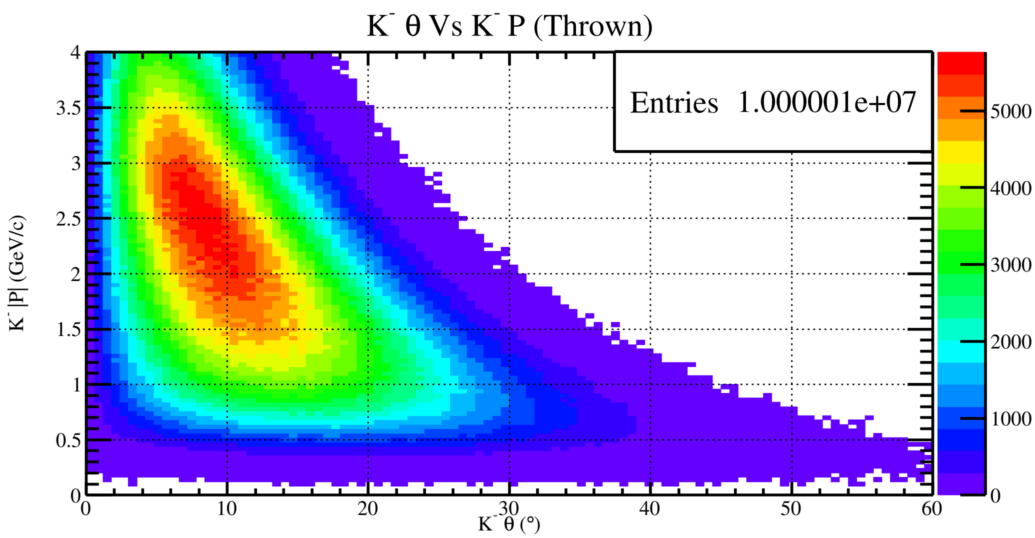

Figure 2.4: A two dimensional histogram which includes the thrown kinematic information of the generated K^-. In the histogram, the horizontal axis represents the generated θ angle in the lab frame, and the vertical axis represents the generated momentum magnitude in the lab frame.

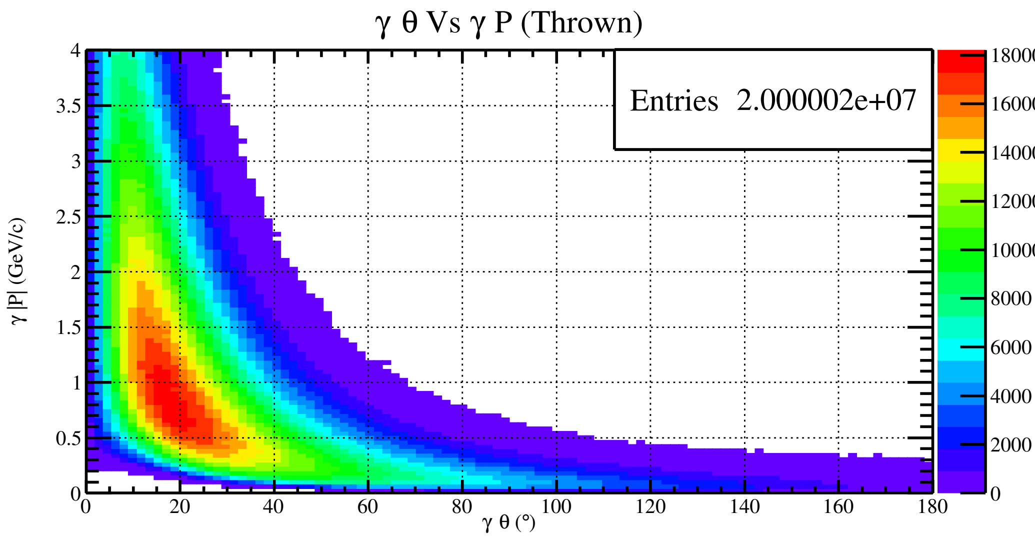

Figure 2.5: A two dimensional histogram which includes the thrown kinematic information of the generated photons. In the histogram, the horizontal axis represents the generated θ angle in the lab frame, and the vertical axis represents the generated momentum magnitude in the lab frame. The reason that the statistics are doubled in this histogram is due to both final state photon measurements being included in the plot.

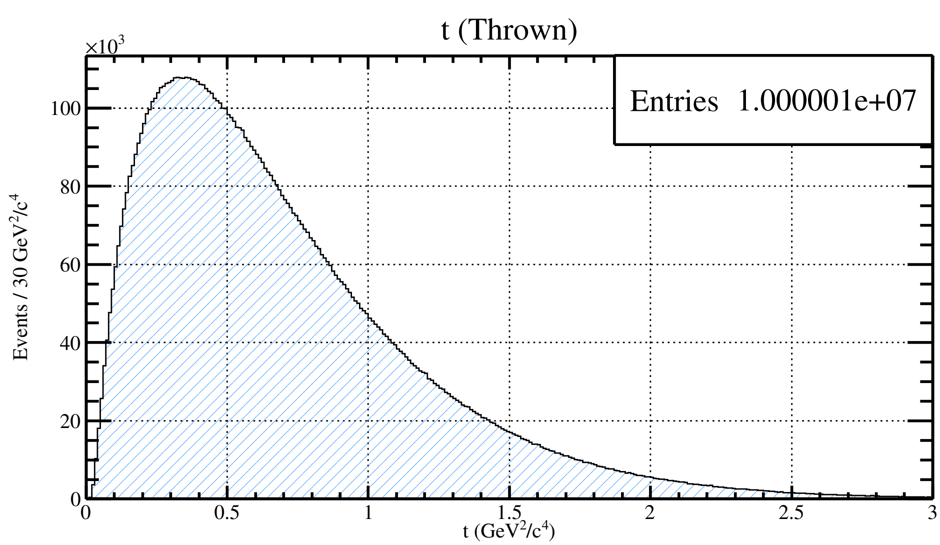

Figure 2.6: A histogram which includes the generated spectrum for the Mandelstam variable, t. The t-slope for the Monte Carlo presented here is 2.5 $\frac{GeV^2}{c^4}$

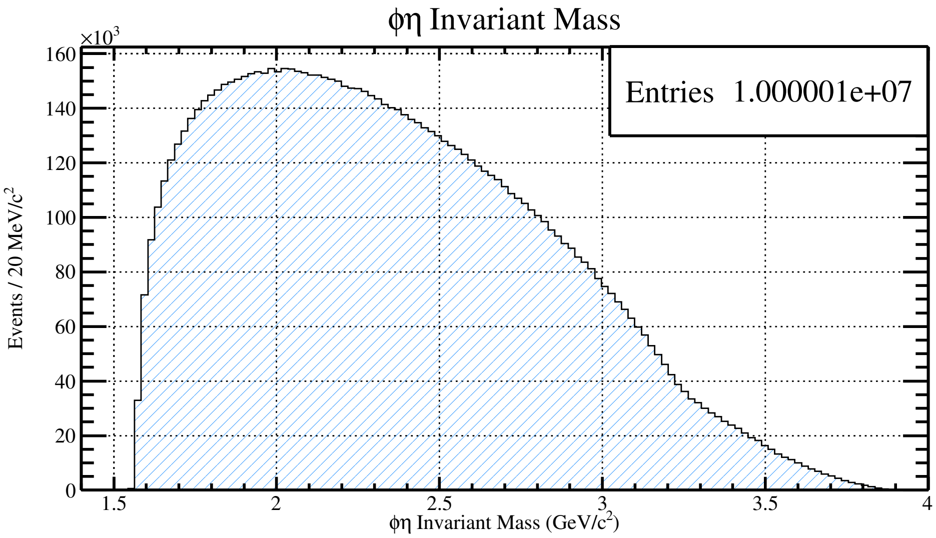

Figure 2.7: A histogram which includes the generated $\phi\eta$ invariant mass. In the figure one can easily see that the invariant mass of the $\phi\eta$ has the shape of phase space until it reaches $\sim$ 3.2 GeV/c^2. From that point, the invariant mass falls less sharply until $\sim$ 4.0 GeV/c^2. This feature of the invariant mass is directly related to the fact that a coherent bremsstrahlung beam energy spectrum was used. The abrupt change in the invariant mass range of $3.3 - 4.0$ GeV/c^2 is caused by the primary coherent peak at $9.0GeV$. To visualize this in two dimensions, see Figure [2.8].

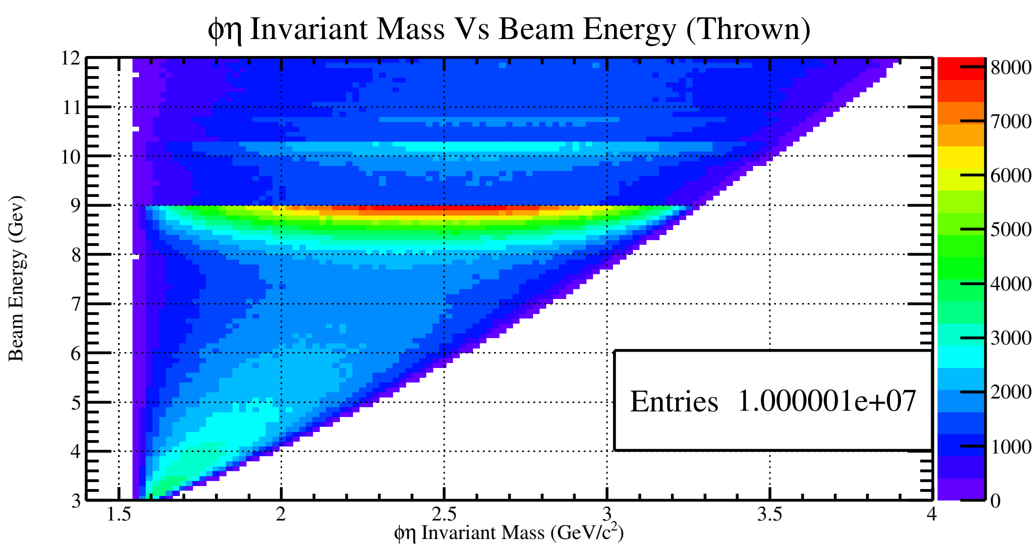

Figure 2.8: A two dimensional histogram which includes the generated $\phi\eta$ invariant mass on the horizontal axis and the Beam Energy on the vertical axis. In the figure one can easily see the effect that the coherent peak has on the shape of the phase space.

Chapter 3

Data Selection

3.1 Identification of $\gamma p \rightarrow pK^+K^-\gamma\gamma$ Events at GlueX

In order to study potential states of bound strangeonia, it is essential to properly identify all final and initial state particles. The final state topology that will be studied for this thesis is $\gamma p \rightarrow pK^+K^-\gamma\gamma$, where the K^+K^- pair are daughter states of the ϕ meson, and the $\gamma\gamma$ pair are daughter states of the η meson. Therefore, the beginning of this analysis section will focus on the particle identification of the proton, kaons, and final state photons, as well as the incident beam and target proton. Once identification of all particles has been well established, this analysis will then provide evidence that the final event sampling enforces exclusivity.

3.1.1 Spring 2017 Run Period

The data presented here is the result of the successful Spring 2017 run period. The Spring 2017 run period spanned from January 23rd to March 13th and accumulated roughly 50 billion physics events. The maximum electron beam energy used was 12 GeV, and the accelerator ran at 250 MHz while in low intensity (beam every 4 ns), and later ran at 500 MHz while in high intensity (beam every 2 ns). Upon entering Hall D, the electron beam was incident upon a radiator. During this run period, both amorphous and diamond radiators were used to produce either incoherent or coherent polarized bremsstrahlung radiation. The diamond radiator was experimentally set up to produce linear photon polarization at four different angles relative to the lab floor - 0°(parallel with floor), 45°, 90°(perpendicular with floor), and 135°. These directions were chosen in order to provide the detector with a uniform sampling of linear polarization in the transverse direction to the incident beam. In order to yield roughly the same amount of statistics for an amorphous radiator run as compared to a diamond radiator run, a beam current of 150 nA was incident upon the amorphous radiator, while a beam current of 100 nA was incident upon the diamond radiator. Farther downstream, a 5 mm collimator hole was used for all radiator configurations. Lastly, the collimated photon beam was incident upon a stationary liquid hydrogen target. This resulted in one petabyte of files and 16 pb^{-1} of integrated luminosity.

3.1.2 Identification of Initial State Particles

Photon Beam

The first step in identifying the initial state beam photon is to select the correct beam bunch. Since the electron beam is delivered from the accelerator every four nanoseconds, the timing of when the beam particles arrive into the hall is well known and we call this the Radio Frequency (RF) time.

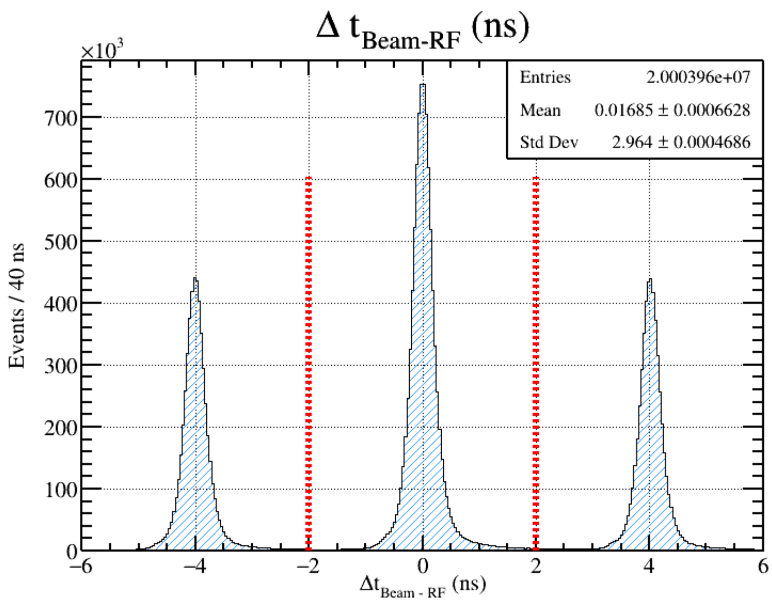

Figure 3.1: An example histogram of beam time as compared to the reported Radio Frequency (RF) time. In the plot there are three peaks, all of which are separated by four nanoseconds. Also included in the plot are two red dashed cut lines at ± 2 ns. These cut lines represent the values used to perform an accidental subtraction on the data.

In addition to the RF time, we also have the beam time. The beam time is defined as the time which the reconstruction converged upon a common vertex time. The common vertex time is found by using the final state charged tracks and their timing, and back tracking them to a common point in space and time. Comparing the beam time with the RF time provides the experiment with the correct beam bunch which should be centered at zero. An example of what this distribution looks like and the cut used for it is given in Figure 3.1. It should be noted that this analysis will enforce a beam timing cut of $\pm$ 6ns in order to allow 3 beam bunches to pass. Once all cuts are made on the data and the final set of events is known, the additional side peaks will be used for accidental subtraction. An accidental subtraction is necessary in this analysis due to the high volume of accidental beam photons in the primary peak at zero. The accidental subtraction will be performed on all final plots shown in this analysis and can be executed by assigning a weight of 1 for any event with a beam timing of $\pm 2ns$, and a weight of -0.5 for any event from the side peaks. The purpose of assigning a weight of -0.5 for the side peaks is simply because there are twice as many side peaks (2) as primary peaks (1).

Target Proton

There are two cuts needed to select the initial state proton. Both of these cuts enforce the reconstructed vertex for all final state particles to be within the geometric volume of the target chamber. Since this analysis does not contain a particle lifetime which would result in a detached vertex, it is imperative to reduce backgrounds from other channels that may have this feature, such as excited baryons with a strange quark. Examples of what the reconstructed vertex for the final state photons looks like in the beam direction and in the transverse beam direction, is given in Figure [3.2a] and Figure [3.2b], respectively.

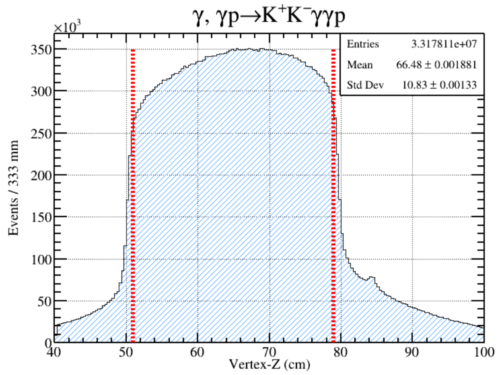

(a) Reconstructed vertex position along the beam direction with cut lines at 51 and 79 cm.

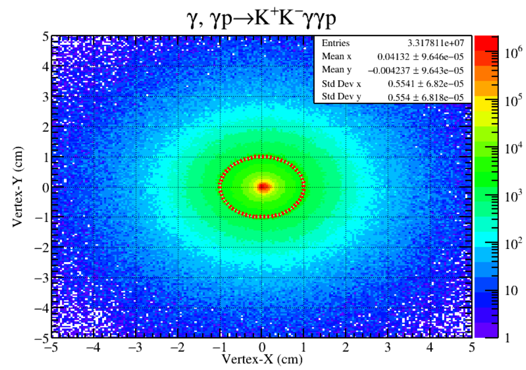

(b) Reconstructed vertex position transverse to the the beam direction with cut a line at 1 cm in the radial direction.

Figure 3.2: An example of what a reconstructed vertex distribution looks like for a final state γ in the reaction $\gamma p \to pK^+K^-\gamma\gamma$. The upper image is the reconstructed vertex position along the beam line, or z axis; and the lower image is the reconstructed vertex position in the directions transverse to the beam line. Both figures contain red dashed lines which represent the cut values for all reconstructed final state particles. In the z direction the cut values are 51 cm $\leq V_z \leq$ 79 cm, and in the transverse direction the cut values are $V_r \leq 1$ cm. The z direction cut values are established from Log Entry 3456336 from a Spring 2017 empty target run. The transverse cuts are simply established by considering the geometric size of the target chamber.

3.1.3 Identification of Final State Particles

Recoil Proton

There are three cuts that were used to identify the recoil proton and remove background. One of the cuts is a standard dE/dX cut, which separates some of the slow moving protons from other particles of positive charge such as e^+, π^+, and K^+. Due to the higher mass of the proton in comparison to the other particles with positive charge, the proton will tend to lose more energy inside of the Central Drift Chamber. This cut is highlighted in the first GlueX paper [2], and can be seen in Figure [3.3].

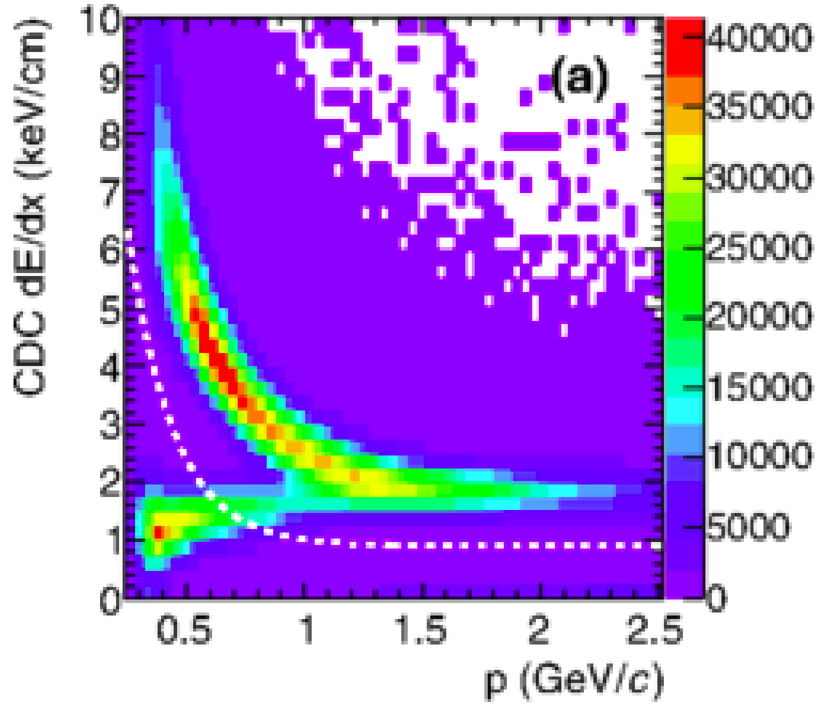

Figure 3.3: A figure which shows the energy lost in the Central Drift Chamber on the vertical axis, and the reconstructed momentum on the horizontal axis. At lower momentum, a proton band can be seen rising sharply towards higher energy loss values. Also contained within the figure is a white dashed line which represents the cut value used to identify slower moving protons. The horizontal band which deviates from the proton band at low momentum comes from positively charged pions and kaons.

The second cut is to enforce the reconstructed vertex position of the charged proton track came from inside the target chamber. This cut is used to reduce any background from particles that may have a detached vertex. The cut used is identical to those found and described in the Target section, specifically Figure [3.2a] and Figure [3.2b]. The third and final cut that is used to identify the recoil proton is the timing difference (Δ T) from the BCAL, FCAL, and TOF. Δ tis defined as the difference between the reconstructed vertex time for the particle and the time when the photon beam arrived. An example of what these distributions look like in data, as a function of momentum, is given in Figure [3.4]. Since the data has a lot of pion background in these plots, it is difficult to determine what the proper timing cuts should be for all of the sub detectors. Due to this, a Monte Carlo sample of $\gamma p \rightarrow pX; X \rightarrow \phi\eta; \phi \rightarrow K^+K^-; \eta \rightarrow \gamma\gamma$ was generated, simulated, and then reconstructed. This greatly reduces the background that is present in the timing plots and therefore can be used to estimate a proper timing cut for the proton and the sub detectors used to measure its time. Examples of these distributions and their associated projections onto the timing axis are given in Figure [3.5] through Figure [3.10]. A summary of all of the timing cuts used for the recoil proton as well as all other final state particles is given in Table [3.1].

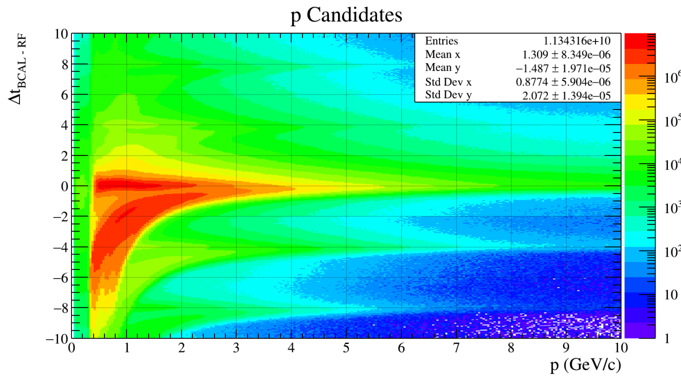

(a) Δt Vs P for Proton candidates that have the Barrel Calorimeter as the timing detector in data.

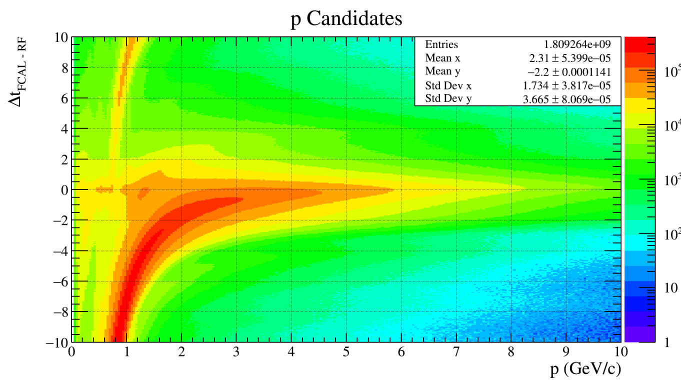

(b) Δt Vs P for Proton candidates that have the Forward Calorimeter as the timing detector in data.

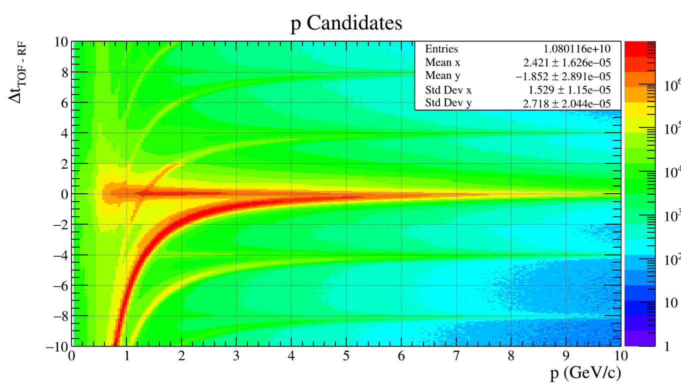

(c) Δt Vs P for Proton candidates that have the Time of Flight as the timing detector in data.

Figure 3.4: Timing plots for recoil proton candidates during the Spring 2017 run period for GlueX. Protons are identified by selecting the horizontal band centered about $\Delta T = 0$. The curved line deviating below the horizontal proton line comes from miss identified π^+ tracks. The additional curved lines above and below $\Delta T = 0$ come from π^+ tracks that are associated with the wrong RF bunch.

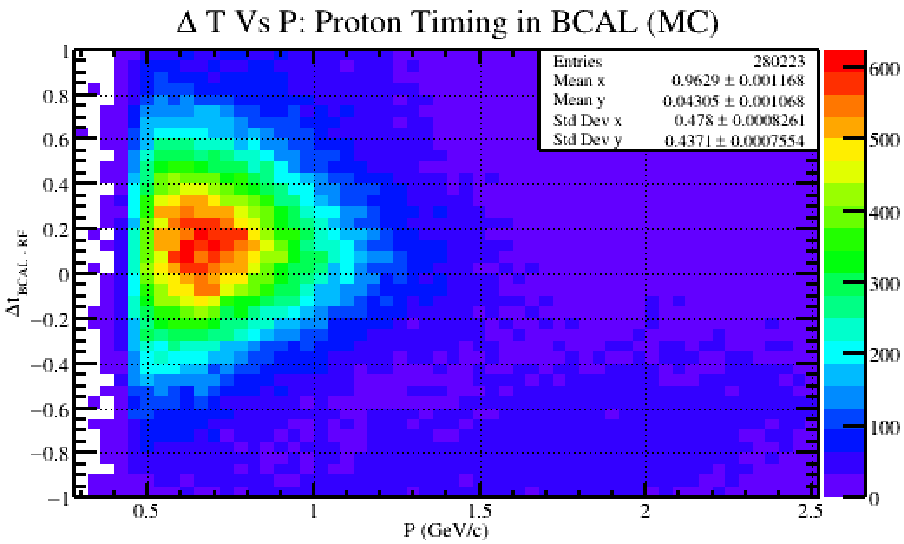

Figure 3.5: A timing plot for accepted recoil protons from the generated reaction $\gamma p \rightarrow pX; X \rightarrow \phi\eta; \phi \rightarrow K^+K^-; \eta \rightarrow \gamma\gamma$. The horizontal axis is the reconstructed momentum of the recoil proton and the vertical axis is the timing difference between the BCAL and RF. The enhancement of statistics in the lower right portion of the plot comes from miss identified kaons that are also present in the accepted Monte Carlo.

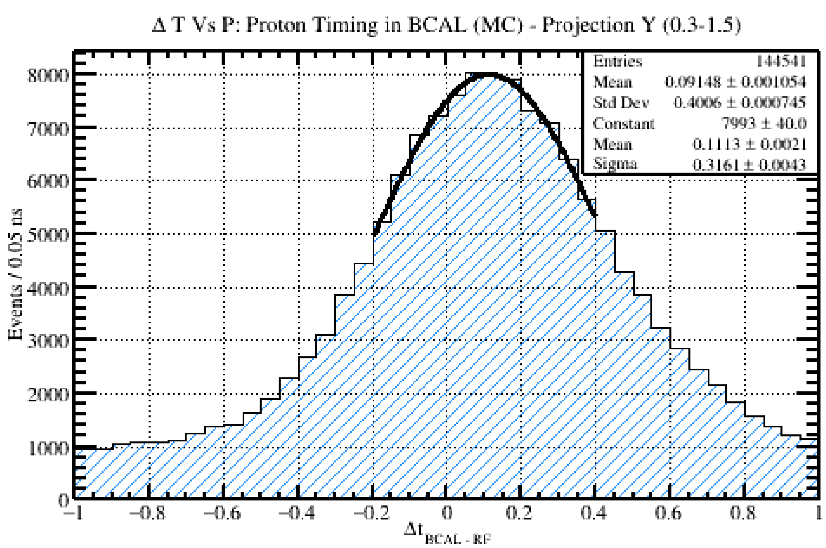

Figure 3.6: A projection of the statistics from Figure [3.5] onto the vertical (timing) axis between the momentum range of 0.3-1.5 GeV/c. This projection range was chosen so that the distortion from the lower kaon band was minimized. A Gaussian fit was performed and is included in the figure where the mean and width of the distribution are given in the legend.

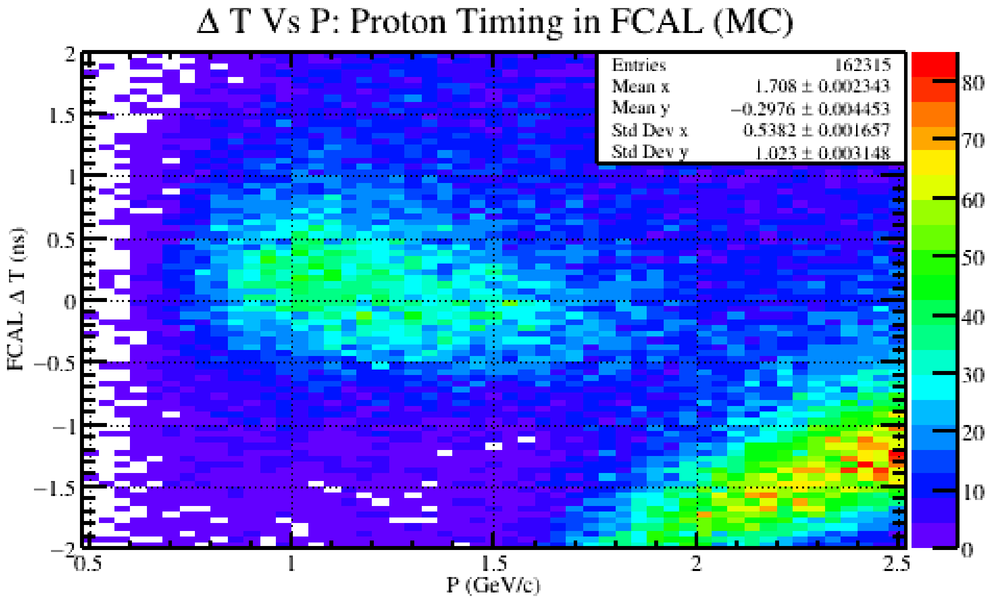

Figure 3.7: A timing plot for accepted recoil protons from the generated reaction $\gamma p \to pX; X \to \phi\eta; \phi \to K^+K^-; \eta \to \gamma\gamma$. The horizontal axis is the reconstructed momentum of the proton and the vertical axis is the timing difference between the FCAL and RF. The enhancement of statistics in the lower right portion of the plot comes from miss identified kaons that are also present in the accepted Monte Carlo.

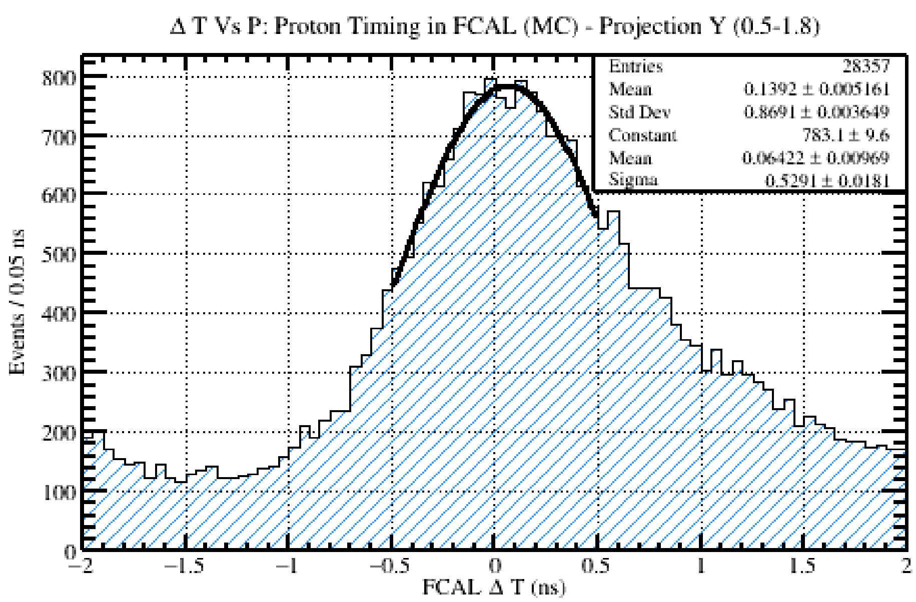

Figure 3.8: A projection of the statistics from Figure [3.7] onto the vertical (timing) axis between the momentum range of 0.5-1.8 GeV/c. This projection range was chosen so that the distortion from the lower kaon band was minimized. A Gaussian fit was performed and is included in the figure where the mean and width of the distribution are given in the legend.

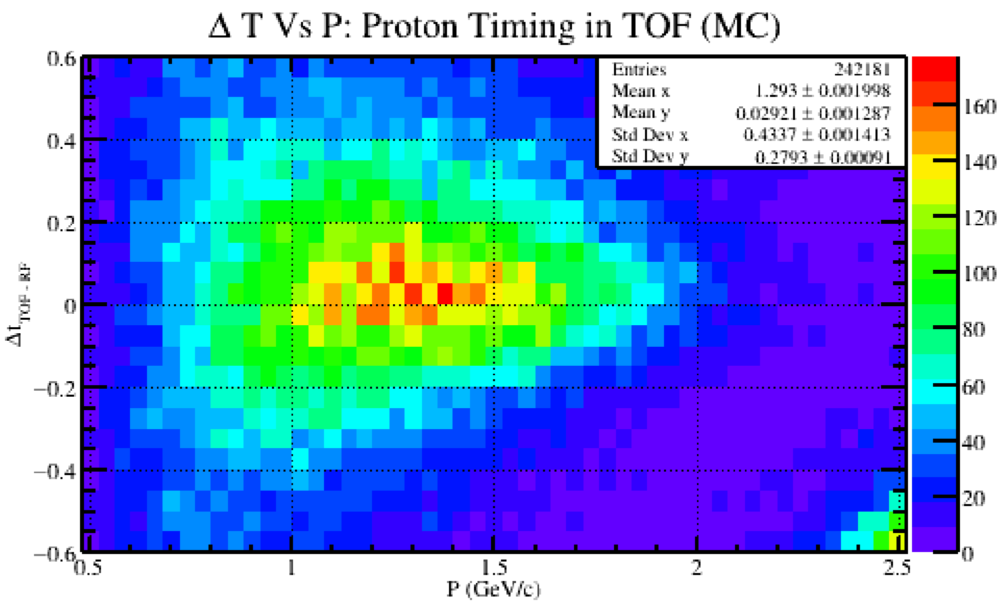

Figure 3.9: A timing plot for accepted recoil protons from the generated reaction $\gamma p \to pX; X \to \phi\eta; \phi \to K^+K^-; \eta \to \gamma\gamma$. The horizontal axis is the reconstructed momentum of the proton and the vertical axis is the timing difference between the TOF and RF. The enhancement of statistics in the lower right portion of the plot comes from miss identified kaons that are also present in the generated Monte Carlo.

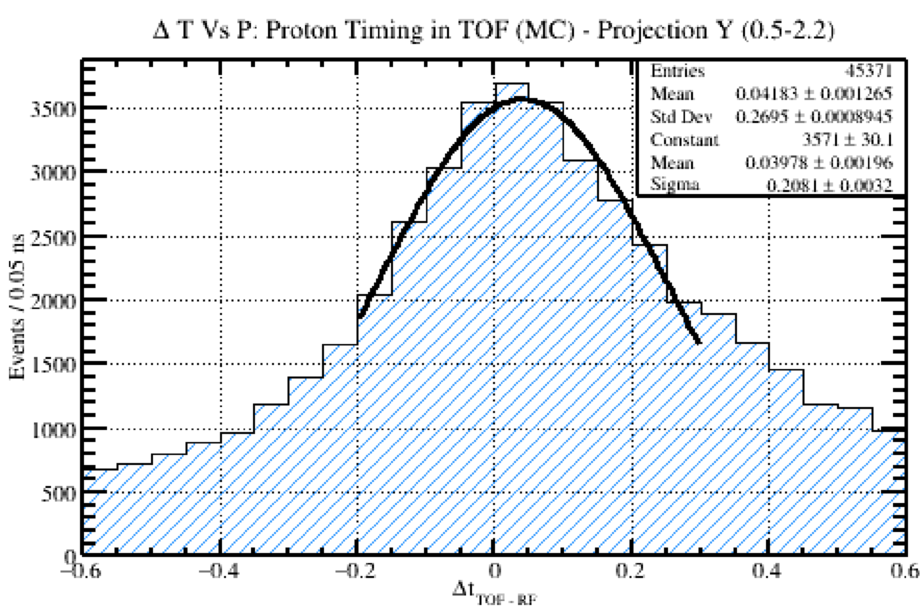

Figure 3.10: A projection of the statistics from Figure [3.9] onto the vertical (timing) axis between the momentum range of 0.5-1.8 GeV/c. This projection range was chosen so that the distortion from the lower kaon band was minimized. A Gaussian fit was performed and is included in the figure where the mean and width of the distribution are given in the legend.

K^+

There are two cuts that were used to identify the final state K^+ and remove background. The first cut is to enforce the reconstructed vertex position of the K^+ track came from inside the target chamber. This cut is used to reduce any parent state of the K^+ that may have a longer lifetime and therefore a detached vertex. The cut used is identical to those found and described in the Target section, specifically Figure [3.2a] and Figure [3.2b].

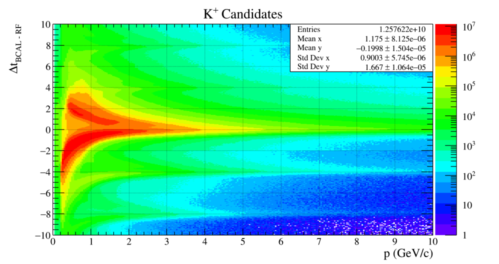

(a) Δ tVs P for K^+ candidates that have the Barrel Calorimeter as the timing detector in data.

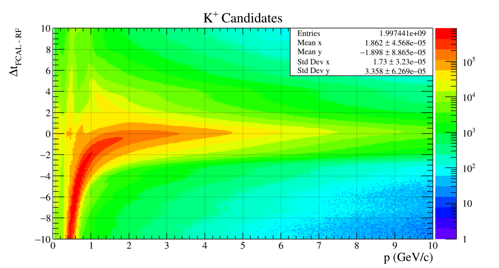

(b) Δ tVs P for K^+ candidates that have the Forward Calorimeter as the timing detector in data.

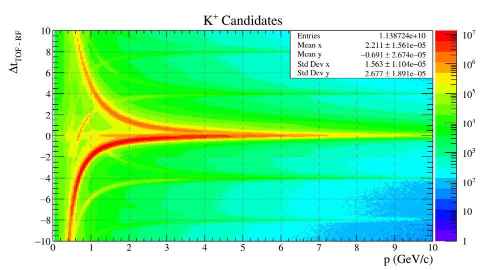

(c) Δ tVs P for K^+ candidates that have the Time of Flight as the timing detector in data.

Figure 3.11: Timing plots for K^+ candidates during the Spring 2017 run period for GlueX. K^+ are identified by selecting the horizontal band centered about $\Delta T = 0$. The curved line deviating below the horizontal K^+ line comes from miss identified π^+ tracks, and the curved line deviating above the horizontal K^+ line comes from miss identified proton tracks. The additional curved lines above and below $\Delta T = 0$ come from π^+ and proton tracks that are associated with the wrong RF bunch.

The other cut that is used to identify the K^+ is the timing (Δ T) from the BCAL, FCAL, and TOF. Δ tis defined as the difference between the reconstructed vertex time for the particle and the time when the photon beam arrived. An example of what these distributions look like in data, as a function of momentum, is given in Figure [3.11]. Since the data has a lot of pion and proton background in these plots, it is difficult to determine what the proper timing cuts should be for all of the sub detectors. Due to this, a Monte Carlo sample of $\gamma p \to pX; X \to \phi\eta; \phi \to K^+K^-; \eta \to \gamma\gamma$ was generated, simulated, and then reconstructed. This greatly reduces the background that is present in the timing plots and therefore can be used to estimate a proper timing cut for the K^+ and the sub detectors used to measure its time. Examples of these distributions and their associated projections onto the timing axis are given in Figure [3.12] through Figure [3.17]. It should be noted that in many of the Monte Carlo plots, there appears to be an additional band from a particle with less mass. This is a consequence of using the *hdgeant* simulator, which will decay particles while in flight. Therefore, the band inside the Monte Carlo plots arises from the weak decay of a kaon to a muon and a neutrino. A summary of all of the timing cuts used for the K^+ as well as all other final state particles is given in Table [3.1].

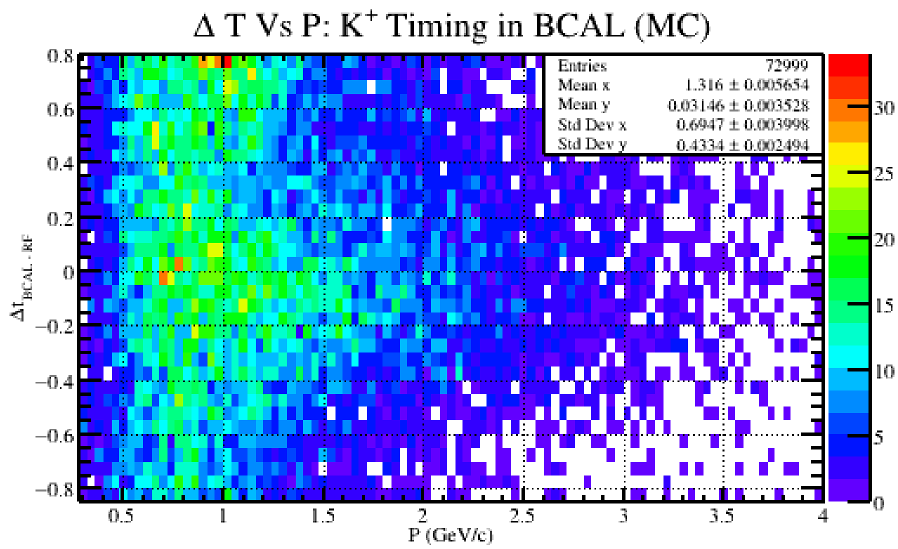

Figure 3.12: A timing plot for accepted K^+ from the generated reaction $\gamma p \to pX; X \to \phi\eta; \phi \to K^+K^-; \eta \to \gamma\gamma$. The horizontal axis is the reconstructed momentum of the K^+ and the vertical axis is the timing difference between the BCAL and RF. It should be noted that the statistics in this sampling are smaller than other plots. This is due to the fact that the kinematics of the generated channel prefer to have the kaons moving in the forward direction; and therefore provide few timing hits in the BCAL. Additionally, the extra statistics present in the upper left portion of the graph are due to protons that are also present in the accepted Monte Carlo.

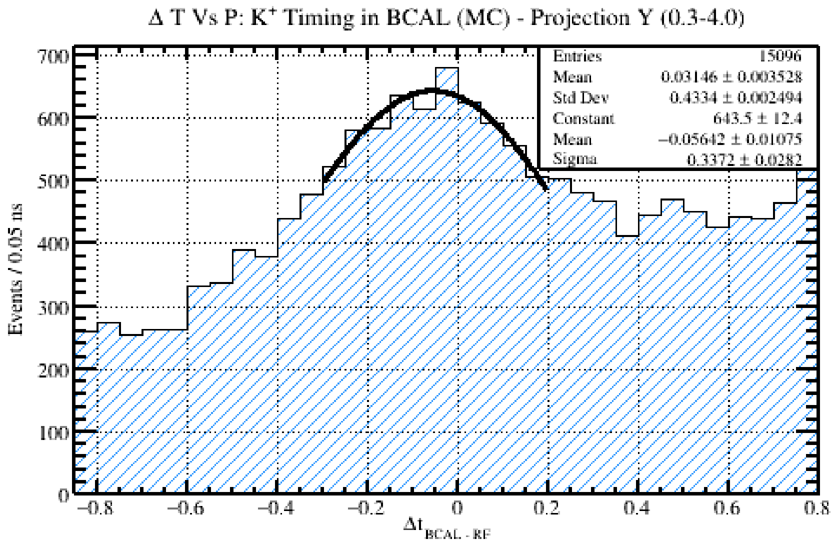

Figure 3.13: A projection of the statistics from Figure [3.12] onto the vertical (timing) axis between the momentum range of 0.3-4.0 GeV/c. A Gaussian fit was performed and is included in the figure where the mean and width of the distribution are given in the legend. The distortion of statistics towards the higher timing differences is due to protons that are also present in the generated Monte Carlo.

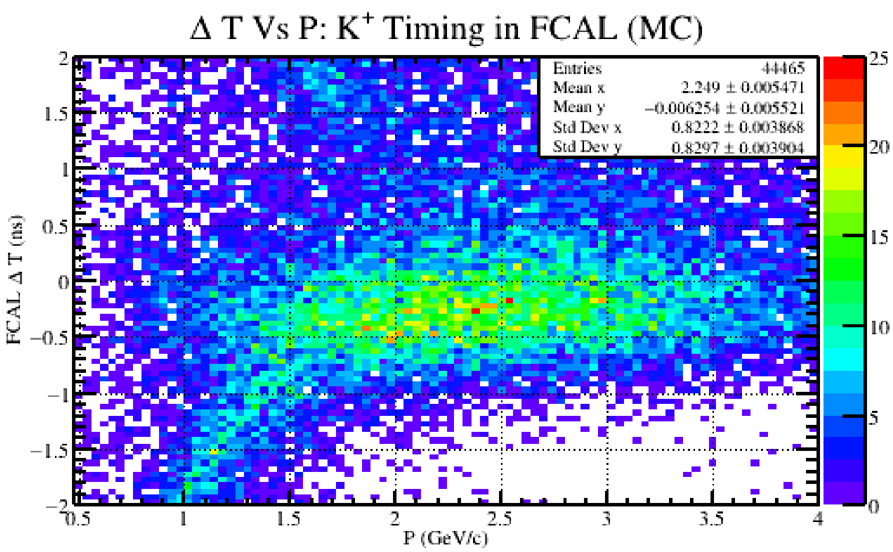

Figure 3.14: A timing plot for accepted K^+ from the generated reaction $\gamma p \to pX; X \to \phi\eta; \phi \to K^+K^-; \eta \to \gamma\gamma$. The horizontal axis is the reconstructed momentum of the K^+ and the vertical axis is the timing difference between the FCAL and RF. The curved band that appears below the K^+ band around 1.5 GeV/c and lower comes from μ^+. Although muons were not explicitly generated, the computer program hdgeant (derived from geant) allows for some fraction of kaons to decay weakly while in flight; resulting in observed muons.

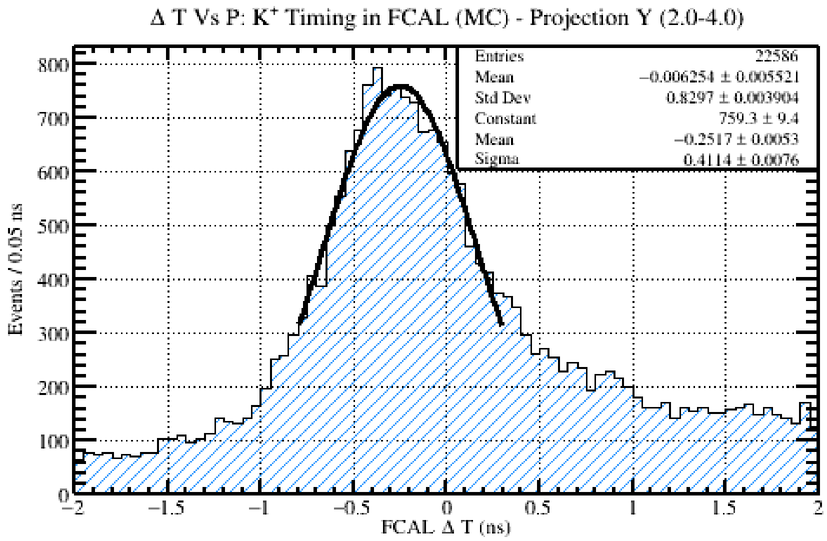

Figure 3.15: A projection of the statistics from Figure [3.14] onto the vertical (timing) axis between the momentum range of 2.0-4.0 GeV/c. This projection range was chosen so that the distortion from the lower muon band and upper proton band was minimized. A Gaussian fit was performed and is included in the figure where the mean and width of the distribution are given in the legend.

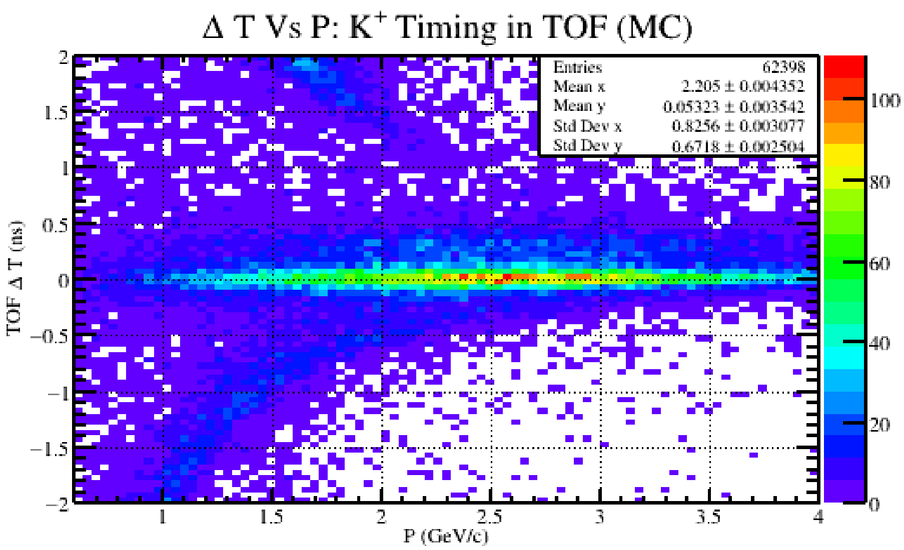

Figure 3.16: A timing plot for accepted K^+ from the generated reaction $\gamma p \to pX; X \to \phi\eta; \phi \to K^+K^-; \eta \to \gamma\gamma$. The horizontal axis is the reconstructed momentum of the K^+ and the vertical axis is the timing difference between the TOF and RF. The curved band that appears below the K^+ band around 2.5 GeV/c and lower comes from μ^+; and the band near the top of the plot comes from protons. Although muons were not explicitly generated, the computer program hdgeant (derived from geant) allows for some fraction of kaons to decay weakly while in flight; resulting in an observed muon.

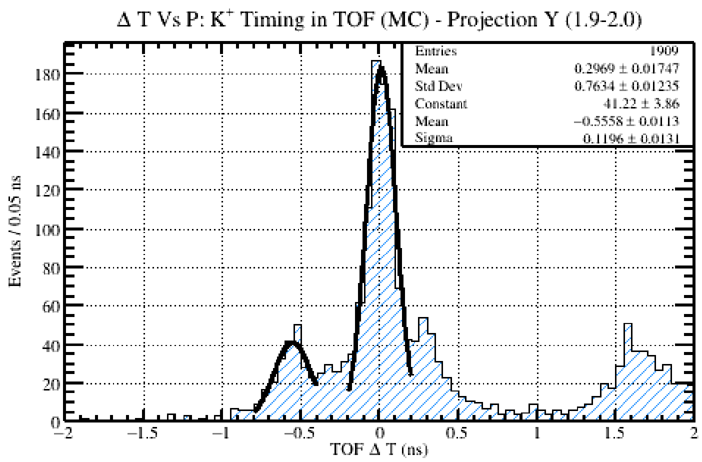

Figure 3.17: A projection of the statistics from Figure [3.16] onto the vertical (timing) axis between the momentum range of 1.9-2.0 GeV/c. This projection range is one out of many that were studied from Figure [3.16]. The purpose of this study is to determine the amount of muon contamination in the kaon band as a function of momentum. The results of this study are provided in Figure [3.18]. Lastly, two Gaussian fits were performed on this data. The mean and width of these Gaussian fits are recorded in Figure [3.18] for each momentum range.

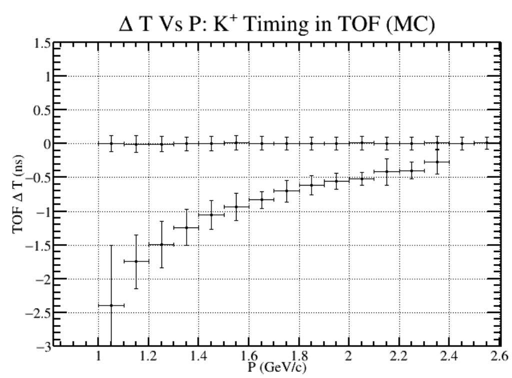

Figure 3.18: The image above is the result of the timing study performed on Figure [3.16]. Using that figure, a number of projection histograms were fit using different momentum ranges. An example of one of these fits is given in Figure [3.17]. The data points close to 0 ΔT correspond to the Gaussian fits performed on the kaon signal, and the data points that approach that band from the bottom correspond to the Gaussian fits performed on the muon signal. The horizontal position of each point is in the middle of the projection range, and the vertical position of each point was assigned based on the mean value of the Gaussian fit for each particle. The horizontal error bars are the size of the projection range, which is always 0.1 GeV/c. The vertical error bars are determined by the width of the Gaussian fits. The average of the widths of the kaon peaks is 0.1 ns which is the value used to determine the timing cut in Table 3.1.

K^-

Just like its antiparticle, the K^- has two cuts; the vertex and timing cuts. The vertex cut is used to eliminate any parent state of the K^- that may have a longer lifetime and therefore a detached vertex.

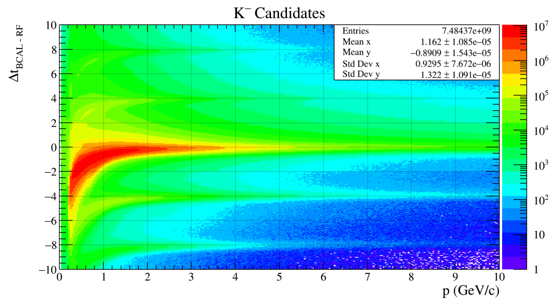

(a) Δ tVs P for K^- candidates that have the Barrel Calorimeter as the timing detector in data.

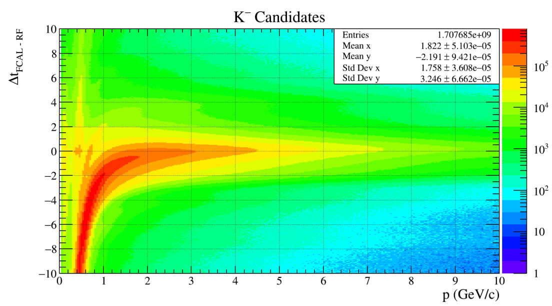

(b) Δ tVs P for K^- candidates that have the Forward Calorimeter as the timing detector in data.

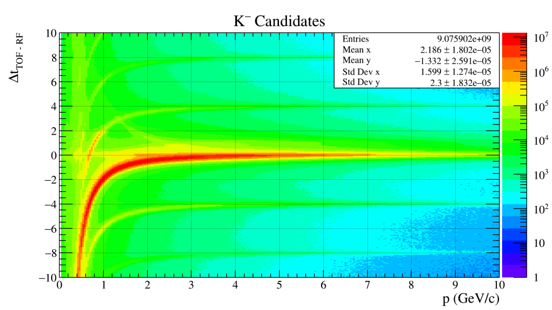

(c) Δ tVs P for K^- candidates that have the Time of Flight as the timing detector in data.

Figure 3.19: Timing plots for K^- candidates during the Spring 2017 run period for GlueX. K^- are identified by selecting the horizontal band centered about $\Delta T = 0$. The curved line deviating below the horizontal K^- line comes from miss identified π^- tracks. The additional curved lines above and below $\Delta T = 0$ come from π^- tracks that are associated with the wrong RF bunch.

The cut used is identical to those found and described in the Target section, specifically Figure [3.2a] and Figure [3.2b]. The timing cuts (Δt) for the K^- are for the BCAL, FCAL, and TOF sub detectors. Δt is defined as the difference between the reconstructed vertex time for the particle and the time when the photon beam arrived. Since the timing distributions from data (Figure [3.19]) have too much background in them, a Monte Carlo sample of $\gamma p \to pX; X \to \phi\eta; \phi \to K^+K^-; \eta \to \gamma\gamma$ was generated, simulated, and then reconstructed. This greatly reduces the background that is present in the timing plots and therefore can be used to estimate a proper timing cut for the K^- and the sub detectors used to measure its time. Examples of these distributions and their associated projections onto the timing axis are given in Figure [3.20] through Figure [3.25]. It should be noted that in many of the Monte Carlo plots, there appears to be an additional band from a particle with less mass. This is a consequence of using the *hdgeant* simulator, which will decay particles while in flight. Therefore, the band inside the Monte Carlo plots arises from the weak decay of a kaon to a muon and a neutrino. A summary of all of the timing cuts used for the K^- as well as all other final state particles is given in Table [3.1].

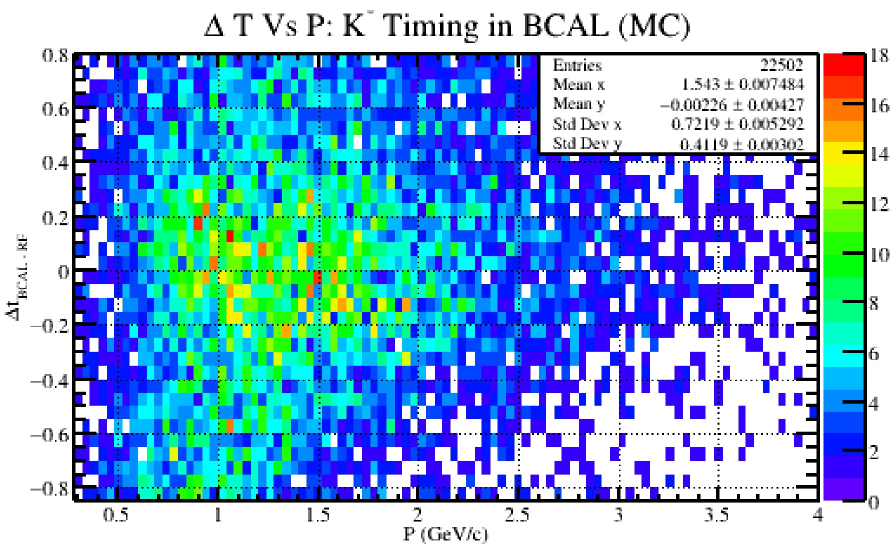

Figure 3.20: A timing plot for accepted K^- from the generated reaction $\gamma p \to pX; X \to \phi\eta; \phi \to K^+K^-; \eta \to \gamma\gamma$. The horizontal axis is the reconstructed momentum of the K^- and the vertical axis is the timing difference between the BCAL and RF. It should be noted that the statistics in this sampling are smaller than other plots. This is due to the fact that the kinematics of the generated channel prefer to have the kaons moving in the forward direction; and therefore provide few timing hits in the BCAL. Additionally, the extra statistics present in the lower left portion of the graph are due to muons. Although muons were not explicitly generated, the computer program hdgeant (derived from geant) allows for some fraction of kaons to decay weakly while in flight; resulting in observed muons.

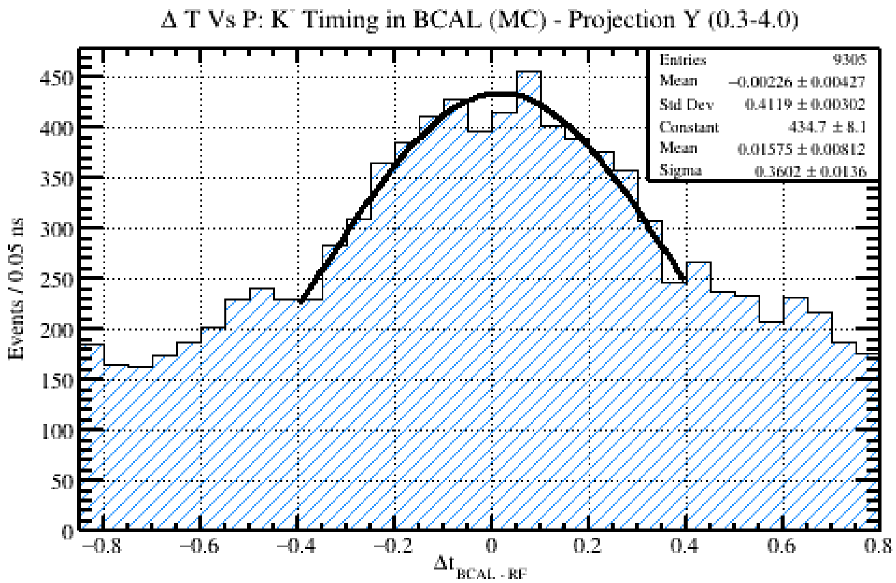

Figure 3.21: A projection of the statistics from Figure [3.20] onto the vertical (timing) axis between the momentum range of 0.3-4.0 GeV/c. A Gaussian fit was performed and is included in the figure where the mean and width of the distribution are given in the legend.

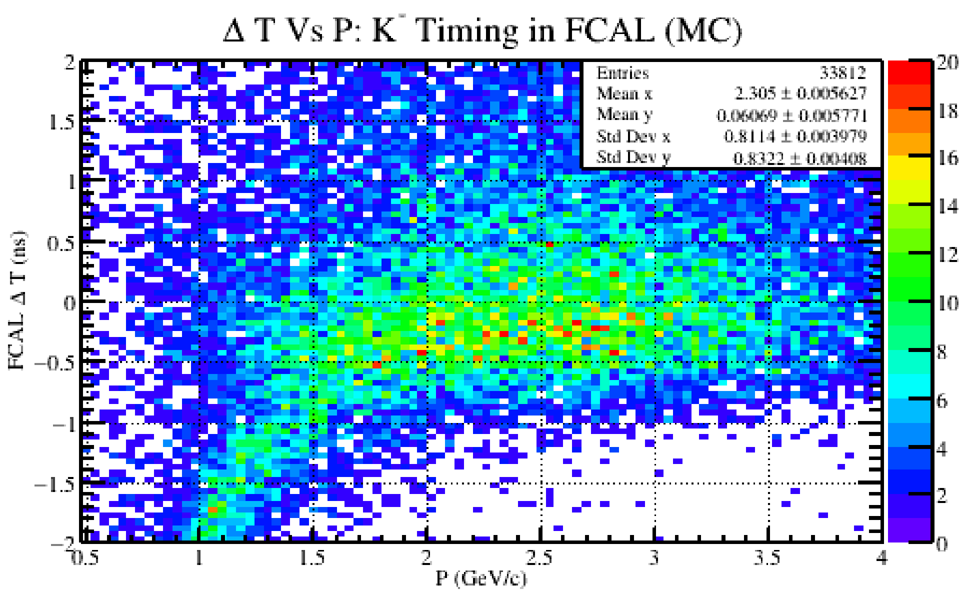

Figure 3.22: A timing plot for accepted K^- from the generated reaction $\gamma p \to pX; X \to \phi\eta; \phi \to K^+K^-; \eta \to \gamma\gamma$. The horizontal axis is the reconstructed momentum of the K^- and the vertical axis is the timing difference between the FCAL and RF. The curved band that appears below the K^- band around 1.5 GeV/c and lower comes from μ^-. Although muons were not explicitly generated, the computer program hdgeant (derived from geant) allows for some fraction of kaons to decay weakly while in flight; resulting in an observed muon.

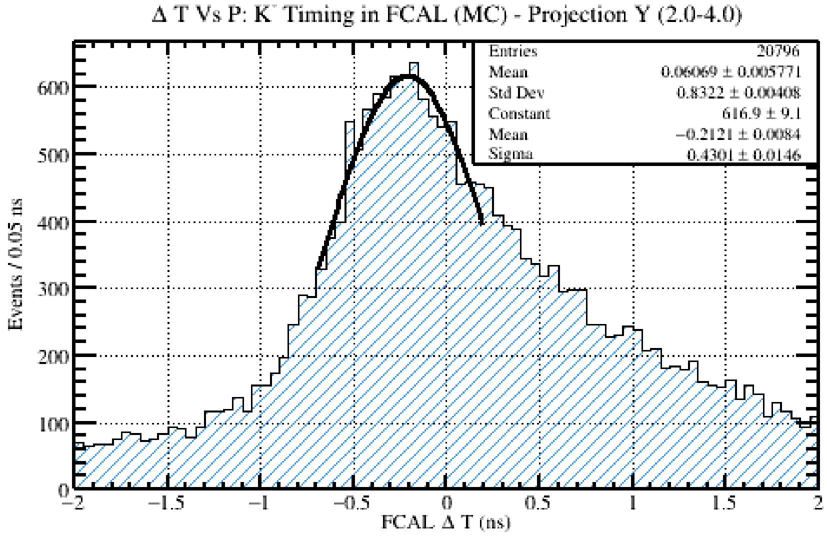

Figure 3.23: A projection of the statistics from Figure [3.22] onto the vertical (timing) axis between the momentum range of 2.0-4.0 GeV/c. This projection range was chosen so that the distortion from the lower muon band was minimized. A Gaussian fit was performed and is included in the figure where the mean and width of the distribution are given in the legend.

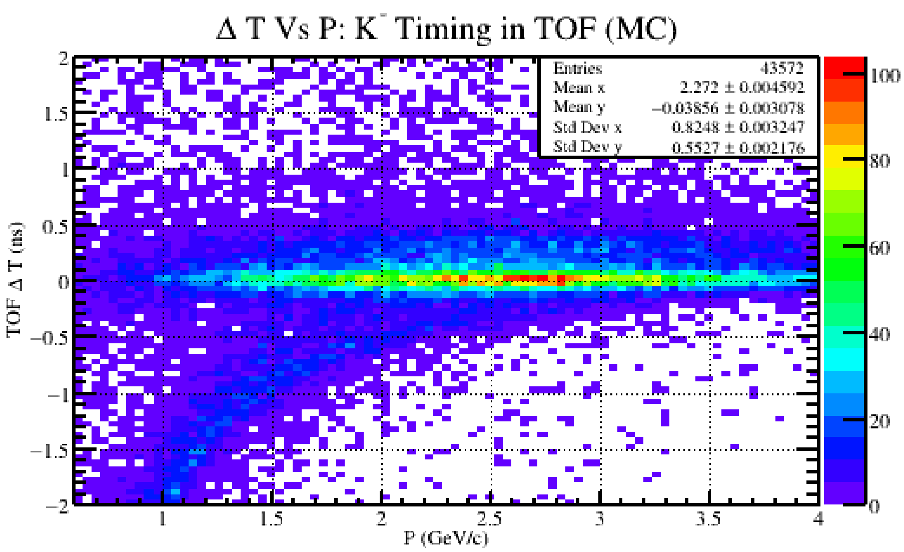

Figure 3.24: A timing plot for accepted K^- from the generated reaction $\gamma p \to pX; X \to \phi\eta; \phi \to K^+K^-; \eta \to \gamma\gamma$. The horizontal axis is the reconstructed momentum of the K^- and the vertical axis is the timing difference between the TOF and RF. The curved band that appears below the K^- band around 2.5 GeV/c and lower comes from μ^-. Although muons were not explicitly generated, the computer program hdgeant (derived from geant) allows for some fraction of kaons to decay weakly while in flight; resulting in an observed muon.

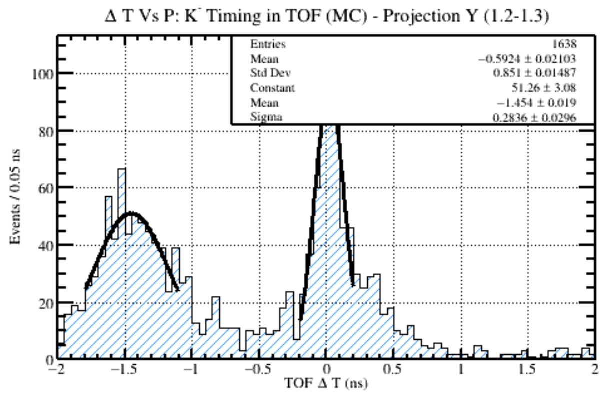

Figure 3.25: A projection of the statistics from Figure [3.24] onto the vertical (timing) axis between the K^- momentum range of 1.2-1.3 GeV/C. This projection range is one out of many that were studied from Figure [3.24]. The purpose of this study is to determine the amount of muon contamination in the kaon band as a function of momentum. The results of this study are provided in Figure [3.26]. Lastly, two Gaussian fits were performed on this data. The mean and width of these Gaussian fits are recorded in Figure [3.26] for each momentum range.

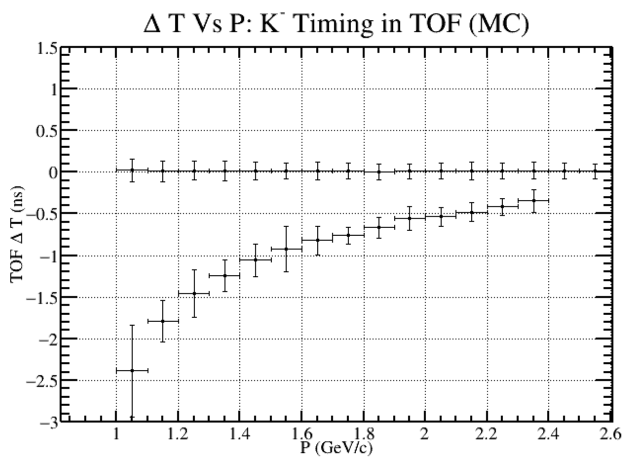

Figure 3.26: The image above is the result of the timing study performed on Figure [3.24]. Using that figure, a number of projection histograms were fit using different momentum ranges. An example of one of these fits is given in Figure [3.25]. The data points close to 0 ΔT correspond to the Gaussian fits performed on the kaon signal, and the data points that approach that band from the bottom correspond to the Gaussian fits performed on the muon signal. The horizontal position of each point is in the middle of the projection range, and the vertical position of each point was assigned based on the mean value of the Gaussian fit for each particle. The horizontal error bars are the size of the projection range, which is always 0.1 GeV/c. The vertical error bars are determined by the width of the Gaussian fits. The average of the widths of the kaon peaks is 0.1 ns which is the value used to determine the timing cut in Table 3.1.

γ

Unlike the other final state particles, the neutral final state photons do not leave a charged track. Therefore, the reconstruction requires at least one charged particle in the event to be used as a reference trajectory towards the event vertex. In the case of this study, there are three charged tracks used to determine the event vertex position. Once the vertex position of the event is known, it is assigned to all neutral particles in the final state. Therefore, the final state photons have a vertex distribution. These distributions and their associated cuts are given in the Target section, specifically Figure [3.2a] and Figure [3.2b]. It should also be mentioned that final state photons do not have a timing cut for the TOF. This is due to the fact that the time of flight can only interact with charged particles, and therefore cannot interact with photons. The timing cuts (Δt) for the γ only come from the BCAL, FCAL. Δ tis defined as the difference between the reconstructed vertex time for the particle and the time when the photon beam arrived. Since the timing distributions from data (Figure [3.27]) have too much neutron background in them, a Monte Carlo sample of $\gamma p \to pX; X \to \phi\eta; \phi \to K^+K^-; \eta \to \gamma\gamma$ was generated, simulated, and then reconstructed. This greatly reduces the background that is present in the timing plots and therefore can be used to estimate a proper timing cut for the γ and the sub detectors used to measure its time. Examples of these distributions and their associated projections onto the timing axis are given in Figure [3.28] through Figure [3.31]. A summary of all of the timing cuts used for the photon as well as all other final state particles is given in Table [3.1].

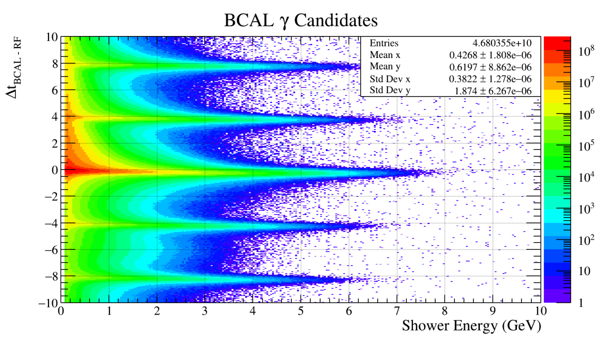

(a) Δ tVs Shower Energy for γ candidates that have the Barrel Calorimeter as the timing detector in data.

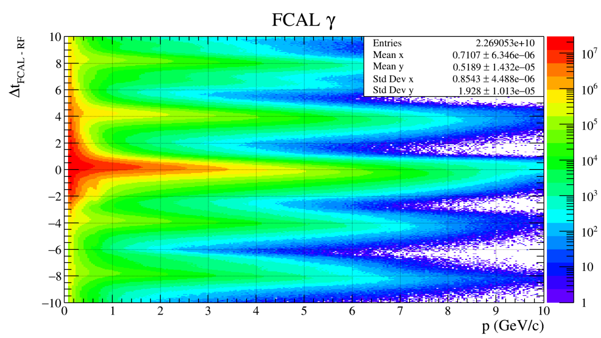

(b) Δ tVs Shower Energy for γ candidates that have the Forward Calorimeter as the timing detector in data.

Figure 3.27: Timing plots for γ candidates during the Spring 2017 run period for GlueX. γ are identified by selecting the horizontal band centered about $\Delta T = 0$. Large enhancement in statistics at low momentum and out of time with the γ line comes from slow moving and poorly timed neutrons. The additional horizontal lines above and below $\Delta T = 0$ come from γ showers that are associated with the wrong RF bunch.

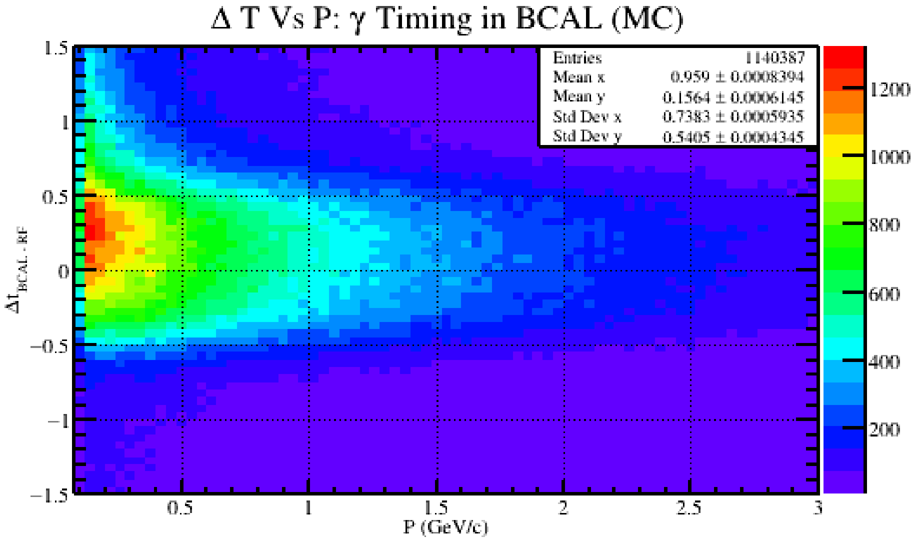

Figure 3.28: A timing plot for accepted γ from the generated reaction $\gamma p \to pX; X \to \phi\eta; \phi \to K^+K^-; \eta \to \gamma\gamma$. The horizontal axis is the reconstructed momentum of the γ and the vertical axis is the timing difference between the BCAL and RF.

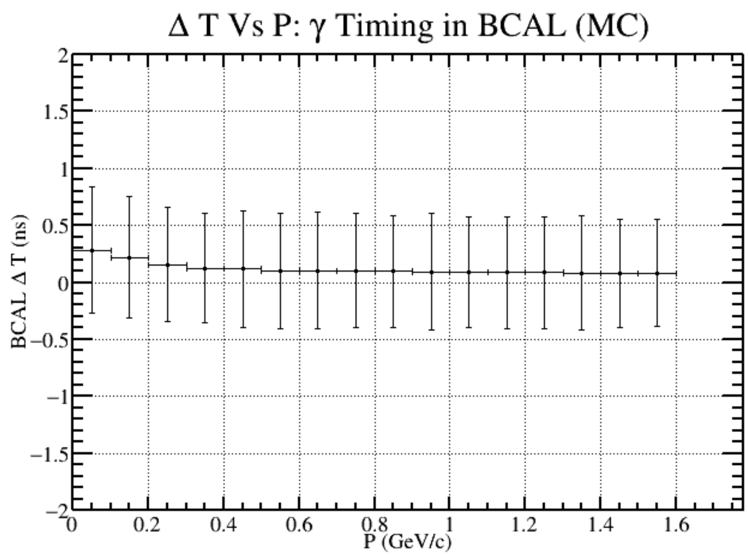

Figure 3.29: The image above is the result of the timing study performed on Figure [3.28]. Using that figure, a number of projection histograms were fit using different momentum ranges. The horizontal position of each point is in the middle of the projection range, and the vertical position of each point was assigned based on the mean value of the Gaussian fit. The horizontal error bars are the size of the projection range, which is always 0.1 GeV/c. The vertical error bars are determined by the width of the Gaussian fit. The average of the widths of the photon peaks is ~ 0.5 ns which is the value used to determine the timing cut in Table [3.1].

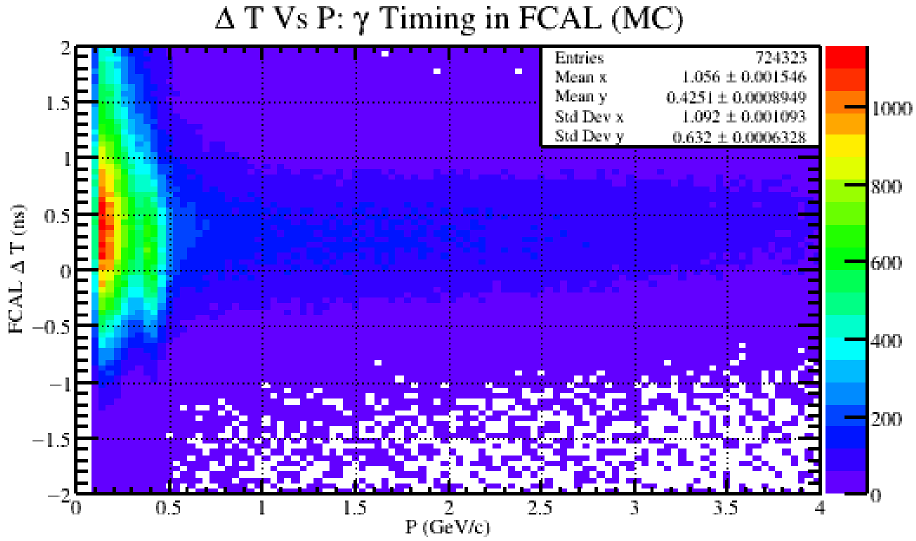

Figure 3.30: A timing plot for accepted γ from the generated reaction $\gamma p \rightarrow pX; X \rightarrow \phi\eta; \phi \rightarrow K^+K^-; \eta \rightarrow \gamma\gamma$. The horizontal axis is the reconstructed momentum of the γ and the vertical axis is the timing difference between the FCAL and RF.

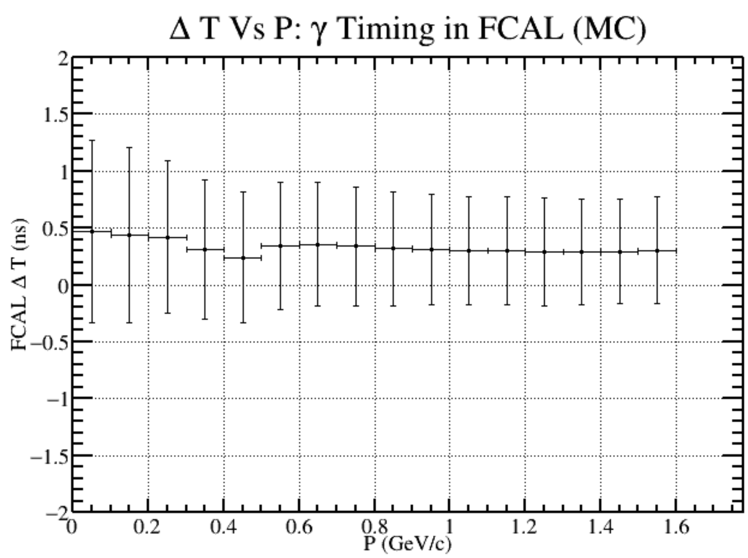

Figure 3.31: The image above is the result of the timing study performed on Figure [3.30]. Using that figure, a number of projection histograms were fit using different momentum ranges. The horizontal position of each point is in the middle of the projection range, and the vertical position of each point was assigned based on the mean value of the Gaussian fit. The horizontal error bars are the size of the projection range, which is always 0.1 GeV/c. The vertical error bars are determined by the width of the Gaussian fit. The average of the widths of the photon peaks is ~ 0.55 ns which is the value used to determine the timing cut in Table [3.1].

3.2 Additional Cuts for $\gamma p \to pK^+K^-\gamma\gamma$

3.2.1 Kaon Selection and Pion Rejection from TOF

One key aspect to performing a $\phi\eta$ analysis is to both identify the ϕ and the η mesons while also reducing the amount of background in each of their invariant mass spectra. One of the issues with the K^+K^- invariant mass spectra is that it contains misidentified pions. This background causes a peak in the K^+K^- invariant mass around 1.2 GeV/c^2. This peak is a manifestation of a ρ^0 which can decay to a $\pi^+\pi^-$ final state. An example of this background is illustrated nicely in Figure 3.32. It should be noted that all of the data used in this subsection is only 20 percent of the total data set.

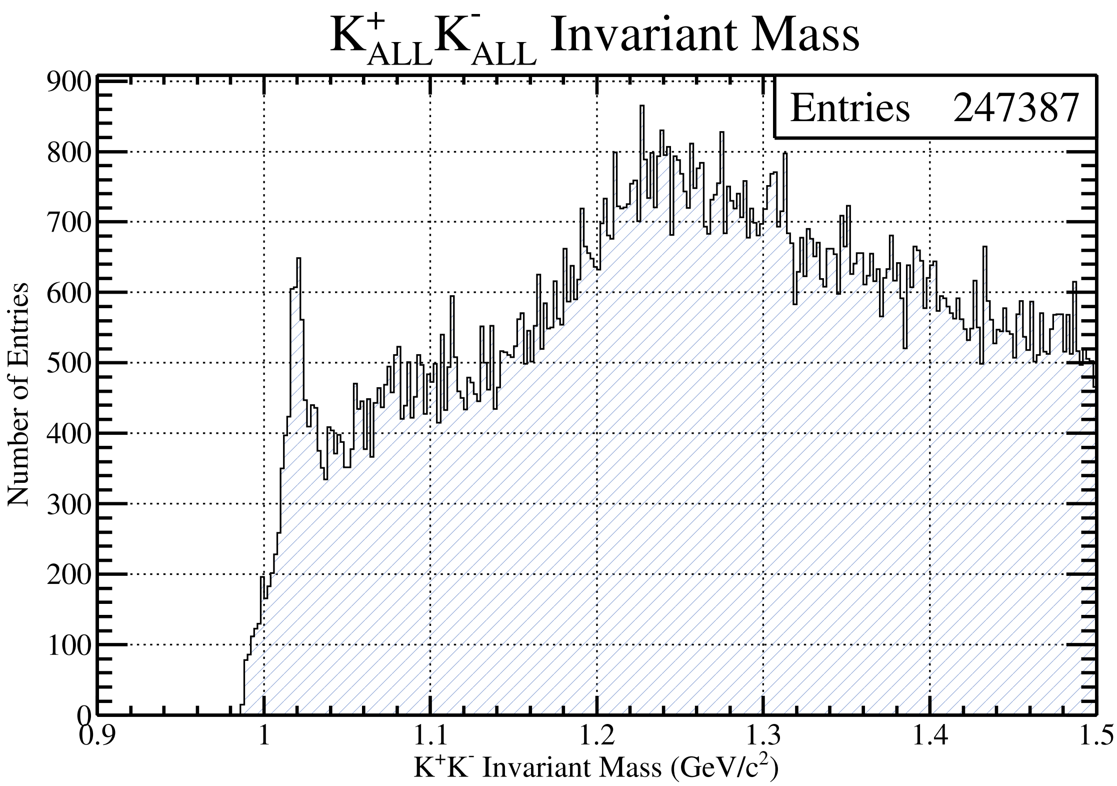

Figure 3.32: An example K^+K^- invariant mass histogram without pion removal from the Time of Flight. A rho peak can be seen around roughly 1.25 GeV/c^2.

One important aspect of QCD and the quark model is the conservation of quark flavor in hadronic decays, or decays which involve the interaction of the strong nuclear force. Conservation of quark flavor states that the initial number flavored quarks minus the initial number of anti-quarks of the same flavor, must be conserved. An example of this can be any strong or electromagnetic interaction which is being studied with the GlueX spectrometer. The GlueX experiment has an initial state photon which has no net quark content, plus a proton which has two up quarks and one down quark. Since the GlueX experiment is designed to study hadronic interactions, the final state must have a net quark flavor of two up quarks and one down quark. Considering the $\gamma p \to p\phi\eta$ interaction, it is clear that this requirement is met. The initial and final state proton are identical in quark flavor, and the ϕ and η mesons have no net quark flavor to them. Moreover, since the K^+K^- decay of the ϕ meson is being considered, the overall strangeness of this decay needs to be conserved as well. To state this more explicitly, the K^+ meson consists of a $u\bar{s}$ composite state, while the the K^- meson consists of a $s\bar{u}$ composite state. Since each kaon carries either a strange or anti-strange quark, it is only necessary to observe one kaon well. The method is based on strangeness conservation.

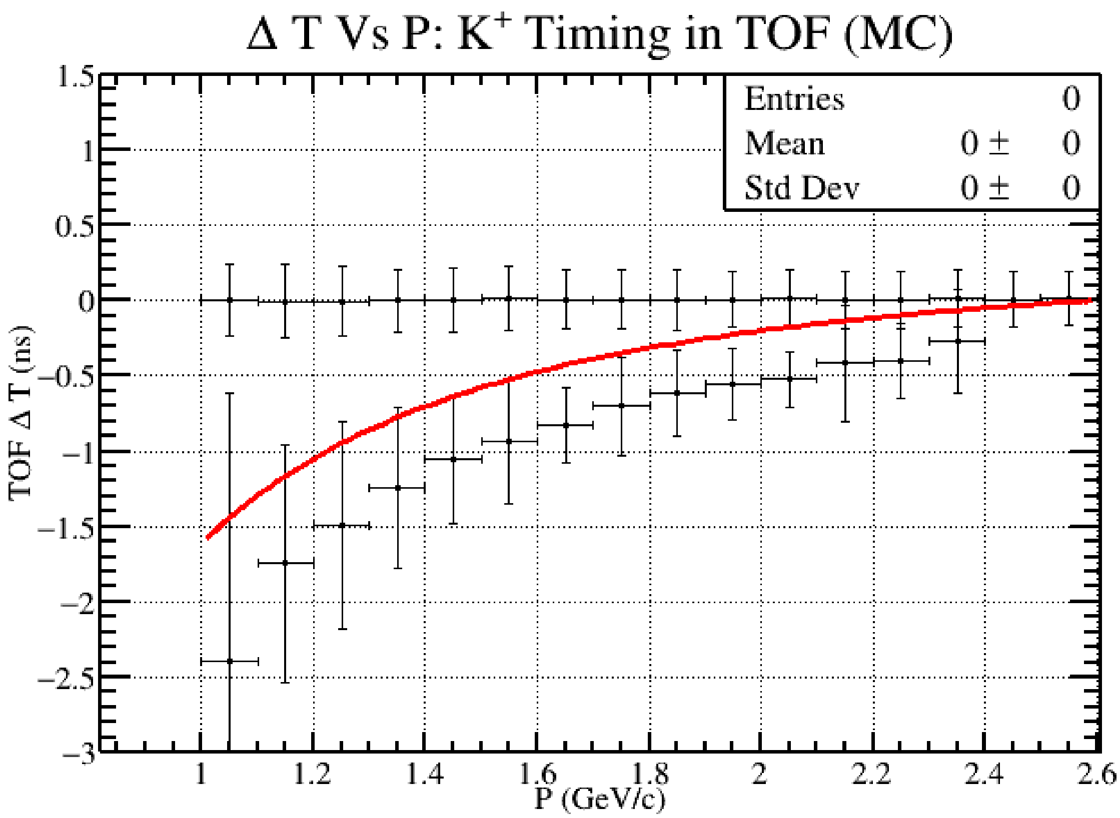

Figure 3.33: A graph which provides the strangeness conservation cut used for kaons that are detected by the Time of Flight detector. This is identical to Figure 3.18, except that the vertical error bars have been multiplied by a factor of 2 in order to visualize a 2σ uncertainty. The graph also contains Equation 3.3, with a timing shift of 0.2 ns.

Strangeness conservation is used to both preserve good $\phi\eta$ statistics, while also reducing the amount of background under the ϕ peak (Figure 3.32). Since the Time of Flight detector has the best timing resolution out of all subdetectors in the GlueX spectrometer, it will be used as an example in this section. In order to understand how strangeness conservation is implemented in this analysis, Figure 3.33 is provided. Contained within this figure is the timing versus momentum plot for the K^+, identical to Figure 3.18. Also contained within this diagram is a red line which represents the cut that will be used to separate particles with 'good strangeness' as opposed to particles that 'do not have good strangeness'. This red line is derived from simple equations of physics in the following way:

The flight time it takes for any relativistic particle to travel a distance δX at a velocity V in the lab frame, can be expressed using Equation 3.1.

$$t = \frac{\delta X}{V} = \frac{\delta X}{\beta c} \tag{3.1}$$

Furthermore, it is well known from Special Relativity that $\beta = P/E$. Using the relativistic equation for invariant mass, we can rewrite Equation 3.1 as Equation 3.2.

$$t = \frac{\delta X}{c} \frac{\sqrt{m_i^2 + P^2}}{P} \tag{3.2}$$

Since Equation 3.2 is true for any particle, we can then use it to describe the timing difference between pions and kaons in the lab frame, as measured by the Time of Flight. This final equation will take the form of Equation 3.3.

$$\delta t = \frac{\delta X}{c} \frac{\sqrt{m_\pi^2 + P^2} - \sqrt{m_K^2 + P^2}}{P} \tag{3.3}$$

The parameters δX, c, m_π, and m_K are known for Equation 3.3 since one is the speed of light, two are invariant masses, and the other is the distance that the charged particle traveled from the target chamber to the Time of Flight wall; which is a measured quantity in our experiment for all charged tracks. Therefore, the only two variables left over are δt and P which serve as the vertical and horizontal axis variables, respectively.

One last modification of Equation 3.3 is needed in order to take the form seen in Figure 3.33. If the equation is left the way that it is, the red line would simply bisect the pion curve, and would therefore not work well as a background cut. Therefore, Equation 3.3 is shifted up by 0.2 ns. This parameter was chosen based on the timing study that was performed on the Monte Carlo and is therefore a 2σ timing shift. It should be noted that since the K^+ and K^- mesons are anti-particles, as well as the π^+ and π^-, the same equation can be used to separate background for both kaons.

Given Equation 3.3 and Figure 3.33, strangeness conservation can now be addressed. In order to enforce strangeness conservation, it is imperative to identify one 'good kaon'. Good kaons will have one characteristic to them which is that they need to be positively identified by the Time of Flight detector. A positive identification will be defined as any kaon candidate that has timing above or to the left of the red line given in Figure [3.33]. Any particle that is to the right or below the red line is not guaranteed to be a kaon, and is therefore 'unknown'. Strangeness conservation allows us to preserve more statistics because all that is needed to justify the observation of a final state which includes a K^+K^- is one 'good kaon'. Therefore, any combination that the has either a K^+ or a K^- with the characteristic mentioned above will be accepted. The only combinations that will be rejected are those which both kaon candidates fail the characteristic mentioned above. To emphasize the importance and effectiveness of this cut, one should see what the K^+K^- invariant mass looks like without strangeness conservation (Figure 3.32), and then compare it to the K^+K^- invariant mass with strangeness conservation (Figure 3.38c).

3.2.2 Kaon Timing Selection Cut

After the particle identification cuts and the kaon selection from the Time of Flight, it was found that there was still a large amount of background in the K^+K^- invariant mass plot. This background was in all likelihood due to misidentified pions that were mistaken for kaons from detectors other than the Time of Flight. This can happen because of the timing and momentum resolutions inherent in any particle physics experiment. Furthermore, as can be seen in many of the timing plots provided, charged particles are in fact indistinguishable at high momentum. An example of the K^+K^- invariant mass histogram can be seen in Figure 3.34.

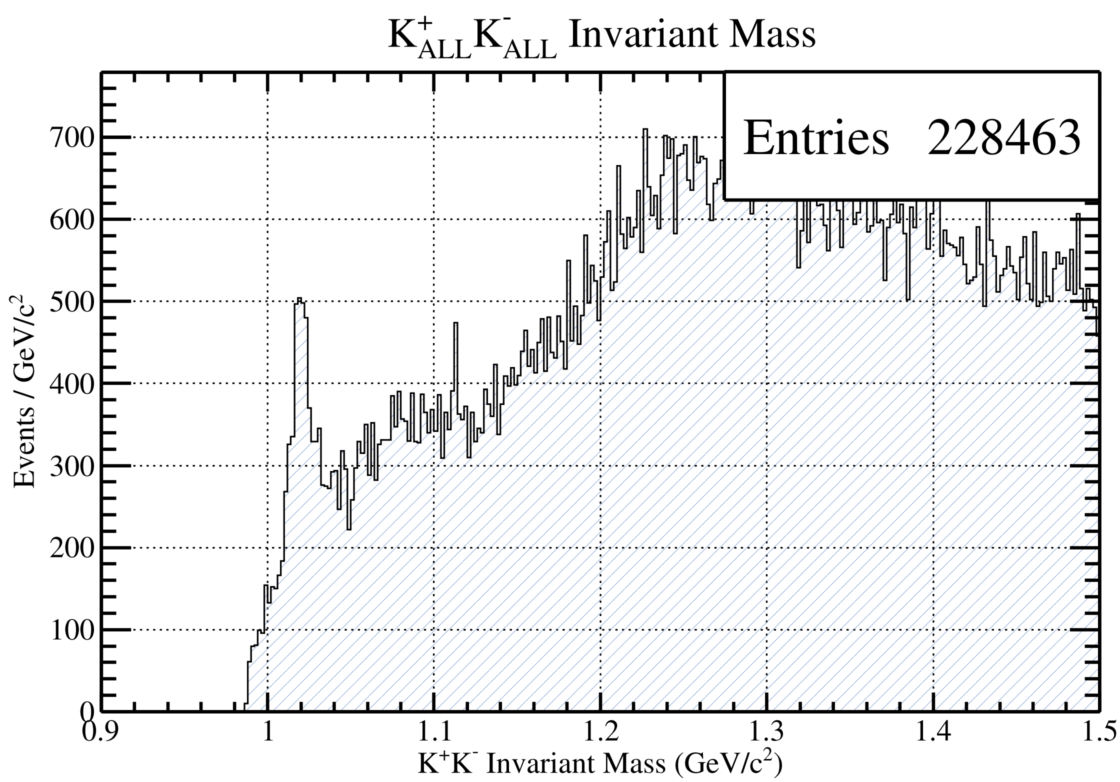

Figure 3.34: A histogram showing the K^+K^- invariant mass after particle identification cuts and the Equation 3.3 cut from the Time of Flight. The figure clearly shows a large amount of background at masses higher than the ϕ. This is due to the misidentification of pions for kaons from detectors other than the Time of Flight.

Due to this background, a study was performed over 5 percent of the data in order to understand where it may be coming from. The answer to this question was found by splitting up the K^+K^- invariant mass into different sub detectors which are responsible for the timing of the kaons. At GlueX, the three sub detectors which are responsible for providing timing and particle identification for charged particles are the Barrel Calorimeter, the Forward Calorimeter, and the Time of Flight. Since both the K^+ and the K^- can interact with any three of these sub detectors, there are nine total possible timing combinations that need to be considered. In order to properly understand these combinations, a two dimensional color

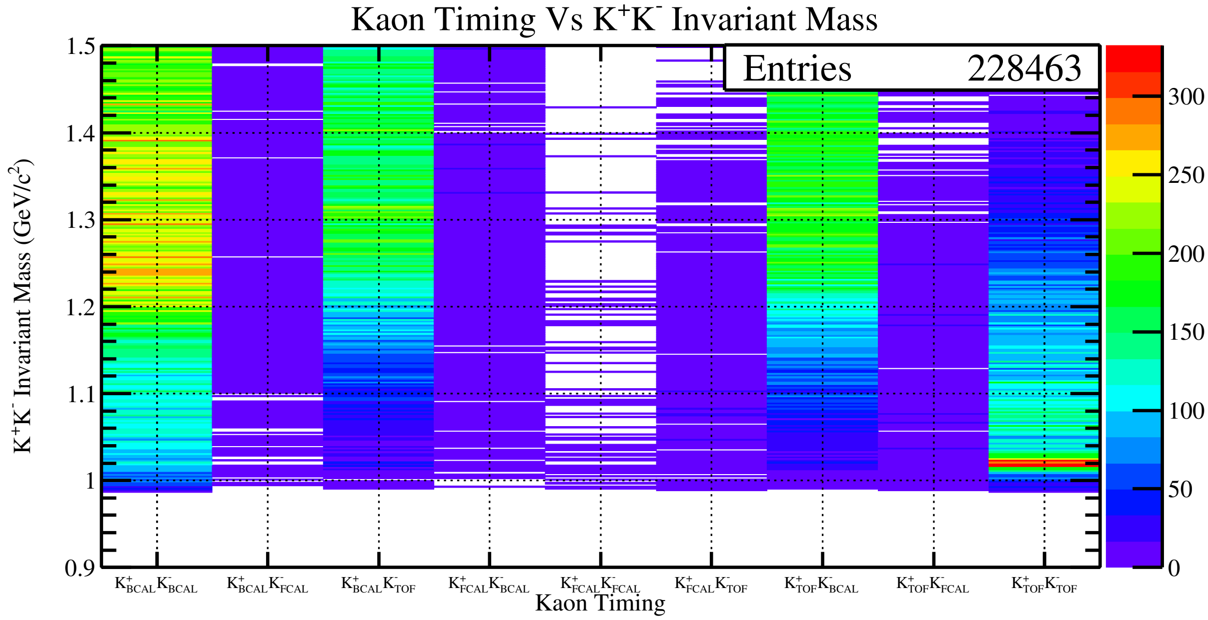

Figure 3.35: A two dimensional color histogram of the K^+K^- invariant mass versus the timing detectors for the kaons.

histogram was provided to show how the K^+K^- invariant mass changes as a function of sub detector timing for the kaons (Figure 3.35).

There are three important observations that can be made from Figure 3.35. One observation is that there is an overwhelming amount of background which comes from the Barrel Calorimeter timing for both K^+ and K^-. The second observation is that the Forward Calorimeter has little to no statistics what so ever. This is because the GlueX reconstruction algorithm prefers timing from sub detectors that have the best timing resolution. Since the Time of Flight and the Forward Calorimeter are in the same geometric direction, they tend to provide timing information for the same charged tracks. Since the timing resolution of the Time of Flight detector is better than the Forward Calorimeter, the majority of forward going charged tracks have timing from the Time of Flight. The last observation of Figure 3.35 is that nearly all of the events which appear to have a ϕ meson reconstructed in them only exist in the last bin which is the TOF/TOF timing bin. More specifically, it appears that most of the relevant $\phi\eta$ events will only have kaon timing that came from the Time of Flight detector. Therefore, all other timing sub detectors for the kaons can be thrown out. To further emphasize this point, projections of all nine bins contained within Figure 3.35 have been provided in Figure [3.36], Figure [3.37], and Figure [3.38]. These figures clearly show K^+K^- invariant mass spectra which contain all background and no sign of a ϕ meson; with the exception of the TOF/TOF projection.

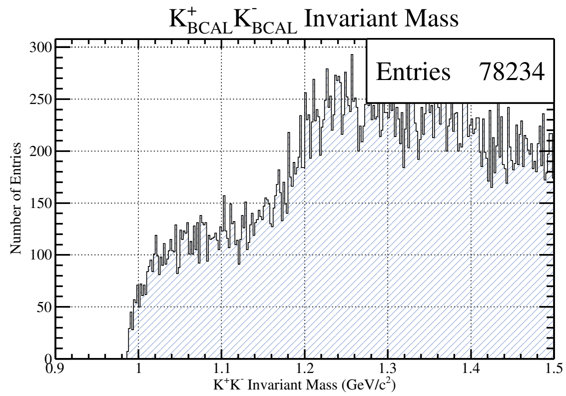

(a) Projection of $K^+_{BCAL}K^-_{BCAL}$ bin from Figure 3.35.

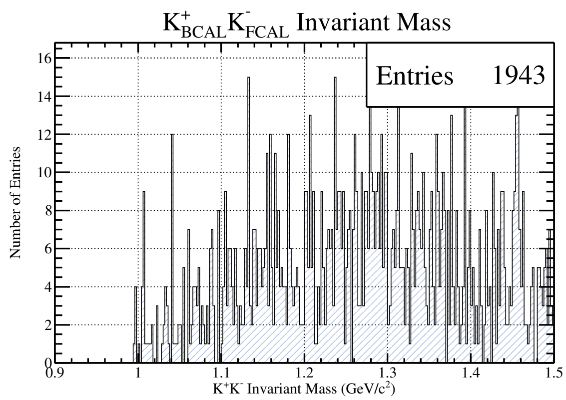

(b) Projection of $K^+_{BCAL}K^-_{FCAL}$ bin from Figure 3.35.

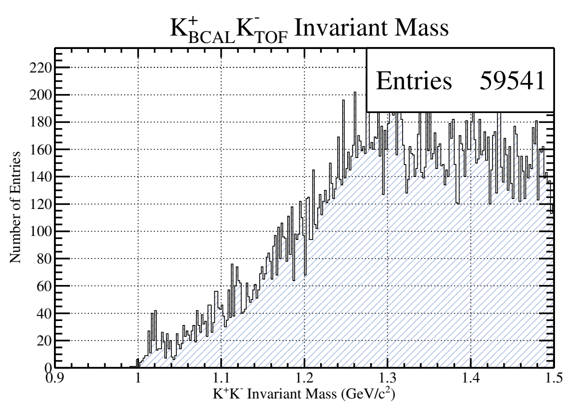

(c) Projection of $K^+_{BCAL}K^-_{TOF}$ bin from Figure 3.35.

Figure 3.36: Projections of $K^+_{BCAL}K^-_{X}$ bins from Figure 3.35.

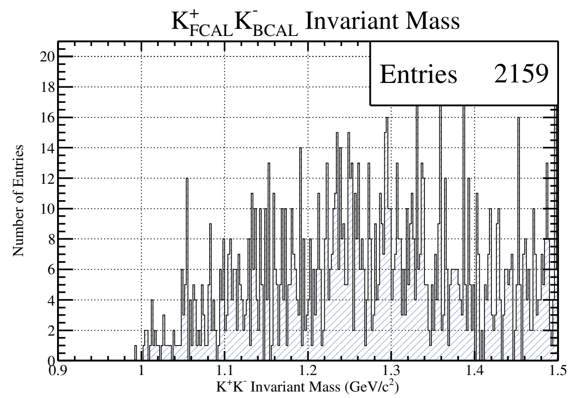

(a) Projection of $K^+_{FCAL}K^-_{BCAL}$ bin from Figure 3.35.

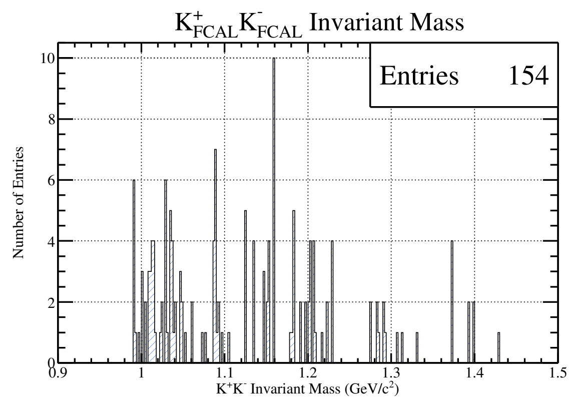

(b) Projection of $K^+_{FCAL}K^-_{FCAL}$ bin from Figure 3.35.

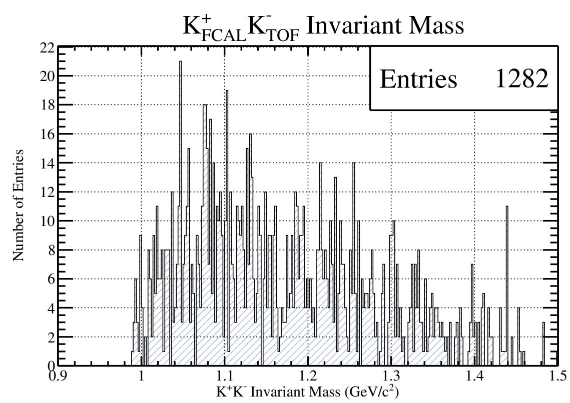

(c) Projection of $K^+_{FCAL}K^-_{TOF}$ bin from Figure 3.35.

Figure 3.37: Projections of $K^+_{FCAL}K^-_X$ bins from Figure 3.35.

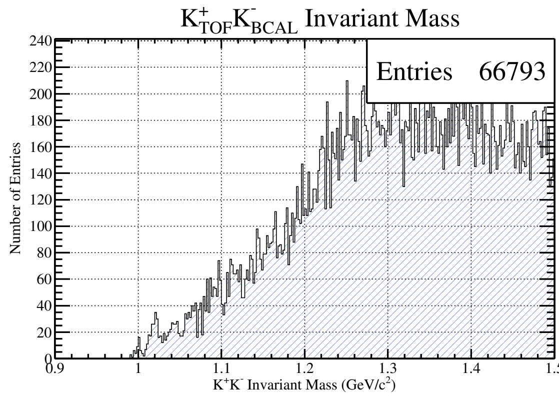

(a) Projection of $K^+_{TOF}K^-_{BCAL}$ bin from Figure 3.35.

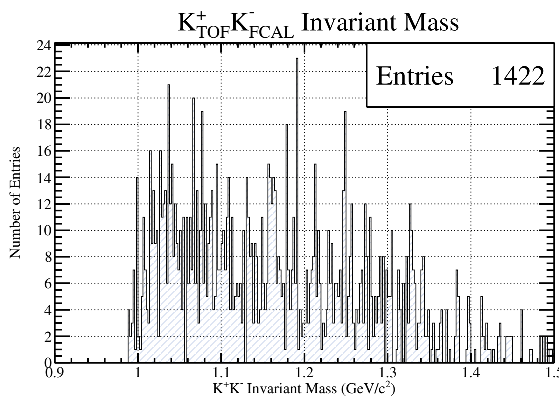

(b) Projection of $K^+_{TOF}K^-_{FCAL}$ bin from Figure 3.35.

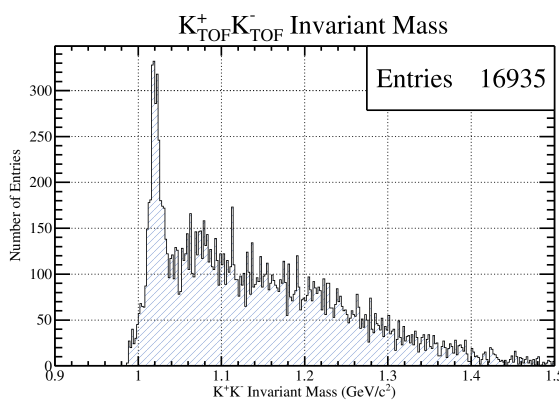

(c) Projection of $K^+_{TOF}K^-_{TOF}$ bin from Figure 3.35.

Figure 3.38: Projections of $K^+_{TOF}K^-_{X}$ bins from Figure 3.35.

3.2.3 Fiducial Photon Cut and Two Photon Cut

Before performing the $\gamma p \rightarrow p\phi\eta$ Monte Carlo study, it was well known that there was a lot of photon background seen in the data. After studying the data for quite some time, it was found that a two photon cut would destroy most of the background associated with photons and would also result in an observed η resonance in a $\gamma\gamma$ invariant mass plot. At the time, it was unknown why the cut appeared to throw out a lot of photon background while simultaneously appearing to enhance signal. After carefully studying accepted Monte Carlo, background generated Monte Carlo (`bggen`), and data, it was found that much of this background is attributed to secondary photons. A secondary photon should be thought of as a photon that did not originate from any photoproduction reaction, nor from any expected decay of parent states. Therefore, a secondary photon can be thought of as a photon that arose from an interaction within the GlueX spectrometer from a final state particle. An example of a secondary photon that would be present in $\gamma p \rightarrow p\phi\eta$ data can be explained by means of high momentum and forward going kaons (Figures [2.3][2.4]). Since it is very likely that most of the kaons in this channel will interact with either the Time of Flight detector or the Forward Calorimeter, it is expected that these particles will deposit a lot of energy in this region of the spectrometer. These high momentum particles will cause a signal in one or both of these detectors and will also cause a hadronic shower in the FCAL. These hadronic showers will be much wider and irregular in comparison to an electromagnetic shower. In addition to hadronic showers, another source of secondary photons are delta-electrons which are knocked out by charged tracks or beam halo anywhere in the downstream direction where they cannot be tracked by the FDC. These additional backgrounds create low energy electromagnetic showers in the FCAL but cannot be vetoed due to an absence of a reconstructed track. The additional reconstructed photons will therefore cause the number of photons reconstructed in an event to be fictitiously higher than what was actually present within the detector. To first order, this perhaps explains why doing a two photon cut on data will both greatly reduce background and enhance a signal. However, many important questions will still remain about this cut. How much signal do we lose by simply performing a two photon cut? Furthermore, is there a better way to cut out the background and preserve as many signal events as possible? This subsection will show that this effect does in fact manifest itself in both Monte Carlo and data; and will perform an analysis on Monte Carlo and data to show the best way of reducing secondary photons.

The first evidence that suggests the existence of secondary photons in $\gamma p \rightarrow p\phi\eta; \phi \rightarrow K^+K^-; \eta \rightarrow \gamma\gamma$ accepted Monte Carlo can be seen by simply plotting the invariant mass of a reconstructed $\gamma\gamma$ pair (Figure [3.39]). The data which went into this plot was created by throwing $\gamma p \rightarrow p\phi\eta; \phi \rightarrow K^+K^-; \eta \rightarrow \gamma\gamma$ into the GlueX detector and then simulating its behavior with `hdgeant` and `mcsmear`. The invariant mass spectrum in Figure [3.39] shows a clear peak from the generated η meson on top of a background that spans to low mass. If this sample initially only threw two photons exactly equal to the η meson invariant mass, then why are there so many low mass photon combinations that appear to be in the shape of background? To answer this question, we can separate our reconstructed Monte Carlo particles into two categories: particles that were generated and particles that were not generated. In doing so, we can see where this background comes from and also how to possibly reduce it.

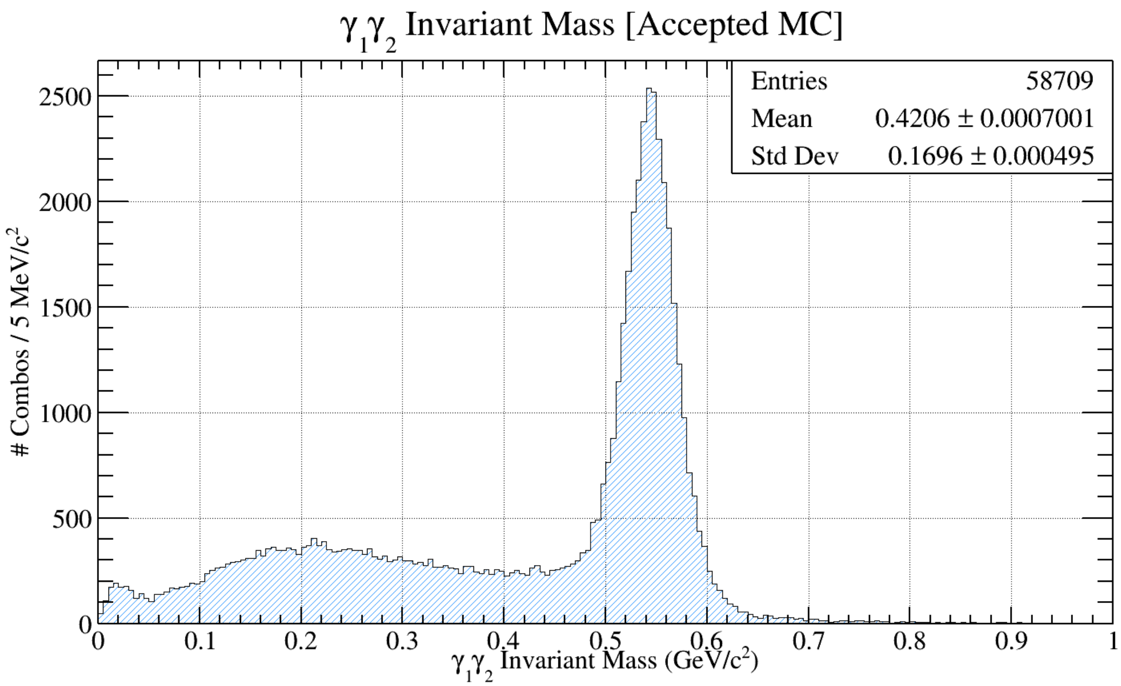

Figure 3.39: Invariant mass of the reconstructed $\gamma\gamma$ pair from accepted Monte Carlo. This Monte Carlo data originally came from a $\gamma p \to p\phi\eta; \phi \to K^+K^-; \eta \to \gamma\gamma$ generated topology. An interesting feature of this invariant mass spectra is that it shows a clear η peak, but also contains a background as well. The source of this background is thoroughly studied in subsection 3.2.3.

The signal and background seen in Figure [3.39] can be studied by displaying P Vs θ and ϕ Vs θ plots for the thrown photons and the secondary photons in Figure [3.40]. The most important feature to take away from these plots is the tendency for secondary photons to be at a shallow angle relative to the beam direction (below 12°) while also having a low three momentum magnitude (below 500 MeV/c). Simply knowing the distribution of these photons gives us some insight into where they came from. Since neutral photons can only be detected by either the Forward Calorimeter or the Barrel Calorimeter and most of these photons appear in the forward direction, it is clear that FCAL showers are causing these photons to appear.

The reconstructed invariant mass for a given $\gamma\gamma$ combination within an event as a function of the number of photons reconstructed within an event can also be shown. By using our Monte Carlo samples, we can also separate these plots into thrown and secondary photons, identical to what we did in Figure [3.40]. The reconstructed invariant mass of two photons versus the number of reconstructed photons in an event is given in Figure [3.41]. There is one important observation that should be taken away from the two sub figures. In Figure 3.41a a clear η resonance can be seen which spans a large number of reconstructed photons per event. This sub figure indicates that performing a two photon cut on the signal data is not good for signal events at this stage.

In fact, after fitting a Gaussian function to the η peaks between 3 and 10 reconstructed

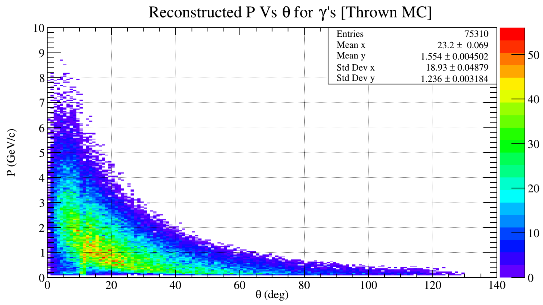

(a) P Vs θ distribution for thrown Monte Carlo photons.

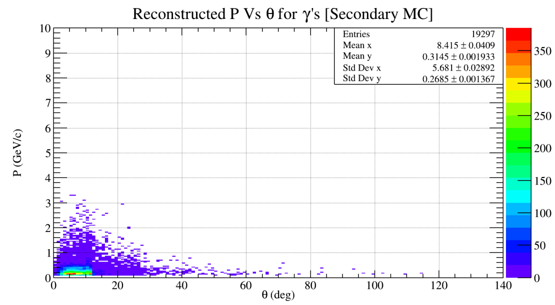

(b) P Vs θ distribution for secondary Monte Carlo photons.

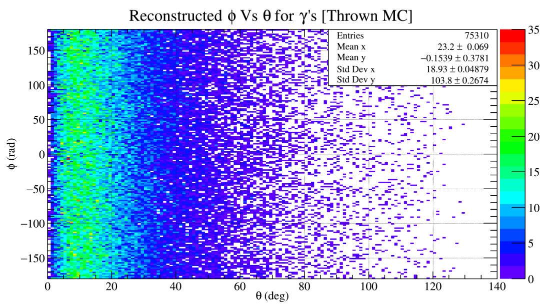

(c) ϕ Vs θ distribution for thrown Monte Carlo photons.

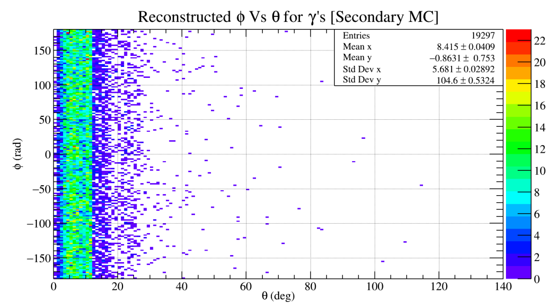

(d) ϕ Vs θ distribution for secondary Monte Carlo photons.

Figure 3.40: P Vs θ and ϕ Vs θ distributions for thrown (left column) and secondary (right column) photons inside accepted Monte Carlo data.

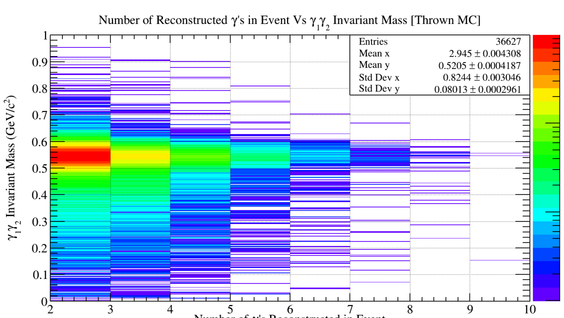

(a) Number of photons reconstructed in an event versus $\gamma\gamma$ Invariant Mass for thrown photons.

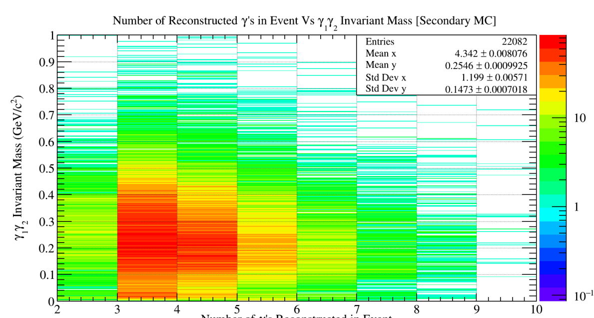

(b) Number of photons reconstructed in an event versus $\gamma\gamma$ Invariant Mass for secondary photons.

Figure 3.41: Comparing how the invariant mass for a given $\gamma\gamma$ pair changes depending on the number of reconstructed photons in an event and whether or not the photons were thrown or secondary photons.

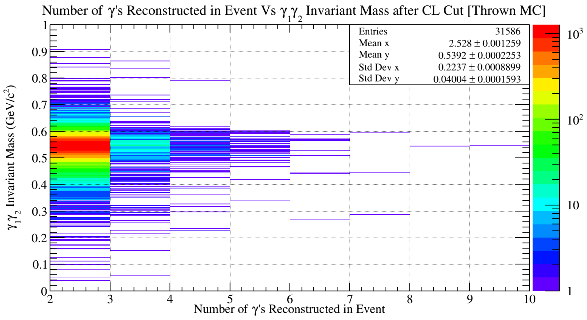

(a) Number of photons reconstructed in an event versus $\gamma\gamma$ Invariant Mass for thrown photons after a $P < 500$ MeV/c and $\theta < 12°$ cut.

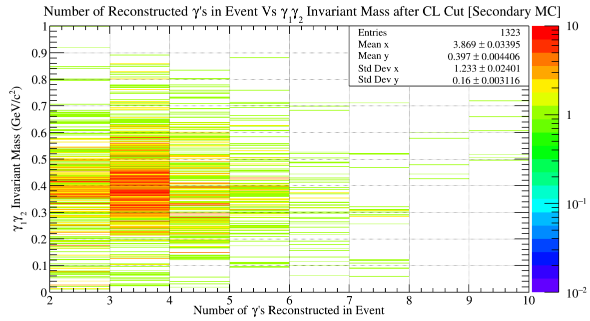

(b) Number of photons reconstructed in an event versus $\gamma\gamma$ Invariant Mass for secondary photons after a $P < 500MeV/c$ and $\theta < 12°$ cut.

Figure 3.42: Number of photons reconstructed in an event versus $\gamma\gamma$ Invariant Mass for thrown photons and secondary photons after a $P < 500MeV/c$ and $\theta < 12°$ cut.

photons, it was found that ∼8,000 combinations would be lost out of a total of ∼30,000; resulting in a 26 percent loss of events. Therefore, it is imperative to perform a P vs θ cut *before* a two photon cut.

Seeing that there is a non negligible amount of secondary photons left in accepted Monte Carlo, the next cut that will be applied to all of the data is a P Vs θ cut, where $P < 500MeV/c$ and $\theta < 12°$. After enforcing these cuts on all photons, the distribution of number of photons reconstructed in an event versus $\gamma\gamma$ invariant mass is shown once again in Figure [3.42]. It is easy to see that most of the η signal has migrated to the two photon bin and simultaneously much of the secondary background has been reduced in the accepted Monte Carlo data set. Due to this, a two photon cut is now necessary to do in order to reduce some of the left over background at higher number of reconstructed photons per event.

In this section it was shown that it is necessary to perform a P Vs θ cut of $P < 500MeV/c$ and $\theta < 12°$ and a two photon cut. After completing this sequence of cuts, it was found that 94 percent of background data was cut, while preserving 93 percent of signal data.

3.2.4 Exclusivity

The last cuts that need to take place in order to observe $\gamma p \to p\phi\eta$ are two; one which reduces the number of photons from the beam, and the other which cuts on the missing mass squared of the system. After all cuts had been made, it was found that there were still residual combinations from events which came directly from the beam photons and not the final state particles. After the proper beam timing cut, the event selection will then loop over available combinations in order to select the best available beam photon. This is done by selecting the beam photon which reconstructs the missing mass squared that is closest to zero. After enforcing this criteria, it is guaranteed that only one combination per event will survive. After this selection of events, an additional cut is placed on the data which enforces exclusivity. This is done by only allowing events with a missing mass squared between -0.02 GeV$^2/c^4 \leq MM^2 \leq 0.02$ GeV$^2/c^4$ (Figure 3.43). The enforcement of exclusivity removes any background that did not properly conserve the measured four momentum from the $\gamma p \rightarrow pK^+K^-\gamma\gamma$ reaction. To finalize this section Table 3.2 is a summarized list of all cuts performed by this analysis.

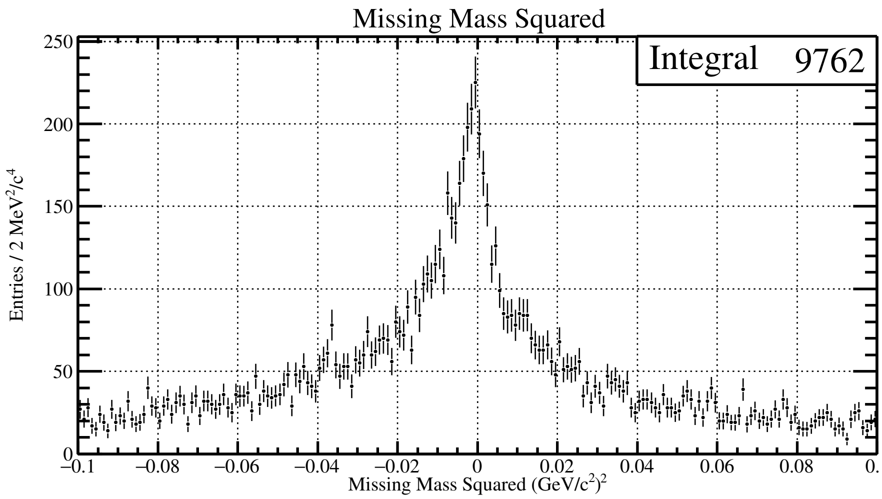

Figure 3.43: A plot of the final missing mass square after all cuts described in this chapter.

3.2.5 Tabular Summary of Particle Identification Cuts

Table 3.1: A table with timing cut values for all final state particles in the reaction $\gamma p \rightarrow pK^+K^-\gamma\gamma$. The values of the timing cuts change depending on both the particle species and detector system resolution. It should be noted that the final state photons only have the calorimeters as possible timing detectors. This is due to the fact that they do not interact with the TOF detector.

Particle	Detector	ΔT Cut [ns] (2σ)
Proton	BCAL	$\pm$ 0.6
Proton	FCAL	$\pm$ 1.0
Proton	TOF	$\pm$ 0.4
K^+	BCAL	$\pm$ 0.7
K^+	FCAL	$\pm$ 0.8
K^+	TOF	$\pm$ 0.2
K^-	BCAL	$\pm$ 0.7
K^-	FCAL	$\pm$ 0.8
K^-	TOF	$\pm$ 0.2
γ	BCAL	$\pm$ 1.0
γ	FCAL	$\pm$ 1.1

Table 3.2: A list which summarizes all cuts used to identify $\gamma p \rightarrow pK^+K^-\gamma\gamma$.

#	Description of Cut	Reference
1	Timing cuts for all final state particles	Table 3.1
2	Vertex cuts for all final state particles	Figures 3.2a, 3.2b
3	Beam timing cut	Figure 3.1
4	Proton dE/dX cut	[2]
5	P vs θ Cut for photons	Subsec: 3.2.3
6	Two Photon Cut	Subsec: 3.2.3
7	Kaon Selection	Subsec: 3.2.1
8	Kaon Timing Selection	Subsec: 3.2.2
9	$-0.02GeV^2/c^4 \leq MM^2 \leq 0.02GeV^2/c^4$	Subsec: 3.2.4
10	γ_{Beam} with MM^2 closest to zero	Subsec: 3.2.4

Chapter 4

Analysis

4.1 Investigation of $\phi\eta$ correlation by means of K^+K^- Vs $\gamma\gamma$ Invariant Mass Plot

The image illustrated in Figure 4.1 is the data in question. On the vertical axis is the K^+K^- invariant mass and on the horizontal axis is the $\gamma\gamma$ invariant mass. To be absolutely clear, this is a plot of invariant mass versus invariant mass and is therefore not a Dalitz Plot. Some interesting features contained within the image are the clear vertical bands for the π^0 and η resonances which have large decay modes to $\gamma\gamma$ final states. In addition, one can also observe a horizontal band slightly above 1 $\frac{GeV}{c^2}$ which corresponds to the ϕ meson decaying to a K^+K^- final state. This analysis will focus on the region where the ϕ meson and η meson bands cross in order to determine if their intersection region contains some type of correlation.

4.1.1 Cuts on the 2D Invariant Mass Plot

In order to analyze the $\phi\eta$ region of this data, only events which fall within $\pm 10\sigma_\phi$ away from the ϕ peak and $\pm 10\sigma_\eta$ away from the η peak will be considered. This was done by taking different slices of either the $\gamma\gamma$ or K^+K^- data, then projecting the invariant mass distribution onto the opposite axis. For example, there were five different ϕ mass regions studied in this analysis. Each fit corresponds to a different $\gamma\gamma$ mass range. The $\gamma\gamma$ mass ranges are all $4\sigma_\eta$ in width, and span a total mass range of $m_\eta - 10\sigma$ to $m_\eta + 10\sigma$. An example with labeled cut lines is provided in Figure 4.2. It should be noted that the analysis of the η mass was not studied symmetrically about the ϕ due to the K^+K^- threshold.

4.1.2 Projections and Fits for ϕ and η

Once the data had been cut and projected in the ten different mass regions, the ϕ and η peaks were fit. In the instance of the ϕ meson, the signal plus background events were fit with a Gaussian plus a second degree polynomial. The fit range used in each histogram projection for the ϕ meson spans from $m_\phi - 6\sigma_\phi$ to $m_\phi + 30\sigma_\phi$. The unusually large fit range was necessary in order to properly estimate the background surrounding the ϕ mass.

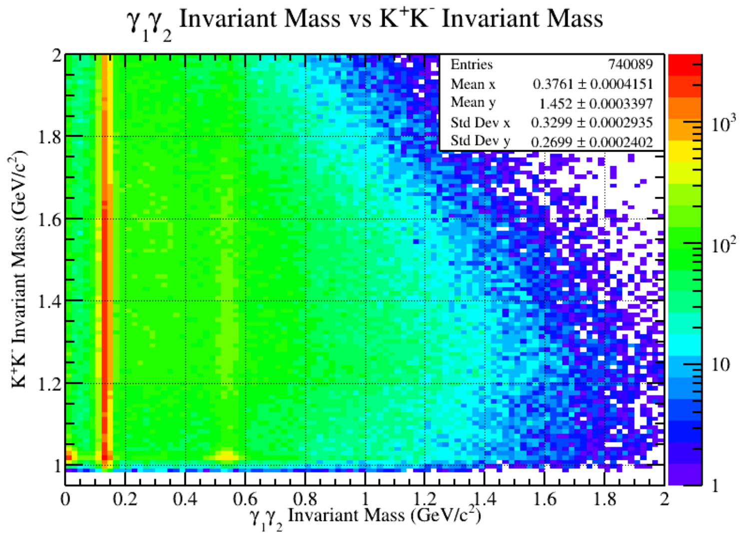

Figure 4.1: A two dimensional invariant mass plot with the K^+K^- invariant mass on the vertical axis, the $\gamma\gamma$ invariant mass on the horizontal axis, and a logarithmically scaled z axis. Some interesting features contained within the image are the clear vertical bands for the π^0 and η resonances which have large decay modes to $\gamma\gamma$ final states. In addition, one can also observe a horizontal band slightly above 1 $\frac{GeV}{c^2}$ which corresponds to the ϕ meson decaying to a K^+K^- final state.

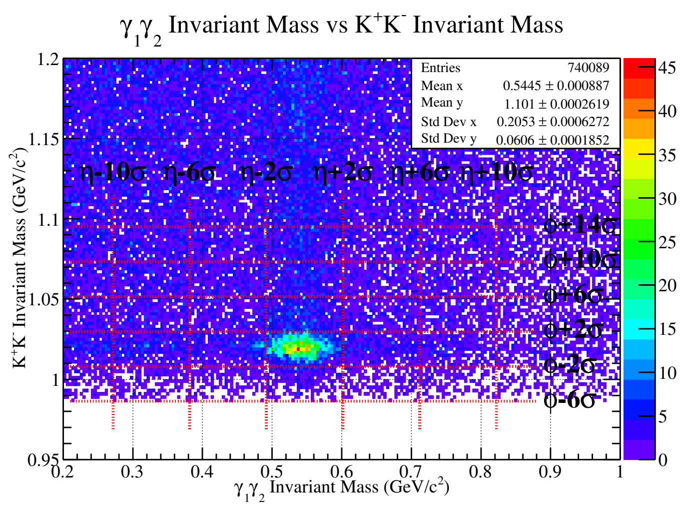

Figure 4.2: An illustrated example of the cuts used for studying the correlation of $\phi\eta$. The figure above is a two dimensional invariant mass plot which clearly shows an η band spanning the vertical direction at ~ 0.547 GeV/c^2 and a ϕ band spanning the horizontal direction at ~ 1.02 GeV/c^2. The red vertical and horizontal cut lines provide the ranges used to study $\phi\eta$ correlation. Examples of what the projected ranges look like are provided in Figures [4.3][4.4].

In the instance of the η meson, the signal plus background events were fit with a Gaussian plus a first degree polynomial due to the relatively flat background surrounding the η peak. The fit range used for the η meson spans $m_\eta \pm 6\sigma_\eta \ \frac{GeV}{c^2}$. The resulting fits are provided in Figures 4.3 and [4.4], where the blue line represents the fit for all events (signal plus background), the green line represents the Gaussian fit (signal events), and the red line represents the polynomial fit (background events). Each histogram contains a title with brackets at the end. The arguments encapsulated by the brackets is the cut range that was used for that particular projection sample.

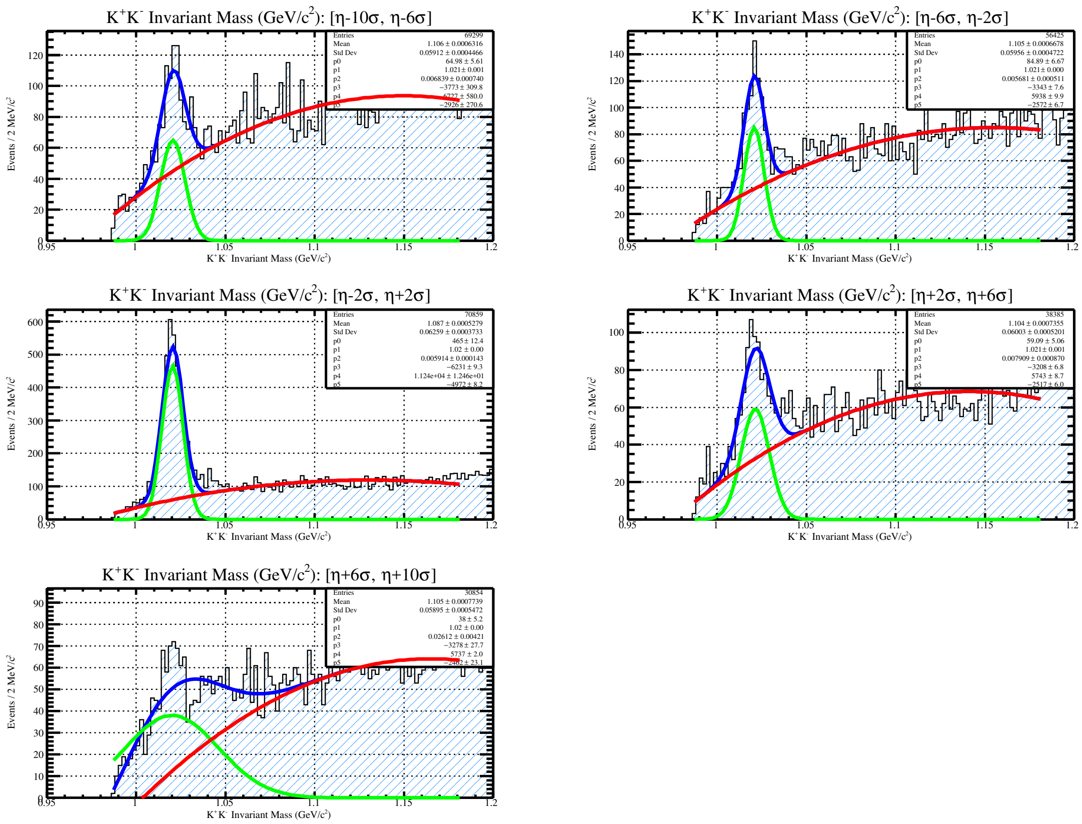

Figure 4.3: A collection of different K^+K^- invariant mass projections as a function of $\gamma\gamma$ invariant mass cut range. Each sub figure includes a red line which is a second degree polynomial used to estimate the shape of the background, a green line which is a Gaussian used to estimate the ϕ signal peak, and a blue line which the sum total of the polynomial fit and Gaussian fit. Lastly, each sub figure also includes the $\gamma\gamma$ invariant mass cut range used to produce the projected figure. This information is in the title of the histogram, inside the brackets.

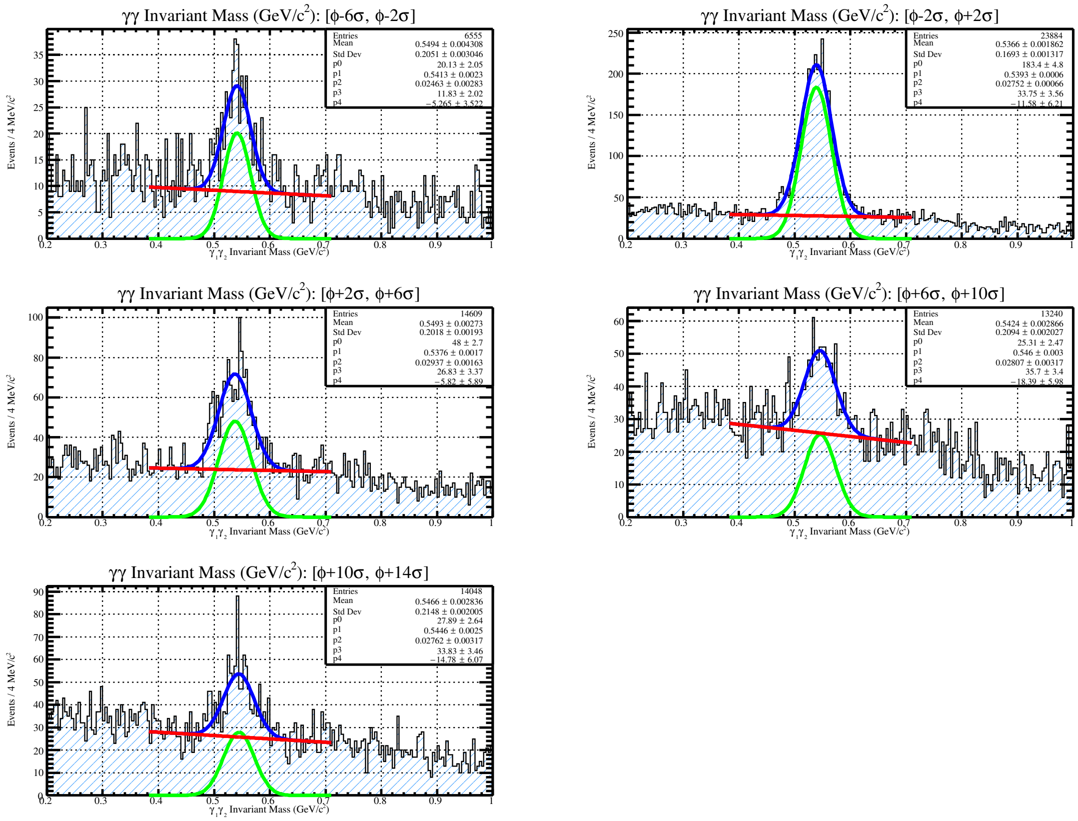

Figure 4.4: A collection of different $\gamma\gamma$ invariant mass projections as a function of K^+K^- invariant mass cut range. Each sub figure includes a red line which is a first degree polynomial used to estimate the shape of the background, a green line which is a Gaussian used to estimate the η signal peak, and a blue line which the sum total of the polynomial fit and Gaussian fit. Lastly, each sub figure also includes the K^+K^- invariant mass cut range used to produce the projected figure. This information is in the title of the histogram, inside the brackets.

4.1.3 Integration Results for ϕ and η

After obtaining accurate fits for all regions, integration of the Gaussian fit functions was performed. Each Gaussian fit was integrated in the range of $m \pm 2\sigma_m$, where m represents either m_ϕ or m_η mass coupled with the addition or subtraction of two standard deviations in each direction. Integration of the Gaussian fits provides an accurate estimate for the number of signal events that exists for that particular sampling of $\gamma\gamma$ Vs K^+K^- phase space. The estimated number of signal events have been added to Figure [4.5], with the exception of the $\phi\eta$ intersection region which will be discussed in more detail in the Conclusion section.

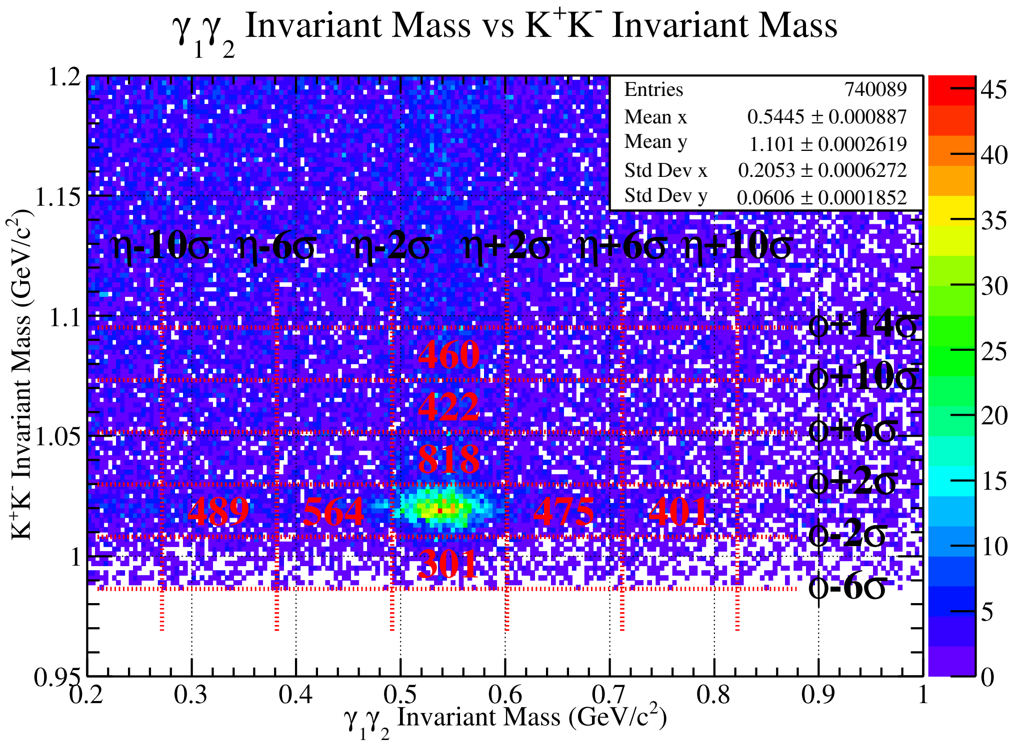

Figure 4.5: The above figure provides the number of events for each projection range studied. These numbers were calculated by means of integrating the Gaussian fit for either the ϕ or η between $\pm 2\sigma$. The vertical column of numbers represents the number of η events for a given K^+K^- invariant mass, and the horizontal row of numbers represents the number of ϕ events for a given $\gamma\gamma$ invariant mass. The number of events observed in the intersection region was not included in the figure due to the amount of space available. There numbers can be found in the Conclusion section.

4.1.4 Additional Statistics Study

In addition to the analysis mentioned above, an alternative study has been included which simply samples the phase space and records the number of events within that sample. To do this, the same cut ranges as before were used. The only difference is that this approach only considers the 3x3 grid surrounding the $\phi\eta$ intersection region. Each region is a box cut which is exactly $4\sigma_\phi$ x $4\sigma_\eta$ in area. Each area is given an index to denote the specific region of phase space that is being sampled and an illustration is provided in Figure [4.6].

Using the diagram as a reference, it is easy to see that the average number of background events within this phase space can be calculated using the formula $N_{BG} = (A_1 + A_3 + A_7 + A_9)/4$. Additionally, the average number of ϕ and η events plus background can be calculated using $N_{BG} + N_\phi = (A_4 + A_6)/2$ and $N_{BG} + N_\eta = (A_2 + A_8)/2$, respectively. Lastly, quantification of the number of correlated events in region 5 is possible by using

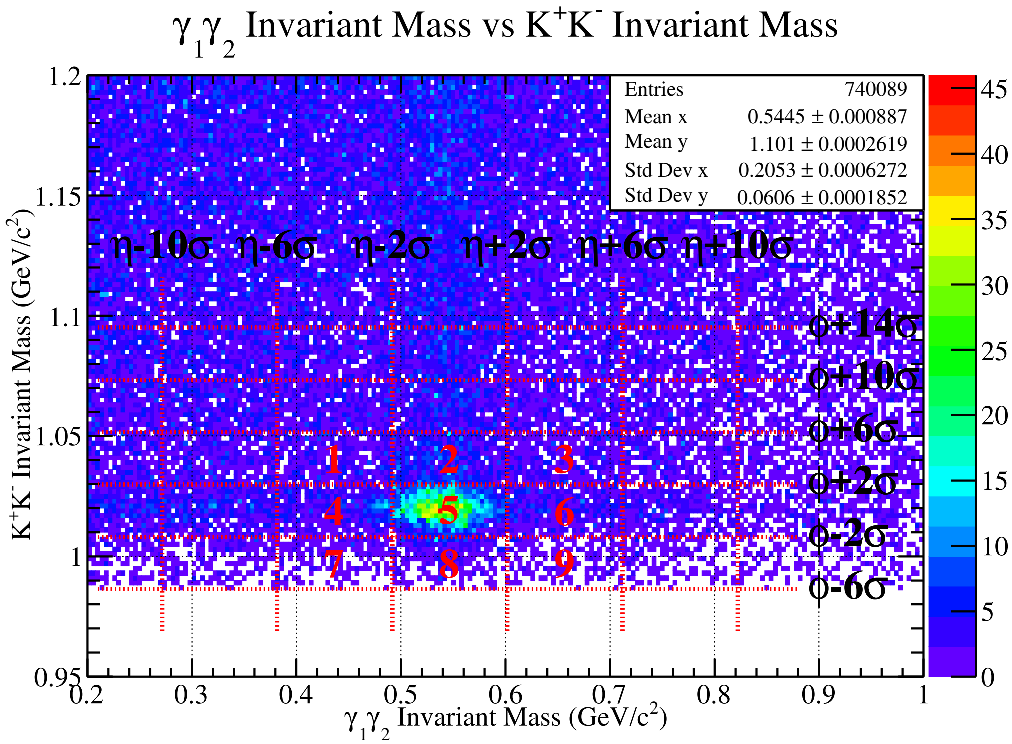

Figure 4.6: An illustration to provide the reader with an idea of how the second statistics study is performed. All of the cut ranges are identical to the first statistics study. The numbers provided in the figure do not represent events, but simply indicate the index associated with a certain area of $\phi\eta$ phase space.

$N_{BG} + N_\phi + N_\eta + N_{correlated} = A_5$. The number of events contained within each region of phase space is given in Figure [4.7].

The first step of this simplistic analysis is to determine what the average number of background events is, which is calculated to be 453. Knowing this, the number of ϕ and η events can now be determined by using the equations $N_{BG} + N_\phi = (A_4 + A_6)/2$ and $N_{BG} + N_\eta = (A_2 + A_8)/2$, and then subtracting the average number of background events. Upon doing this, it was found that N_ϕ is 423 and N_η is 433. To complete this analysis, the number of correlated events can now be estimated by using the equation $N_{BG} + N_\phi + N_\eta + N_{correlated} = A_5$, and subtracting N_{BG}, N_ϕ, and N_η. The total number of correlated events is 2446. This calculation shows once again that there is an overflow of events within the $\phi\eta$ intersection region that cannot be explained by the presence of background or the addition of events from the ϕ and η bands.

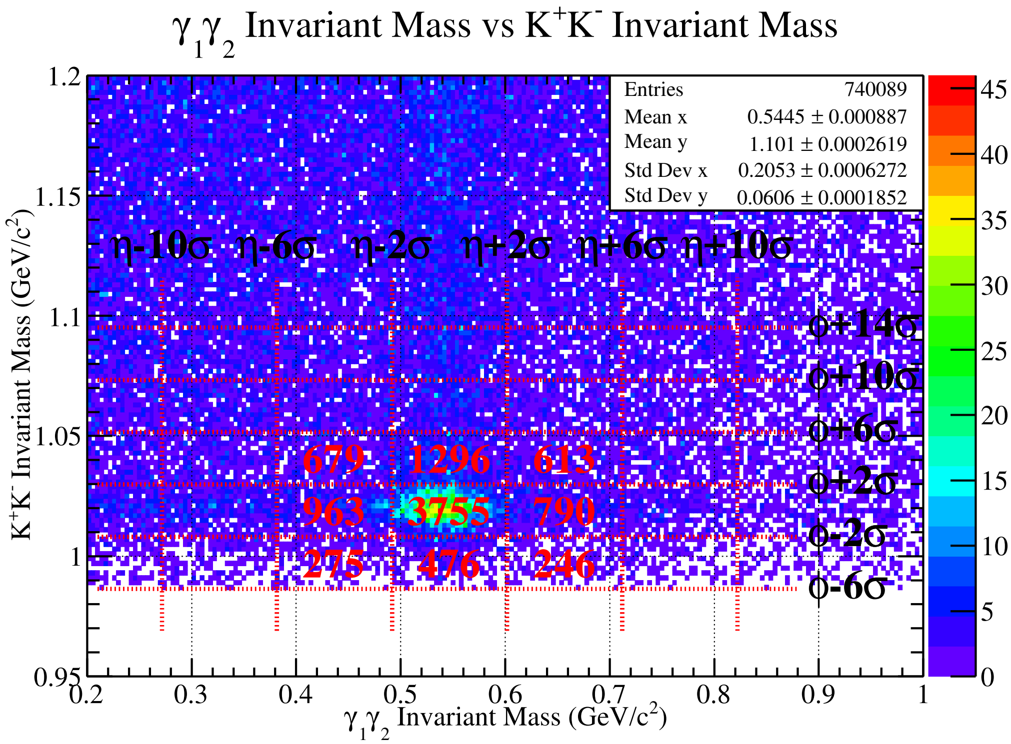

Figure 4.7: This figure shows the total number of counts in each box. To be clear, the numbers in each box do not represent the total number of events, but rather the precise amount of statistics contained within the cut lines. Upon inspection, one can see evidence of $\phi\eta$ correlation, which is explained in the Conclusion section.

4.1.5 Conclusion of K^+K^- Vs $\gamma\gamma$ Invariant Mass Plot Study

Figure [4.5] provides the estimated number of signal events for the ϕ and η bands near the $\phi\eta$ intersection region. If there is no correlation between ϕ and η events, the total number of signal events in the intersection region should be equal to the sum of an η peak plus a ϕ peak. Taking the numbers from Figure [4.5], the average number of signal events in the ϕ band is $\overline{\phi_{events}} \sim 482$, and the average number of signal events in the η band is $\overline{\eta_{events}} \sim 500$. Therefore, it is estimated that the number of signal events within the $\phi\eta$ intersection region should be just shy of 1000 events if there is no correlation present. After integrating the Gaussian fit for the ϕ and η mesons in the intersection region, it was found that there were 3194 events corresponding to the ϕ fit, and 2993 events corresponding to the η fit. Both of these fits not only yield roughly the same number of events, but they also produce an event estimate which is a factor of three higher than what would have been there from the ϕ and η bands alone. The large increase in event statistics within the $\phi\eta$ intersection region strongly suggests that some type of correlation is present within this area of K^+K^- $\gamma\gamma$ phase space. It should be clearly noted that the nature of this correlation is not identified at this time.

Moreover, it is unclear if this $\phi\eta$ enhancement corresponds to a $\phi\eta$ bound state, or comes from some other topology such as $\gamma p \to N^*\phi$ and $\gamma p \to N^*\eta$.

4.2 Probabilistic Weightings for $\phi\eta$ Events

Throughout the course of history, physicists have tried clever ways of reducing the amount of background that is present under a given signal, or resonance. An example of this may be the classic side band subtraction, where the signal region will be defined by some average mass value, plus or minus a well defined width. If one were to perform a cut about this region after particle identification and cuts, there still may be background underneath the peak. In order to eliminated the background under the signal, one thing to do is use the background near the peak as reference for subtraction. To do this, one would use background events that are located at both higher and lower mass values far away from the signal, so long as the total mass range used is equal to the mass range for selecting the signal region. The side band subtraction method works well for some physics analyses, but not all. Side band subtraction is an issue with this analysis because the primary purpose is to observe structures in the $\phi\eta$ invariant mass spectra. Performing a side band subtraction is problematic because it allows events well below the $\phi\eta$ threshold to exist in the background spectra. Subtracting off these events from the primary signal region results in a final $\phi\eta$ invariant mass spectra which has negative event counts at low $\phi\eta$ mass values. Therefore, it is imperative to seek alternative background subtraction methods. The method that will be presented in this analysis uses a probabilistic weighting procedure which will be explained in this section.

4.2.1 Introduction to Probabilistic Event Weightings

One of the issues with a side band subtraction method is that it treats all events with a relative weight of one. The purpose of this section is to describe and propose a new method which does not treat all events with a value of one, but instead assigns a fractional weight to an event based on a quality factor, or Q-factor. The quality value idea was first introduced in 2008 by M. Williams, M. Bellis, and C. A. Meyer in a paper titled "*Separating Signals from Non-Interfering Backgrounds using Probabilistic Event Weightings.*" [3]. The paper considers a generic situation in which there is a data set of n total events described by m coordinates, which will be written as $\vec{\xi}$. Within the data set, there exists n_s total signal events and n_b total background events, and therefore $n = n_s + n_b$. In addition, both the signal and the background distributions are functions of the coordinates, such that $S(\vec{\xi})$ can be thought of as a signal distribution and $B(\vec{\xi})$ can be thought of as a background distribution. Contained within the set of coordinates $\vec{\xi}$, there exists a *reference coordinate* (ξ_r) with which we know the functional form of $S(\xi_r)$ and $B(\xi_r)$ *a priori*. The reference coordinate that is used in this thesis as well as in the paper mentioned above is the invariant mass of a final state. For many invariant mass distributions, the functional form of the signal distribution, $S(\xi_r)$ can be represented with a well known signal function. Some examples of well known signal functions are Gaussian, Voigtian, and Breit-Wigner distributions. In addition, the background distribution, $B(\xi_r)$, can be represented with an n^{th} degree polynomial function.

Since the signal and background distributions are not necessarily known *a priori* for the other coordinates, we use them to calculate a kinematic distance on an event by event basis. This is done by using the Equation (4.1).

$$d_{ij}^2 = \sum_{k \neq r} \left[\frac{\xi_k^i - \xi_k^j}{R_k} \right]^2 \tag{4.1}$$

In Equation(4.1), the total kinematic distance is calculated between some event i, as compared to another event j. This is done by taking the sum of the squared difference over all of the coordinates ξ_k, except for the reference coordinate ξ_r. The difference between coordinates is then normalized by the parameter R_k. The parameter R_k is the total maximum difference for a given coordinate ξ_k. An example of this may be the measurement of an azimuthal angle which spans from 0 to 2π. Therefore, the R_k for an azimuthal angle would be 2π. Upon closer inspection, one should realize that Equation(4.1) is simply a representation of the Pythagorean Theorem in a normalized $m-1$ dimensional kinematic space.

After calculating all of the kinematic distances for an event i, as compared to all other events within the data set $1...j...n$, it is then necessary to only keep the *nearest neighbors*. The nearest neighbors, by definition, are a subset of the n events which have the smallest kinematic distance with respect to the i^{th} event that is being considering. The purpose of only keeping the nearest neighbors stems from the assumption that a signal or background events will share similar kinematic measurements with other signal or background events. The number of nearest neighbors for a set of events n is an arbitrary amount, and does not greatly effect the quality factor calculation; so long as the amount is a small fraction of the total events n. Once the list of nearest neighbors is known for the i^{th} event, it is then necessary to plot their reference coordinate, ξ_r, onto a histogram. This histogram should contain a well understood signal distribution $S(\xi_r, \vec{\alpha})$, and background distribution $B(\xi_r, \vec{\alpha})$, as mentioned above; where $\vec{\alpha}$ is the set of known/unknown fit parameters used to describe the signal or background distribution. The histogram will then be fit by the sum of the signal and background distributions such that $F(\xi_r, \vec{\alpha}) = S(\xi_r, \vec{\alpha}) + B(\xi_r, \vec{\alpha})$. The quality factor can then be calculated by using the reference coordinate value for the i^{th} event and plugging it into the signal and background functions by using Equation(4.2), where $\hat{\alpha}$ is the set of fitted parameters for the signal or background distribution.

$$Q_i = \frac{S(\xi_r^i, \hat{\alpha}_i)}{S(\xi_r^i, \hat{\alpha}_i) + B(\xi_r^i, \hat{\alpha}_i)} \tag{4.2}$$

Once the quality factor is known for an event i, it can be recorded, and then the analysis can consider the next event and repeat the sequence all over again. Once all events have been run over, the quality factors for each event are used as a weight for plotting inside histograms. If the quality factor is correctly calculated for each event, the method should be able to separate signal from background. More specifically, if a histogram of the K^+K^- invariant mass is plotted with Q_i as the weight for the i^{th} event, one should see a 'pure' ϕ peak with absolutely no background. In addition, if the K^+K^- invariant mass is plotted with $1 - Q_i$ as the weight for the i^{th} event, one should see all background and absolutely no ϕ peak. Therefore, the sum of the signal histogram plus the background histogram should be equal to the K^+K^- invariant mass with all events having a weight of 1.

Determining the Number of Nearest Neighbors

After the kinematic distances are calculated for all events with respect to the i^{th} event, they are sorted in order from smallest kinematic distance to largest kinematic distance. Only the the nearest neighbors, or the set of events with the smallest kinematic distance, will be used to determine the quality factor of a given event. For this analysis, there were a total of 16,981 events after selection cuts, and the number of nearest neighbors used was 500. This number was chosen somewhat arbitrarily; it is important to pick the smallest number possible such that the events used truly are those which share the most similar kinematic features to the event that is being considering. If the number was extremely large with respect to the total number of events, the analysis will not work properly. Events that are background will have some nearest neighbors that are signal, and vice versa. Furthermore, the number of nearest neighbors needs to be large enough such that a fit can converge with the filled histogram. If the number of nearest neighbors is too small, ROOT will fail to provide any signal or background information inside the histogram, and therefore calculation of a quality factor will be impossible. Considering these two constraints and testing with different values, it was found that the smallest number which did not result in *any* fitting failures was 500.

Fitting the K^+K^- Invariant Mass

Upon determining the nearest neighbors of the i^{th} event, the next step is to plot and fit the set of K^+K^- and $\gamma\gamma$ invariant mass distributions. As mentioned above, it is extremely difficult to model the invariant mass distribution for the K^+K^- final state. Simply picking a signal distribution plus a polynomial background is not enough to properly parameterize the K^+K^- invariant mass near or around the ϕ peak. After attempting several different combinations of signal and background functions, it was found that the best way to accurately describe both the ϕ and the background near it is to use convoluted functions. A convolution is the operation between two functions which expresses how the shape of one function is modified by the other. The purpose for utilizing a convoluted function when attempting to fit an invariant mass histogram is to describe both the shape of the distribution as well as the inherent resolution of the data. Since both the ϕ peak and the background surrounding it contain similar resolutions, it is appropriate to fit the K^+K^- invariant mass distribution with the summation of a signal function plus a background function, both of which are then convoluted by a third function which manages the resolution.

The signal function chosen to describe the ϕ peak is a relativistic Breit-Wigner (Equation 4.3).

$$|Q_1(m)|^2 = A * |F_1(m) * \Delta_1(m)|^2 \tag{4.3}$$

Contained within this equation is a fit parameter, A, which simply scales the function in order to match the distribution. Also contained in this equation are two functions of mass, the Blatt-Weisskopf centrifugal-barrier factor for a spin 1 particle (Equation 4.4),

$$F_1(m) = \sqrt{\frac{2\sqrt{m^2/4 - m_K^2}}{\sqrt{m^2/4 - m_K^2} + p_R/c}} \tag{4.4}$$

and a standard Breit-Wigner (Equation 4.5) for a particle with spin 1.

$$\Delta_1(m) = \frac{m_o * \Gamma_o}{m_o^2 - m^2 - i m_o \Gamma_1(m)} \tag{4.5}$$

The Blatt-Weisskopf function plays an important role in the fit since it forces the signal function to be equal to zero when the K^+K^- mass is at threshold. It should be noted that $\sqrt{m^2/4 - m_K^2}$ appears throughout many of the equations mentioned. This smaller function represents the magnitude of the breakup momentum for either the K^+ or K^- daughter particle, given some parent mass m, in the rest frame of the parent particle. Additionally, the mass dependent width (Equation 4.6) also helps to describe the changing width of the ϕ due to the K^+K^- mass near threshold.

$$\Gamma_1(m) = \Gamma_o \frac{m_o}{m} \frac{\sqrt{m^2/4 - m_K^2}}{\sqrt{m_o^2/4 - m_K^2}} \frac{F_1^2(m)}{F_1^2(m_o)} \tag{4.6}$$

Finally, in many of the equations, m_K is the mass of a $K^{+/-}$, m_o is the ϕ mass value as determined by the fit, and Γ_o is the natural width of the ϕ. The value chosen for this parameter was taken from the PDG and is $\Gamma_o = 0.004266 \frac{GeV}{c^2}$.

Plotted along with the signal function is the background function which is simply a third degree polynomial, given by Equation (4.7).

$$b(m) = C_1 * (m - C_0)^3 + C_2 * (m - C_0)^2 + C_3 * (m - C_0) \tag{4.7}$$

The background equation has three free parameters and one fixed parameter. The free parameters are the coefficients in front of the powered terms of m; specifically C_1, C_2, and C_3. Since the background shape can drastically change due to the event and its nearest neighbors, these parameters are not given any restriction on their values (Table 4.1). The one fixed parameter is C_0 which is set to $0.987354 \frac{GeV}{c^2}$. This value is the smallest possible mass which can produce the K^+K^- final state, and is easily derived by simply performing the calculation $m_{K^+} + m_{K^-} = 2 * m_{K^\pm} = 0.987354 \frac{GeV}{c^2}$. The purpose of fixing this parameter is force the polynomial background to have a root at the K^+K^- threshold. While attempting different fit functions to describe the K^+K^- invariant mass, it was found that the polynomial function often exaggerated, or over fit the area near the K^+K^- threshold. This caused an effect which resulted in weighted histograms that took away good events near the low mass side of the ϕ peak. Forcing the background function to be equal to zero at the K^+K^- threshold fixed this issue.

To complete the fit of the K^+K^- invariant mass, the signal and background function are added together, then convoluted by a Gaussian in order to compensate for the kaon momentum resolution of the GlueX spectrometer. Although the signal and background functions mentioned above had to be programmed by hand, the convolution of these functions with a Gaussian could be fed into the ROOT library using the TF1Convolution object. More precisely, the total function used to describe the K^+K^- invariant mass for all events is given in Equation (4.8).

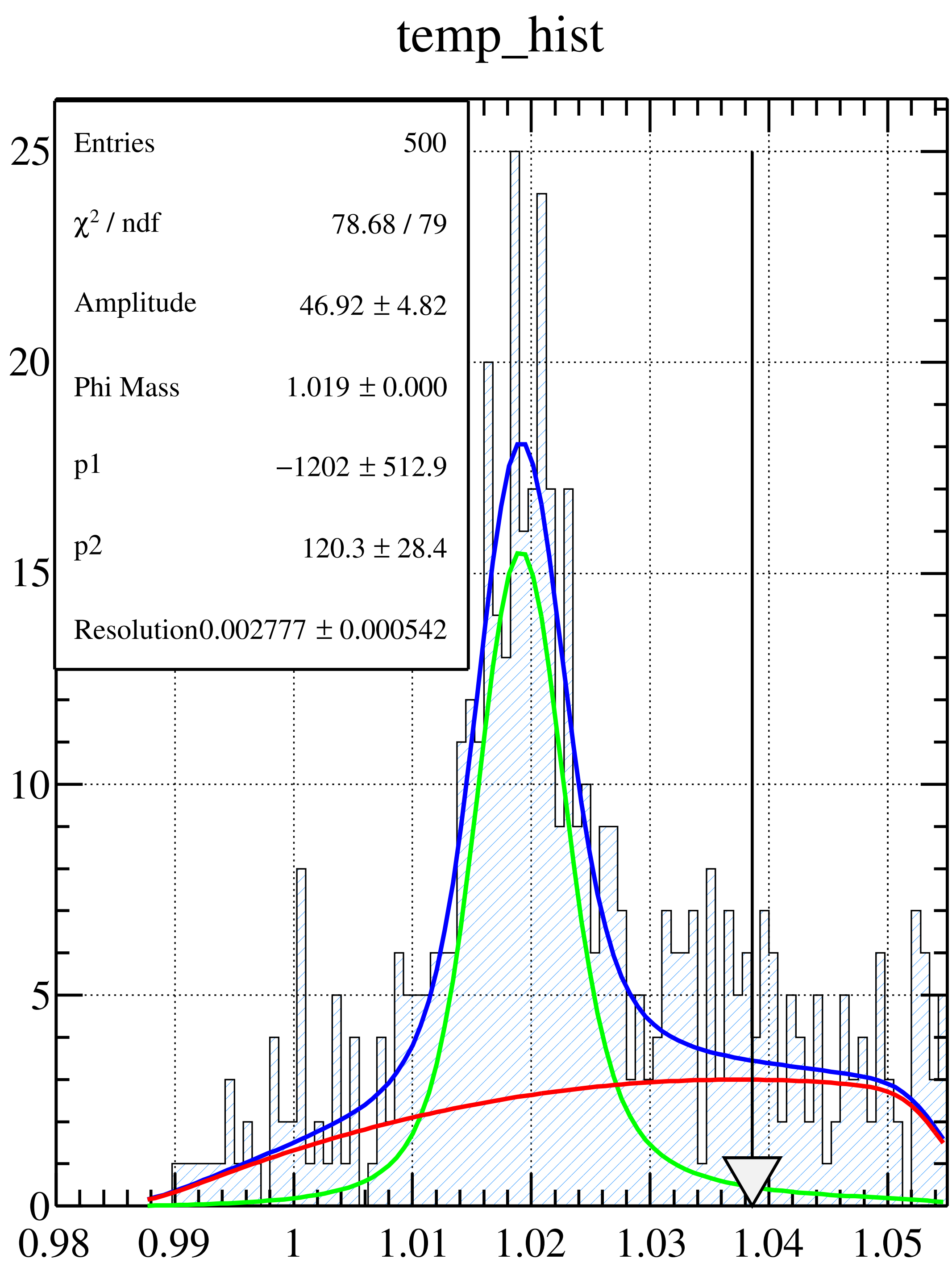

Figure 4.8: A fit which will result in an extremely low quality factor due to the very few signal events in comparison to background events at the location of the arrow, or invariant mass of the event being considered.

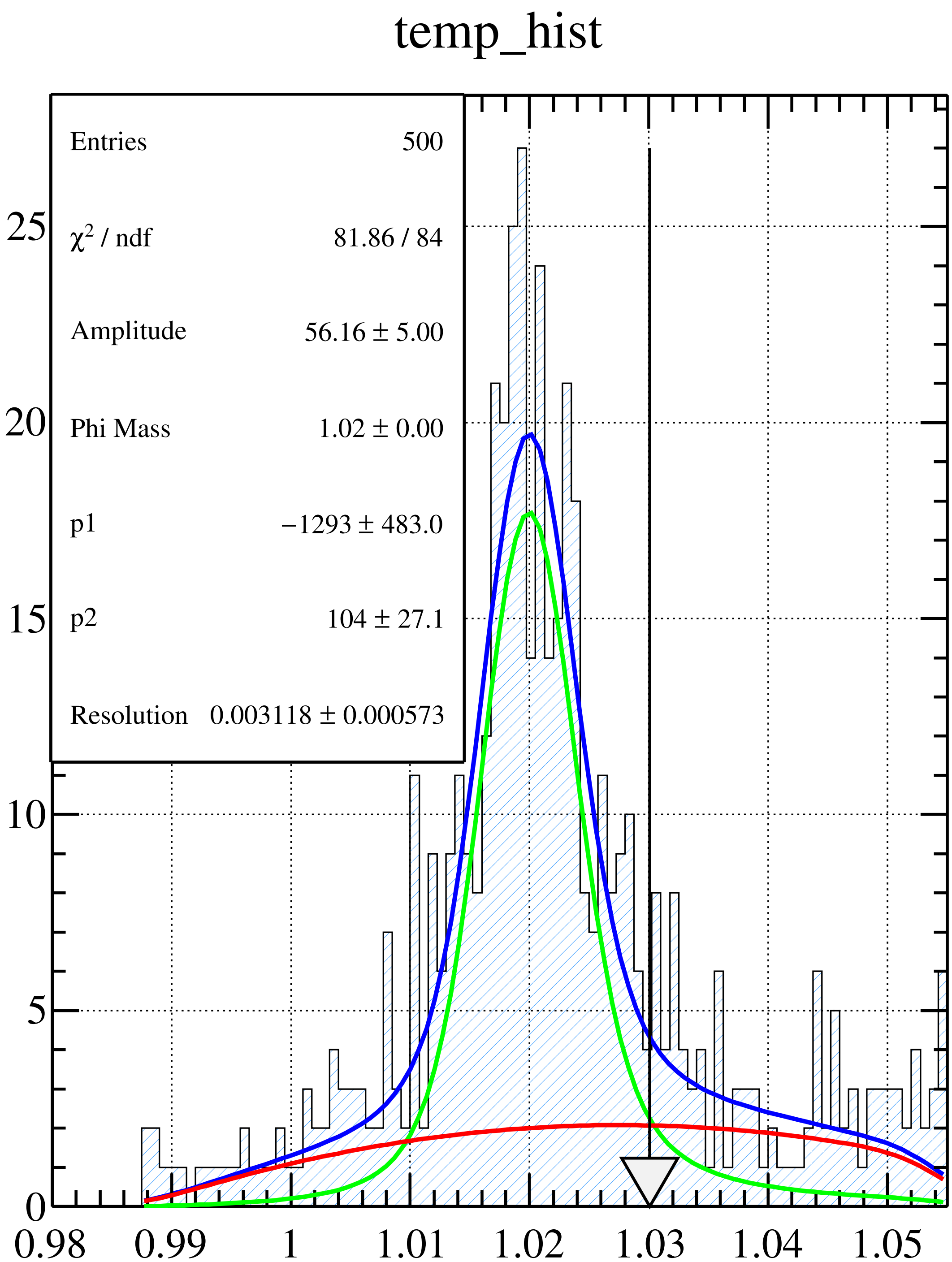

Figure 4.9: A fit which will result in a quality factor around 0.5, due to the fact that there are roughly the same signal and background events at the location of the arrow, or invariant mass of the event being considered.

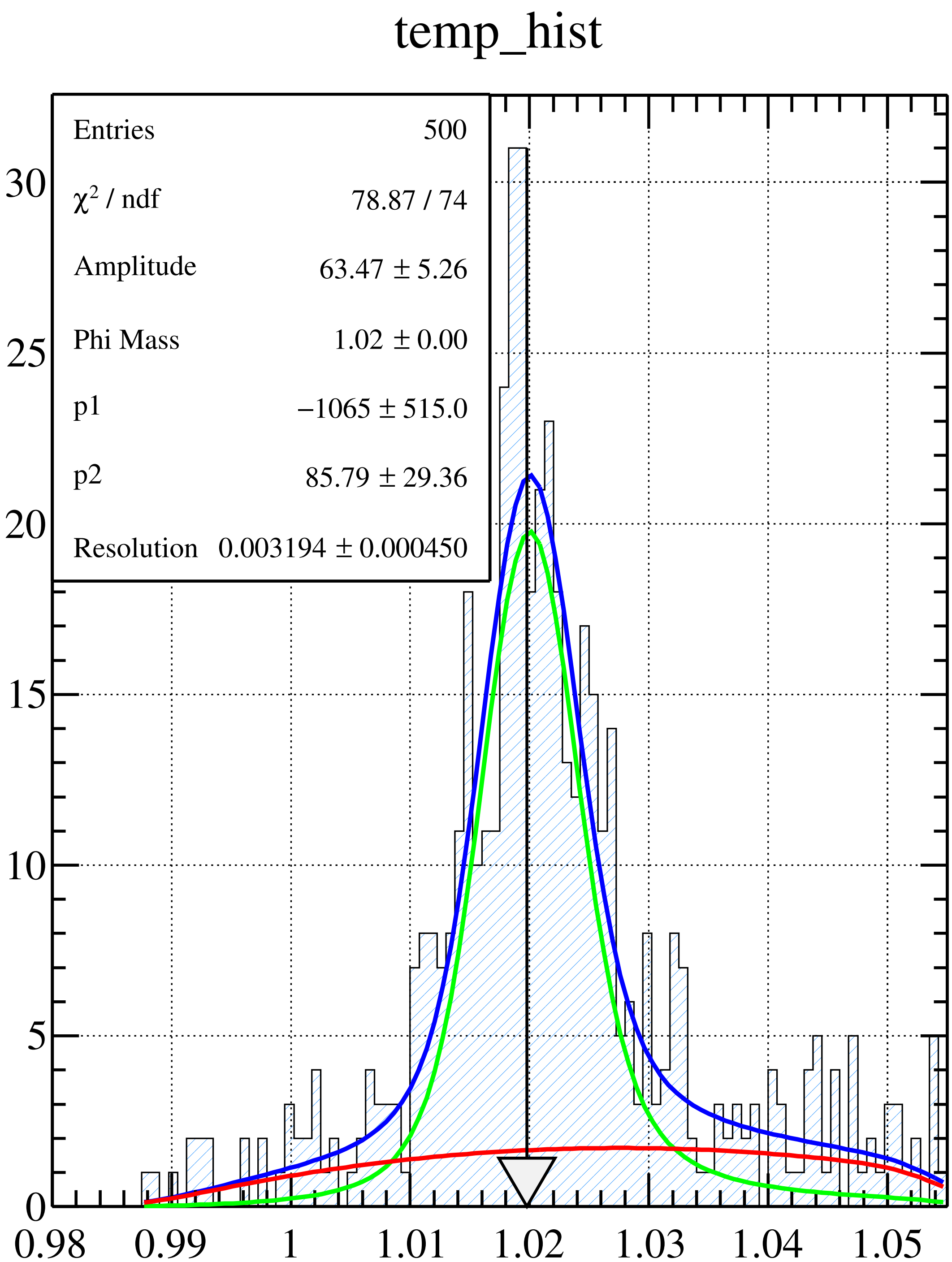

Figure 4.10: A fit which will result in a very high quality factor due to the large number signal events in comparison to background events at the location of the arrow, or invariant mass of the event being considered.

$$T(m) = \int [s(m') + b(m')]\, G(m - m')dm' \tag{4.8}$$

In the equation above, m' is simply a dummy variable for integration, and m represents the K^+K^- invariant mass. The function $s(m')$ is a relativistic Breit-Wigner (Equation 4.3), and the $b(m')$ is the polynomial background function referenced in Equation (4.7). Finally, $G(m - m')$ is the Gaussian function which is responsible for describing the resolution. This particular Gaussian function has one free parameter, and one fixed parameter. The free parameter is the width of the Gaussian, and the fixed parameter is the mean of the Gaussian which is simply set to zero. Because the Gaussian is being convoluted over the range of the fit, the value of the mean in this instance does not matter. Adding all things together, the total function listed in Equation (4.8) has one independent variable, two fixed parameters, and six free parameters, half of which are restricted (Table 4.1). Once a fit has converged, the parameters of the total function can be extracted and used to plot a signal function and a background function. This procedure is mathematically allowed due to the distributive property of convolutions; and therefore the final background and signal function can be written in Equation (4.9) and Equation (4.10), respectively.

$$B(m) = \int b(m')G(m - m')dm' \tag{4.9}$$

$$S(m) = \int s(m')G(m - m')dm' \tag{4.10}$$

Examples of different fits of the K^+K^- invariant mass distributions have been provided in Figures[4.8][4.9][4.10]. Each figure contains a blue line which represents the total fit of the data (Equation 4.8), a green line which represents the signal portion of the fit (Equation 4.10), and a red line which represents the background portion of the fit (Equation 4.9). Located within each plot is also a vertical arrow which is pointed in the downward direction. This arrow represents the invariant mass value of the event for which the quality factor is being calculated. Also contained within each figure is a legend with the values of the parameters for each fit.

Table 4.1: A table which summarizes the parameters and functions used to fit the K^+K^- invariant mass histograms.

K^+K^- invariant mass Functions:

Function	Parameters	Initial Values	Restricted Range
Relativistic B.W.	Amplitude	10	$0 - 100$
	m_ϕ	1.019	$1.01 - 1.03$
3^{rd} Degree Polynomial	C_0	0.987354	Fixed
	C_1, C_2, C_3	$-1200, 200, 200$	Free
Gaussian	μ	0	Fixed
	σ	0.005	$0 - 0.05$

Fitting the $\gamma\gamma$ Invariant Mass

On top of fitting the K^+K^- invariant mass, it is also necessary to fit the $\gamma\gamma$ invariant mass. Fitting this distribution is far more simple than what was needed to describe the K^+K^- invariant mass. The η resonance sits on top of a simple background, and is far enough away from the dominant π^0 peak that further inspection of the background is not necessary. In addition, since the η resonance is nowhere near the threshold for $\gamma\gamma$, performing any type of advanced fit to include breakup momentum and resolution effects is not necessary. Therefore, the $\gamma\gamma$ invariant mass spectra was fit by utilizing the summation of a signal function and a background function. The signal function is a Voigtian (Equation 4.12), which is technically a non relativistic Breit-Wigner (Equation 4.11) convoluted with a Gaussian. This convolution is necessary because the GlueX resolution of the η resonance is much greater than the natural width of the η meson, which is on the order of a keV. In the total signal function (Equation 4.12) there is one independent variable, and three fit parameters, and one fixed parameter. The independent variable is the $\gamma\gamma$ invariant mass, and the fixed parameter is the natural width of the η meson which is listed in the PDG as $\Gamma_o = 1.31keV$. The fit parameters of the function are the amplitude, A which simply scales the function to fit the statistics, the mass value of the η for the fit parameter μ, and the resolution of the η. The limits and starting values of all parameters are summarized in Table 4.2.

$$|\Delta(m)|^2 = \frac{\Gamma_o}{(m-\mu)^2 + \frac{\Gamma_o^2}{4}} \tag{4.11}$$

$$S(m) = A\int |\Delta(m')|^2 G(m-m')dm' \tag{4.12}$$

The background function that was chosen to describe the $\gamma\gamma$ background was a Chebyshev polynomial (Equation 4.13). It should be noted that the functional form of this third order polynomial is different than the one that was used to describe the K^+K^- because there is no threshold effect that has to be accounted for in the $\gamma\gamma$ invariant mass. This function has four free fit parameters with no restrictions on value due to the variability of background shapes in this analysis.

$$B(m) = C_3 * x^3 + C_2 * x^2 + C_1 * x + C_0 \tag{4.13}$$

Finally, the total function that was used to ultimately fit the $\gamma\gamma$ invariant mass distributions was the sum of Equation 4.12 and Equation 4.13. A summary of all parameters and functions used to fit the $\gamma\gamma$ invariant mass is given in Table 4.2.

Examples of different fits of the $\gamma\gamma$ invariant mass distributions have been provided in Figures[4.11][4.12][4.13]. Just like the examples given for the K^+K^- invariant mass fits, each figure contains a blue line which represents the total fit of the data. The total fit in this particular instance is simply the sum of a Voigtian and a third degree Chebyshev polynomial. The figures also contain a green line which represents the signal portion of the fit and a red line which represents the background portion of the fit. These are described by a Voigtian and third degree Chebyshev polynomial, respectively. Located within each plot is also a vertical arrow which is pointed in the downward direction. This arrow represents

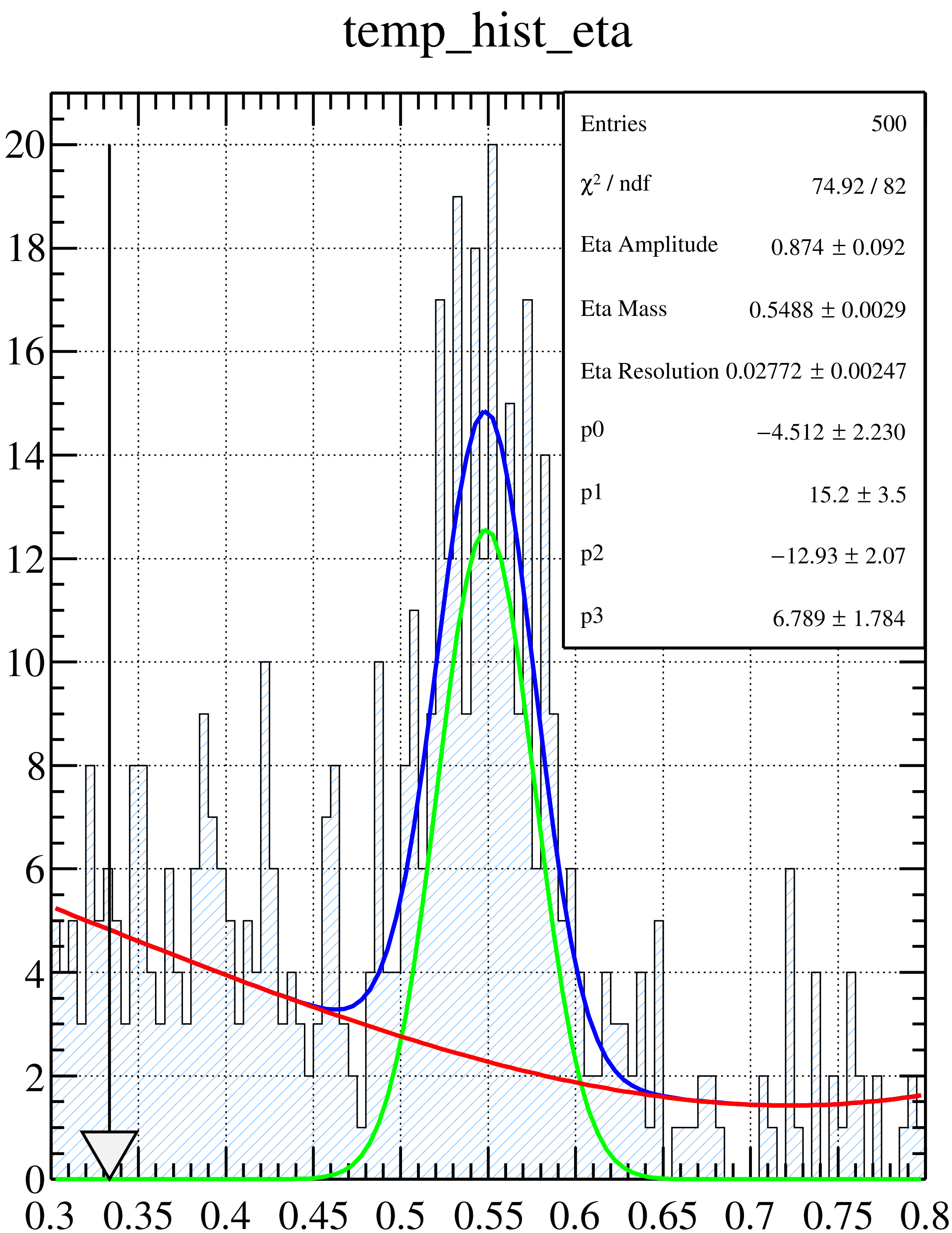

Figure 4.11: A fit which will result in an extremely low quality factor due to the very few signal events in comparison to background events at the location of the arrow, or invariant mass of the event being considered.

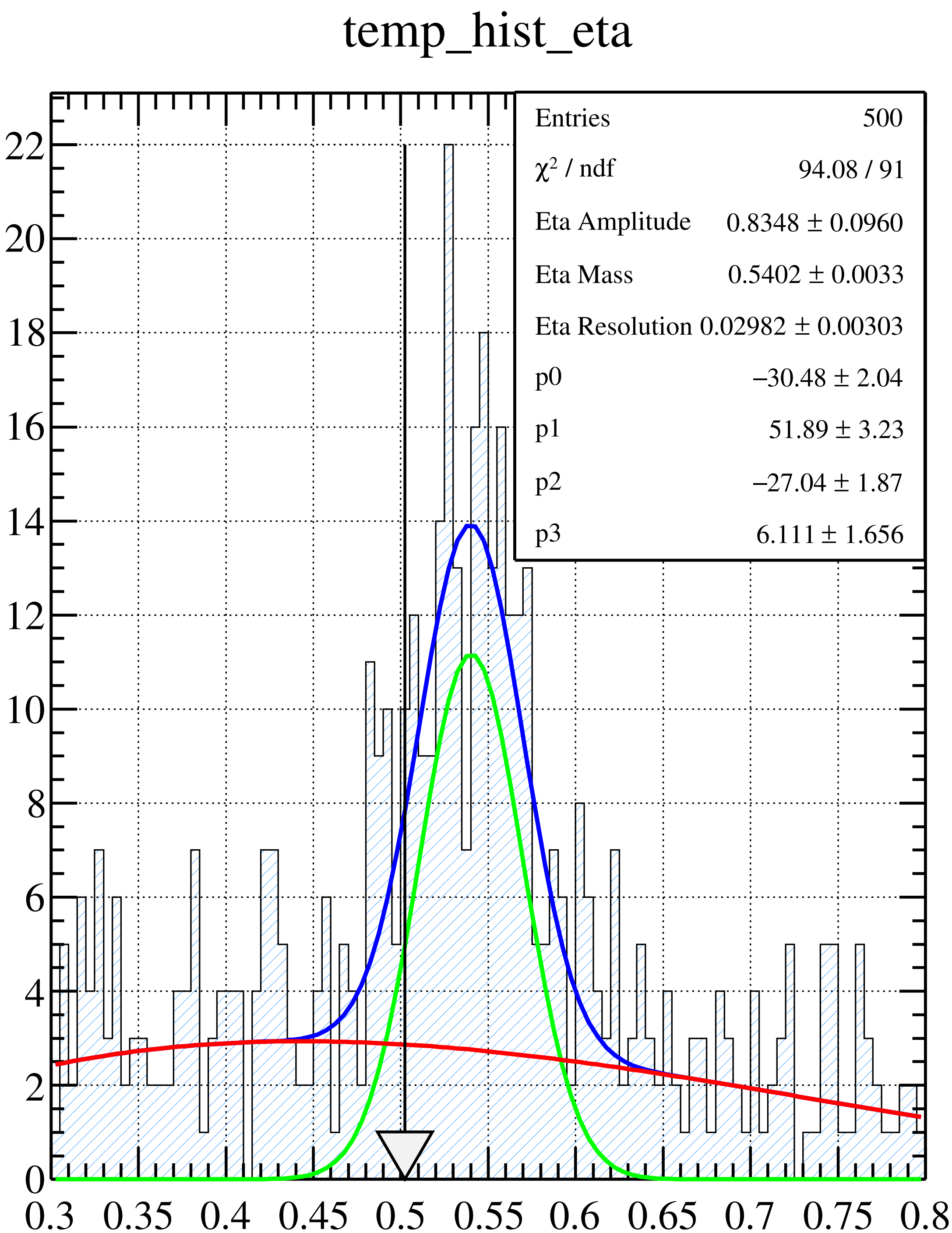

Figure 4.12: A fit which will result in a quality factor somewhat above 0.5, due to the fact that there are slightly more signal events as compared to background events at the location of the arrow, or invariant mass of the event being considered.

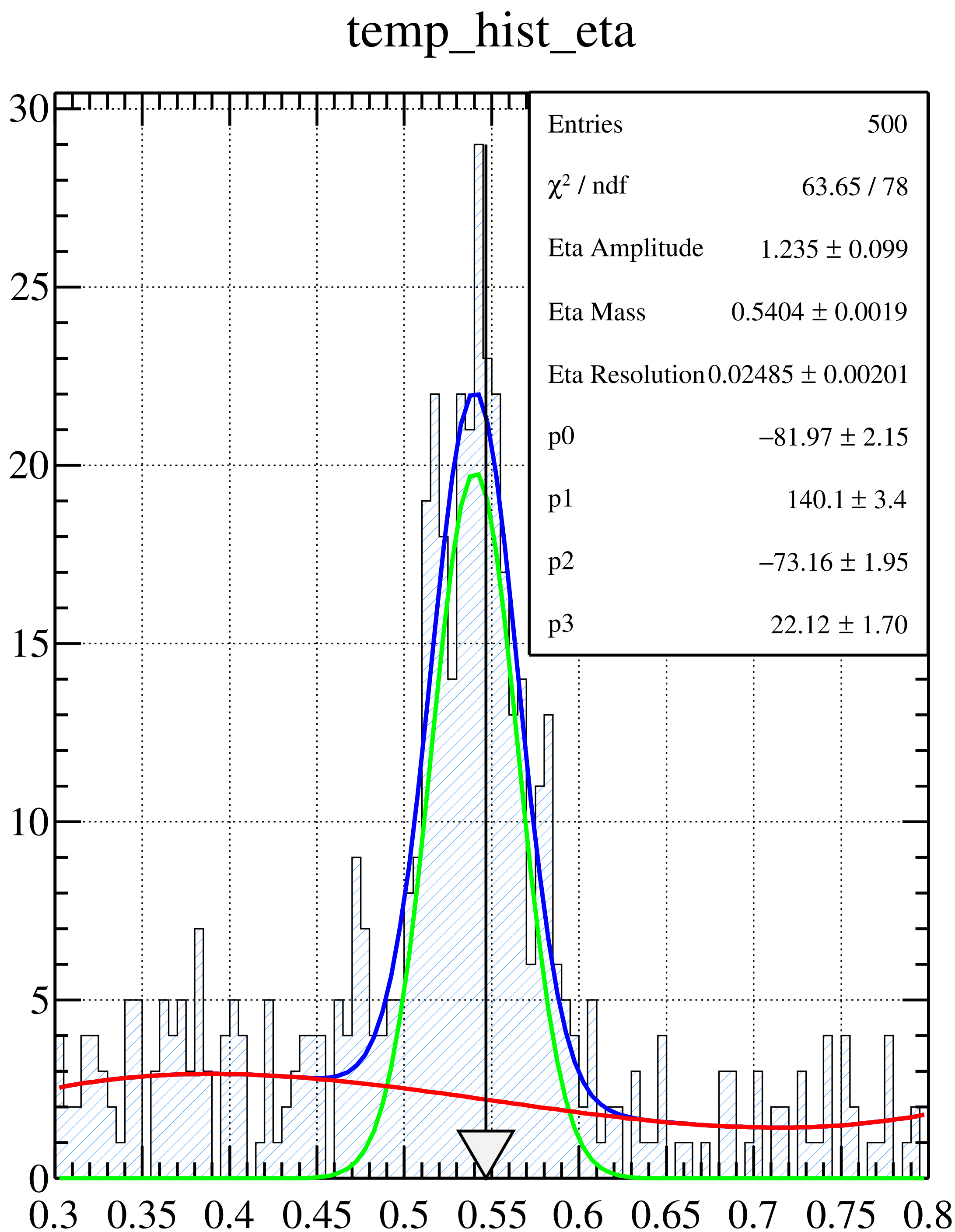

Figure 4.13: A fit which will result in a very high quality factor due to the large number signal events in comparison to background events at the location of the arrow, or invariant mass of the event being considered.

the invariant mass value of the event for which the quality factor is being calculated. Also contained within each figure is a legend with the values of the parameters for each fit.

Table 4.2: A table which summarizes the parameters and functions used to fit the $\gamma\gamma$ invariant mass histograms.

$\gamma\gamma$ invariant mass Functions:

Function	Parameters	Initial Values	Restricted Range
Voigtian	Amplitude	2	$0 - 5$
	m_η	0.547	$0.52 - 0.56$
	σ	0.02	$0.001 - 0.1$
	Γ	0.00000131	Fixed
3^{rd} Chebyshev Polynomial	C_0, C_1, C_2, C_3	None	Free

4.2.2 Three Quality Factor Methods

In order to thoroughly study the $\phi\eta$ final state, a total of three unique quality factor methods were attempted. Each of these analyses follow the standard quality factor prescription detailed in Subsection 4.2.1. Each analysis is unique because a different set of kinematic observables was used to find the set nearest neighbors for each event.

1. (ϕ Only) The first quality factor method considers the kinematic observables of the K^+K^- system, and therefore can only separate the ϕ signal from the K^+K^- background. The quality factor for this analysis will be denoted with Q_ϕ.

2. (η Only) The second quality factor method only considers the kinematics observables of the $\gamma\gamma$ system, and therefore only separates the η signal from the $\gamma\gamma$ background. The quality factor for this analysis will be denoted with Q_η.

3. ($\phi\eta$) The third and final quality factor analysis considers the kinematics observables for *both* the K^+K^- system and the $\gamma\gamma$ system. The quality factor for this analysis will be denoted with $Q_{\phi\eta}$.

The specific list of kinematic observables and how a quality factor was calculated for each analysis is detailed in Subsections 4.2.2, 4.2.2, and 4.2.2, respectively.

It should be noted that the ϕ Only analysis will use the same fit functions for the K^+K^- invariant mass distribution (Subsection 4.2.1), and it will not fit the $\gamma\gamma$ invariant mass distribution. The η Only analysis will use the same fit functions for the $\gamma\gamma$ invariant mass distribution (Subsection 4.2.1), and it will not fit the K^+K^- invariant mass distribution. Finally, the $\phi\eta$ analysis will use both the function for the K^+K^- invariant mass distribution (Subsection 4.2.1), and the function for the $\gamma\gamma$ invariant mass distribution (Subsection 4.2.1). Lastly, all three analyses only accept the 500 nearest neighbors (Subsection 4.2.1).

Calculating the Kinematic Distance Between Events

As mentioned in Subsection 4.2.2, there are a total of three unique quality factor analyses attempted in this thesis, and therefore there are three unique calculations to find the kinematic distance between events.

ϕ Only

The list of kinematic observables used to identify the ϕ meson and to ultimately calculate Q_ϕ are given in Table 4.3.

Table 4.3: A table which summarizes the coordinates used to describe the $\gamma p \rightarrow pX; X \rightarrow \phi Y$ $\phi \rightarrow K^+K^-$; final state. This set of coordinates will ultimately lead to the calculation of Q_ϕ. The coordinates ξ_0 through ξ_5 are used in the kinematic distance equation, described by Equation (4.1). The last coordinate is the reference coordinate for this analysis.

ξ_k	Coordinate	Maximum Range of Coordinate
ξ_0	$K^+_{HE\cos(\theta)}$	2
ξ_1	$K^+_{HE\phi}$	2π radians
ξ_2	$GJ, \cos(\theta)$	2
ξ_3	GJ, ϕ	2π radians
ξ_4	E_{beam}	9 GeV
ξ_5	t	$3.3\frac{GeV^2}{c^4}$
ξ_r	K^+K^- invariant mass	Reference Coordinate

Since this quality factor analysis is only attempting to separate the ϕ from K^+K^- background, there is no need to include any information about the η or its decay products, $\gamma\gamma$. Therefore, in order to properly identify the $\gamma p \rightarrow pX$; $X \rightarrow \phi Y$ $\phi \rightarrow K^+K^-$ final state, a total of six coordinates are needed. Two of the six coordinates come from the angular distributions of the daughter states of ϕ: $K^+_{HE\cos(\theta)}$, $K^+_{HE\phi}$; where the angles ϕ and θ are the polar coordinates in the helicity reference frame, or the rest frame of the ϕ. Two more of the eight total coordinates will come from the angular distributions of ϕ. Much like the kaons, these coordinates will be $GJ, \cos(\theta)$ and GJ, ϕ; where ϕ and $\cos(\theta)$ are polar angles in the Gottfried-Jackson frame; or the rest frame of the $K^+K^-\gamma\gamma$ parent state. The last two coordinates needed are the beam energy (E_{beam}), and the momentum transfer, t. Since t is the well known Mandelstam variable, t is related to the beam energy and the four momentum of the $\phi\eta$ parent state, such that $t^2 = (\gamma^\mu - X^\mu)^2$; where γ^μ is the energy-momentum four vector for the beam, and X^μ is the energy-momentum four vector for the $\phi\eta$ parent state. Since t, the beam energy E_{beam}, and the mass of the $K^+K^-\gamma\gamma$ parent state is known, the magnitude of the $K^+K^-\gamma\gamma$ parent state momentum is directly proportional to these measurements. Knowing the magnitude of the momentum and the mass of the $K^+K^-\gamma\gamma$ parent state allows us to fully describe the $\gamma p \rightarrow pX$; $X \rightarrow \phi Y$ $\phi \rightarrow K^+K^-$ reaction. The final detail that needs to be mentioned is the reference coordinate that is used in this quality factor analysis. Because it is imperative to have a pure ϕ signal, the reference coordinate for this procedure will be the K^+K^- invariant mass. Although this coordinate does not play a role in the calculation of the kinematic distance, it is imperative to define it as the reference coordinate which will ultimately serve as the tool to separate signal events from background events, and to calculate Q_ϕ.

η Only

The list of kinematic observables used to identify the η meson and to ultimately calculate Q_η are given in Table 4.4.

Table 4.4: A table which summarizes the coordinates used to describe the $\gamma p \to pX$; $X \to \eta Y$; $\eta \to \gamma\gamma$ final state. This set of coordinates will ultimately lead to the calculation of Q_η The coordinates ξ_0 through ξ_5 are used in the kinematic distance equation, described by Equation (4.1). The last coordinate is the reference coordinate for this analysis.

ξ_k	Coordinate	Maximum Range of Coordinate
ξ_0	$\gamma_{HE\cos(\theta)}$	2
ξ_1	$\gamma_{HE\phi}$	2π radians
ξ_2	$GJ, \cos(\theta)$	2
ξ_3	GJ, ϕ	2π radians
ξ_4	E_{beam}	9 GeV
ξ_5	t	$3.3\frac{GeV^2}{c^4}$
ξ_r	$\gamma\gamma$ invariant mass	Reference Coordinate

This quality factor analysis is only attempting to separate the η from $\gamma\gamma$ background, there is no need to include any information about the ϕ or its decay products, K^+K^-. Therefore, in order to properly identify the $\gamma p \to pX$; $X \to \eta Y$; $\eta \to \gamma\gamma$ final state, a total of six coordinates are needed. Two of the six coordinates come from the angular distributions of the daughter states of η: $\gamma_{HE\cos(\theta)}$, $\gamma_{HE\phi}$; where the angles ϕ and θ are the polar coordinates in the helicity reference frame, or the rest frame of the η. Two more of the eight total coordinates will come from the angular distributions of η. Much like the photon, these coordinates will be $GJ, \cos(\theta)$ and GJ, ϕ; where ϕ and $\cos(\theta)$ are polar angles in the Gottfried-Jackson frame; or the rest frame of the $K^+K^-\gamma\gamma$ parent state. The last two coordinates needed are the beam energy (E_{beam}), and the momentum transfer, t. Since t is the well known Mandelstam variable, t is related to the beam energy and the four momentum of the $\phi\eta$ parent state, such that $t^2 = (\gamma^\mu - X^\mu)^2$; where γ^μ is the energy-momentum four vector for the beam, and X^μ is the energy-momentum four vector for the $\phi\eta$ parent state. Since t, the beam energy E_{beam}, and the mass of the $K^+K^-\gamma\gamma$ parent state is known, the magnitude of the $K^+K^-\gamma\gamma$ parent state momentum is directly proportional to these measurements. Knowing the magnitude of the momentum and the mass of the $K^+K^-\gamma\gamma$ parent state allows us to fully describe the $\gamma p \to pX$; $X \to \eta Y$; $\eta \to \gamma\gamma$ reaction. The final detail that needs to be mentioned is the reference coordinate that is used in this quality factor analysis. Because it is imperative to have a pure η signal, the reference coordinate for this procedure will be the $\gamma\gamma$ invariant mass. Although this coordinate does not play a role in the calculation of the kinematic distance, it is imperative to define it as the reference coordinate which will ultimately serve as the tool to separate signal events from background events, and to calculate Q_η.

$\phi\eta$

The list of kinematic observables used to identify the ϕ meson and the η meson; and to ultimately calculate $Q_{\phi\eta}$ are given in Table 4.5.

Table 4.5: A table which summarizes the coordinates used to describe the $\gamma p \to pX$; $X \to \phi\eta$ $\phi \to K^+K^-$; $\eta \to \gamma\gamma$ final state. This set of coordinates will ultimately lead to the calculation of $Q_{\phi\eta}$ The coordinates ξ_0 through ξ_7 are used in the kinematic distance equation, described by Equation (4.1). The last two coordinates are the reference coordinates for this analysis.

ξ_k	Coordinate	Maximum Range of Coordinate
ξ_0	$K^+_{HE\cos(\theta)}$	2
ξ_1	$K^+_{HE\phi}$	2π radians
ξ_2	$\gamma_{HE\cos(\theta)}$	2
ξ_3	$\gamma_{HE\phi}$	2π radians
ξ_4	$GJ, \cos(\theta)$	2
ξ_5	GJ, ϕ	2π radians
ξ_6	E_{beam}	9 GeV
ξ_7	t	$3.3\frac{GeV^2}{c^4}$
ξ_r	K^+K^- invariant mass	Reference Coordinate
ξ_r	$\gamma\gamma$ invariant mass	Reference Coordinate

The final quality factor analysis is attempting to identify both the ϕ and η mesons and to also reject any background. It should be noted that the backgrounds for this analysis are different and include $\phi\gamma\gamma$, ηK^+K^-, and $K^+K{-}\gamma\gamma$. Therefore, in order to properly identify the $\gamma p \to pX$; $X \to \phi\eta$ $\phi \to K^+K^-$; $\eta \to \gamma\gamma$ final state, a total of eight coordinates are needed. Four of the eight coordinates come from the angular distributions of the daughter states of ϕ and η. More specifically, the four coordinates are $K^+_{HE\cos(\theta)}$, $K^+_{HE\phi}$, $\gamma_{HE\cos(\theta)}$, $\gamma_{HE\phi}$; where the angles ϕ and θ are the polar coordinates in the helicity reference frame. It should be noted that since the K^+ and γ particles are daughters of different parent states, they will have different helicity frames which are relative to the rest frames of ϕ and η mesons, respectively. Two more of the eight total coordinates will come from the angular distributions of ϕ and η. Much like the K^+ and γ particles, these coordinates will be $GJ, \cos(\theta)$ and GJ, ϕ; where ϕ and $\cos(\theta)$ are polar angles in the Gottfried-Jackson frame; or the rest frame of the $\phi\eta$ parent state. The last two coordinates needed to describe the $\gamma p \to p\phi\eta$ final state is the beam energy (E_{beam}), and the momentum transfer, t. Since t is the well known Mandelstam variable, t is related to the beam energy and the four momentum of the $\phi\eta$ parent state, such that $t^2 = (\gamma^\mu - X^\mu)^2$; where γ^μ is the energy-momentum four vector for the beam, and X^μ is the energy-momentum four vector for the $\phi\eta$ parent state. Since t, the beam energy E_{beam}, and the mass of the $\phi\eta$ parent state is known, the magnitude of the $\phi\eta$ parent state momentum is directly proportional to these measurements. Knowing the magnitude of the momentum and the mass of the $\phi\eta$ parent state allows us to fully describe the $\gamma p \to p\phi\eta$ reaction. The final detail that needs to be mentioned is the reference coordinates that are used in this quality factor analysis. Because it is imperative to have a pure $\phi\eta$ signal, there will be two reference coordinates for this procedure. One of them will be the K^+K^- invariant mass, and the other will be the $\gamma\gamma$ invariant mass. Although these coordinates do not play a role in the calculation of the kinematic distance, it is imperative to define them as the reference coordinates which will ultimately serve as the tool to separate signal events from background events, and to calculate $Q_{\phi\eta}$.

Calculating the Quality Factor

Once the fits of the K^+K^- and $\gamma\gamma$ invariant mass histograms have converged, the final step of calculating a quality factor can be performed. This is done by knowing the signal and background functions, as well as their fitted parameters, for both the K^+K^- and $\gamma\gamma$ distributions. Knowing the parameters of the fit will allow the user to accurately estimate the number of signal events and the number of background events for a given invariant mass value. The invariant mass value that should be used is the one which corresponds to the event that is being studied, and the parameters are determined by the fit of the invariant mass distribution of nearest neighbors. More specifically, the quality factor associated with the K^+K^- invariant mass distribution will be Equation 4.14.

$$Q_\phi = \frac{S(m_{KK})}{S(m_{KK}) + B(m_{KK})} \tag{4.14}$$

In Equation (4.14), the function $S(m)$ is the convoluted relativistic Breit-Wigner described by Equation (4.10), and the function $B(m)$ is the convoluted third degree polynomial described by Equation (4.9). Lastly, the m_{KK} variable describes the K^+K^- mass of the event being considered. The quality factor associated with the $\gamma\gamma$ invariant mass distribution will be Equation 4.15.

$$Q_\eta = \frac{S(m_{\gamma\gamma})}{S(m_{\gamma\gamma}) + B(m_{\gamma\gamma})} \tag{4.15}$$

In Equation 4.15, the function $S(m)$ is a Voigtian function, which is the convolution of a non-relativistic Breit-Wigner with a Gaussian, described by Equation 4.12. The function $B(m)$ is the simply a third degree Chevyshev polynomial described by Equation 4.13. Lastly, the $m_{\gamma\gamma}$ variable describes the $\gamma\gamma$ invariant mass of the event being considered. The last quality factor which considers both the kinematics of the ϕ and the η is given in Equation (4.16).

$$Q_{\phi\eta} = \frac{S(m_{KK})}{S(m_{KK}) + B(m_{KK})} * \frac{S(m_{\gamma\gamma})}{S(m_{\gamma\gamma}) + B(m_{\gamma\gamma})} \tag{4.16}$$

In Equation (4.16), the signal and background functions for the K^+K^- and $\gamma\gamma$ invariant mass distributions are the same as those mentioned in Equation 4.14 and Equation 4.15, respectively.

The key difference between all three quality factor calculations comes from the fact that they are all using a different set of kinematic variables to determine a set of nearest neighbors. Therefore, the K^+K^- invariant mass distribution using the ϕ Only method will be different from the K^+K^- invariant mass distribution using the $\phi\eta$ method. Conversely, the $\gamma\gamma$ invariant mass distribution using the η Only method will be different from the $\gamma\gamma$ invariant mass distribution using the $\phi\eta$ method. This subtlety will result in different $\phi\eta$ invariant mass yields, depending on the quality factor method that is being considered.

Quality Factor Highlights

The effectiveness of the quality factor approach is highlighted in Figure 4.14 and Figure 4.15. Figure 4.14 shows what the K^+K^- invariant mass distribution looks like when plotting events with weights Q_ϕ and with weights $1 - Q_\phi$. One can clearly see that the quality factor effectively separated the signal ϕ meson from the K^+K^- background. Figure 4.15 shows what the $\gamma\gamma$ invariant mass distribution looks like when plotting events with weights Q_η and with weights $1 - Q_\eta$. One can clearly see that the quality factor effectively separated the signal η meson from the $\gamma\gamma$ background.

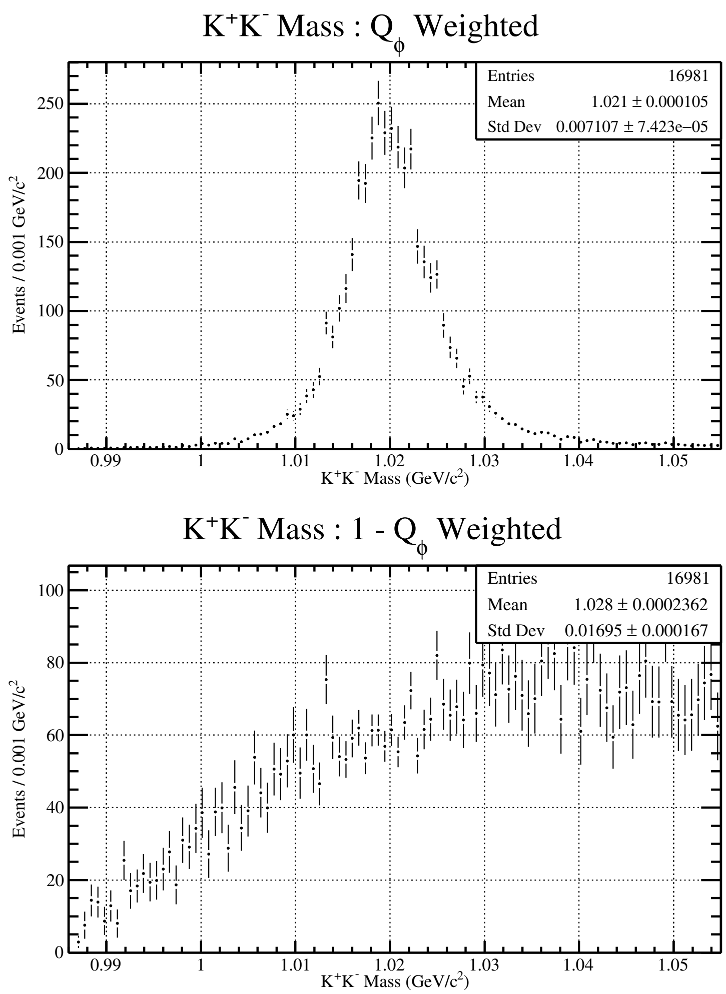

Figure 4.14: The K^+K^- invariant mass distribution plotted with the signal weight, Q_ϕ and the background weight $1 - Q_\phi$.

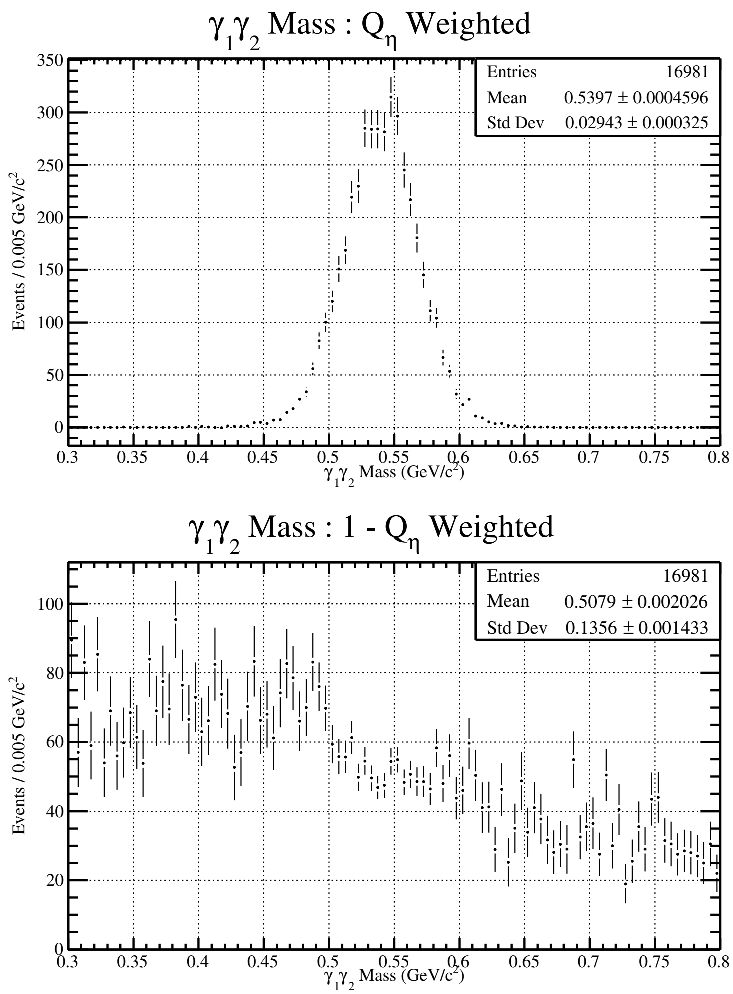

Figure 4.15: The $\gamma\gamma$ invariant mass distribution plotted with the signal weight, Q_η and the background weight $1 - Q_\eta$.

4.3 Removal of N* Background

After all particle identification cuts, selection cuts, and the determination of Quality Factors, an N* structure was found in the signal data *a posteriori* (Figure [4.16]). Also contained within the signal data were possible low mass structures in the $\phi\eta$ invariant mass (Figure [4.17]).

The reason that an N* background can be seen in $\gamma p \to p\phi\eta$ data is due to the fact that an N* can decay into a proton and η. More specifically, this background will have the reaction $\gamma p \to N^*\phi$; $N^* \to p\eta$. As you can see, this baryonic reaction has an identical final state to $\gamma p \to p\phi\eta$, but is a completely different reaction. What's worse is that this background can have a missing mass/energy that is near zero. Therefore, it is imperative to search of a method that will effectively separate this background from signal.

Many avenues were researched in order to remove the N* background; all but one were shown not to work properly. Some of the background subtraction methods that were at-

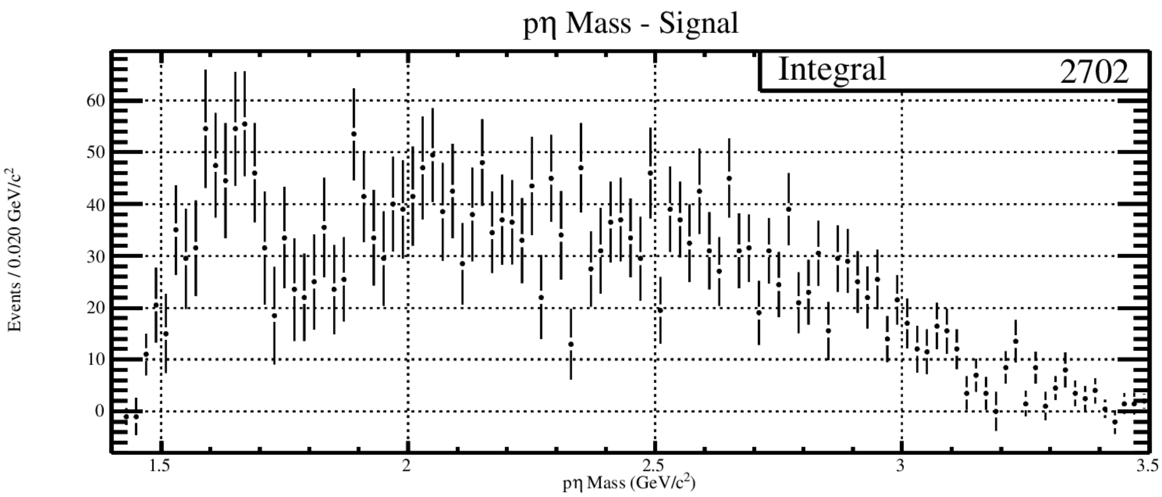

Figure 4.16: The $p\gamma\gamma$ invariant mass for the Elliptical Subtraction method (Subsec: 4.5.1). This distribution shows a possible N* structure around 1650 MeV/c^2.

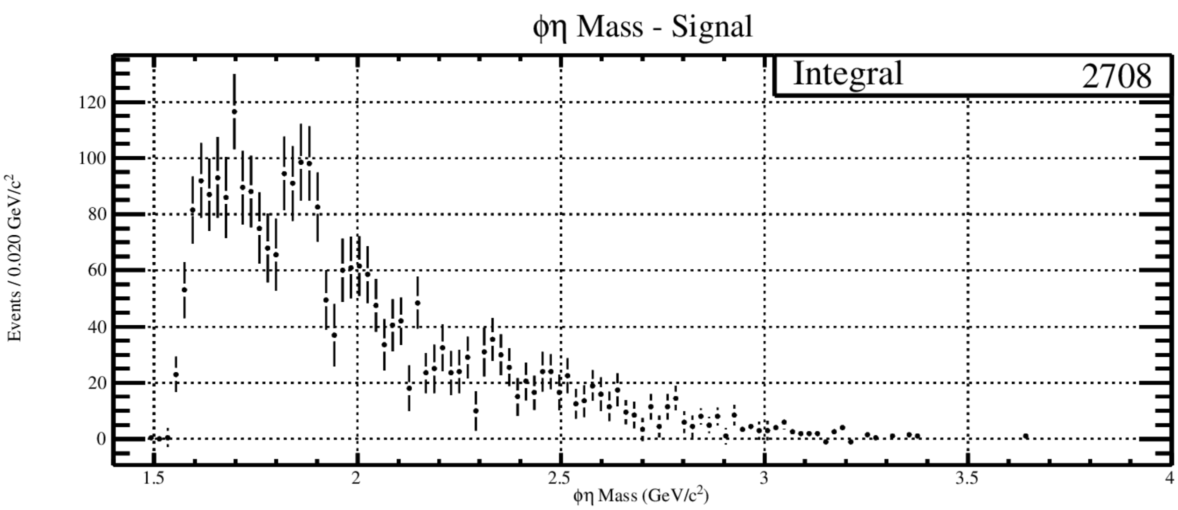

Figure 4.17: The $\phi\eta$ invariant mass for the Elliptical Subtraction method (Subsec: 4.5.1) before N* removal. This distribution shows two possible structures at lower mass.

tempted included a t cut, a beam energy cut, and a p$\gamma\gamma$ mass cut. All of these methods either did not effectively remove the N* background or removed too many signal events.

The one method which did remove the most N* background while also preserving the most signal statistics was cutting on the lab frame angle of the η meson. This cut was shown to effectively separate N* background from low mass $\phi\eta$ structures by generating three different sets of Monte Carlo data. It should be noted that these data sets are completely different from the one mentioned in Chapter 3.

1. $\gamma p \to pX(1680); X(1680) \to \phi\eta$
2. $\gamma p \to pX(1850); X(1850) \to \phi\eta$
3. $\gamma p \to N^*(1650)\phi; N^*(1650) \to p\eta$

Each of these Monte Carlo data sets were generated with a t-slope of 2.5. This slope was chosen because it closely matched the data at this stage. All three Monte Carlo data sets were also generated with a flat beam distribution. The purpose of this was to understand how certain cuts would effect the statistics at different beam energies; all of which would have roughly the same amount of statistics. An example of this is given in Figure [4.18] through Figure [4.20].

In all figures, the vertical axis is the angle the η meson and the horizontal axis is the beam energy. The angle θ is the polar coordinate in the lab frame which is the angle between the beam direction and the direction of the η. The first two figures ([4.18] and [4.19]) show similar behavior. In both Monte Carlo samples the direction of the η relative to beam direction is very shallow, and for the most part is always below 12° at higher beam energies. However, the last figure ([4.20]) shows completely different kinematic behavior. The N* Monte Carlo has very few events below 12°, and on average will decay the η at angles between 20° and 40°. Knowing this, a study of these Monte Carlo sets as a function of θ cut was performed.

Figure [4.21] provides the number of events as a function of different θ cut values for each Monte Carlo sample. This particular study looks at cut values in 1.5° increments, starting at 0° and going as high as 45°. The most important observation that this figure provides is that the number of signal events rises rapidly at lower θ cut values, whereas the N* background loses a large amount of statistics at lower θ cut values.To find the optimal θ cut value which contains the most signal events on top of background events, the same set of data is used and plotted in Figure [4.22]. The difference between Figure [4.21] and Figure [4.22] is that the N* statistics have been subtracted from all Monte Carlo data sets. This method of subtraction shows that the optimal θ cut is in the range of 15°-18°. Since the most signal statistics should be preserved, the higher cut value of 18° was chosen.

At a cut value of 18°, 10 percent of the signal Monte Carlo is lost and 82 percent of the background is removed. However, it should be mentioned again that all three Monte Carlo samples were generated with a flat beam spectrum. In order to approximate the data more accurately, the same samples were generated with a coherent beam spectrum. Since the coherent beam spectrum will force a higher density of events in the range of 8 GeV - 9 GeV, the amount of lost signal events will drop and the the amount of removed background will stay the same (Figure [4.18]-Figure [4.20]). After performing the same study with a coherent beam distribution for all Monte Carlo samples, a cut value of 18° was still optimal. At this cut, 6 percent of the signal Monte Carlo was lost and 82 percent of the background was removed.

After the completion of this Monte Carlo study, the cut of 18° θ was enforced on the data sample. The results of this cut and the effect that it has on the N* background can be seen in Figure [4.23]. The effect that it has on the $\phi\eta$ invariant mass can be seen in Figure [4.24]. Approximately 500 events were lost after the θ cut at 18°. However, the majority of these statistics were lost in the N* peak, while the apparent low mass structures in the $\phi\eta$ invariant mass remained the same.

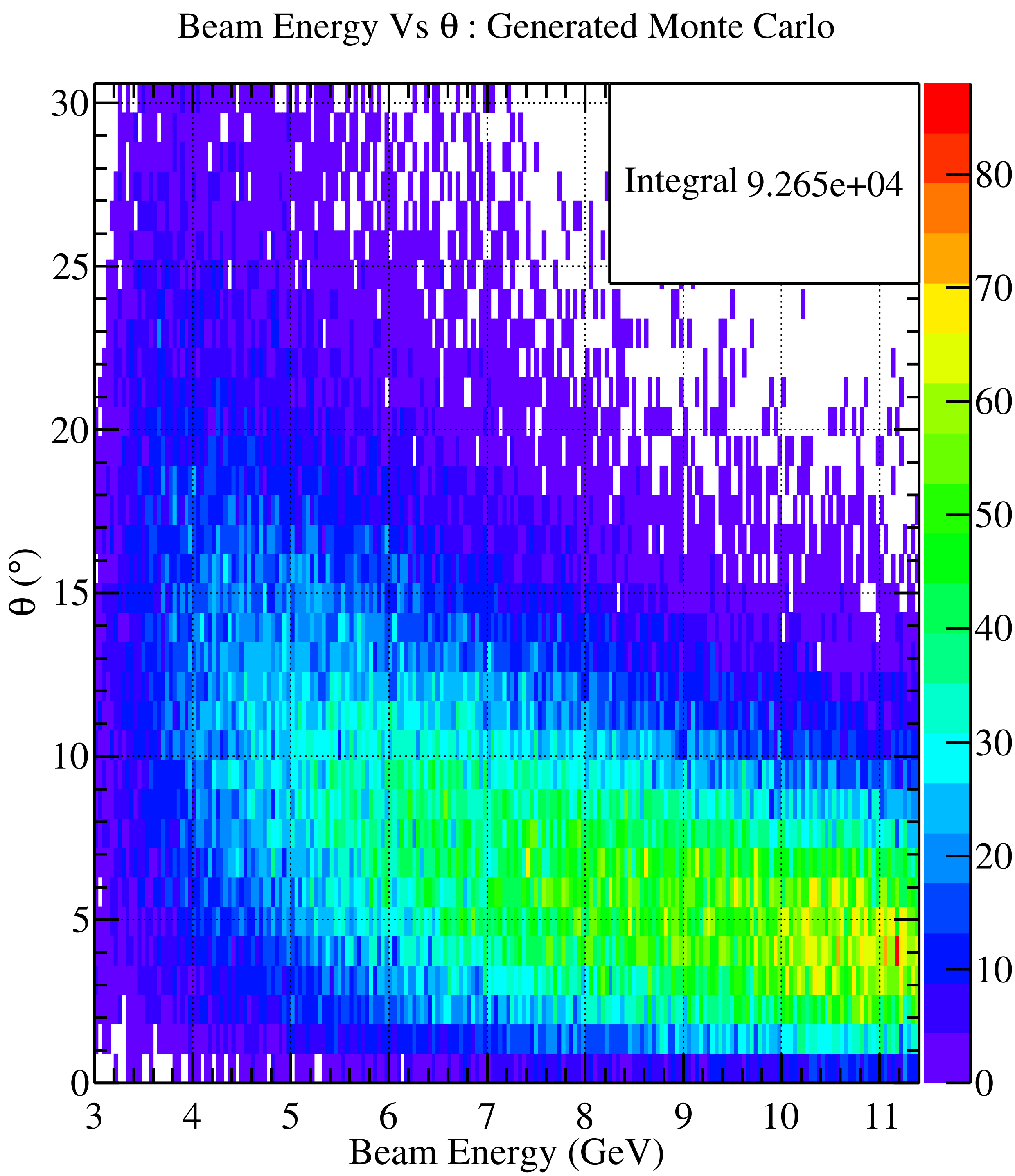

Figure 4.18: The angle of the η meson with respect to the beam direction in the lab frame versus the beam energy for $\gamma p \to pX(1680); X(1680) \to \phi\eta$ Monte Carlo sample.

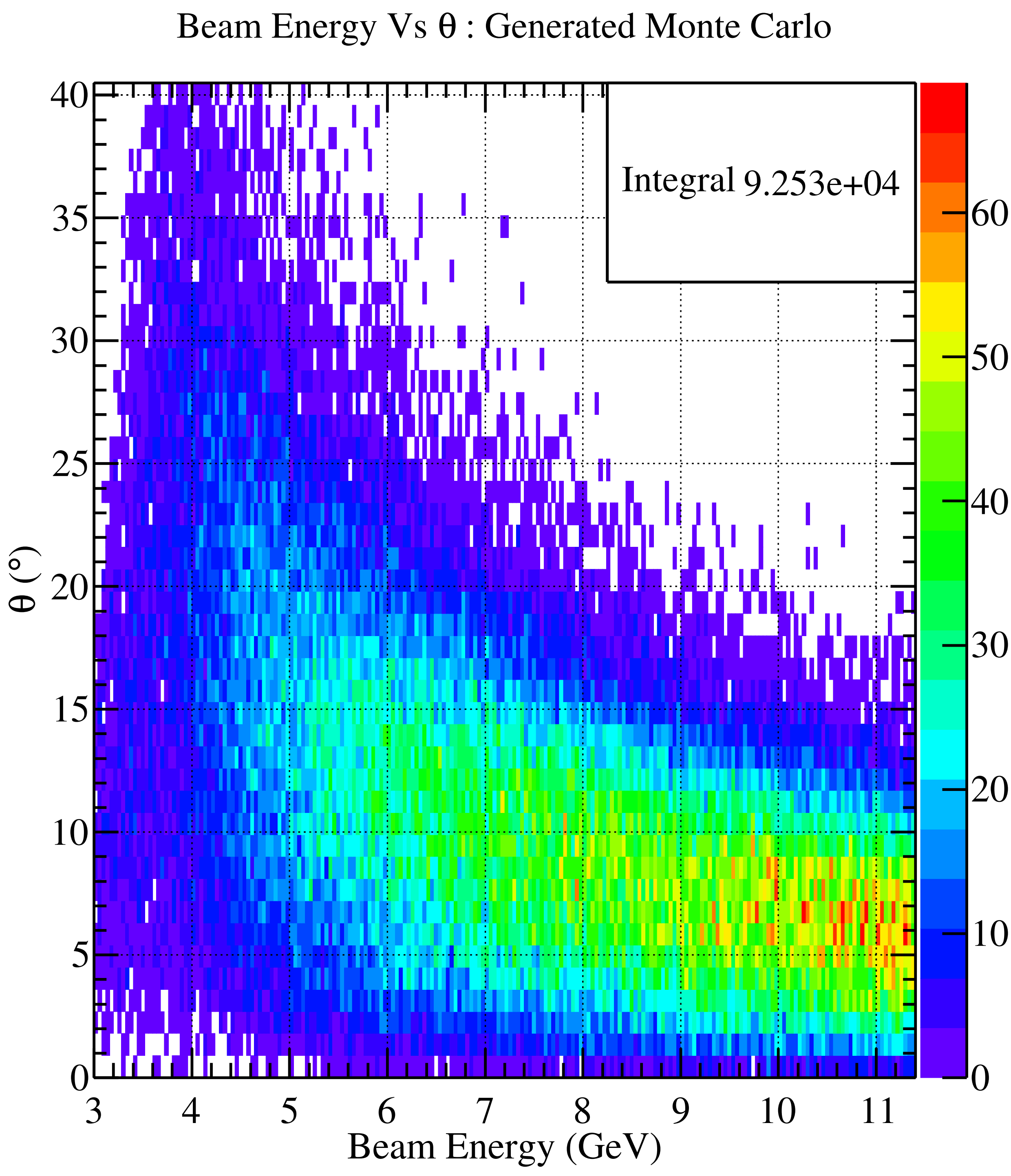

Figure 4.19: The angle of the η meson with respect to the beam direction in the lab frame versus the beam energy for $\gamma p \to pX(1850); X(1850) \to \phi\eta$ Monte Carlo sample.

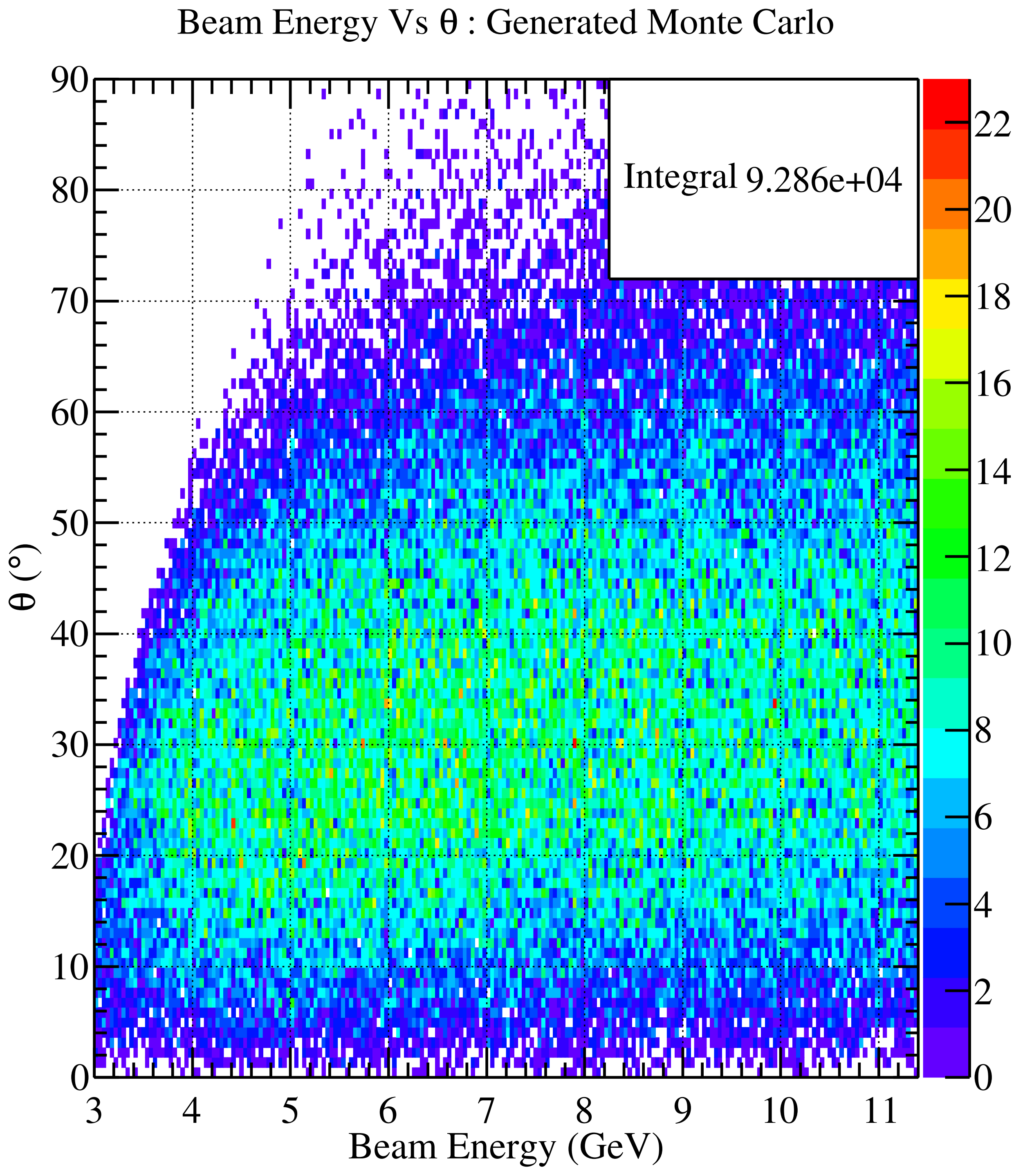

Figure 4.20: The angle of the η meson with respect to the beam direction in the lab frame versus the beam energy for $\gamma p \to N^*(1650)\phi; N^*(1650) \to p\eta$ Monte Carlo sample.

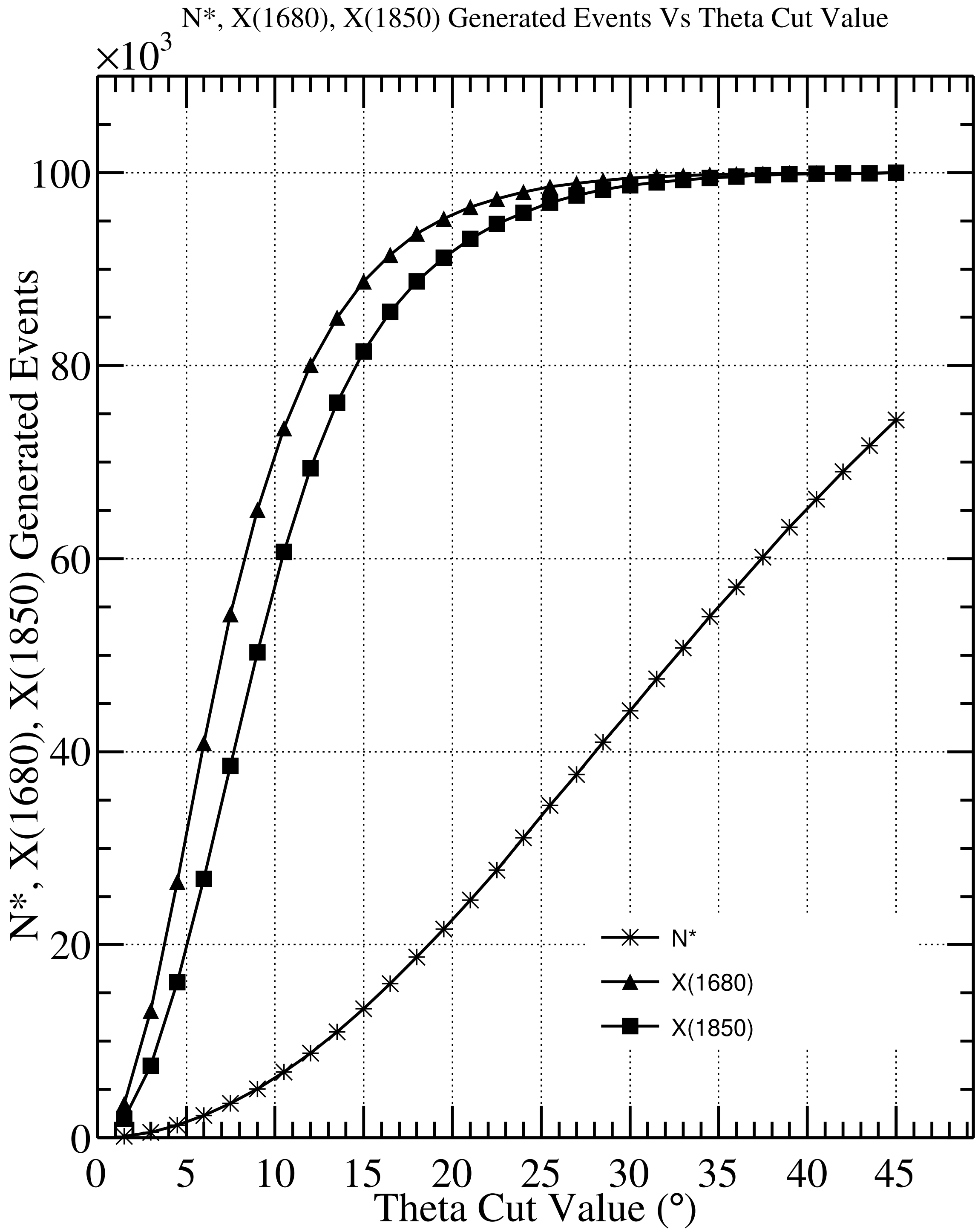

Figure 4.21: The number of N*, X(1680), and X(1850) events as a function of θ cut value.

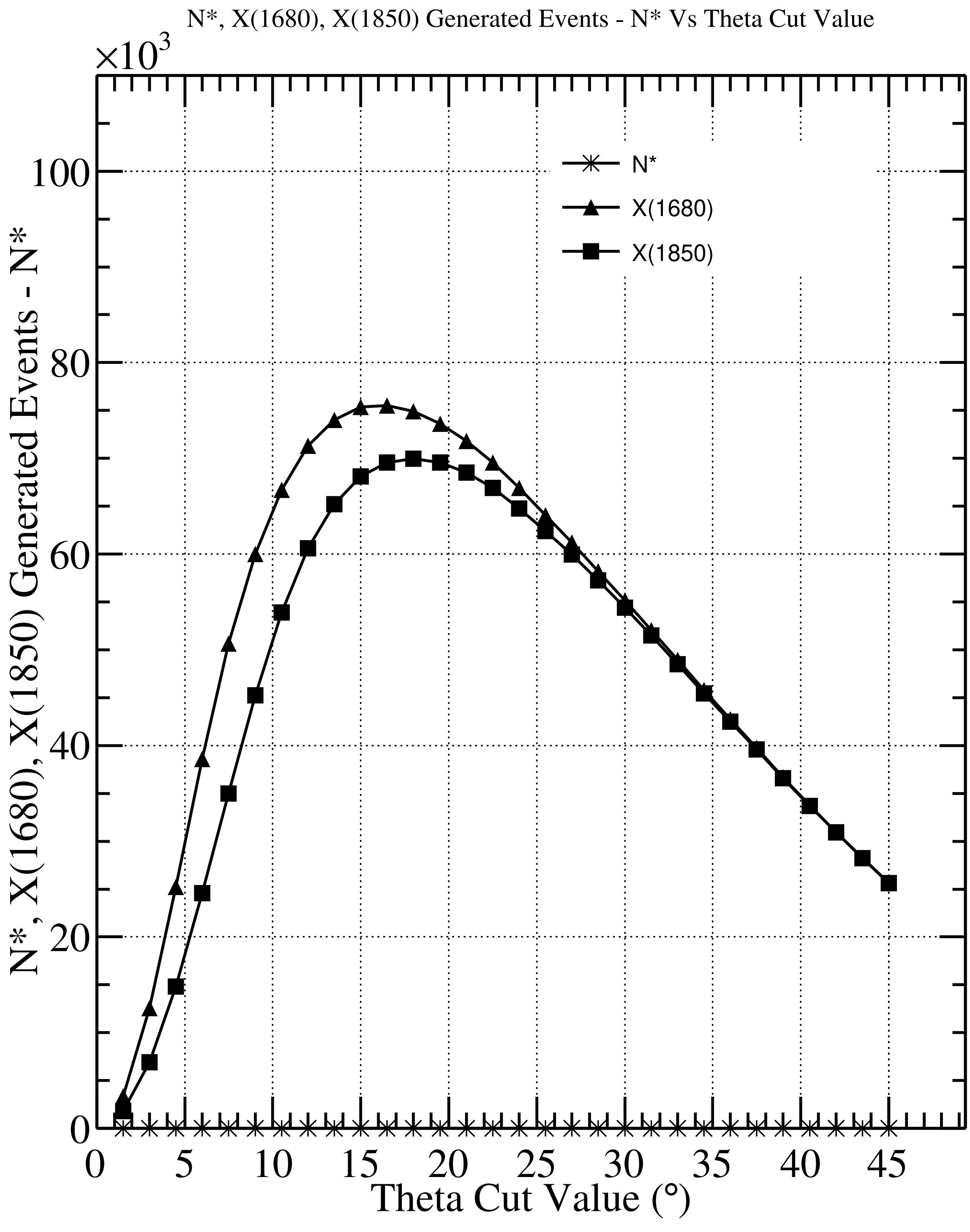

Figure 4.22: The number of N*, X(1680), and X(1850) events minus the number of N* events, as a function of θ cut value.

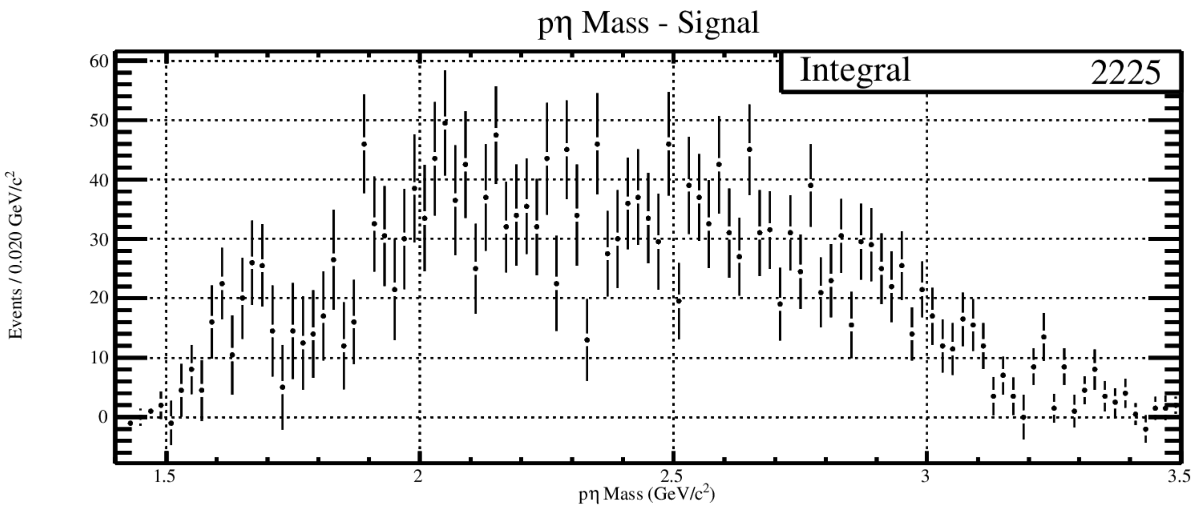

Figure 4.23: The $p\gamma\gamma$ invariant mass for the Elliptical Subtraction method (Subsec: 4.5.1) after a θ cut of 18°.

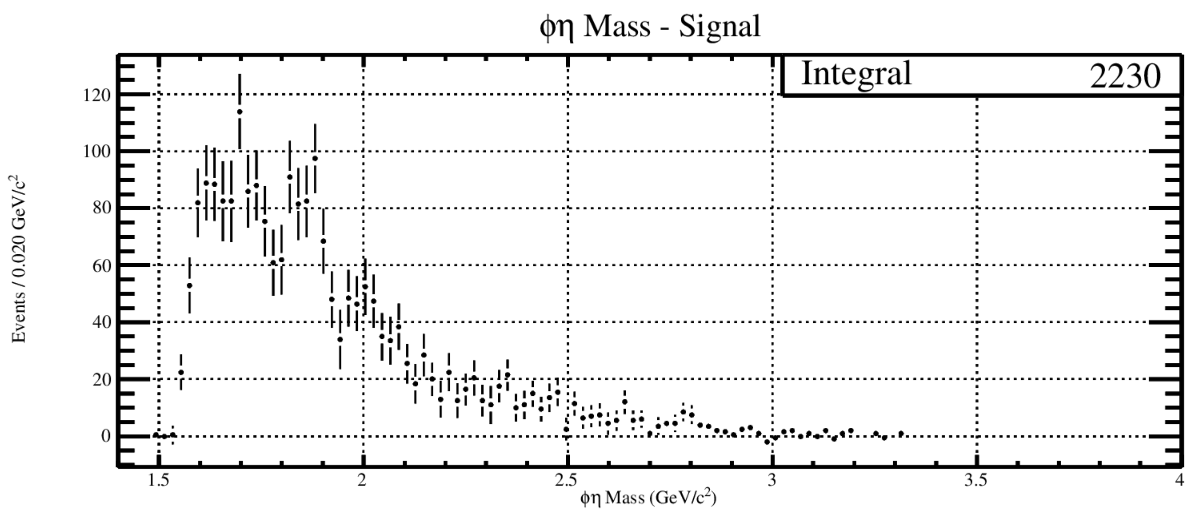

Figure 4.24: The $\phi\eta$ invariant mass for the Elliptical Subtraction method (Subsec: 4.5.1) after a θ cut of 18°.

4.4 Acceptance Corrections for $\phi\eta$ Invariant Mass and $cos(\theta)_{GJ}$

Before the final results of the $\phi\eta$ invariant mass and $cos(\theta)_{GJ}$ are shown, the acceptance corrections for each distribution are given. The acceptance corrections were found by using the generated Monte Carlo sample highlighted in Chapter 3.

This Monte Carlo sample was then simulated inside the detector using **hdgeant**, a software package inside the GlueX library which allows users to simulate what generated Monte Carlo will look like inside the detector. Once the simulation is complete, the simulated data

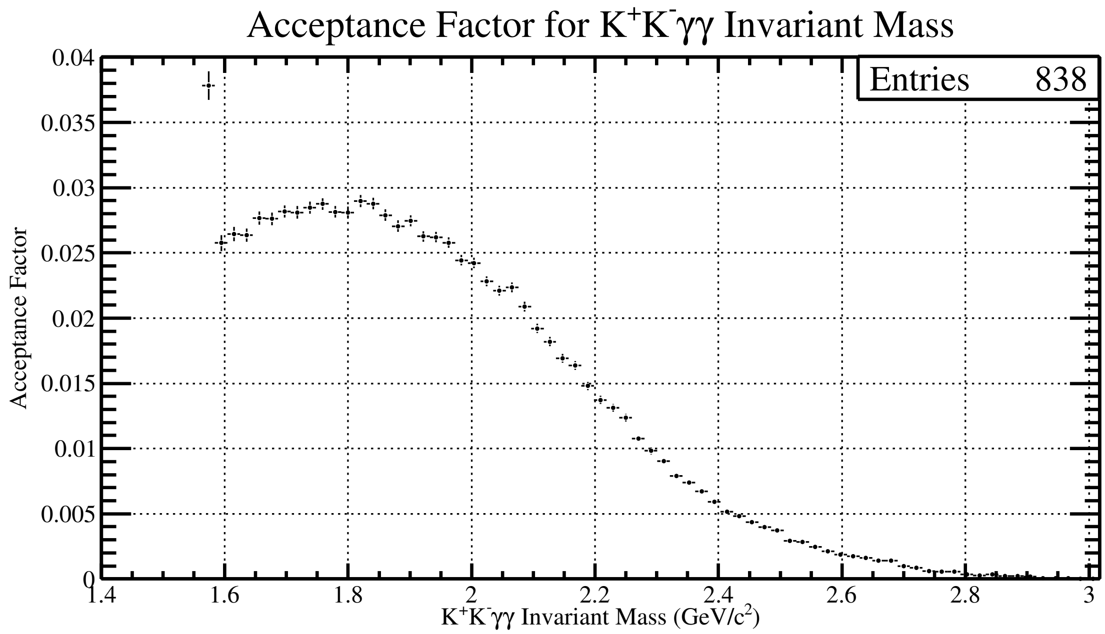

Figure 4.25: The $\phi\eta$ invariant mass acceptance factor.

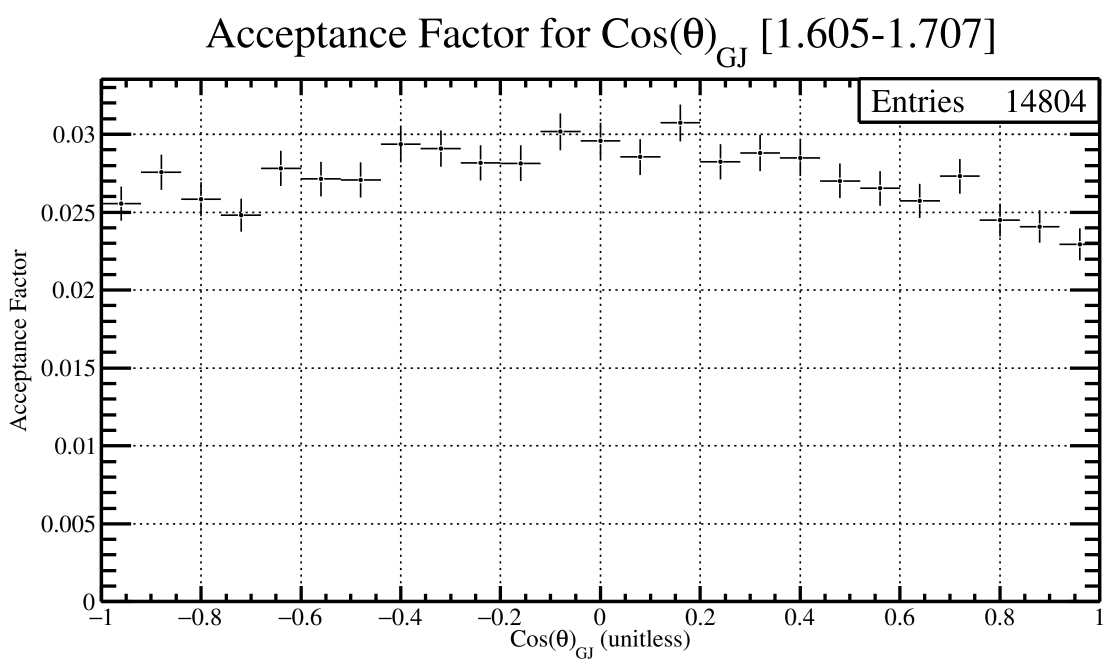

Figure 4.26: The $cos(\theta)_{GJ}$ acceptance factor for $\phi\eta$ invariant mass range between 1.605-1.707 GeV/c^2.

will then be passed to **mcsmear**. Much like **hdgeant**, this is another software package inside the GlueX library which allows users to simulate the resolution of the GlueX detector after the simulation phase. After the Monte Carlo data has resolution effects added, it is then passed into the final stage, **hdroot**, which provides reconstruction to the Monte Carlo sam-

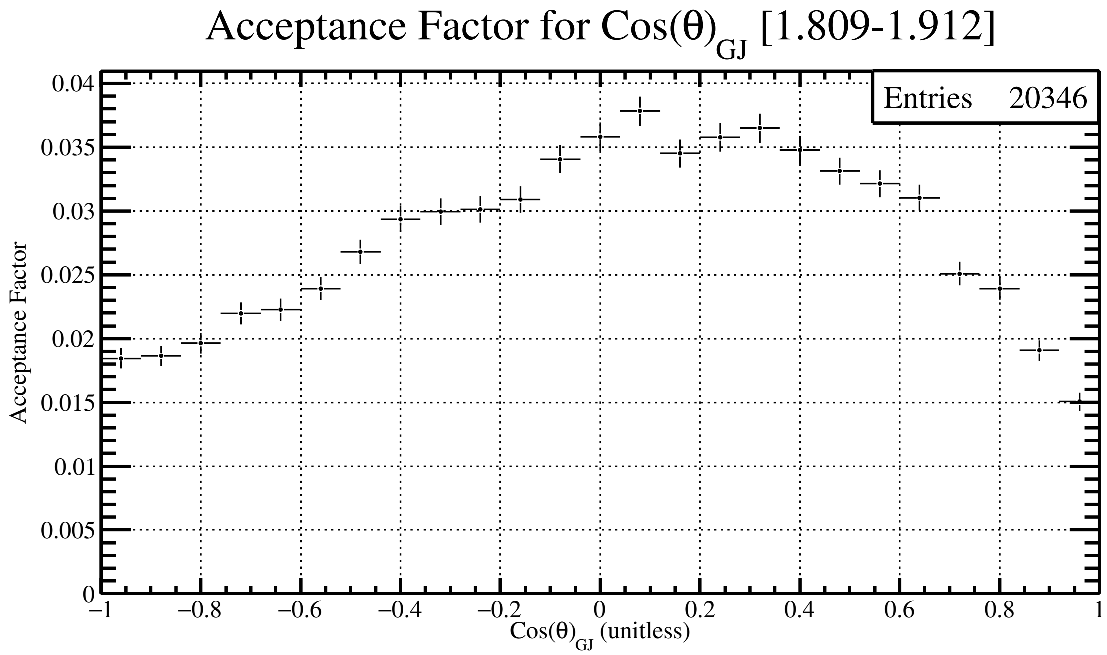

Figure 4.27: The $cos(\theta)_{GJ}$ acceptance factor for $\phi\eta$ invariant mass range between 1.809-1.912 GeV/c^2.

ple. After **hdroot** has completed reconstruction, a data file is reproduced which is identical to a real GlueX data file. Once this file is created, the same selection cuts that were used on the data will be enforced on the Monte Carlo sample. All Monte Carlo events that survive all phases of this simulation process are called the accepted Monte Carlo events. Finding the acceptance factors after this is very simple. To calculate the acceptance factors for a given observable, a histogram must be filled with the accepted Monte Carlo, then divided by another histogram which is filled with the generated Monte Carlo. The two observables that will be studied in this thesis are the $\phi\eta$ invariant mass and the $cos(\theta)_{GJ}$ distributions for different $\phi\eta$ invariant mass ranges. The acceptance factors for the $\phi\eta$ invariant mass are given in Figure [4.25]. There are two important results from this figure. The first observation is that there appears to be a large spike in the acceptance factor at very low $\phi\eta$ invariant mass. This is expected and is due to the $\phi\eta$ threshold being very close to this value. Since the generated Monte Carlo cannot create an invariant mass that is less than $m_\phi + m_\eta$, there are very few events in this region. However, once the generated Monte Carlo is passed through the simulation, it is completely possible to have reconstructed events with a $\phi\eta$ invariant mass below threshold. Since the acceptance factor is defined as the number of accepted Monte Carlo divided by the number of generated Monte Carlo, the acceptance factor jumps in this region of the invariant mass. The second important observation to take away from this figure is that the acceptance factors in the region of interest is relatively smooth and well behaved. Since it appears that there may be structures from data (Figure [4.24]) in the $\phi\eta$ mass range from 1.6 to 2 GeV/c^2 it is important that the best acceptance in the Monte Carlo is also in the region.

4.5 Analysis of $\phi\eta$ Invariant Mass Plot and $cos(\theta)_{GJ}$ Distributions

After performing all cuts on the input data and establishing quality factors for three different nearest neighbor approaches, the $\phi\eta$ invariant mass can be studied. In order to study this distribution, a total of four different methods were used to identify a $\phi\eta$ final state. Each approach, along with supporting plots, are given in the subsections below.

4.5.1 Elliptical Mass Approach

There was no weighting method used for this approach. Every event has a relative weight of 1, with the exception of events which came from beam photons that were out of time. This analysis has three sets of histograms, one of them is signal plus background, another is just background and the third is the difference between the previous two, which can be interpreted at a signal distribution. An example of what the overall data set looks like is given in Figure [4.28], and an example of the signal and background selection is given in Figure [4.29].

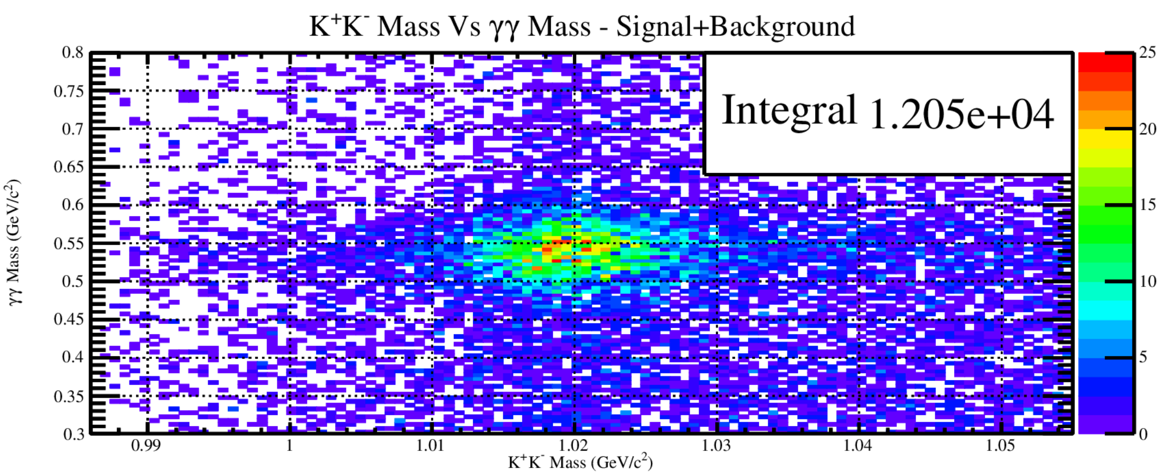

Figure 4.28: The K^+K^- invariant mass Vs $\gamma\gamma$ invariant mass before elliptical Mass selection.

The area which selects the $\phi\eta$ intersection can be defined using the equation for an ellipse (Equation 4.17), where the variable x will be substituted for the K^+K^- invariant mass, and the variable y will be substituted for the $\gamma\gamma$ invariant mass. Furthermore, the ellipse will need to be centered at the ϕ and η intersection. Therefore, the x variable will need to be shifted by m_ϕ, and the y variable will need to be shifted by m_η. Lastly, the semi-minor axis (a) and the semi-major axis (b) will need to be proportional to the width of the ϕ meson and the η meson, respectively. Since both resonances should have statistics which resemble that of a Gaussian distribution, a 2σ width was chosen to select the signal region. This will ensure that roughly 95 percent of the signal events will be selected. Therefore, the equation which describes the $\phi\eta$ intersection in Figure [4.29] can be written as Equation 4.18.

$$1 = \frac{x^2}{a^2} + \frac{y^2}{b^2} \tag{4.17}$$

$$1 = \frac{(m_{KK} - m_\phi)^2}{(2\sigma_\phi)^2} + \frac{(m_{\gamma\gamma} - m_\eta)^2}{(2\sigma_\eta)^2} \tag{4.18}$$

The elliptical subtraction method requires that the same amount of K^+K^- vs $\gamma\gamma$ area is used to select signal and background regions. The area for an ellipse is well known, and is given in Equation 4.19. We can take the semi-major and semi-minor axis parameters from Equation 4.18 and plug it into Equation 4.19 in order to derive the total K^+K^- vs $\gamma\gamma$ signal area (Equation 4.20).

$$A = \pi ab \tag{4.19}$$

$$A_{\phi\eta} = \pi(2\sigma_\phi)(2\sigma_\eta) = 4\pi\sigma_\phi\sigma_\eta \tag{4.20}$$

Knowing that the total signal area is equal to $4\pi\sigma_\phi\sigma_\eta$, it is easy to define the background area. The first parameter that needs to be chosen is the inner radius of the background selection. Once again, it is assumed that both resonances resemble a Gaussian distribution. Therefore, an inner radius of 3σ was chosen so that less that 1 percent of signal events would be selected, and therefore the majority of events would be background. Knowing that the inner radius will be 3σ, it is easy to derive the outer radius of the background selection. Once again, the total area of the background must be equal to the signal selection area of $4\pi\sigma_\phi\sigma_\eta$. Therefore, the outer radius of the background selection will be $\sqrt{13}\sigma$. The derivation of this area is given in Equation 4.21, and the selection is shown in the second histogram of Figure [4.29].

$$A_{BG} = \pi(\sqrt{13}\sigma_\phi)(\sqrt{13}\sigma_\eta) - \pi(3\sigma_\phi)(3\sigma_\eta) = 4\pi\sigma_\phi\sigma_\eta \tag{4.21}$$

Now that the signal and background selections have been well defined for this method, the relevant invariant mass and angular distributions can be shown. Figure [4.30] shows the $\phi\eta$ invariant mass distributions corresponding to different elliptical mass selections. The upper histogram of Figure [4.30] shows an immediate indication of two structures at lower $\phi\eta$ invariant mass. This distribution is compared to the second histogram in Figure [4.30] which is not a $\phi\eta$ selection. The histogram may show a possible structure at low invariant mass which causes the signal distribution to become slightly distorted. It should be noted that this structure is seen in other background invariant mass plots and may be an indication of a decay mode to ηKK.

The two structures seen in Figure [4.30] can be investigated by studying the angular distribution of the daughter particles in the Gottfried-Jackson frame. This distribution is important since its structure can provide an indication of what the parents spin state is. These distributions are produced by selecting $\phi\eta$ invariant mass ranges which correlate to the positions of the two structures, but do not overlap with each other. The range that was selected for the first structure is between (1.605-1.707) GeV/c^2, and the range that was selected for the seconds structure is between (1.809-1.912) GeV/c^2. The $cos(\theta)$ distribution for the first structure is given in Figure [4.31], and the $cos(\theta)$ distribution for the second

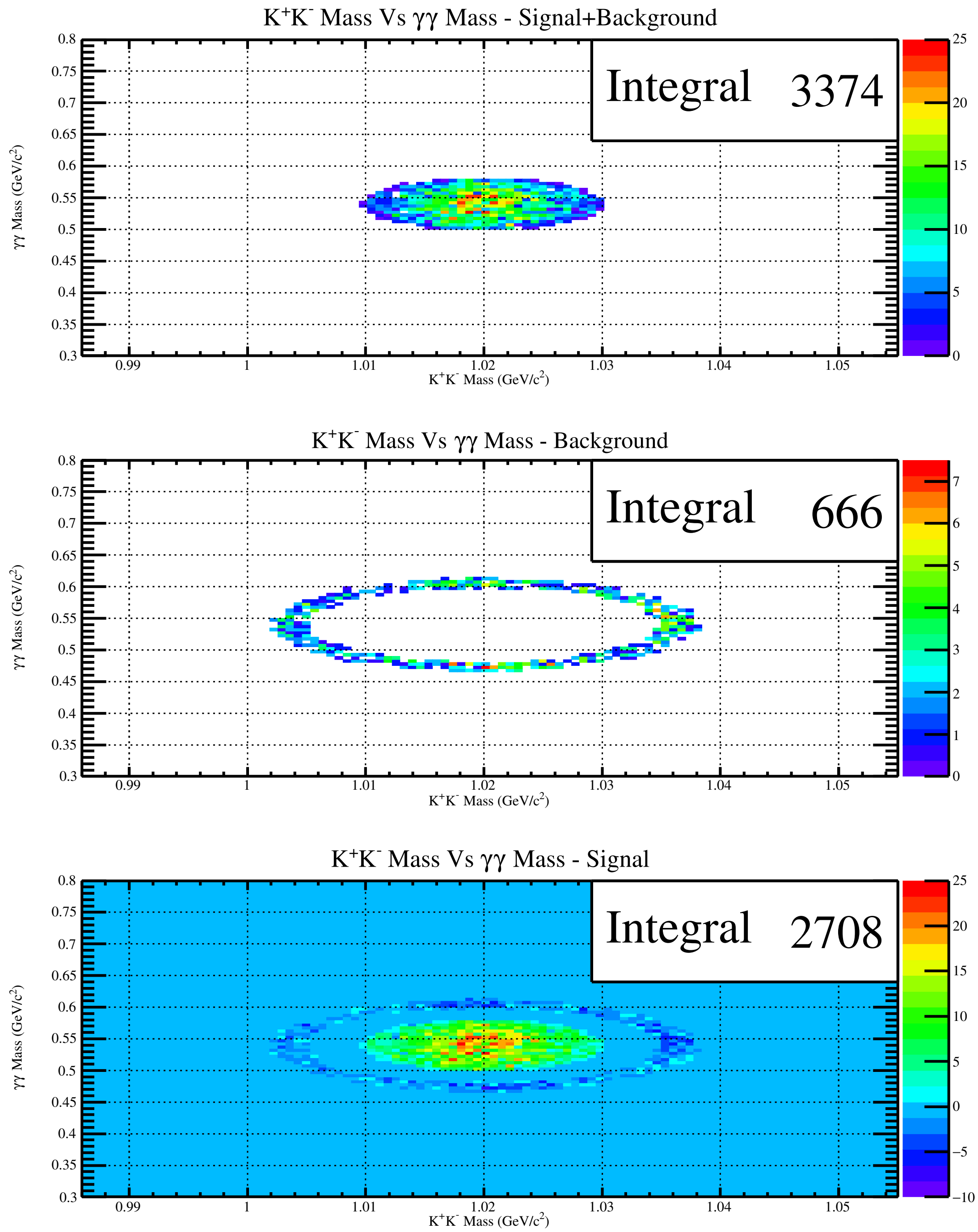

Figure 4.29: The K^+K^- invariant mass Vs $\gamma\gamma$ invariant mass showing the elliptical mass selection method. The upper most histogram shows the ellipse which selects the $\phi\eta$ intersection region, described by Equation 4.18. The middle histogram shows the ring which selects the background and is described by Equation 4.21. The bottom most histogram shows the difference between the upper and middle histograms.

structure is given in Figure [4.32]. The $cos(\theta)$ distribution for each structure does not currently provide information which may help to identify the spin state. However, it is clear that the $cos(\theta)$ distribution is different for each structure.

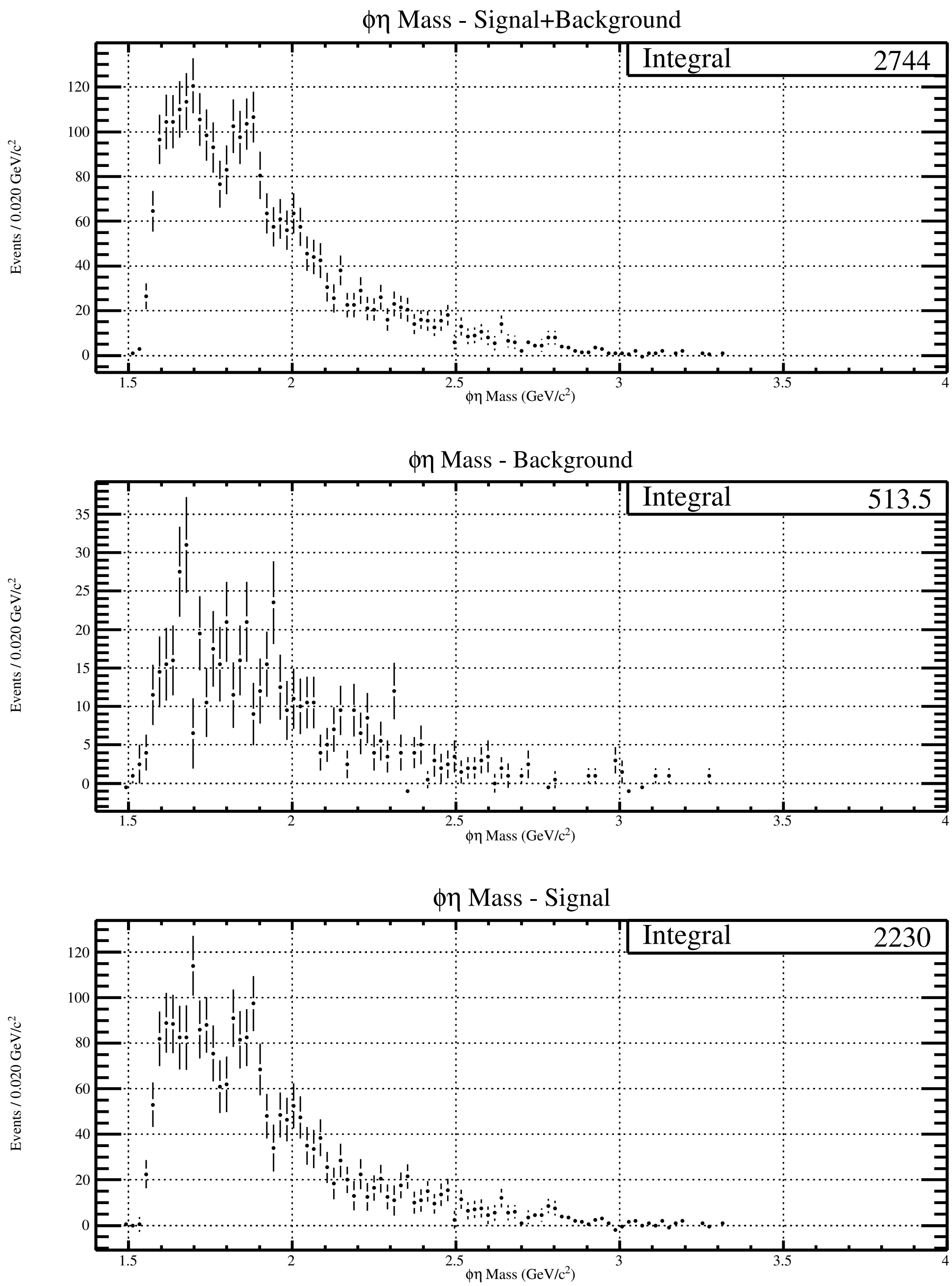

Figure 4.30: The $\phi\eta$ invariant mass for elliptical mass selection, not acceptance corrected.

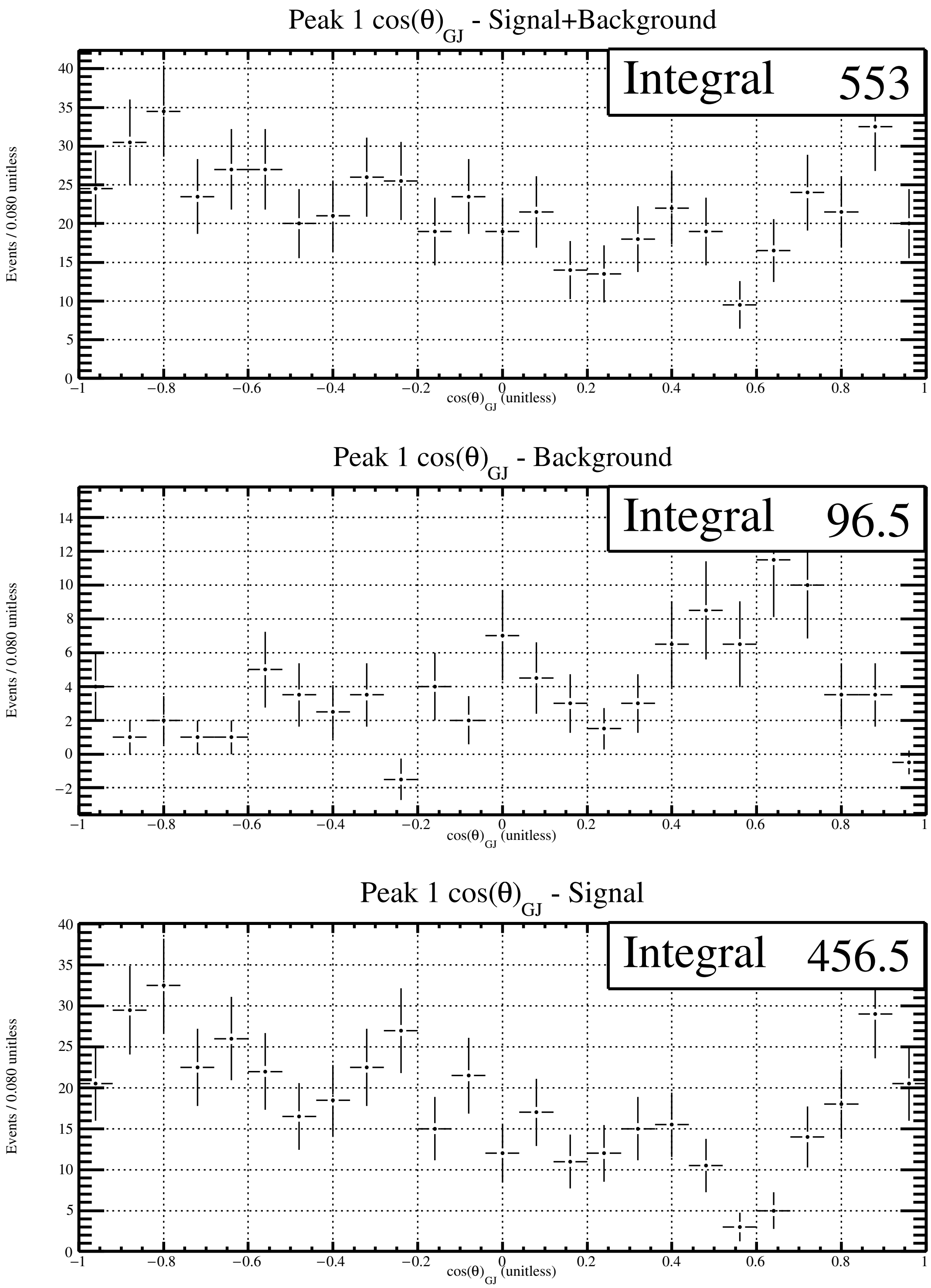

Figure 4.31: The $cos(\theta)_{GJ}$ distribution for $\phi\eta$ invariant mass between 1.605-1.707 GeV/c^2, not acceptance corrected.

Using only the signal plots from Figure [4.30], [4.31], and [4.32], the acceptance corrections provided in Subsection 4.4 can be used to understand the amount of statistics that were lost

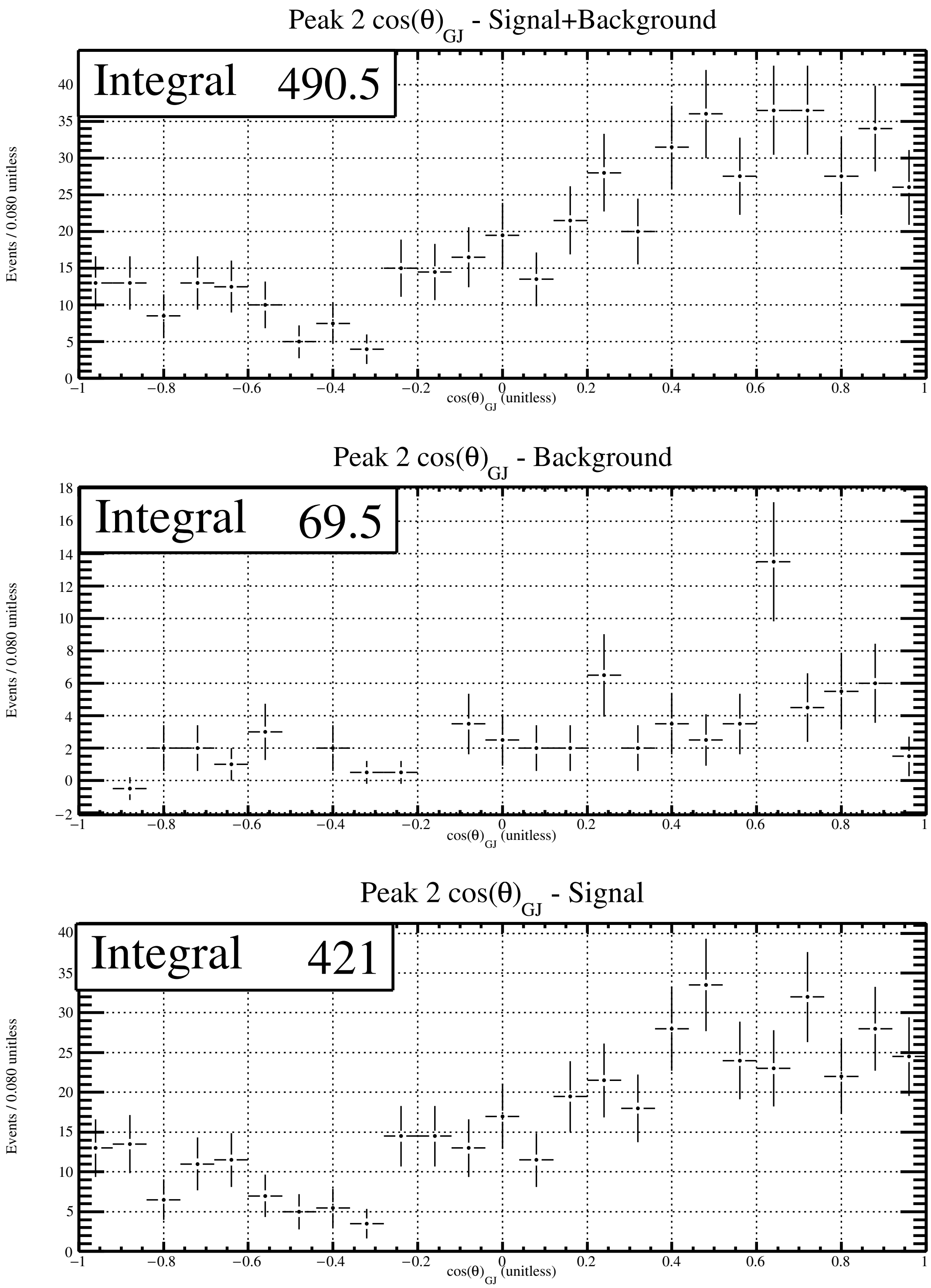

Figure 4.32: The $cos(\theta)_{GJ}$ distribution for $\phi\eta$ invariant mass between 1.809-1.912 GeV/c^2, not acceptance corrected.

due to detector acceptance. The acceptance corrected figures are provided in [4.33][4.34][4.35] below. Due to the mostly flat acceptance for all figures, none of the final plots presented here are greatly altered other than the amount of statistics in each bin.

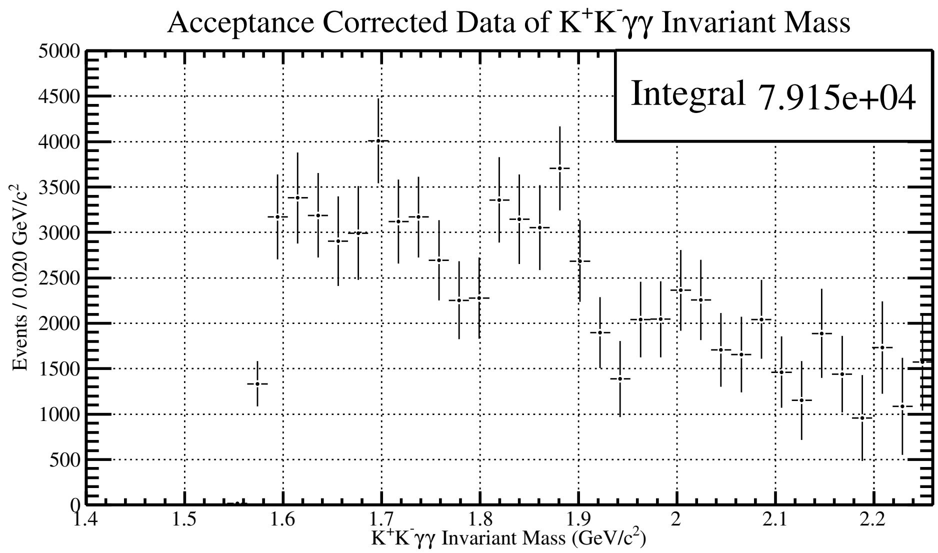

Figure 4.33: The signal $\phi\eta$ invariant mass for elliptical mass selection with the acceptance correction factors described in Figure [4.25]. The range of the distribution has been changed due to the large error bars at high $\phi\eta$ invariant mass values.

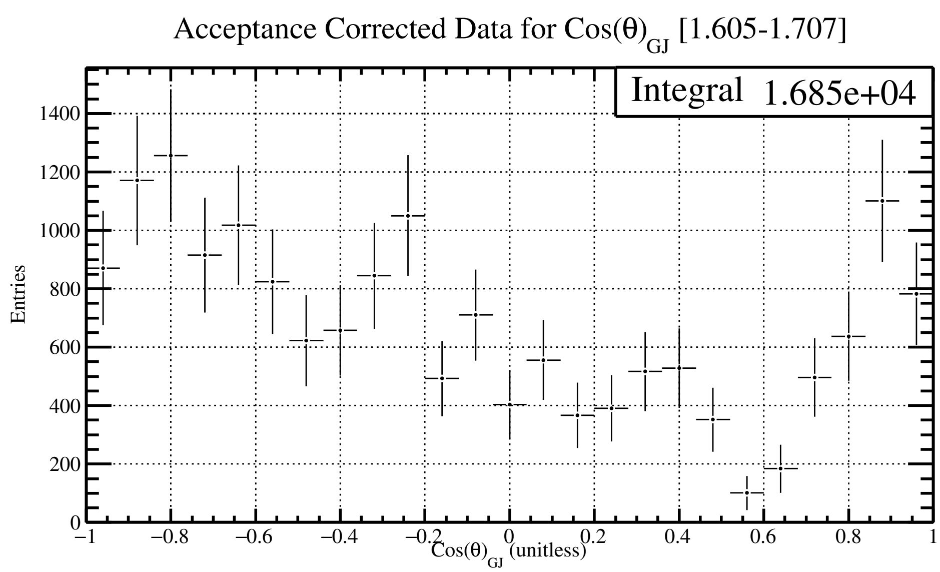

Figure 4.34: The $cos(\theta)_{GJ}$ distribution for $\phi\eta$ invariant mass between 1.605-1.707 GeV/c^2 with the acceptance correction factors described in Figure [4.26].

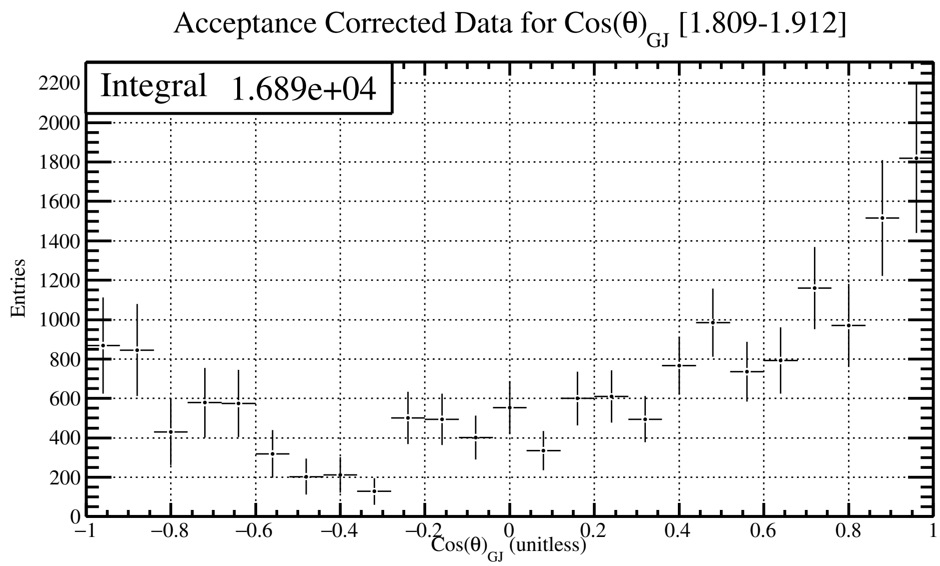

Figure 4.35: The $cos(\theta)_{GJ}$ distribution for $\phi\eta$ invariant mass between 1.809-1.912 GeV/c^2 with the acceptance correction factors described in Figure [4.27].

4.5.2 Q_ϕ Weighting, η Side-band Subtracted

This analysis uses the quality factor weights for the ϕ only method described in Subsection 4.2.2. Since this method only separates ϕ signal from K^+K^- background, it does not separate the η signal from $\gamma\gamma$ background with just Q_ϕ weighting. An example of the Q_ϕ weighted $\gamma\gamma$ invariant mass distribution is given in Figure [4.36].

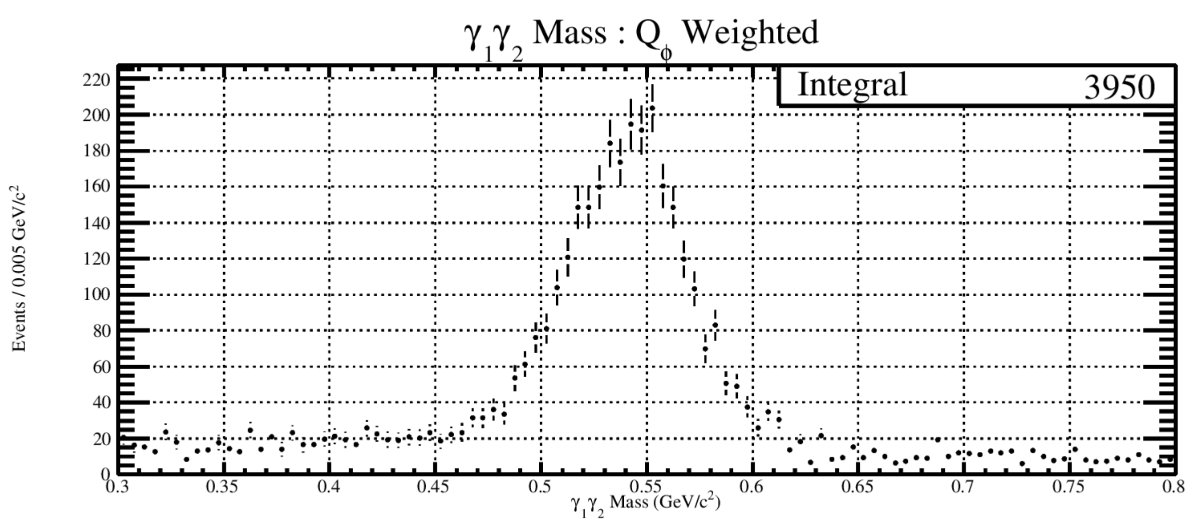

Figure 4.36: The $\gamma\gamma$ invariant mass spectrum with all events weighted by Q_ϕ.

In order to select the $\phi\eta$ final state, a $\gamma\gamma$ invariant mass cut of $\pm 2\sigma_\eta$ was enforced to select the η signal region. This selection was chosen because the η peak is assumed to have a shape which resembles a Gaussian distribution. A 2σ selection cut ensures that roughly 95 percent of the η signal will be selected. In addition to this signal selection, a side-band cut

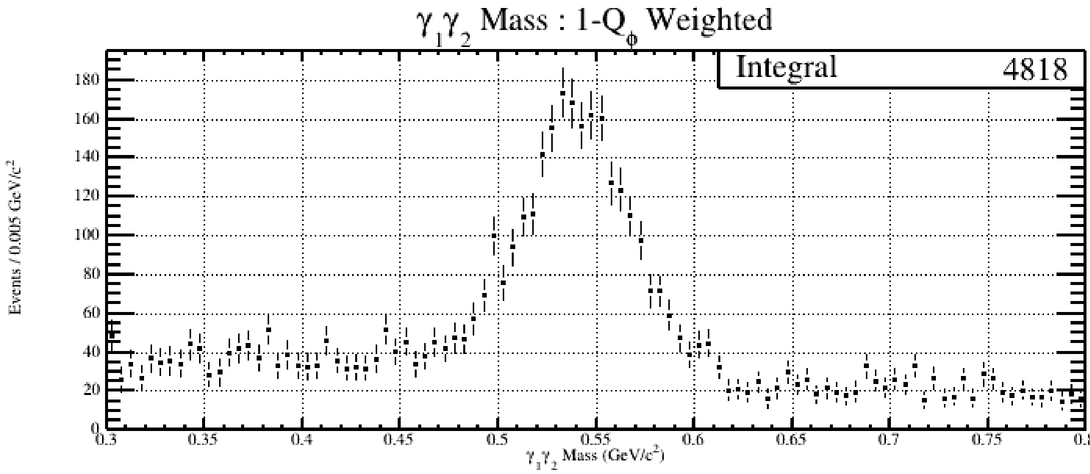

Figure 4.37: The $\gamma\gamma$ invariant mass spectrum with all events weighted by $1 - Q_\phi$.

was enforced on the $\gamma\gamma$ invariant mass in order to approximate the background. One of the side-band regions ranged from $m_\eta - 5\sigma_\eta \leq m_{\gamma\gamma} \leq m_\eta - 3\sigma_\eta$, and the other side-band region ranged from $m_\eta + 3\sigma_\eta \leq m_{\gamma\gamma} \leq m_\eta + 5\sigma_\eta$. These regions were chosen for two reasons. One of which is the fact that the total $m_{\gamma\gamma}$ range used to select the η signal region must be equal to the range used to select the background region. The second reason is to ensure that less than 1 percent of data would be contained within the background selection.

Once the signal and background selections are established, the $\phi\eta$ final state can be studied with this weighting method. The $\phi\eta$ final state is found by weighting all events with Q_ϕ, then selecting the η signal region. Once this distribution is known, a second distribution is filled with the $\gamma\gamma$ side-band selection. Taking the difference between the two distributions provides a $\phi\eta$ final state. An example of what all of these distributions look like is provided in Figure [4.38]. The top histogram of Figure [4.38] is the $K^+K^-\gamma\gamma$ invariant mass weighted by Q_ϕ and a 2σ selection of the η peak. The middle histogram is the $K^+K^-\gamma\gamma$ invariant mass weighted by Q_ϕ and a $\gamma\gamma$ side-band selection. Finally, the bottom histogram is the difference between the top histogram and the middle histogram. The bottom histogram of Figure [4.38] is considered to be the $\phi\eta$ invariant mass plot for this weighting method. The reason that this is the signal plot for this method is because the ϕ has been identified by means of the nearest neighbors approach described in Subsection 4.2.2; and the η has been identified by means of a side-band subtraction.

Contained within the signal histogram of Figure [4.38] are two structures which resemble the structures also seen in Subsection 4.5.1. In order to better understand the nature of these structures, the $cos(\theta)_{GJ}$ angles are extracted for these regions of $\phi\eta$ invariant mass. The $cos(\theta)_{GJ}$ angles for the first structure are given in Figure [4.39] and are found by imposing a cut on the $\phi\eta$ invariant mass with a range of 1.605-1.707 GeV/c^2. The $cos(\theta)_{GJ}$ angles for the second structure are given in Figure [4.40] and are found by imposing a cut on the $\phi\eta$ invariant mass with a range of 1.809-1.912 GeV/c^2. There is no clear angular structure in Figure [4.39] or Figure [4.40]. The only clear observation that is made is that the angular distributions of each region are different from one another.

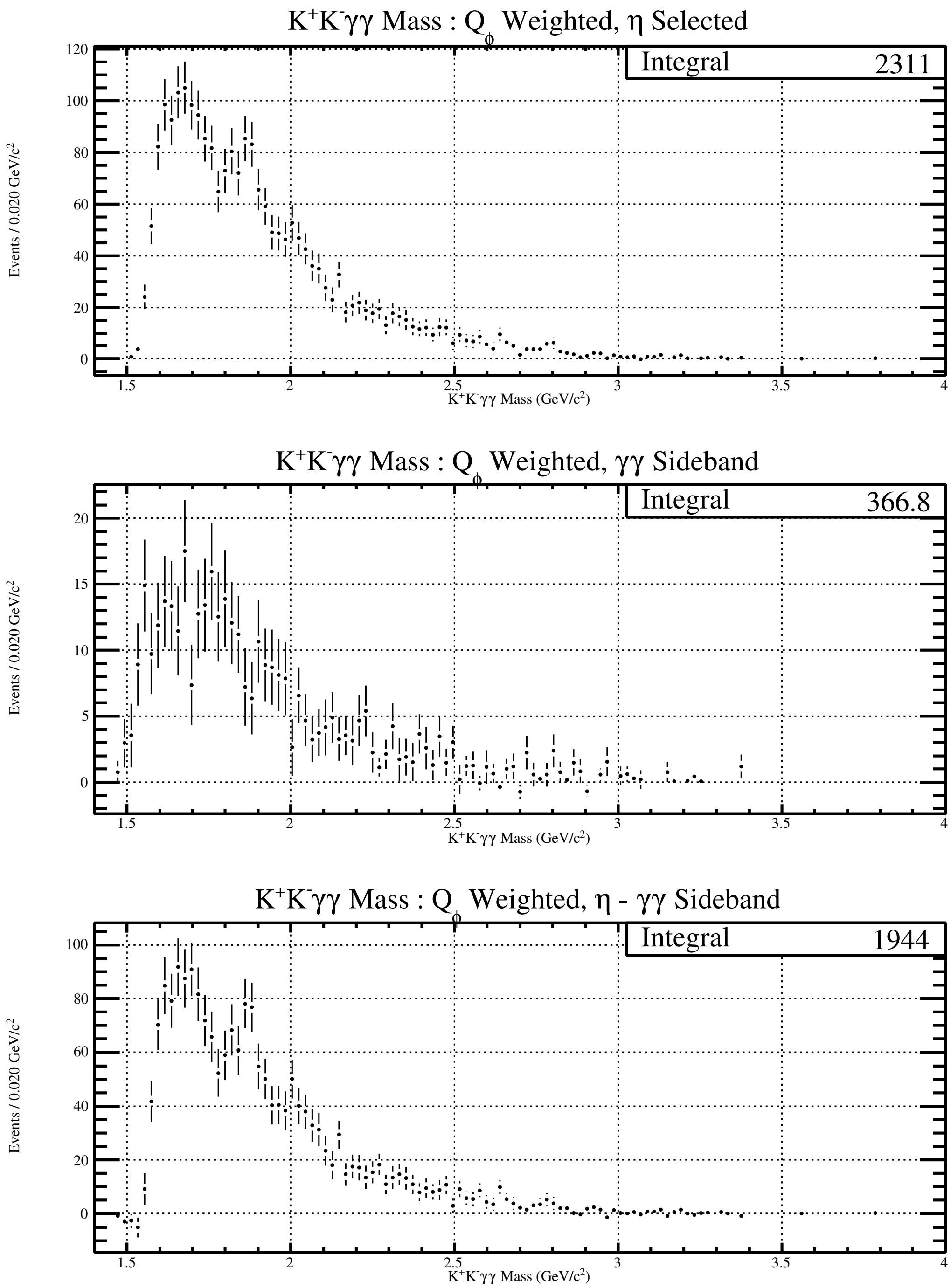

Figure 4.38: The $K^+K^-\gamma\gamma$ invariant mass spectrum with all signal events weighted by Q_ϕ, not acceptance corrected. The top histogram is the data which selects the η peak contained in Figure [4.36]. The middle histogram is the data which selects the $\gamma\gamma$ side-band data. The bottom histogram is the $\phi\eta$ signal and is the difference between the first histogram and the second histogram.

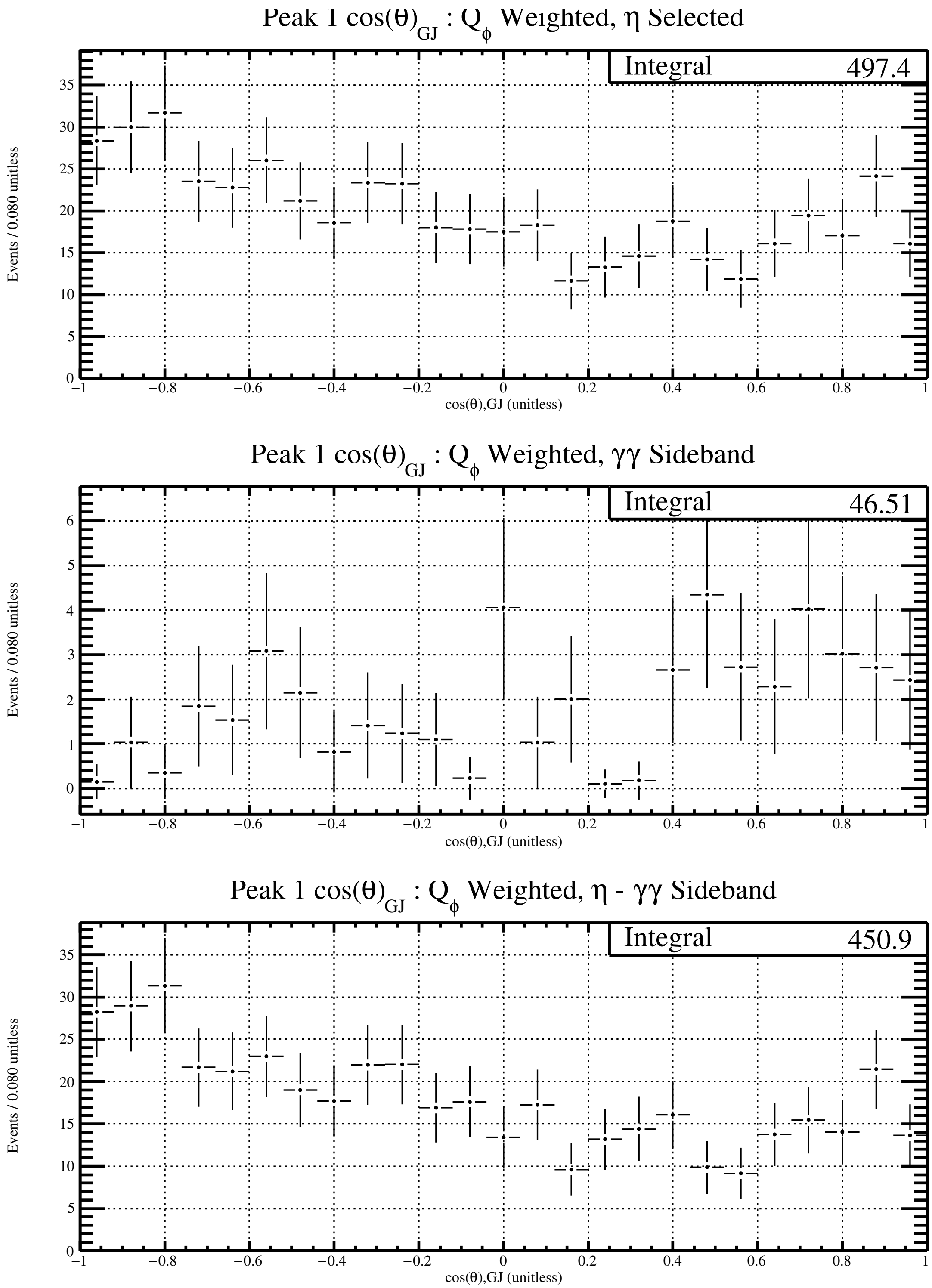

Figure 4.39: The $cos(\theta)_{GJ}$ distribution for $\phi\eta$ invariant mass between 1.605-1.707 GeV/c^2, not acceptance corrected.

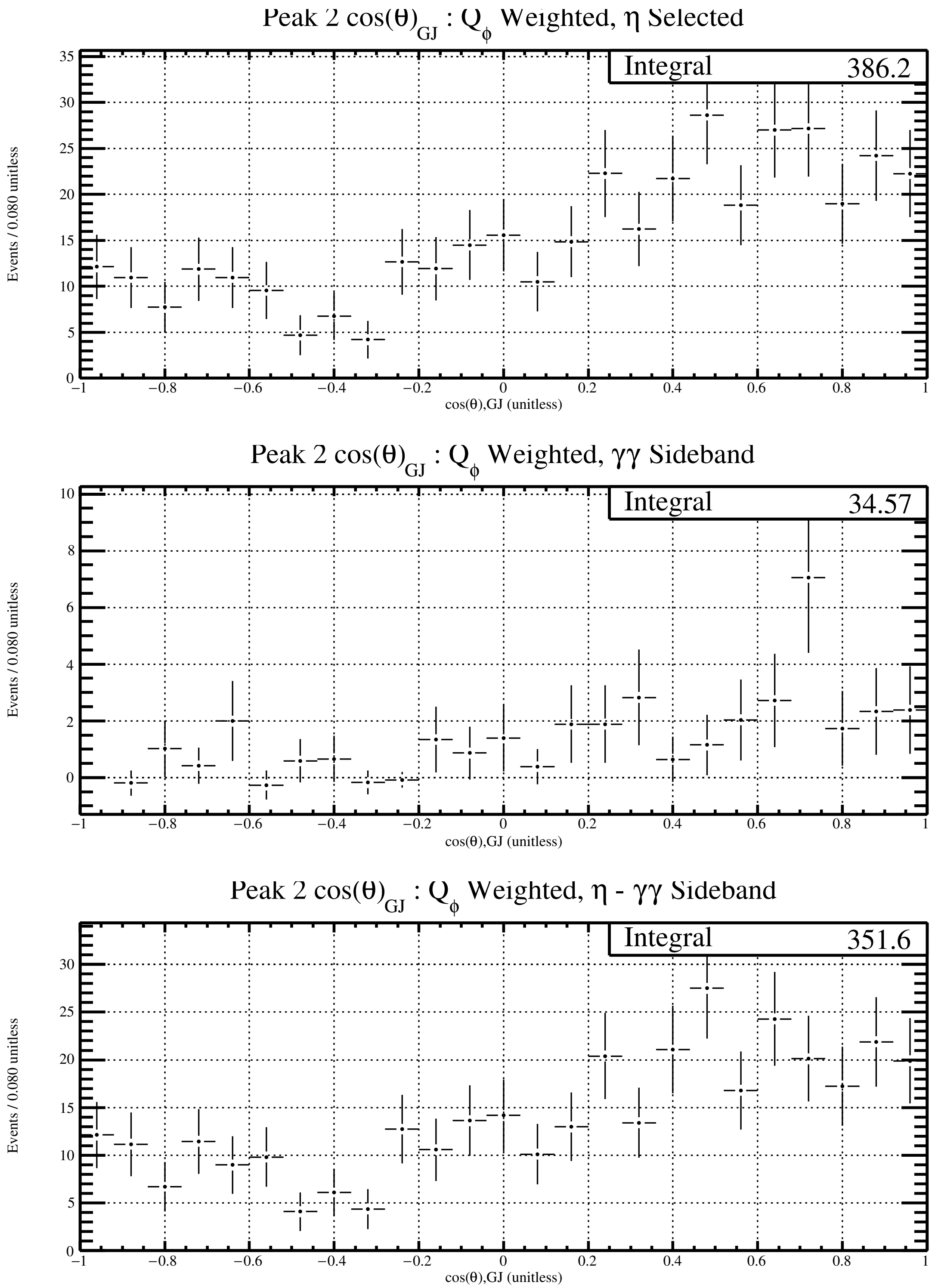

Figure 4.40: The $cos(\theta)_{GJ}$ distribution for $\phi\eta$ invariant mass between 1.809-1.912 GeV/c^2, not acceptance corrected.

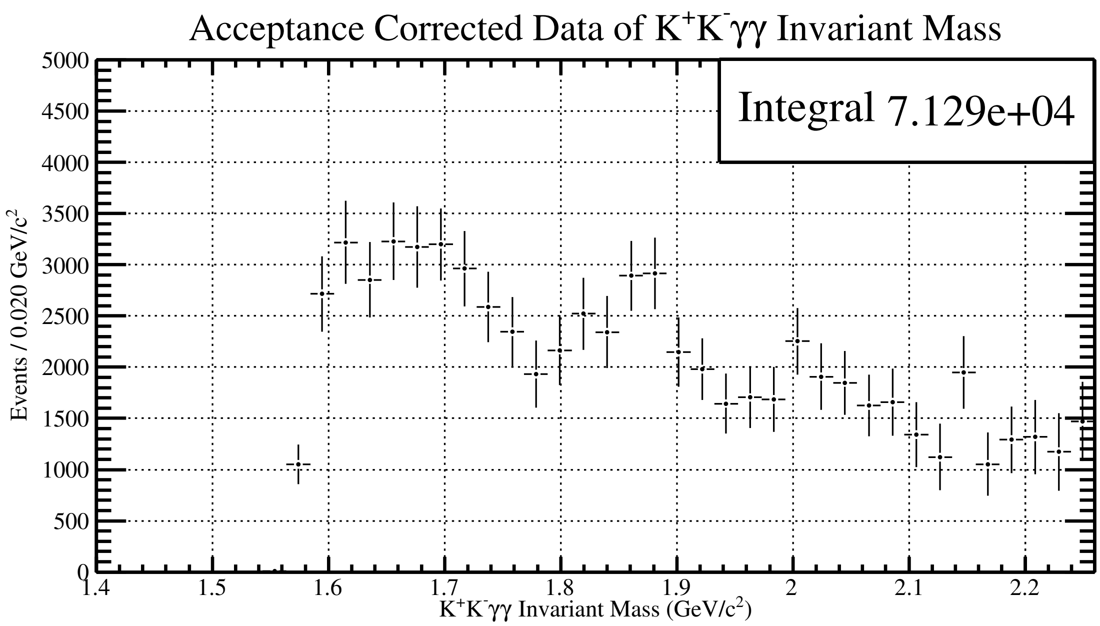

Figure 4.41: The $K^+K^-\gamma\gamma$ invariant mass spectrum with all signal events weighted by Q_ϕ, and the η is selected by side-band subtraction. The spectrum is acceptance corrected as described by Figure [4.25]. The range of the distribution has been changed due to the large error bars at high $\phi\eta$ invariant mass values.

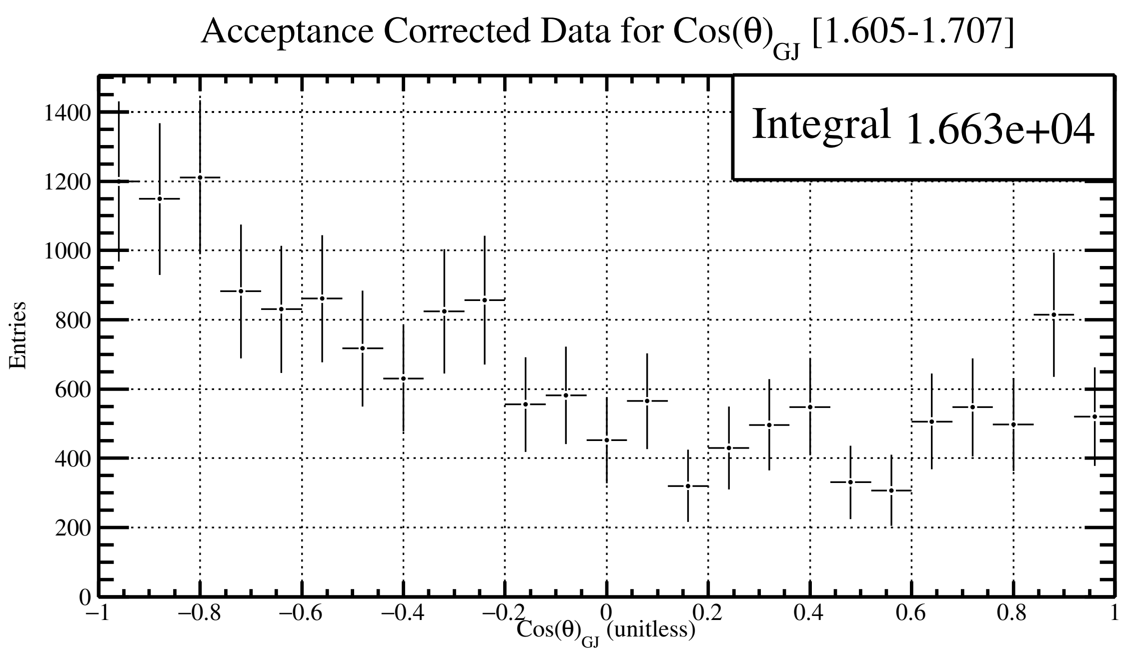

Figure 4.42: The $cos(\theta)_{GJ}$ distribution for $\phi\eta$ invariant mass between 1.605-1.707 GeV/c^2 with the acceptance correction factors described in Figure [4.26].

Using only the signal plots from Figure [4.38], [4.39], and [4.40], the acceptance corrections provided in Subsection 4.4 can be used to correct any detector effects. The acceptance corrected figures are provided in [4.41][4.42][4.43] below. Due to the mostly flat acceptance for all figures, none of the final plots presented here are greatly altered other than the amount of statistics in each bin.

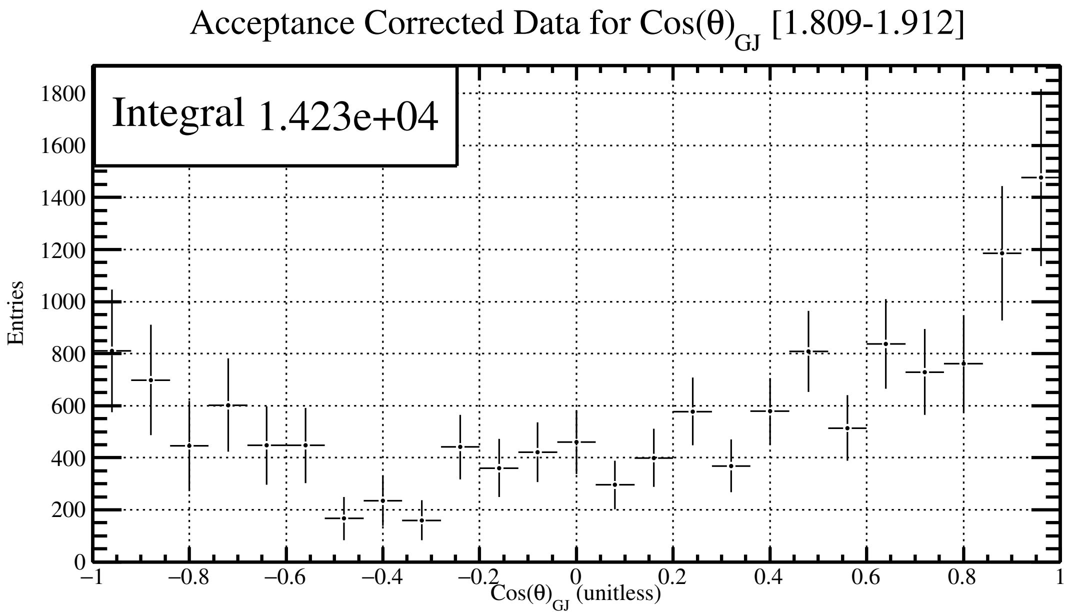

Figure 4.43: The $cos(\theta)_{GJ}$ distribution for $\phi\eta$ invariant mass between 1.809-1.912 GeV/c^2 with the acceptance correction factors described in Figure [4.27].

4.5.3 Q_η Weighting, ϕ Side-band Subtracted

This analysis uses the quality factor weights for the η only method described in Subsection 4.2.2. Since this method only separates η signal from $\gamma\gamma$ background, it does not separate the ϕ signal from K^+K^- background with just Q_η weighting. An example of the Q_η weighted K^+K^- invariant mass distribution is given in Figure [4.44].

In order to select the $\phi\eta$ final state, a K^+K^- invariant mass cut of $\pm 2\sigma_\phi$ was enforced to select the ϕ signal region. This selection was chosen because the ϕ peak is assumed to have a shape which resembles a Gaussian distribution. A 2σ selection cut ensures that roughly 95 percent of the ϕ signal will be selected. In addition to this signal selection, a side-band cut was enforced on the K^+K^- invariant mass in order to approximate the background. One of the side-band regions ranged from $m_\phi - 5\sigma_\phi \leq m_{K^+K^-} \leq m_\phi - 3\sigma_\phi$, and the other side-band region ranged from $m_\phi + 3\sigma_\phi \leq m_{K^+K^-} \leq m_\phi + 5\sigma_\phi$. These regions were chosen for two reasons. One of which is the fact that the total $m_{K^+K^-}$ range used to select the ϕ signal region must be equal to the range used to select the background region. The second reason is to ensure that less than 1 percent of data would be contained within the background selection.

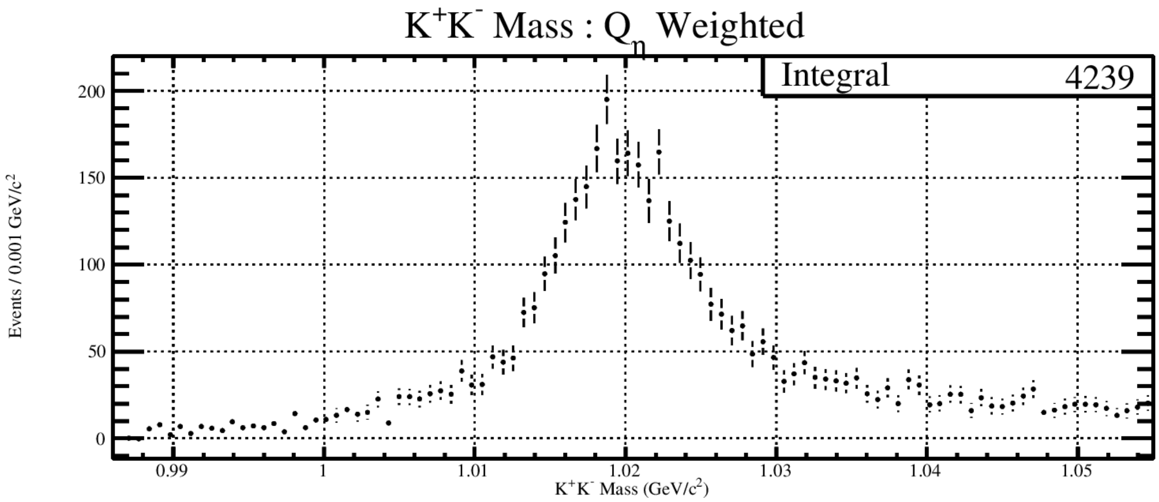

Figure 4.44: The fit of the K^+K^- invariant mass spectrum with all events weighted by Q_η.

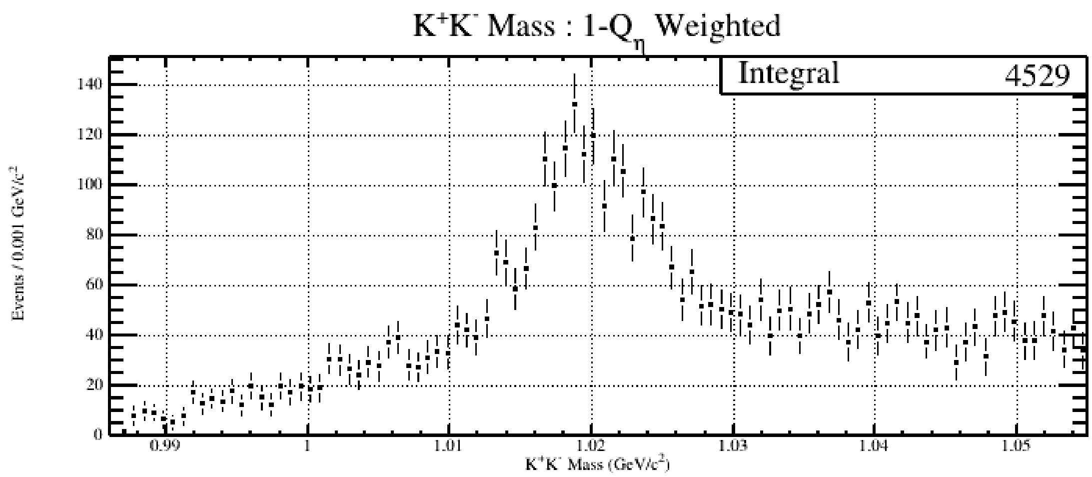

Figure 4.45: The K^+K^- invariant mass spectrum with all events weighted by $1 - Q_\eta$.

Once the signal and background selections are established, the $\phi\eta$ final state can be studied with this weighting method. The $\phi\eta$ final state is found by weighting all events with Q_η, then selecting the ϕ signal region. Once this distribution is know, a second distribution is filled with the K^+K^- side-band selection. Taking the difference between the two distributions provides a $\phi\eta$ final state. An example of what all of these distributions look like is provided in Figure [4.46]. The top histogram of Figure [4.46] is the $K^+K^-\gamma\gamma$ invariant mass weighted by Q_η and a 2σ selection of the ϕ peak. The middle histogram is the $K^+K^-\gamma\gamma$ invariant mass weighted by Q_η and a K^+K^- side-band selection. Finally, the bottom histogram is the difference between the top histogram and the middle histogram. The bottom histogram of Figure [4.46] is considered to be the $\phi\eta$ invariant mass plot for this weighting method. The reason that this is the signal plot for this method is because the η has been identified by means of the nearest neighbors approach described in Subsection 4.2.2; and the ϕ has been identified by means of a side-band subtraction.

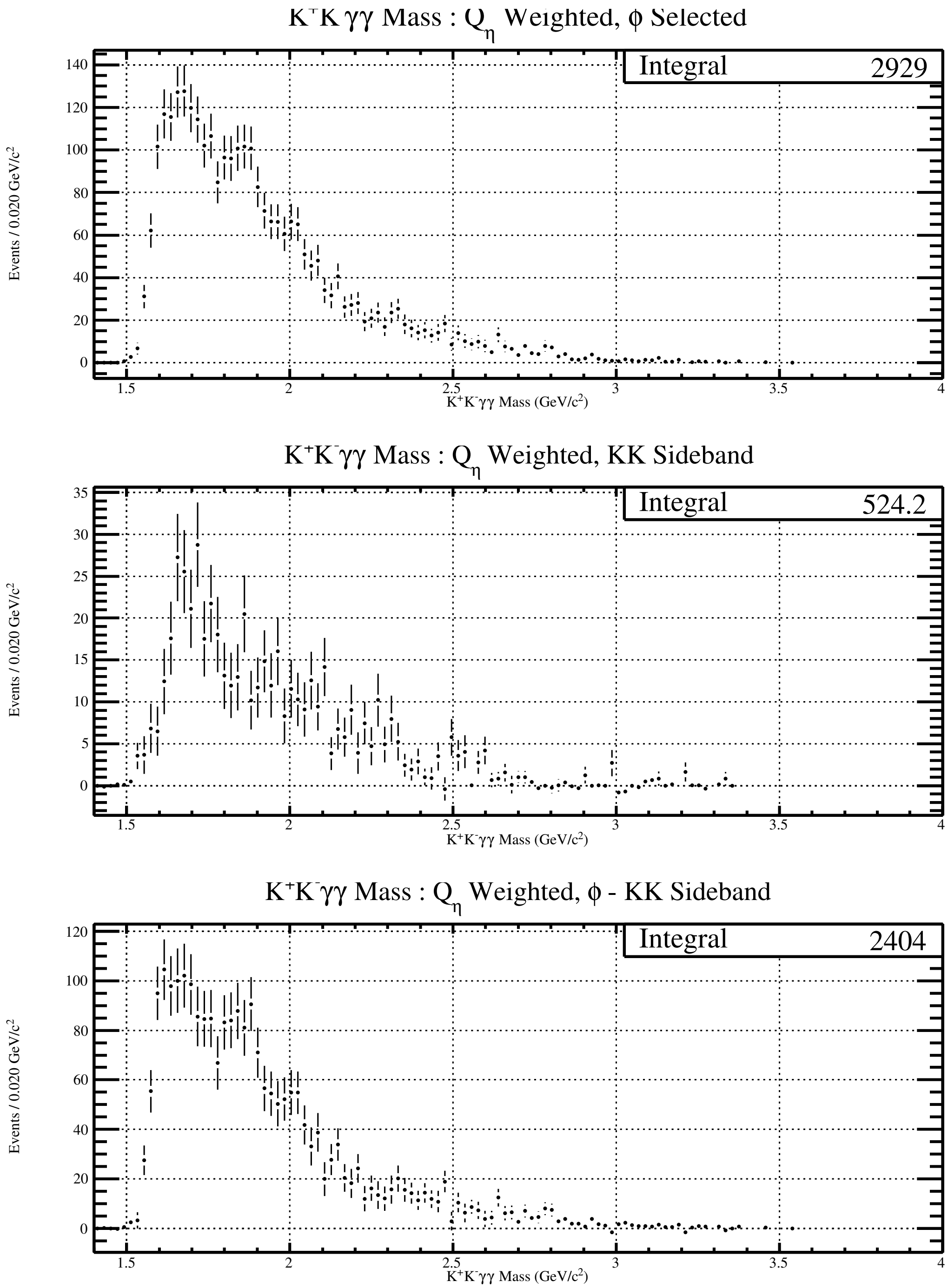

Figure 4.46: The $K^+K^-\gamma\gamma$ invariant mass spectrum with all signal events weighted by Q_η, not acceptance corrected. The top histogram is the data which selects the ϕ peak contained in Figure [4.44]. The middle histogram is the data which selects the K^+K^- side-band data. The bottom histogram is the $\phi\eta$ signal and is the difference between the first histogram and the second histogram.

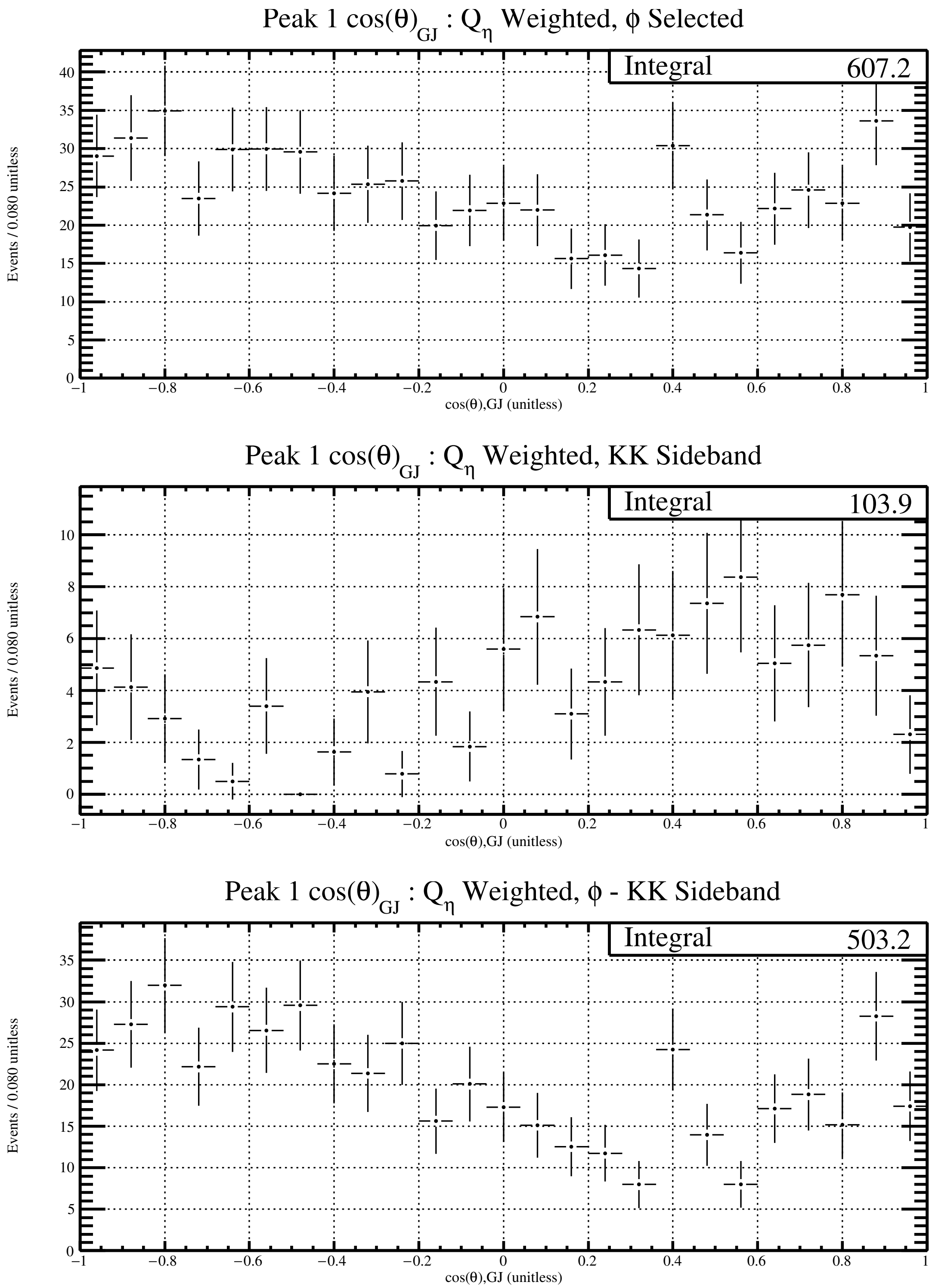

Figure 4.47: The $cos(\theta)_{GJ}$ distribution for $\phi\eta$ invariant mass between 1.605-1.707 GeV/c^2, not acceptance corrected.

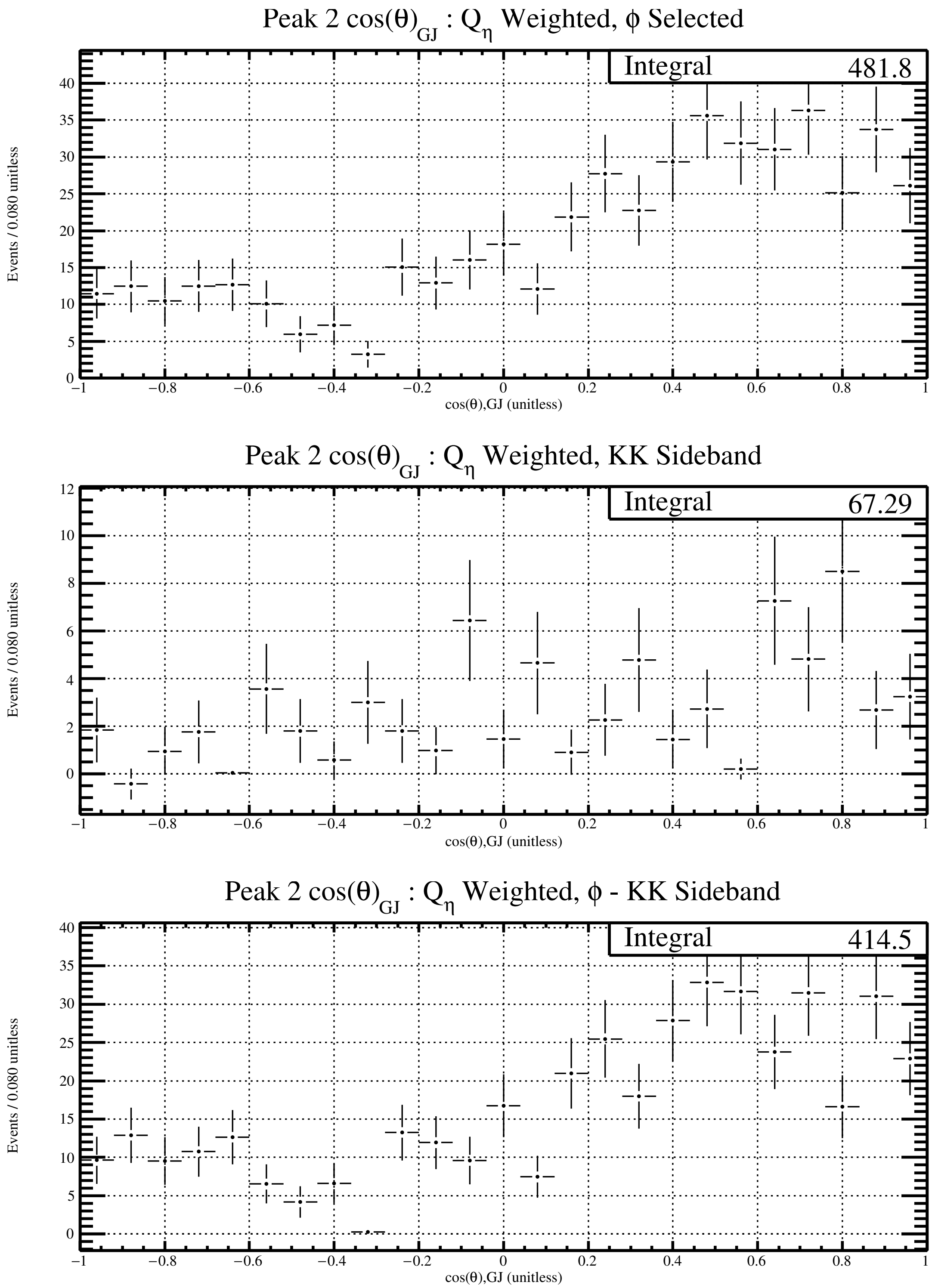

Figure 4.48: The $cos(\theta)_{GJ}$ distribution for $\phi\eta$ invariant mass between 1.809-1.912 GeV/c^2, not acceptance corrected.

One interesting result from this method and the others presented in this thesis is the ability to study backgrounds. The middle histogram of Figure [4.46] shows a clear indication that a structure is present in the ηKK invariant mass. This structure is also seen in the background histograms of Figure [4.30] and Figure [4.54]. However, this structure is *not* seen in the background histogram of Figure [4.38]. The consistency of this structure showing up in some backgrounds, but not all, provides evidence that it may have a decay mode to both $\phi\eta$ and ηKK.

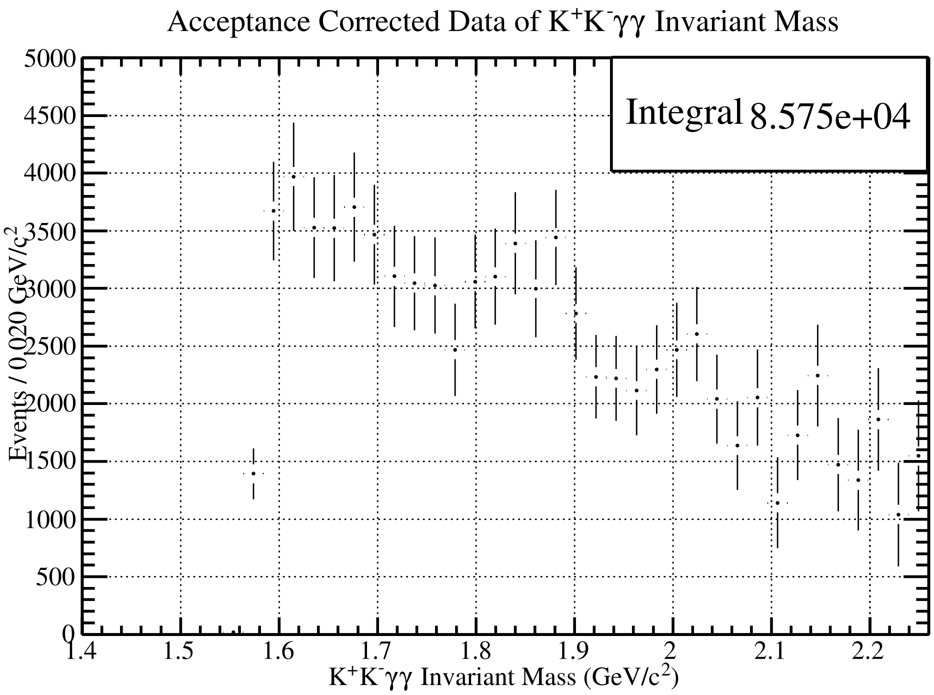

Figure 4.49: The $K^+K^-\gamma\gamma$ invariant mass spectrum with all signal events weighted by Q_η, and the ϕ is selected by side-band subtraction. The spectrum is acceptance corrected as described by Figure [4.25]. The range of the distribution has been changed due to the large error bars at high $\phi\eta$ invariant mass values.

Contained within the signal histogram of Figure [4.46] are two structures which resemble the structures also seen in Subsection 4.5.1, Subsection 4.5.2. In order to better understand the nature of these structures, the $cos(\theta)_{GJ}$ angles are extracted for these regions of $\phi\eta$ invariant mass. The $cos(\theta)_{GJ}$ angles for the first structure are given in Figure [4.47] and are found by imposing a cut on the $\phi\eta$ invariant mass with a range of 1.605-1.707 GeV/c^2. The $cos(\theta)_{GJ}$ angles for the second structure are given in Figure [4.48] and are found by imposing a cut on the $\phi\eta$ invariant mass with a range of 1.809-1.912 GeV/c^2. There is no clear angular structure in Figure [4.47] or Figure [4.48]. The only clear observation that is made is that the angular distributions of each region are different from one another.

Using only the signal plots from Figure [4.46], [4.47], and [4.48], the acceptance corrections provided in Subsection 4.4 can be used to correct any detector effects. The acceptance corrected figures are provided in [4.49][4.50][4.51] below. Due to the mostly flat acceptance for all figures, none of the final plots presented here are greatly altered other than the amount of statistics in each bin.

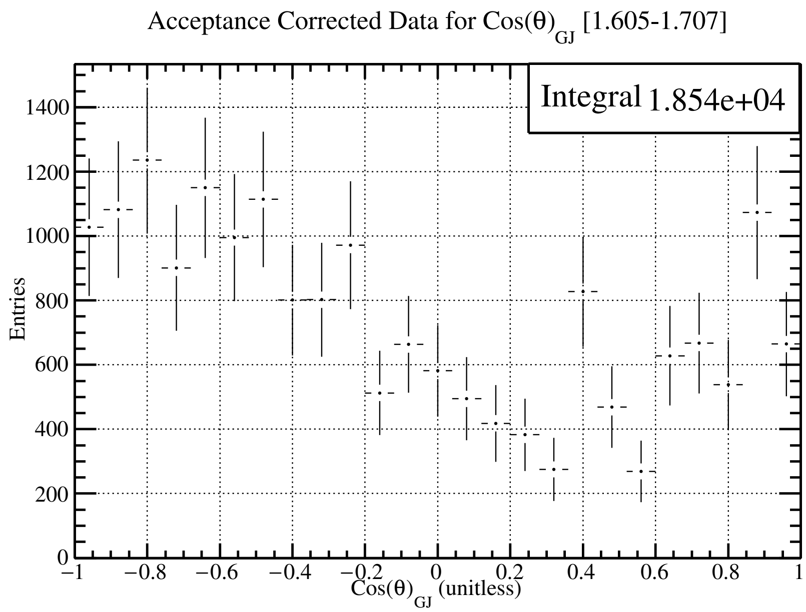

Figure 4.50: The $cos(\theta)_{GJ}$ distribution for $\phi\eta$ invariant mass between 1.605-1.707 GeV/c^2 with the acceptance correction factors described in Figure [4.26].

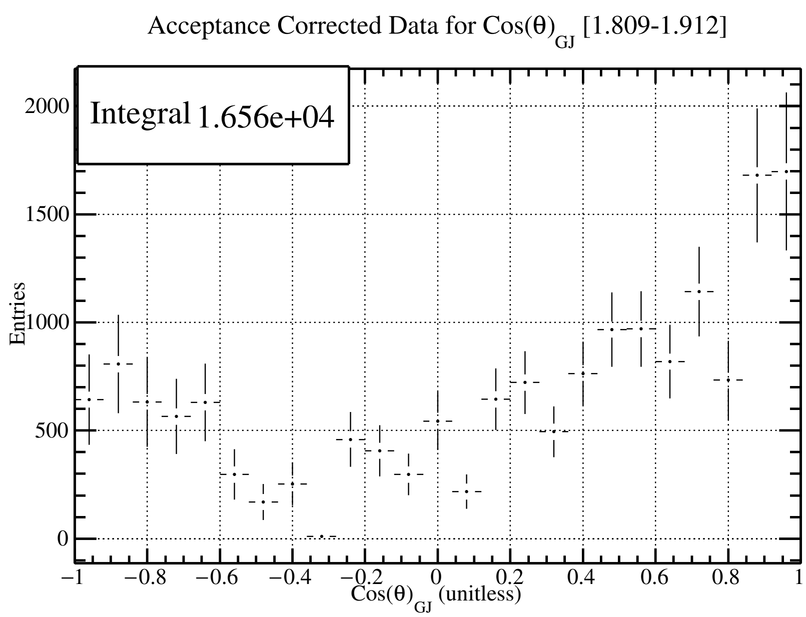

Figure 4.51: The $cos(\theta)_{GJ}$ distribution for $\phi\eta$ invariant mass between 1.809-1.912 GeV/c^2 with the acceptance correction factors described in Figure [4.27].

4.5.4 $Q_{\phi\eta}$ Weighting

This analysis uses the quality factor weights for the $\phi\eta$ only method described in Subsection 4.2.2. Since this method separates both η signal from $\gamma\gamma$ background, and ϕ signal from K^+K^- background, the only weight that is needed event by event is $Q_{\phi\eta}$. An example of the $Q_{\phi\eta}$ weighted $K^+K^-\gamma\gamma$ invariant mass distribution and the corresponding background plot is given in Figure [4.54].

One interesting result from this method and the others presented in this thesis is the ability to study backgrounds. The lower histogram of Figure [4.54] shows a clear indication that a structure is present in the $1-Q_{\phi\eta}$ weighted invariant mass. This structure is also seen in the background histograms of Figure [4.30] and Figure [4.46]. However, this structure is *not* seen in the background histogram of Figure [4.38].

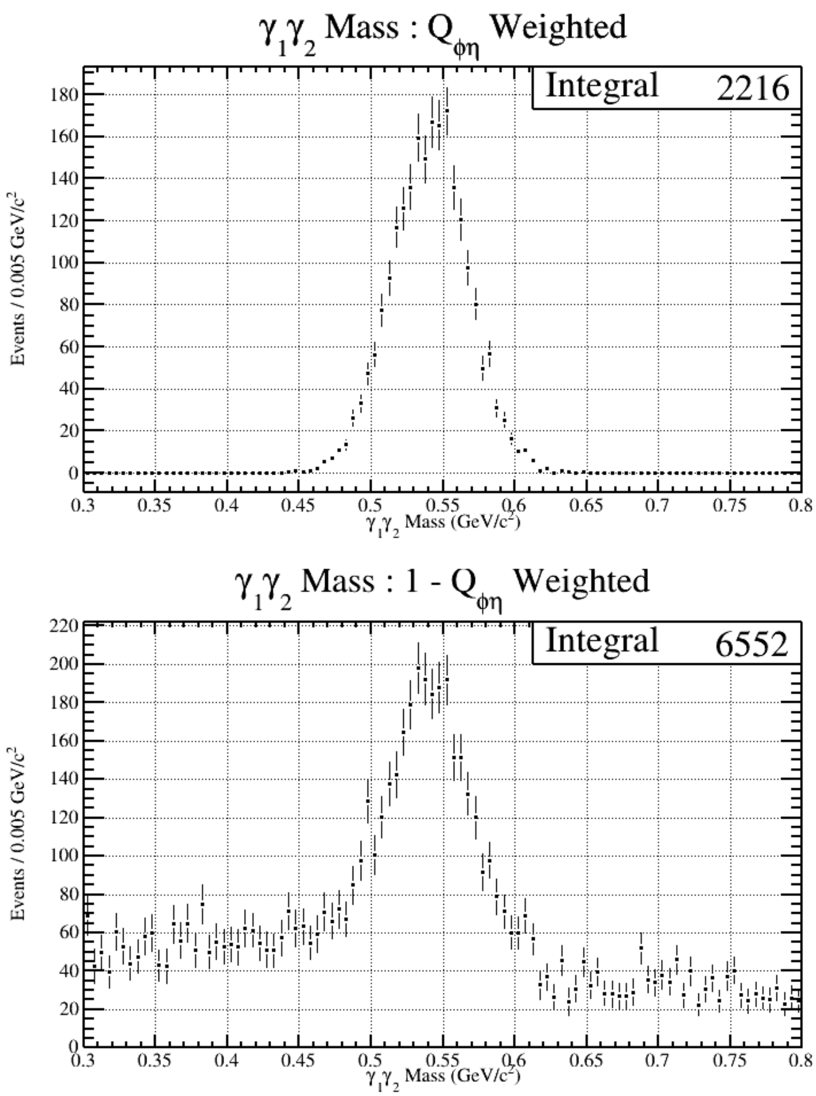

Figure 4.52: The $\gamma\gamma$ invariant mass spectrum with all signal events weighted by $Q_{\phi\eta}$, not acceptance corrected.

Contained within the signal histogram of Figure [4.54] are two structures which resemble the structures also seen in Subsection 4.5.1, Subsection 4.5.2, and and Subsection 4.5.3. In order to better understand the nature of these structures, the $cos(\theta)_{GJ}$ angles are extracted for these regions of $\phi\eta$ invariant mass. The $cos(\theta)_{GJ}$ angles for the first structure are given in Figure [4.55] and are found by imposing a cut on the $\phi\eta$ invariant mass with a range of 1.605-1.707 GeV/c^2. The $cos(\theta)_{GJ}$ angles for the second structure are given in Figure [4.56] and are found by imposing a cut on the $\phi\eta$ invariant mass with a range of 1.809-1.912 GeV/c^2. There is no clear angular structure in Figure [4.55] or Figure [4.56]. The only clear observation that is made is that the angular distributions of each region are different from one another.

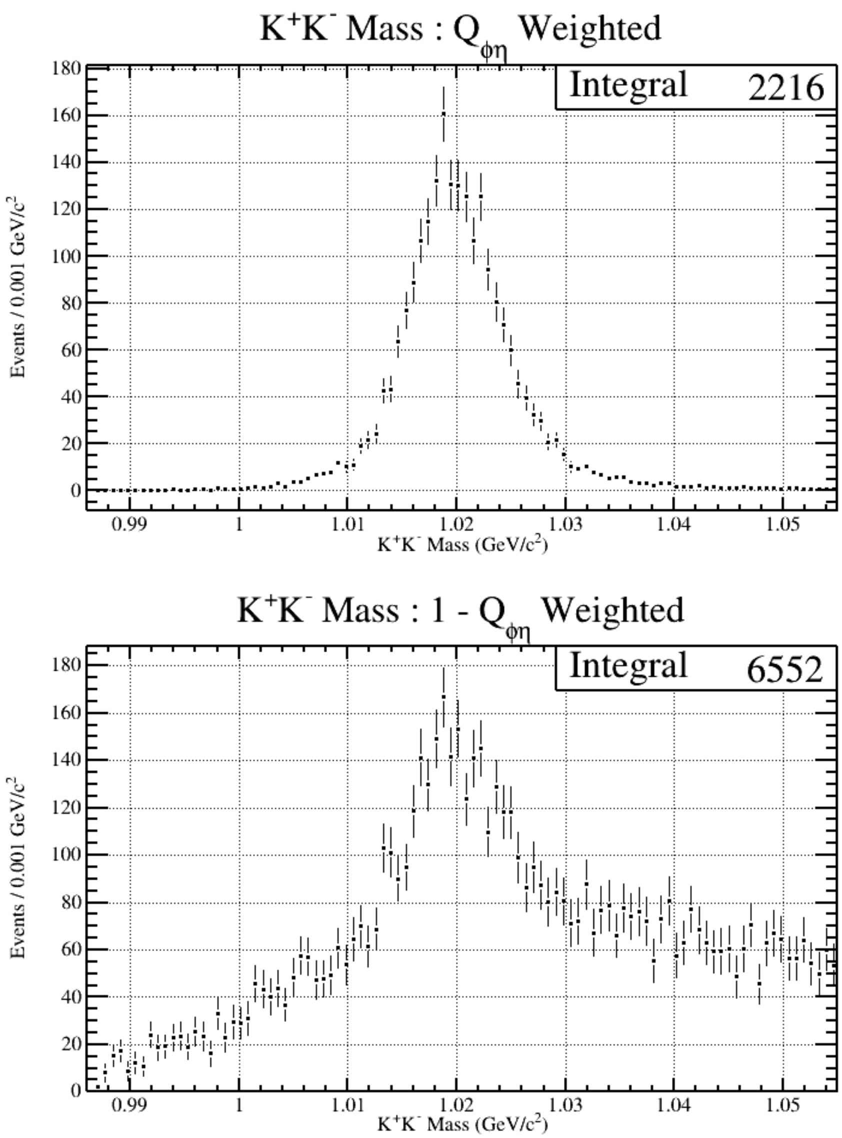

Figure 4.53: The K^+K^- invariant mass spectrum with all signal events weighted by $Q_{\phi\eta}$, not acceptance corrected.

Using only the signal plots from Figure [4.54], [4.55], and [4.56], the acceptance corrections provided in Subsection 4.4 can be used to improve the statistics in each figure as well as correct any detector effects. The acceptance corrected figures are provided in [4.57][4.58][4.59] below. Due to the mostly flat acceptance for all figures, none of the final plots presented here are greatly altered other than the amount of statistics in each bin.

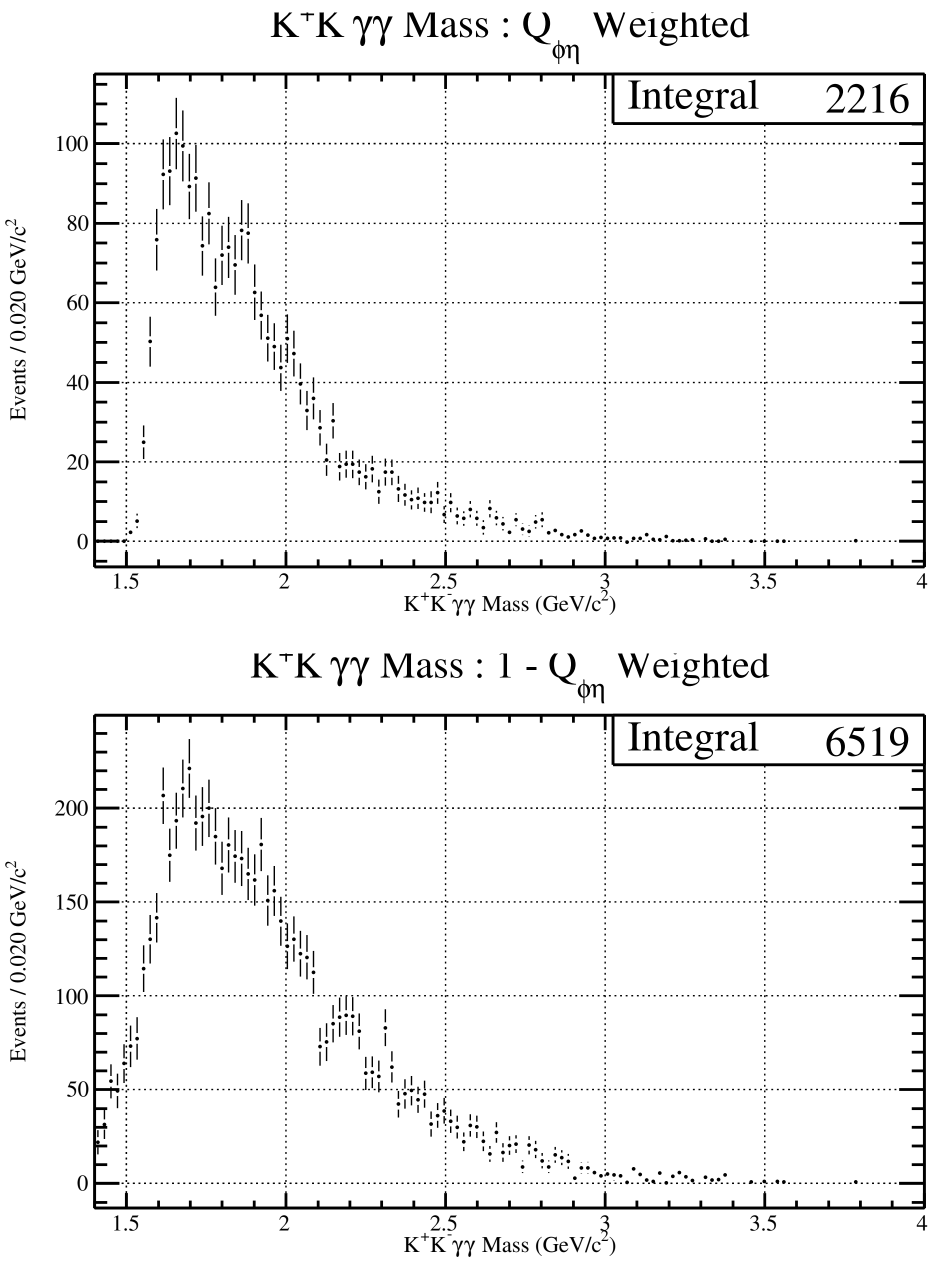

Figure 4.54: The $K^+K^-\gamma\gamma$ invariant mass spectrum with all signal events weighted by $Q_{\phi\eta}$, not acceptance corrected.

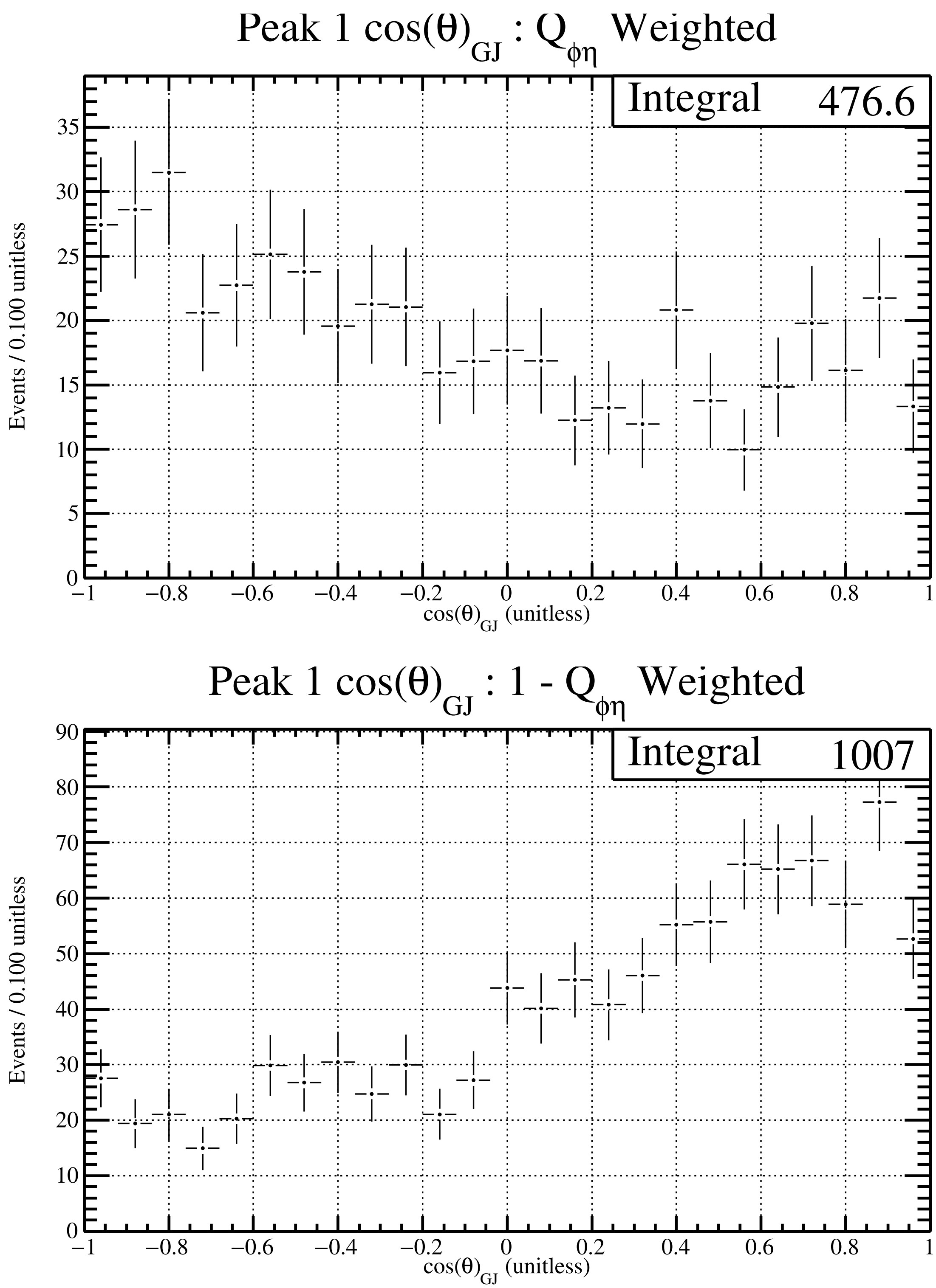

Figure 4.55: The $cos(\theta)_{GJ}$ distribution for $\phi\eta$ invariant mass between 1.605-1.707 GeV/c^2, not acceptance corrected.

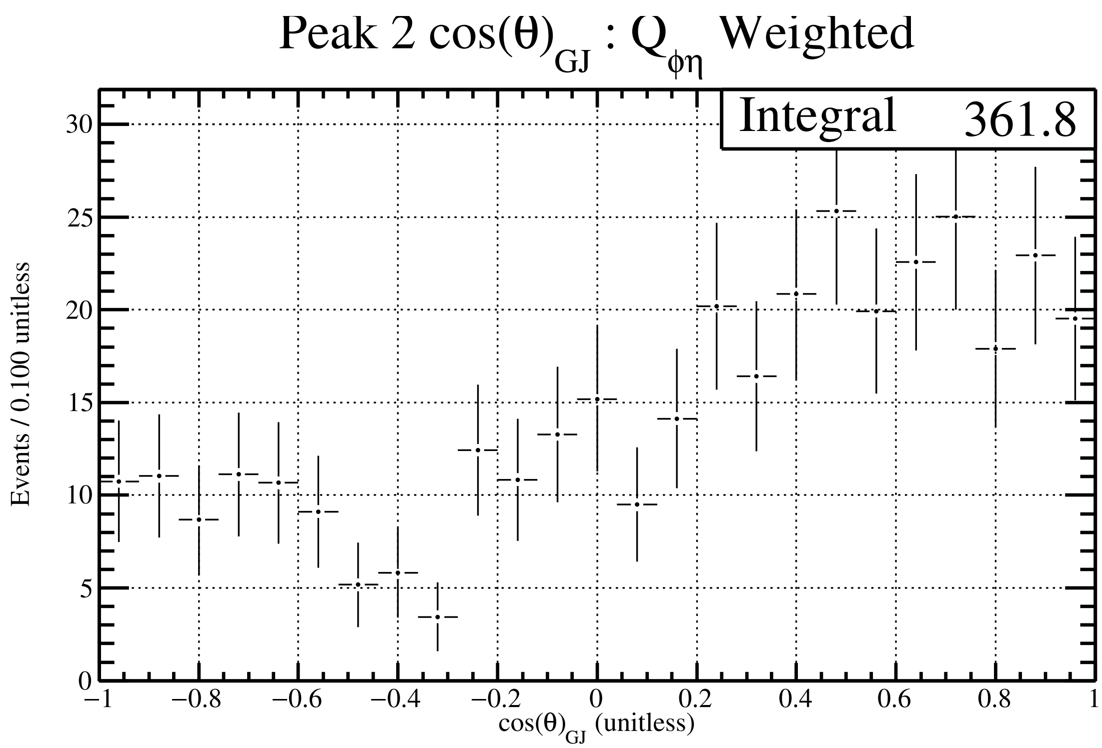

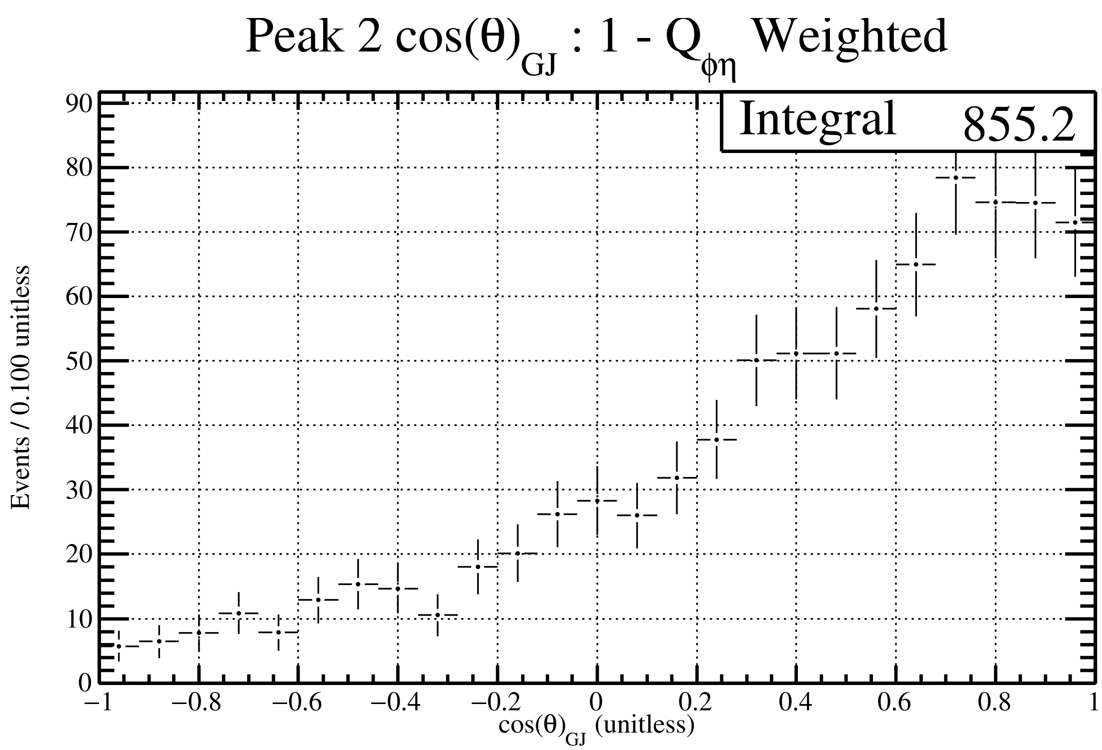

Figure 4.56: The $cos(\theta)_{GJ}$ distribution for $\phi\eta$ invariant mass between 1.809-1.912 GeV/c^2, not acceptance corrected.

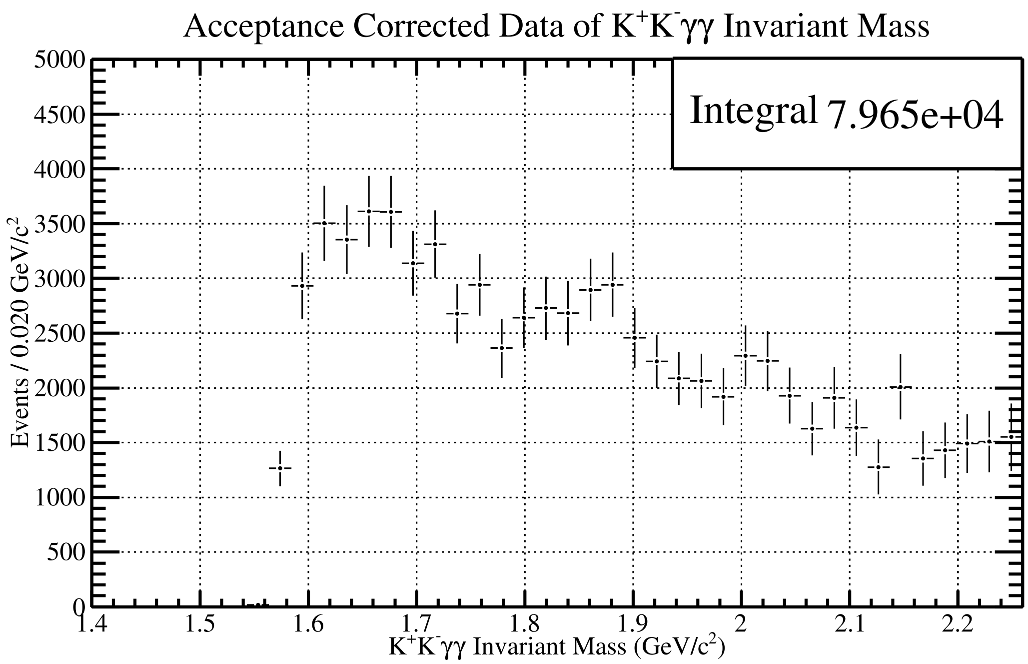

Figure 4.57: he $K^+K^-\gamma\gamma$ invariant mass spectrum with all signal events weighted by $Q_{\phi\eta}$. The spectrum is acceptance corrected as described by Figure [4.25]. The range of the distribution has been changed due to the large error bars at high $\phi\eta$ invariant mass values.

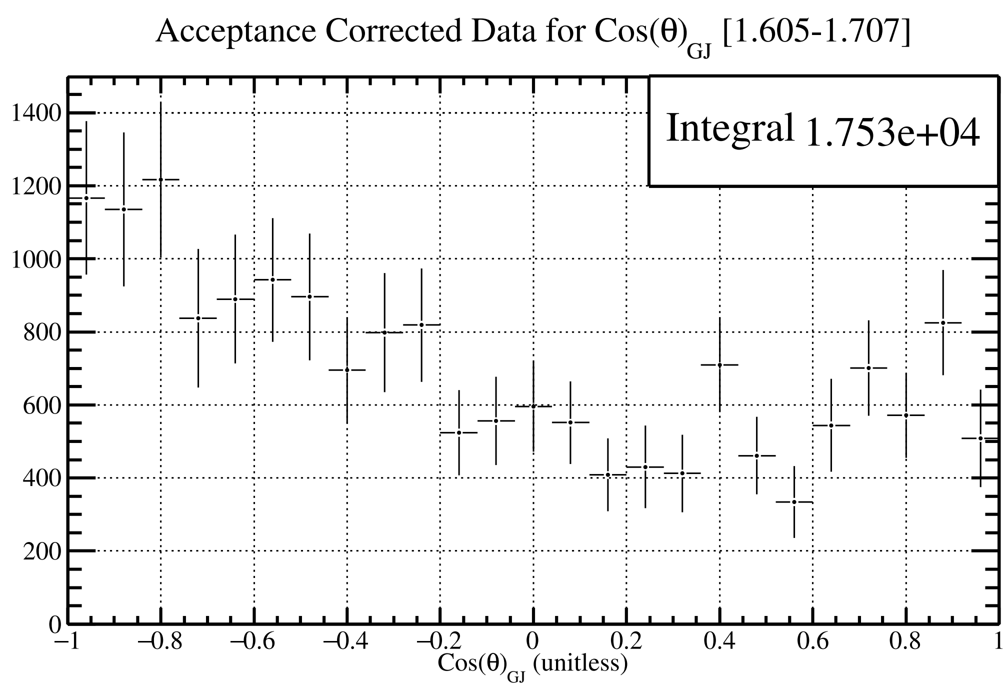

Figure 4.58: The $cos(\theta)_{GJ}$ distribution for $\phi\eta$ invariant mass between 1.605-1.707 GeV/c^2 with the acceptance correction factors described in Figure [4.26].

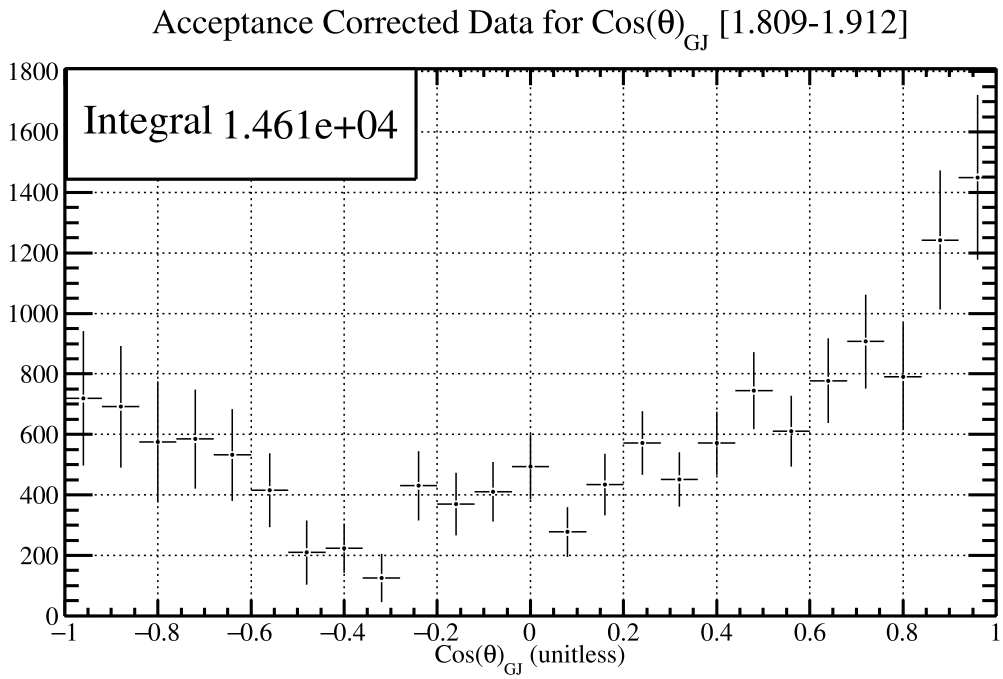

Figure 4.59: The $cos(\theta)_{GJ}$ distribution for $\phi\eta$ invariant mass between 1.809-1.912 GeV/c^2 with the acceptance correction factors described in Figure [4.27].

4.6 Fitting $\phi\eta$ Invariant Mass Plots for Signal Distributions

Since the acceptance of the $\phi\eta$ invariant mass is not reliable near threshold (Figure 4.25), the signal distributions without acceptance corrections will be fit. Using the signal distributions for all selections methods mentioned above, the $\phi\eta$ invariant mass distribution will be tested with four different functions. Each function contains accepted Monte Carlo as a background function. It should be noted that this accepted Monte Carlo sample has a t, and beam energy distribution which matches data. The four different functions are the following:

1. Two interfering relativistic Breit-Wigners as signal, plus a scaled accepted Monte Carlo distribution as background.

2. One low mass relativistic Breit-Wigner as signal, plus a scaled accepted Monte Carlo distribution as background.

3. One high mass relativistic Breit-Wigner as signal, plus a scaled accepted Monte Carlo distribution as background.

4. No signal distribution, only a scaled accepted Monte Carlo distribution as background.

The purpose of fitting the signal distributions with each function mentioned above is to test the probability of structures existing within the data set. More specifically, this method will test the probability of observing: two structures, only one low mass structure, only one

high mass structure, or no structures at all.
The signal fit that will be used for each function is described by Equation 4.22.

$$|Q(m)|^2 = A * |\frac{F_1(m)}{F_1(m_{Peak1})} * \Delta_1(m) + re^{i\varphi} * \frac{F_3(m)}{F_3(m_{Peak2})} * \Delta_3(m)|^2 \quad (4.22)$$

This equation in closely related to Equation 4.3 except that there is an additional relativistic Breit-Wigner, and the Blatt-Weisskopf centrifugal-barrier factors are normalized. This additional relativistic Breit-Wigner contains an imaginary coefficient and a Blatt-Weisskopf centrifugal-barrier factor for a spin 3 particle. The purpose of normalizing the Blatt-Weisskopf centrifugal-barrier factors is to have the fit parameter r represent the relative ratio between the amplitudes of the first peak and the second peak. The spin values of 1 and 3 for the first and second peaks were chosen because their mass and width values are comparable to known s$\bar{s}$ resonances in the PDG. The first peak has a similar mass and width to the $\phi(1680)$, which is reported as $(m_{\phi(1680)} = 1680 \pm 20, \sigma_{\phi(1680)} = 150 \pm 50) MeV/c^2$ in the PDG. The second peak has a similar mass and width to the $\phi_3(1850)$, which is reported as $(m_{\phi(1850)} = 1854 \pm 7, \sigma_{\phi(1850)} = 87^{+28}_{-23}) MeV/c^2$ in the PDG.

The signal fit for each distribution will use a total of 7 parameters, 4 of them will be the mass and width of the first and second peak, another 2 will come from the phase and ratio values contained within the complex coefficient, and the last parameter is the overall normalization. The background for each fit is simply the phase space produced by the accepted Monte Carlo multiplied by a normalization coefficient. Therefore, the total function used to fit the $\phi\eta$ invariant mass will have 8 parameters. The difference in each fitting method in terms of their free or fixed parameter values is given in Table 4.6.

Table 4.6: A table which summarizes the parameter ranges or fixed values in rows corresponding to different fit functions for the $\phi\eta$ invariant mass. The parameters A_{sig}, and A_{bg} have units of number of events, m_{Peak1}, σ_{Peak1}, m_{Peak2}, and σ_{Peak2} have units of GeV/c^2, φ has units of radians, and r is unit less.

$\phi\eta$ Invariant Mass Parameter Ranges and Functions:

Functions	A_{sig}	m_{Peak1}	σ_{Peak1}	m_{Peak2}	σ_{Peak2}	r	φ	A_{bg}
1) 2BW + BG	0-100	1.6-1.7	0-0.3	1.8-1.9	0-0.3	0-10	-3.15-3.15	0-0.02
2) Low BW + BG	0-100	1.6-1.7	0-0.3	1.850	0	0	0	0-0.02
3) High BW + BG	0-100	1.680	0	1.8-1.9	0-0.3	1	0	0-0.02
4) BG Only	0	1.680	0	1.850	0	0	0	0-0.02

The last technicality of the $\phi\eta$ invariant mass fit that needs to be addressed is the method for representing the breakup momentum, which will clearly be different than the form used in Subsection 4.2.1. Deriving the breakup momentum in the rest frame of the $\phi\eta$ parent state is straight forward and has the form given in Equation 4.23.

$$|P| = \frac{\sqrt{m^2(m^2 - 2(m_\eta^2 + m_\phi^2)) + (m_\eta^2 - m_\phi^2)}}{2m} \quad (4.23)$$

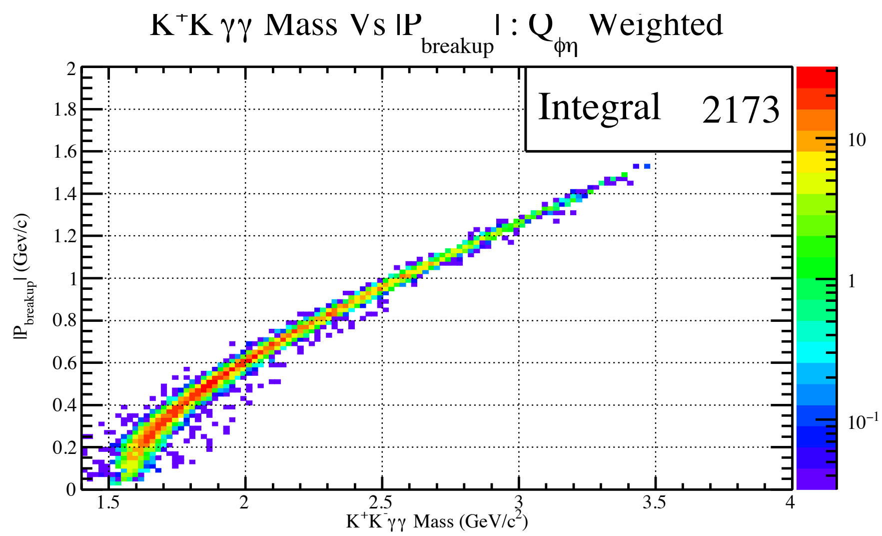

Figure 4.60: The two dimensional color plot of the $K^+K^-\gamma\gamma$ invariant mass vs the break-up momentum. All events are weighted by $Q_{\phi\eta}$.

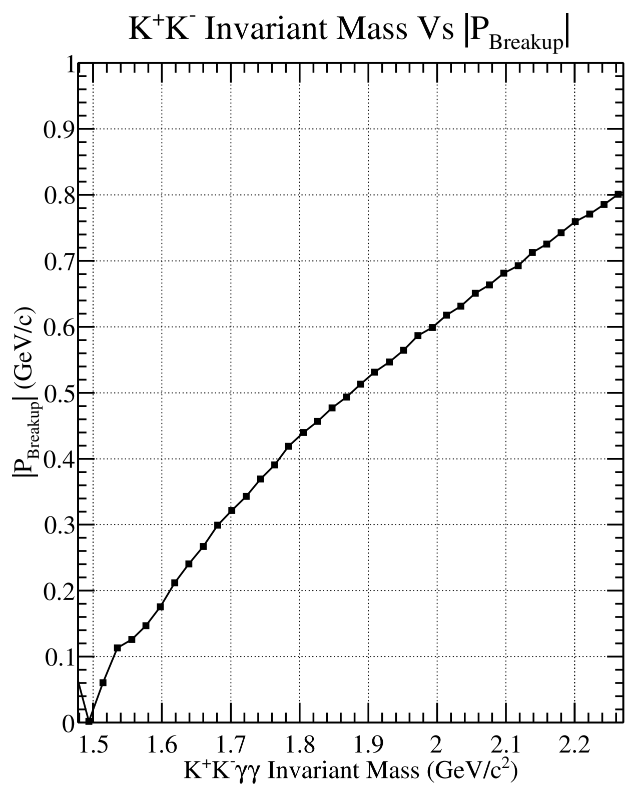

Figure 4.61: An interpolation graph, where the horizontal points are the bin values from Figure [4.60], and the vertical values are the mean values for the break-up momentum projections.

The issue with this Equation 4.23 as compared to $\sqrt{m^2 - (2m_K)^2}$ is the fact that the invariant mass values of m_η and m_ϕ have a width, whereas m_K does not. This means that the breakup momentum for the $\phi\eta$ invariant mass cannot be represented functionally, and therefore data must be used. To do this, the breakup momentum and $\phi\eta$ invariant mass is plotted on a two dimensional color plot for each event (Figure [4.60]). All events are weighted with $Q_{\phi\eta}$ in order to use the purest sample.

Looping through each bin of $K^+K^-\gamma\gamma$ invariant mass from Figure [4.60] and projecting onto the vertical axis will provide the $\phi\eta$ break-up momentum spread for that mass range. Taking the mean break-up momentum value for each bin provides a data driven interpolation for Equation 4.23. More specifically, for a given $\phi\eta$ invariant mass value, a breakup momentum is assigned based on the linear fit between two points given in Figure [4.61]. Using this breakup momentum, the signal distribution for each selection method can be fit.

4.6.1 Elliptical Fits

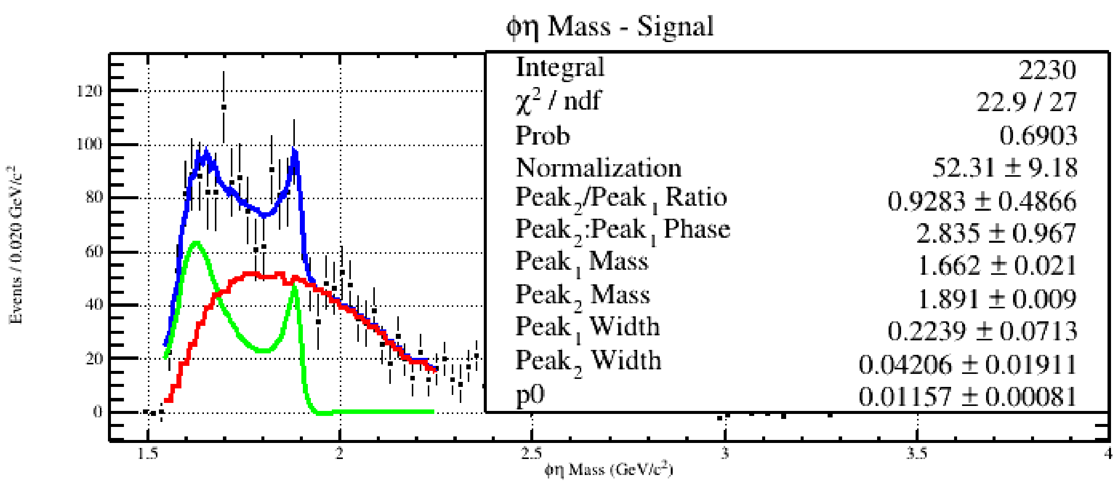

Figure 4.62: Fit of the $\phi\eta$ mass using the elliptical signal distribution in Figure [4.30]. The fit contains two interfering relativistic Breit-Wigners as signal, plus a scaled accepted Monte Carlo distribution as background. The χ^2/ndf, probability, and fit parameters are all given in the stat box.

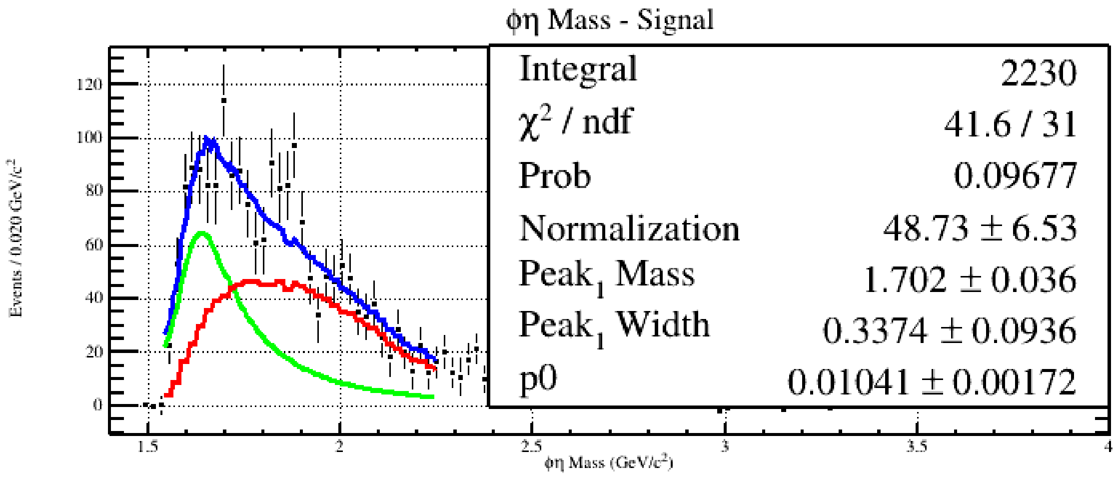

Figure 4.63: Fit of the $\phi\eta$ mass using the elliptical signal distribution in Figure [4.30]. The fit contains one low mass relativistic Breit-Wigner as signal, plus a scaled accepted Monte Carlo distribution as background. The χ^2/ndf, probability, and fit parameters are all given in the stat box.

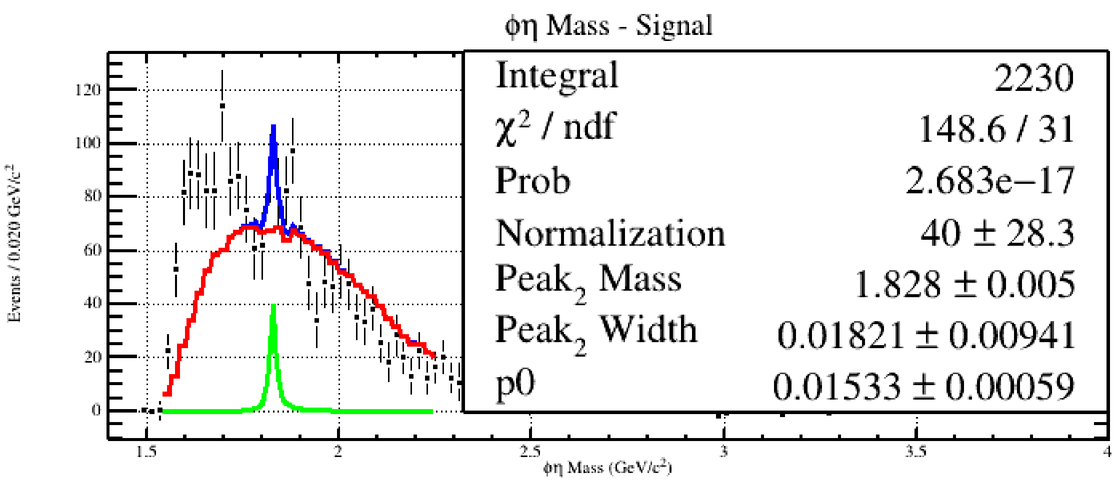

Figure 4.64: Fit of the $\phi\eta$ mass using the elliptical signal distribution in Figure [4.30]. The fit contains one high mass relativistic Breit-Wigner as signal, plus a scaled accepted Monte Carlo distribution as background. The χ^2/ndf, probability, and fit parameters are all given in the stat box.

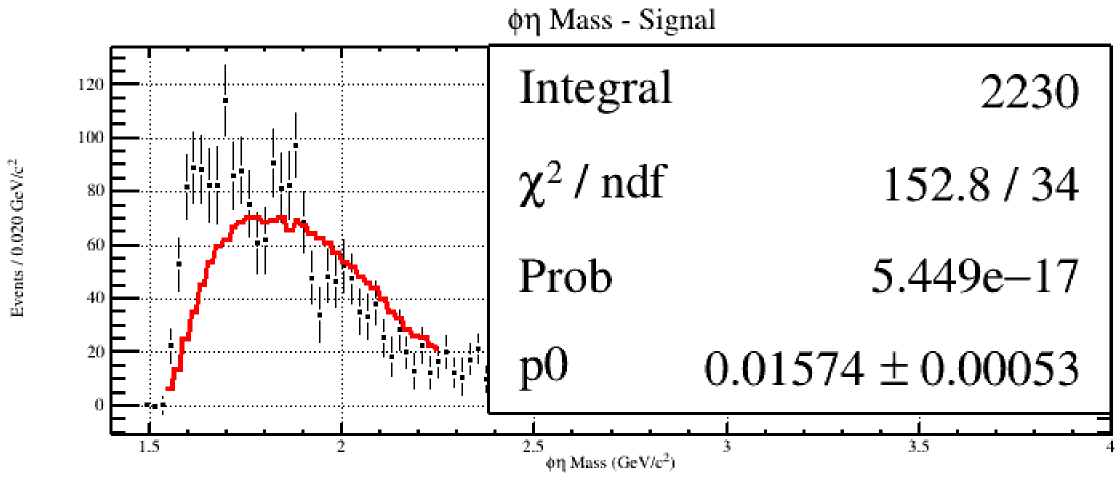

Figure 4.65: Fit of the $\phi\eta$ mass using the elliptical signal distribution in Figure [4.30]. The fit contains no signal distribution, only a scaled accepted Monte Carlo distribution as background. The χ^2/ndf, probability, and fit parameters are all given in the stat box.

4.6.2 Q_ϕ Weighting, η Side-band Subtracted Fits

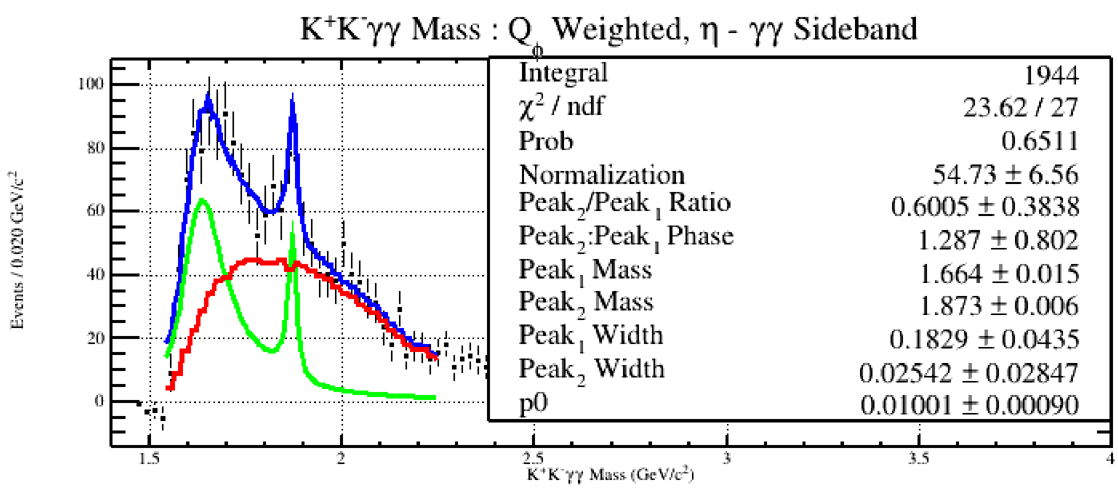

Figure 4.66: Fit of the $\phi\eta$ mass using the Q_ϕ Weighted, $\eta - \gamma\gamma$ Sideband distribution in Figure [4.38]. The fit contains two interfering relativistic Breit-Wigners as signal, plus a scaled accepted Monte Carlo distribution as background. The χ^2/ndf, probability, and fit parameters are all given in the stat box.

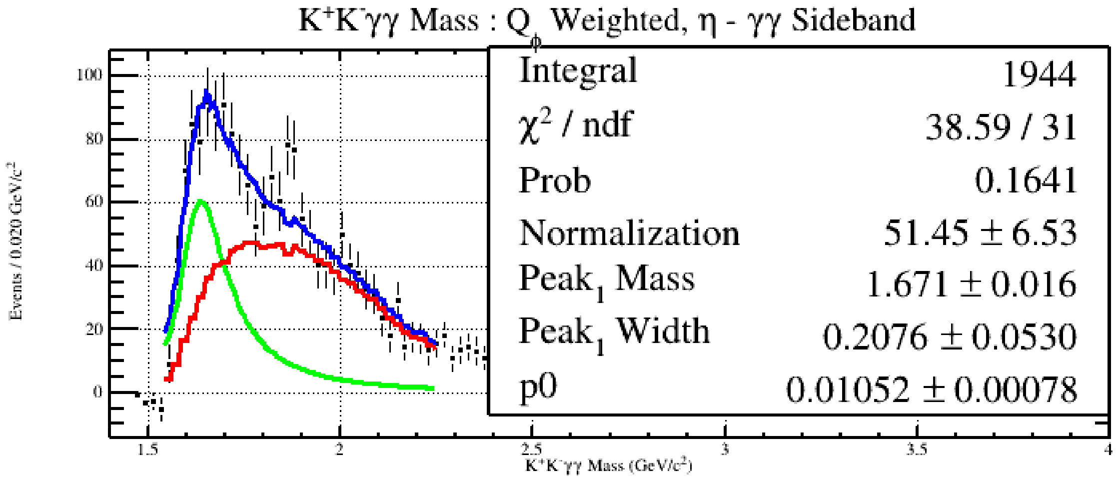

Figure 4.67: Fit of the $\phi\eta$ mass using the Q_ϕ Weighted, $\eta - \gamma\gamma$ Sideband distribution in Figure [4.38]. The fit contains one low mass relativistic Breit-Wigner as signal, plus a scaled accepted Monte Carlo distribution as background. The χ^2/ndf, probability, and fit parameters are all given in the stat box.

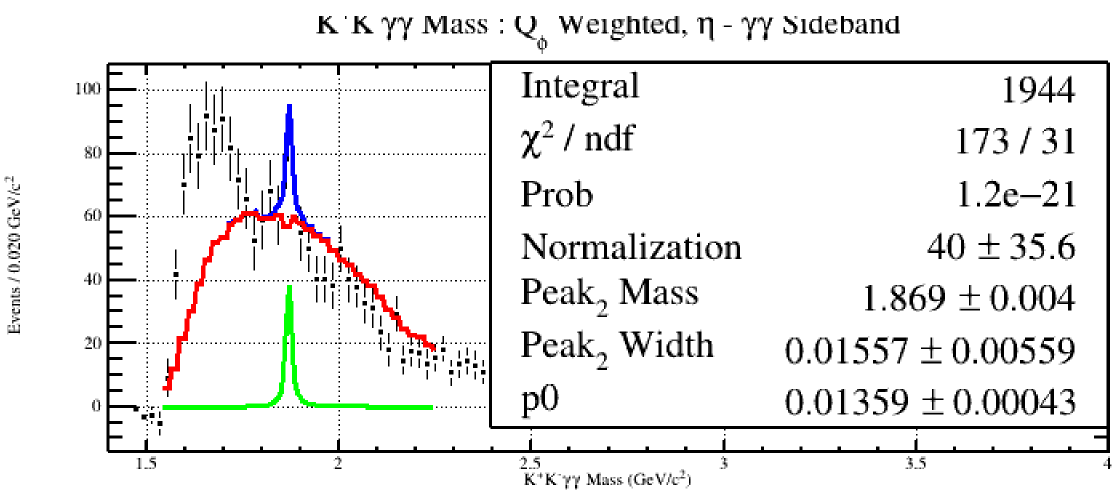

Figure 4.68: Fit of the $\phi\eta$ mass using the Q_ϕ Weighted, $\eta - \gamma\gamma$ Sideband distribution in Figure [4.38]. The fit contains one high mass relativistic Breit-Wigner as signal, plus a scaled accepted Monte Carlo distribution as background. The χ^2/ndf, probability, and fit parameters are all given in the stat box.

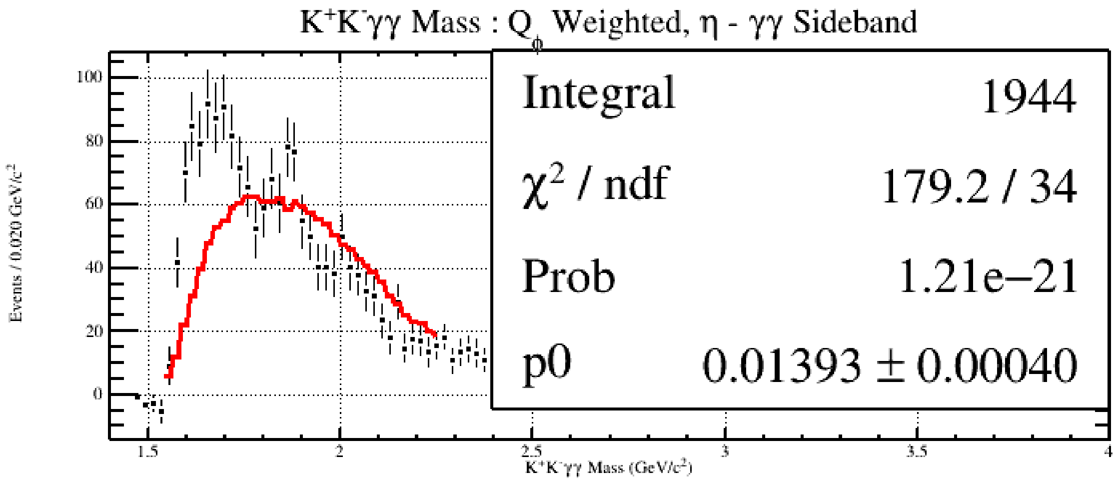

Figure 4.69: Fit of the $\phi\eta$ mass using the Q_ϕ Weighted, $\eta - \gamma\gamma$ Sideband distribution in Figure [4.38]. The fit contains no signal distribution, only a scaled accepted Monte Carlo distribution as background. The χ^2/ndf, probability, and fit parameters are all given in the stat box.

4.6.3 Q_η Weighting, K^+K^- Side-band Subtracted Fits

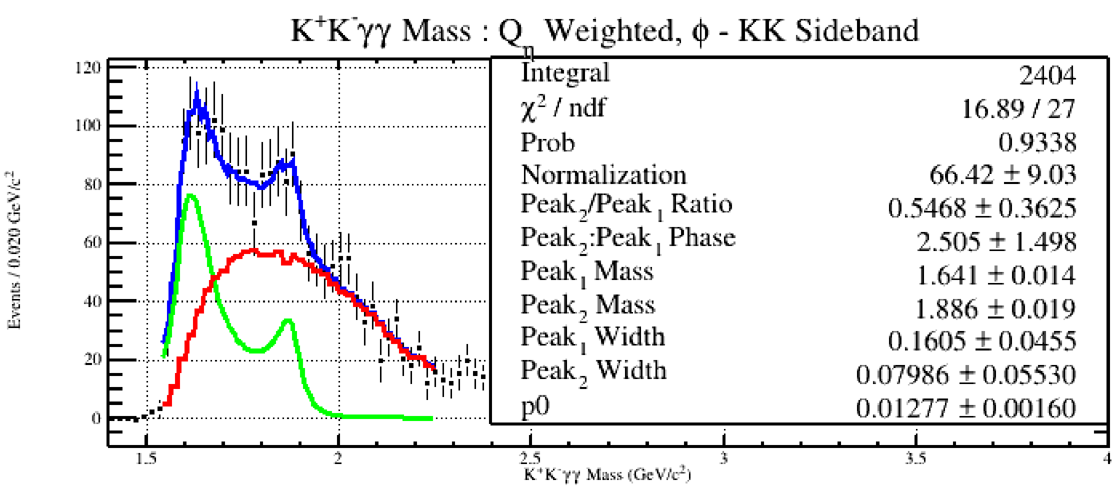

Figure 4.70: Fit of the $\phi\eta$ mass using the Q_η Weighted, ϕ−KK Sideband distribution in Figure [4.46]. The fit contains two interfering relativistic Breit-Wigners as signal, plus a scaled accepted Monte Carlo distribution as background. The χ^2/ndf, probability, and fit parameters are all given in the stat box.

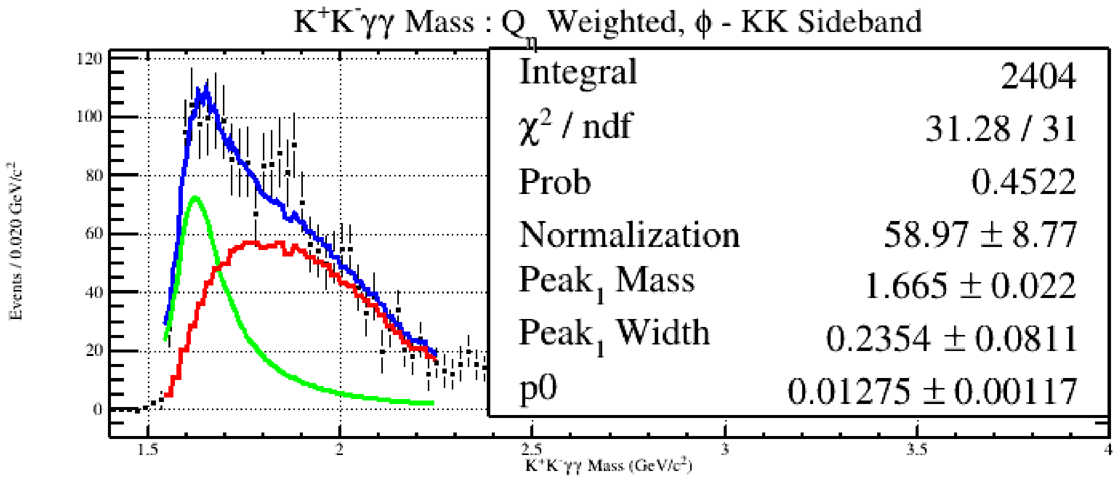

Figure 4.71: Fit of the $\phi\eta$ mass using the Q_η Weighted, $\phi-$KK Sideband distribution in Figure [4.46]. The fit contains one low mass relativistic Breit-Wigner as signal, plus a scaled accepted Monte Carlo distribution as background. The χ^2/ndf, probability, and fit parameters are all given in the stat box.

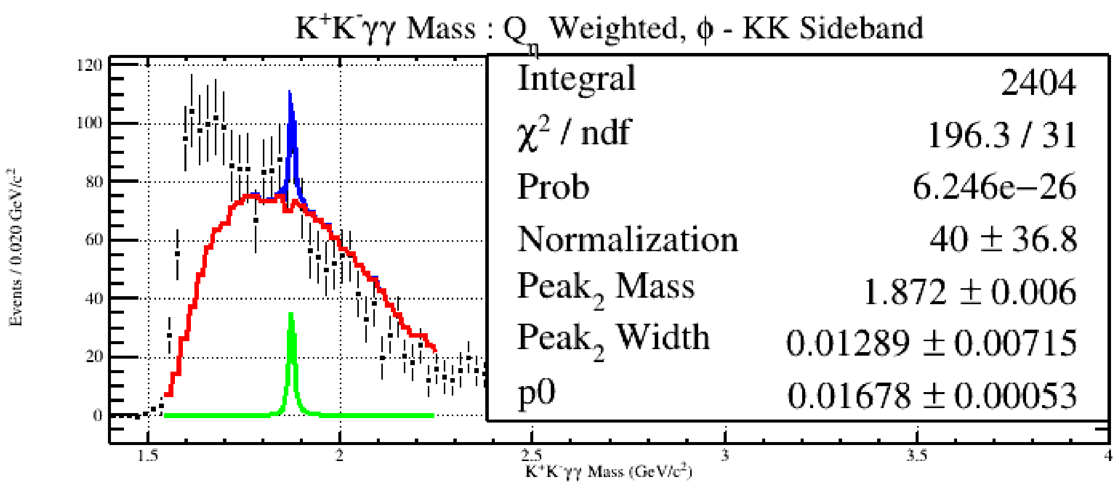

Figure 4.72: Fit of the $\phi\eta$ mass using the Q_η Weighted, $\phi-$KK Sideband distribution in Figure [4.46]. The fit contains one high mass relativistic Breit-Wigner as signal, plus a scaled accepted Monte Carlo distribution as background. The χ^2/ndf, probability, and fit parameters are all given in the stat box.

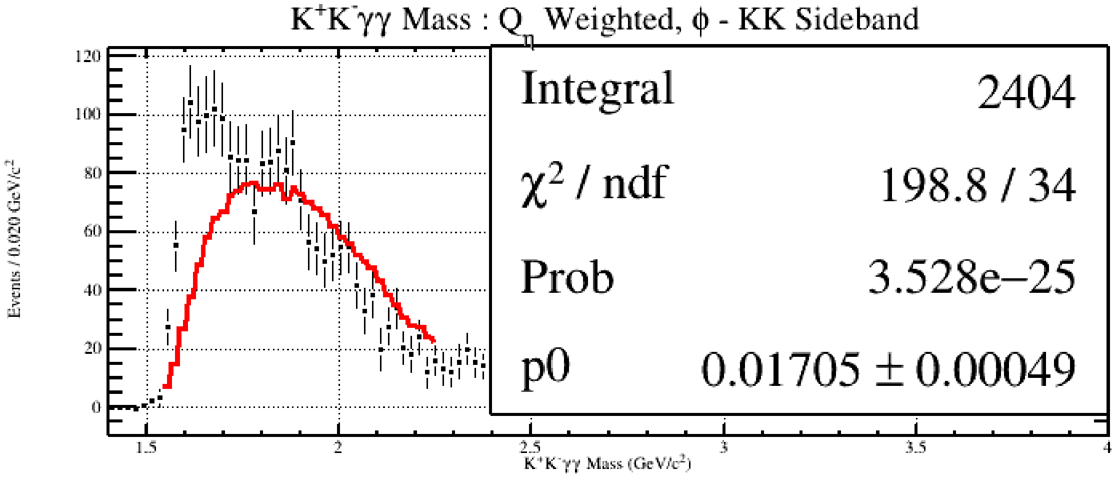

Figure 4.73: Fit of the $\phi\eta$ mass using the Q_η Weighted, ϕ−KK Sideband distribution in Figure [4.46]. The fit contains no signal distribution, only a scaled accepted Monte Carlo distribution as background. The χ^2/ndf, probability, and fit parameters are all given in the stat box.

4.6.4 $Q_{\phi\eta}$ Weighting Fits

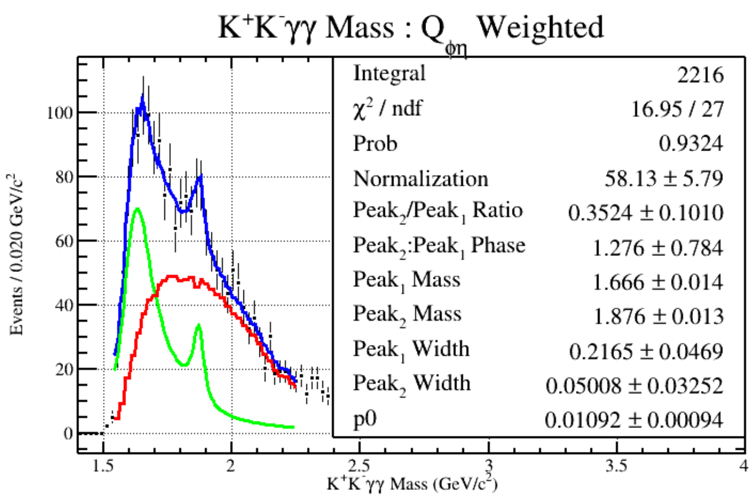

Figure 4.74: Fit of the $\phi\eta$ mass using the $Q_{\phi\eta}$ Weighted distribution in Figure [4.54]. The fit contains two interfering relativistic Breit-Wigners as signal, plus a scaled accepted Monte Carlo distribution as background. The χ^2/ndf, probability, and fit parameters are all given in the stat box.

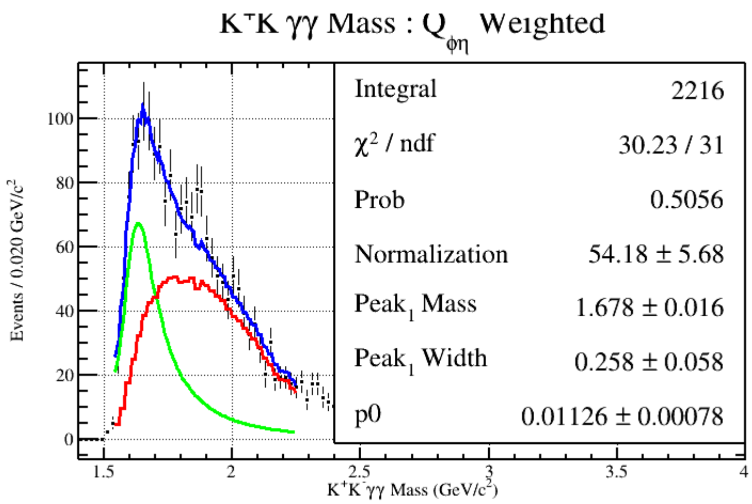

Figure 4.75: Fit of the $\phi\eta$ mass using the $Q_{\phi\eta}$ Weighted distribution in Figure [4.54]. The fit contains one low mass relativistic Breit-Wigner as signal, plus a scaled accepted Monte Carlo distribution as background. The χ^2/ndf, probability, and fit parameters are all given in the stat box.

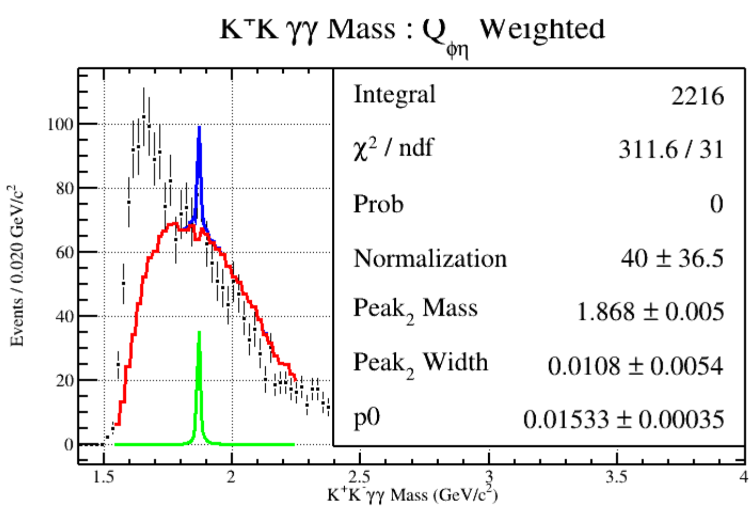

Figure 4.76: Fit of the $\phi\eta$ mass using the $Q_{\phi\eta}$ Weighted distribution in Figure [4.54]. The fit contains one high mass relativistic Breit-Wigner as signal, plus a scaled accepted Monte Carlo distribution as background. The χ^2/ndf, probability, and fit parameters are all given in the stat box.

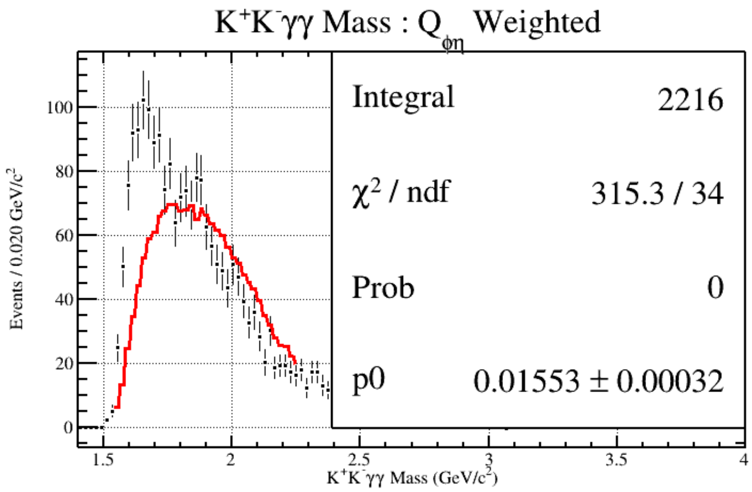

Figure 4.77: Fit of the $\phi\eta$ mass using the $Q_{\phi\eta}$ Weighted distribution in Figure [4.54]. The fit contains no signal distribution, only a scaled accepted Monte Carlo distribution as background. The χ^2/ndf, probability, and fit parameters are all given in the stat box.

4.6.5 Tabular Summary of Fit Results and Discussion

Table 4.7: A table which summarizes the fits which utilized two interfering relativistic Breit-Wigners as signal, plus a scaled accepted Monte Carlo distribution as background.

Two Interfering Relativistic Breit-Wigners + Accepted Monte Carlo:

Selection Method	Peak$_1$ Mass (GeV/c^2) Peak$_2$ Mass (GeV/c^2)	Peak$_1$ Width (GeV/c^2) Peak$_2$ Width (GeV/c^2)	Probability
Elliptical	1.662 ± 0.021 1.891 ± 0.009	0.2239 ± 0.0713 0.04206 ± 0.01911	0.6903
Q_ϕ, $\eta-\gamma\gamma$	1.664 ± 0.015 1.873 ± 0.006	0.1829 ± 0.0435 0.02542 ± 0.02847	0.6511
Q_η, $\phi-$KK	1.641 ± 0.014 1.886 ± 0.019	0.1605 ± 0.0455 0.07986 ± 0.05530	0.9338
$Q_{\phi\eta}$	1.666 ± 0.014 1.876 ± 0.013	0.2165 ± 0.0469 0.05008 ± 0.03252	0.9324

Table 4.8: A table which summarizes the fits which utilized one low mass relativistic Breit-Wigner as signal, plus a scaled accepted Monte Carlo distribution as background.

Low Mass Relativistic Breit-Wigner + Accepted Monte Carlo:

Selection Method	Peak$_1$ Mass (GeV/c^2)	Peak$_1$ Width (GeV/c^2)	Probability
Elliptical	1.702 ± 0.036	0.3374 ± 0.0936	0.09677
Q_ϕ, $\eta-\gamma\gamma$	1.671 ± 0.016	0.2076 ± 0.0530	0.1641
GeV/c^2 Q_η, $\phi-$KK	1.665 ± 0.022	0.2354 ± 0.0811	0.4522
$Q_{\phi\eta}$	1.678 ± 0.016	0.258 ± 0.058	0.5056

Table 4.9: A table which summarizes the fits which utilized one high mass relativistic Breit-Wigner as signal, plus a scaled accepted Monte Carlo distribution as background.

High Mass Relativistic Breit-Wigner + Accepted Monte Carlo:

Selection Method	Peak$_2$ Mass (GeV/c^2)	Peak$_2$ Width (GeV/c^2)	Probability
Elliptical	1.828 ± 0.005	0.01821 ± 0.00941	2.683e-17
Q_ϕ, $\eta-\gamma\gamma$	1.869 ± 0.004	0.01557 ± 0.00559	1.2e-21
Q_η, $\phi-$KK	1.872 ± 0.006	0.01289 ± 0.00715	6.246e-26
$Q_{\phi\eta}$	1.868 ± 0.005	0.0108 ± 0.0054	0

Table 4.10: A table which summarizes the fits which utilized only the accepted Monte Carlo distribution.

Accepted Monte Carlo:

Selection Method	Probability
Elliptical	5.449e-17
Q_ϕ	1.21e-21
Q_η	3.528e-25
$Q_{\phi\eta}$	0

Since each selection method appeared to contain two different structures in the $\phi\eta$ invariant mass, it was necessary study the validity of them by means of fitting with several different functions. Each function returned a different set of parameters, and a probability. Using the probability of each function, a number of deductions can be made. Given the set of probabilities presented in Table 4.10, it is clear that the signal data for each selection method is not a manifestation of $\phi\eta$ phase space. In addition, the probabilities presented in Table 4.8 as compared to Table 4.9, may indicated that the first peak carries a greater significance than the second peak. Lastly, the probabilities presented in Table 4.7 as compared to all other tables shows that the fit that contains two interfering relativistic Breit-Wigners always has a higher probability than any other function, regardless of selection method. This large difference in probability is good evidence that there are two structures in the $\phi\eta$ invariant mass.

Since Table 4.7 always contains the highest probabilities, the parameter values from that table will be used to approximate the mass and width of each peak. The weighted average for the mass, width, and errors for each peak will be calculated using Equation 4.24 and Equation 4.25.

$$\bar{x} \pm \delta\bar{x} = \frac{\Sigma_i w_i x_i}{\Sigma_i w_i} \pm (\Sigma_i w_i)^{-1/2} \tag{4.24}$$

$$w_i = 1/(\delta x_i)^2 \tag{4.25}$$

Plugging in the mass, width, and error values for each selection method in Table 4.7, it was found that the first peak had a weighted average of $(m_{Peak1} = 1.657 \pm 0.008)\frac{GeV}{c^2}$ for the invariant mass, and a weighted average of $(\sigma_{Peak1} = 0.190 \pm 0.024)\frac{GeV}{c^2}$ for the width. In addition, the second structure had a weighted average of $(m_{Peak2} = 1.879 \pm 0.004)\frac{GeV}{c^2}$ for the invariant mass, and a weighted average of $(\sigma_{Peak2} = 0.042 \pm 0.014)\frac{GeV}{c^2}$ for the width.

The weighted mass and width values for the first peak closely resemble that of the $\phi(1680)$, which is the radially excited version of the $\phi(1020)$, and has been mentioned several times throughout this thesis. The $\phi(1680)$ is assumed to be a pure $s\bar{s}$ state according to the PDG. However, the structure observed in this data cannot be identified as the $\phi(1680)$ due to the lack of statistics and therefore the inability to perform a partial wave analysis which provides the quantum numbers of the state. The $\phi(1680)$ has been seen in photoproduction, but only from KK final states and not from $\phi\eta$. It should be noted that the $\phi(1680)$ invariant mass value reported by photoproduction experiments is significantly higher than those reported by e^+e^- collider experiments.

Furthermore, the weighted mass and width values for the second peak closely resemble that of the $\phi_3(1850)$. The $\phi_3(1850)$ is assumed to be a pure $s\bar{s}$ state according to the PDG. However, the structure observed in this data cannot be identified as the $\phi_3(1850)$ due to the lack of statistics and therefore the inability to perform a partial wave analysis which provides the quantum numbers of the state. Some interesting facts about the $\phi_3(1850)$ is that it has only been seen in KK and KK^* final states from experiments with a kaon beam. The $\phi_3(1850)$ has never been seen in photoproduction or e^+e^- collider experiments. It should also be noted that an s$\bar{s}$ triplet state of $(1^{--}, 2^{--}, 3^{--})$ is expected to be close to this invariant mass value [4]. Given Table 1.2 from Chapter 1, it is clear that all of these states, as well as the $\phi(1680)$, can decay to a $\phi\eta$ final state. However, further investigation of this final state is needed in order to properly identify the observed structures. Analyzing the Spring 2018 Physics Run and the Fall 2018 Physics run at GlueX will more than quadruple the current physics data set, and will allow for a more diverse investigation of these structures. Some of these additional investigations may include a beam asymmetry, cross section, or a partial wave analysis.

Bibliography

[1] Bradford E. Cannon. *Search for New and Unusual Strangeonia States Using $\gamma p \to p\phi\eta$ with GlueX at Thomas Jefferson National Accelerator Facility*. PhD thesis, Florida State University, 2019.

[2] H. Al Ghoul *et al.* Measurement of the beam asymmetry Σ for π^0 and η photoproduction on the proton at E_γ=9 GeV. *Phys. Rev. C*, 2017.

[3] C.A. Meyer M. Williams, M. Bellis. Separating signals from non-interfering backgrounds using probabilistic event weightings. *arXiv preprint arXiv:0804.3382*, 2008.

[4] P. Eugenio *et al.* Search for new forms of hadronic matter in photoproduction. *JLab Proposal E-04-005*, 2010.